

**UCSF**

**UC San Francisco Electronic Theses and Dissertations**

**Title**

Investigating the impacts of lymphocytes on recovery from brain injury

**Permalink**

<https://escholarship.org/uc/item/1f2274s9>

**Author**

Mroz, Nicholas M

**Publication Date**

2024

Peer reviewed|Thesis/dissertation

Investigating the impacts of lymphocytes on recovery from brain injury

by  
Nicholas Mroz

DISSERTATION  
Submitted in partial satisfaction of the requirements for degree of  
DOCTOR OF PHILOSOPHY

in  
Biomedical Sciences

in the  
GRADUATE DIVISION  
of the  
UNIVERSITY OF CALIFORNIA, SAN FRANCISCO

Approved:

DocuSigned by:  
*Adrian Erlebacher* Adrian Erlebacher  
F0E47A73FD8E419... Chair

DocuSigned by:  
*Eric Huang* Eric Huang

DocuSigned by:  
*Anna Victoria Molofsky* Anna Victoria Molofsky

DocuSigned by:  
*Ari Molofsky* Ari Molofsky

DocuSigned by:  
*Tien Peng* Tien Peng  
256E38508AB94C9... Committee Members



## Acknowledgements

Working towards a PhD has been the most difficult undertaking of my life to date. It has redefined the lowest points in my life and brought me to my breaking point more times than I can count. Over the course of my PhD, I endured a global pandemic, the deaths of a best friend and a grandmother, countless heartbreaks, a contentious and drawn-out strike, an apartment fire and subsequent burglary that temporarily made me unhoused, and crippling anxiety and depression, all on top of the seemingly endless existential dread of pursuing a long-term research project with unclear checkpoints and an ambiguous endpoint. It has been the most challenging, dark, and isolating phase of my life. I could not have made it through without an amazing support system.

I am incredibly lucky to have joined Ari Molofsky's lab. Ari is the best mentor I have ever had, and I am fortunate to have been able to work under his guidance over the past 6.5 years. Ari was invaluable to my training as a scientist. Ari taught me how to analyze data, how to make figures and slides, and how to effectively present my work. He had an uncanny ability to think of new ideas and experiments – sometimes overwhelmingly so – and I admire his knowledge that seemingly spans across every organ system and field of research. I appreciate his ability to see the 'forest through the trees,' his never-ending optimism (even if it at times teetered towards delusion), and his earnest approach to science – namely "find cool shit and publish cool shit." Ari is not only an intelligent scientist and physician, but one of the most honest and collaborative people in academia and, in my opinion, the gold standard of what principal investigators should be. Ari was always transparent about the shortcomings of our work and never hesitated to help someone else with their research by sharing our mice, our reagents, or his time. Ari is a kind, caring, amicable mentor who not only cares about your science and career, but sees you as a human deserving of respect, empathy, and happiness at all times. Ari never puts you down, but instead addresses problems or shortcomings with compassion and kindness. Ari never stopped believing in me and my capabilities, even at times when I had. Ari was there for me at my darkest

moments and always respected my bandwidth, mental health, and work/life balance. I am so thankful and honored to have been your first graduate student. I could not have done this in any other lab or with any other advisor. I am grateful to be staying in the greater Molofsky family, and I look forward to years of work and friendship to come.

Ari also cultivated a phenomenal lab environment full of some of the smartest, kindest, and most collaborative scientists I have ever met. It was a pleasure to work with my labmates every day, and I can honestly say that I am friends with each and every one of them. In particular, I am extremely appreciative of Madelene Dahlgren, who mentored me during my rotation and taught me everything I know about flow cytometry, sorting, co-cultures, and mouse work. I am thankful to all the mentors and friends I have had in Ari's lab, including (but not limited to) Kelly Cautivo, Julia Sbierski-Kind, Marcela Taruselli, Joanna Balcerek, Julia Nilsson, and Dean Merrill – I have learned so much from you all and respect you all so deeply as scientists. Thank you to Peri Matatia, Elina Wells, and Abram Rodriguez for being amazing lab managers on top of being talented technicians. I am particularly grateful for my fellow grad students in the lab: Anthony Chang, Sofia Caryotakis, and Nathan Ewing-Crystal. I'm so lucky that I was able to work alongside such caring and intelligent people in the same position as me, who were able to understand what I was going through. I'm so glad we were able commiserate, laugh, drink, and work together (not all at the same time). I'm especially thankful for Nathan, my fellow neuroimmunologist, for all of his help with my projects, for his reliability and trustworthiness, and for his endless patience in teaching me over and over again how to use Imaris. I'm grateful to have mentored you as my rotation student, proud of the scientist you've become, and lucky to call you a close friend. In many ways, the lab was my home away from home and I will greatly miss my lab family.

I am lucky that I was able to closely collaborate with Anna Molofsky and her lab and to be *de facto* co-mentored by Anna. I am so grateful to Anna for teaching me neuroscience fundamentals and for her critical feedback and perspective as a neuroscientist throughout my PhD. None of my research could not have been accomplished without Anna's guidance, foresight,

and expertise. I'm also grateful for the mentors and collaborators I've worked with in Anna's lab, especially Rafael Han, Leah Dorman, and Jerika Barron. Rafael began the ILC2 stoke project and taught me how to perform brain surgery on mice. Rafael and I worked together on many critical experiments across both of my main projects (including a stressful single cell RNA sequencing experiment and comically large TBI flow harvests), none of which could have been accomplished without his help and guidance. Leah was my bioinformatic mentor and taught me everything I know about single cell RNA sequencing analysis – without her time, expertise, and code, I could not have analyzed any of this data. Jerika was also a close collaborator who taught me everything I know about brain imaging and synapse staining and quantification, and also provided me with numerous mouse lines. I am so grateful to have helped Jerika with many key experiments for her paper, as I learned a great deal from her about how to be a rigorous scientist and how to assemble, write, and submit a manuscript. I thank Jerika tremendously for all of her help, guidance, and mentorship over the years. I also want to thank Anna's former lab manager, Hiromi Inoue, who was instrumental in helping us establish a working stereotactic surgical set up at Parnassus, and Iliia Vainchtein, who was instrumental in processing our single cell RNA sequencing samples. I am so lucky to have been peripherally part of a second Molofsky lab and I am so grateful to be joining this lab shortly.

I also want to thank all of my other mentors at UCSF. Thank you to the PIs on HSW12 – Mike Rosenblum, Tiffany Scharschmidt, and Cliff Lowell – for cultivating a healthy, friendly, and collaborative research environment. I cannot imagine a better place to work during my PhD. I am grateful for all of the feedback and ideas from everyone on HSW12 over the years at floor meeting, for all the help and sharing of reagents and resources, and for all of the fun happy hours and Lab Olympics. Thank you to Richard Locksley for teaching me everything I know about type 2 immunity and for taking me on as a fresh and naive rotation student. Rich is a pillar of the type 2 immunity research community and a wealth of knowledge, and I am still grateful for being able to learn so much from the small amount of time I was in Rich's lab. Rich and his lab also created a

majority of the mutant mouse lines used throughout my PhD, and I am so thankful that Rich and his current and former trainees so generously shared all of these mice. I want to thank Claire O'Leary and Maya Kotas for being such excellent rotation mentors and for teaching me so many fundamental techniques and concepts in tissue immunology research. Working with you both made me fall in love with tissue immunology and mouse work and I am so grateful to have been mentored by you so early on in my PhD career. Thank you to Hong-Erh for all of your help and for your countless Nippo harvests and to Roberto Ricardo-Gonzalez for sharing mouse lines. Thank you to the members of my thesis committee – Adrian Erlebacher, Tien Peng, and Eric Huang – for your feedback and guidance over the years that greatly improved my research projects. I am also incredibly grateful for my amazing collaborators, Jeanne Paz and Agnieszka Ciesielska, without whom our project on TBI could not be possible. I am thankful for all of Agnieszka's work on our project, as she spent countless hours performing TBI surgeries, preparing samples for me, and analyzing seizure recordings. I am also grateful for Jeanne for all of her guidance and feedback on the project over the years and for her perspective and expertise on neuroscience and epilepsy. I truly could not have worked on such interdisciplinary projects and used such sophisticated mouse tools without the resources and collaborative research community at UCSF and the Gladstone.

Lastly, I want to thank my family and friends for being such an amazing support system. An absolutely massive thank you to my parents, Dee and Tony, for their unconditional love and support. I am insanely lucky to have such caring, kind, understanding, generous, and supportive parents. I could not have made it through grad school without your emotional and financial support. I am so thankful that you encouraged me to pursue science from an early age and supported me even when I decided to move across the country to 'follow my dreams.' Thank you for believing in me, for always having my back, for guiding me through my darkest moments, and for seeing my worth when I cannot. Thank you to my friends Catherine Zhang, Rachel Sarnie, Candy Rui, Jake Gardner, Frank Buquicchio, and Russell DeBarge for your unconditional support

throughout this process, for helping to escape and distract myself, and for helping me to have fun and enjoy my life despite being in grad school. I am grateful that Frank, Russell, and I all went through graduate school at the same time, as we were able to support each other through all of the associated trials and tribulations and make each other laugh and see the bigger picture. I'm grateful for all of the bioinformatic help that Frank and Russell provided me over the years, as their coding skills far exceed mine. I want to particularly thank my best friend Russell for being one of the first friends I made in the program and for truly understanding me and my various quirks and neuroses. I am so thankful for your unwavering friendship over the years, as you made me feel like I was not alone, and for always being there for me. If there is one positive thing to have come from grad school, it was meeting you. Lastly, I have to thank my pup niece Sadie (a.k.a., Stinky, Nasty, Babygirl, Bby, etc.) for being a constant light in my life and for being the cutest, sweetest angel of a dog. I'm so glad you were in my life and able to anchor me throughout grad school.



## Author Contributions

**Chapters 1 and 5** were written by Nicholas Mroz.

**Chapter 2** was written by the following authors:

Nicholas M. Mroz<sup>#</sup>, Agnieszka Ciesielska<sup>#</sup>, Nathan A. Ewing-Crystal, Leah C. Dorman, Rafael (Taeho) Han, Jerika J. Barron, Vivianna DeNittis, Nicholas J. Silva, Anna V. Molofsky, Jeanne T. Paz<sup>\*</sup>, Ari B. Molofsky<sup>\*</sup>

<sup>#</sup> these authors contributed equally

<sup>\*</sup>co-corresponding authors

*This chapter is reprinted as a manuscript in preparation for submission to a peer-reviewed journal.*

Conceptualization: N.M.M, A.C., A.V.M, J.T.P, A.B.M.; Methodology: N.M.M., A.C., L.C.D., A.V.M., J.T.P., A.B.M.; Investigation: N.M.M., A.C., N.A.E-C., L.C.D., R.T.H., J.J.B., V.D., N.J.S. Visualization: N.M.M., A.C., L.C.D., A.B.M.; Funding acquisition: A.V.M., J.T.P., A.B.M.; Supervision: J.T.P., A.B.M.; Writing – original draft: N.M.M., A.C., J.T.P., A.B.M.; Writing – review and editing: all authors.

**Chapter 3** was written by the following authors:

Nicholas M. Mroz, Rafael (Taeho) Han, Nathan A. Ewing-Crystal, Leah C. Dorman, Madelene W. Dahlgren, Ilia D. Vainchtein, Anna V. Molofsky, Ari B. Molofsky

Conceptualization: N.M.M, R.T.H., A.V.M, A.B.M.; Methodology: N.M.M., R.T.H., L.C.D., A.V.M., A.B.M.; Investigation: N.M.M., R.T.H., N.A.E-C., M.W.D., I.D.V. Visualization: N.M.M., R.T.H., L.C.D., A.B.M.; Funding acquisition: A.V.M., A.B.M.; Supervision: A.V.M., A.B.M.; Writing – original draft: N.M.M., A.B.M.; Writing – review and editing: all authors.

**Chapter 4** was written by the following authors:

Nicholas M. Mroz<sup>#</sup>, Pailin Chiaranunt<sup>#</sup>, Ari B. Molofsky<sup>\*</sup>, Anna V. Molofsky<sup>\*</sup>

# these authors contributed equally

\*co-corresponding authors

*Chapter 4 is reprinted as a manuscript under review.*

Conceptualization: N.M.M, P.C., A.V.M, A.B.M.; Supervision: A.V.M., A.B.M.; Writing –

original draft: N.M.M., P.C.; Writing – review and editing: N.M.M, P.C., A.V.M, A.B.M.

# Investigating the impacts of lymphocytes on recovery from brain injury

Nicholas M. Mroz

## **Abstract**

Central nervous system (CNS) injuries are a leading cause of mortality and morbidity worldwide. Brain damage, including ischemic stroke and traumatic brain injury (TBI), initiates sterile inflammatory responses within CNS and the surrounding meningeal membranes. While the CNS is largely immune privileged at steady state, the adjacent meninges contain a large diversity of tissue-resident lymphocytes and, following brain damage, lymphocytes also infiltrate and take up residence within the brain parenchyma. The function of meningeal and brain-infiltrating lymphocytes and whether they beneficially or detrimentally impact the injury response after brain damage remains poorly defined. This study investigates how different lymphocyte populations impact wound healing and neurological sequelae after brain injury. First, using a mouse model of TBI, we identify a population of interferon- $\gamma$  (IFN $\gamma$ )-producing type 1 lymphocytes that infiltrates the thalamus at chronic timepoints following cortical injury and acts to restrict seizure susceptibility. Next, we investigate the role of meningeal type 2 innate lymphoid cells (ILC2s) in regulating the wound healing response to cortical photothrombotic (PT) injury. Finally, we review the reciprocal interactions between the nervous and immune systems, focusing on type 2 'allergic' immunity, and highlighting the roles of type 2 neuroimmune crosstalk in both normal physiology and pathology. Together, this work further elucidates many key details about the impact of lymphocytes and other immune cells on the nervous system and reveals potential therapeutic opportunities that could be harnessed to treat human diseases, including brain injuries and related sequelae.

# TABLE OF CONTENTS

<b>CHAPTER 1: INTRODUCTION</b> .....	<b>1</b>
1.1 OVERVIEW.....	1
1.2 CNS INJURIES AND RELATED SEQUALAE.....	2
1.3 IMMUNE RESPONSES TO STERILE BRAIN INJURIES.....	2
1.4 'FLAVORS' OF LYMPHOCYTE RESPONSES.....	3
<b>CHAPTER 2: THALAMIC TYPE 1 LYMPHOCYTES AND INTERFERON-<math>\gamma</math> (IFN<math>\gamma</math>) RESTRICT SEIZURE SUSCEPTIBILITY FOLLOWING TRAUMATIC BRAIN INJURY (TBI).....</b>	<b>5</b>
2.1 ABSTRACT.....	5
2.2 INTRODUCTION.....	6
2.3 RESULTS.....	8
2.3.1 <i>Type 1 lymphocyte infiltrates persist in the thalamus several weeks after TBI.</i> .....	8
2.3.2 <i>IFN<math>\gamma</math> is elevated in the thalamus following TBI and is produced primarily by infiltrating CD8<sup>+</sup> T Cells.</i> .....	10
2.3.3 <i>TBI induces a subregion-specific IFN<math>\gamma</math> response within the ipsilateral thalamus.</i> .....	11
2.3.4 <i>CD4<sup>+</sup> T cell depletion recues TBI-induced seizure susceptibility and increases disease-associated microglia (DAMs) and type 1 lymphocytes in the ipsilateral thalamus.</i> .....	12
2.3.5 <i>IFN<math>\gamma</math> treatment reduces TBI-induced seizure susceptibility.</i> .....	16
2.4 DISCUSSION.....	17
2.5 FIGURES .....	21
2.6 MATERIALS AND METHODS.....	48

<b>CHAPTER 3: DEFINING THE IMPACT OF TYPE 2 INNATE LYMPHOID CELLS (ILC2S) ON THE RECOVERY FROM BRAIN INJURY.....</b>	<b>57</b>
3.1 ABSTRACT .....	57
3.2 INTRODUCTION.....	58
3.3 RESULTS.....	60
3.3.1 <i>Myeloid cells infiltrate and expand in the brain following PT injury .....</i>	<i>60</i>
3.3.2 <i>Meningeal ILC2s colocalize with IL-33<sup>+</sup> fibroblasts and are activated after PT     damage .....</i>	<i>63</i>
3.3.3 <i>IL-33 signaling in ILC2s does not impact myeloid or lymphoid populations in     the meninges or cortex after PT damage.....</i>	<i>64</i>
3.3.4 <i>IL-33 signaling in ILC2s does not impact lesion size or gliosis after PT damage .....</i>	<i>67</i>
3.3.5. <i>IL-33 signaling in ILC2s promotes cortical inhibitory synapse numbers after PT     injury .....</i>	<i>68</i>
3.3.6 <i>IL-33 signaling in ILC2s does not impact seizure susceptibility, cognition, or     sensorimotor behaviors after PT stroke .....</i>	<i>69</i>
3.3.7 <i>Meningeal Arg1 expression partially depends on monocyte trafficking and IL-     4/13 signaling, while cortical Arg1 expression is fully dependent on monocyte     trafficking.....</i>	<i>71</i>
3.3.8 <i>Monocyte infiltration modestly limits cortical damage but does not impact     fibrosis after PT stroke, while IL-4/13 is dispensable for both.....</i>	<i>72</i>
3.4 DISCUSSION.....	72
3.5 FIGURES .....	76
3.6 MATERIALS AND METHODS.....	99
<b>CHAPTER 4: CROSS-REGULATORY INTERACTIONS BETWEEN THE NERVOUS SYSTEM AND TYPE 2 IMMUNITY .....</b>	<b>111</b>

4.1 ABSTRACT .....	111
4.2 INTRODUCTION.....	112
4.3 COMPONENTS OF TYPE 2 IMMUNITY AND THE NERVOUS SYSTEM .....	113
4.4 TYPE 2 IMMUNE REGULATION OF THE BRAIN .....	115
4.4.1 <i>CNS Development, Synapses, and Cognition</i> .....	116
4.4.2 <i>CNS Injury</i> .....	119
4.4.3 <i>Alzheimer's Disease and Aging</i> .....	121
4.4.4 <i>Cytokine signaling in the periphery</i> .....	122
4.5 NEURONAL AND IMMUNE REGULATION OF PHYSIOLOGY AND BEHAVIOR.....	124
4.6 PERIPHERAL NEURON REGULATION OF TISSUE TYPE 2 IMMUNE RESPONSES.....	127
4.6.1 <i>Neurotransmitters: Amplifying immune responses</i> .....	127
4.6.2 <i>A neuropeptide code for immune cell modulation</i> .....	129
4.7 FUTURE DIRECTIONS AND THERAPEUTIC OPPORTUNITIES .....	131
4.8 FIGURES .....	133
<b>CHAPTER 5: CLOSING AND FUTURE DIRECTIONS</b> .....	<b>135</b>
<b>REFERENCES</b> .....	<b>138</b>

## List of Figures

<b>Figure 2.1.</b> Type 1 lymphocytes infiltrate the thalamus with different kinetics than the cortex following TBI, persisting for several weeks.....	21
<b>Figure 2.2.</b> Minimal lymphocyte infiltration into the hippocampus following TBI.....	23
<b>Figure 2.3.</b> Brain-infiltrating lymphocytes have a tissue-resident memory phenotype.....	25
<b>Figure 2.4.</b> IFN $\gamma$ is elevated in the thalamus following TBI and is produced primarily by infiltrating CD8 $^+$ T Cells.....	27
<b>Figure 2.5.</b> CD8 $^+$ T Cells produce IFN $\gamma$ across brain regions following TBI.....	29
<b>Figure 2.6.</b> TBI induces a subregion-specific IFN $\gamma$ response within the ipsilateral thalamus.....	31
<b>Figure 2.7.</b> Neuronal loss observed after TBI and additional thalamic ISG imaging.....	33
<b>Figure 2.8.</b> CD4 $^+$ T cell depletion recues TBI-induced seizure susceptibility and increases disease-associated microglia (DAMs) and type 1 lymphocytes in the ipsilateral thalamus.....	35
<b>Figure 2.9.</b> CD4 $^+$ T cell depletion does not impact PTZ-induced mortality, seizure frequency, or latency to Racine stages after TBI.....	37
<b>Figure 2.10.</b> Quality controls metrics and cell type assignment of scRNAseq data.....	39
<b>Figure 2.11.</b> CD4 $^+$ T cell depletion does not impact DAMs and type 1 lymphocytes in other brain regions or in circulation.....	41
<b>Figure 2.12.</b> IFN $\gamma$ treatment reduces TBI-induced seizure susceptibility and severity.....	43
<b>Figure 3.1.</b> Characterization of myeloid infiltrate kinetics in the meninges and cortex following PT damage.....	76
<b>Figure 3.2.</b> CCR2 fate-mapping demonstrates monocyte differentiation into macrophages and cDCs within the cortex following PT injury.....	78
<b>Figure 3.3.</b> Meningeal ILC2s closely localize to IL-33 $^+$ fibroblasts and produce IL-5 and IL-13 following PT damage.....	80
<b>Figure 3.4.</b> Meningeal single cell RNA sequencing (scRNAseq) reveals potential retention	

of pro-inflammatory myeloid cells in ILC2 <sup>ΔST2</sup> mice 14 days after PT injury.....	82
<b>Figure 3.5.</b> Cortical single cell RNA sequencing (scRNAseq) reveals potential retention of tissue-resident CD8+ T cells and inappropriate microglial phenotypic polarization in ILC2 <sup>ΔST2</sup> mice 14 days after PT injury.....	84
<b>Figure 3.6.</b> IL-33 signaling in ILC2s does not impact meningeal or cortical myeloid population abundance 2 or 14 days after PT injury.....	86
<b>Figure 3.7.</b> IL-33 signaling in ILC2s does not impact meningeal or cortical lymphocyte population abundance or expression of tissue-residency markers 14 days after PT injury.....	88
<b>Figure 3.8.</b> IL-33 signaling in ILC2s promotes cortical inhibitory synapse numbers but does not impact cortical lesion size, gliosis, or fibrosis.....	90
<b>Figure 3.9.</b> IL-33 signaling in ILC2s does not impact seizure susceptibility or other behaviors after PT damage.....	92
<b>Figure 3.10.</b> CCR2-dependent monocyte trafficking contributes to Arg1 <sup>+</sup> myeloid and limits cortical damage after PT damage.....	94
<b>Figure 4.1.</b> Interactions between the nervous system and type 2 immunity occur across multiple organs depending on the context of allergic triggers or injury.....	133
<b>Figure 4.2:</b> Molecular mechanisms of type 2 neuroimmune crosstalk.....	134



## List of Tables

<b>Table 2.1.</b> Antibodies used for flow cytometry in Chapter 2.....	45
<b>Table 2.2.</b> Antibodies used for immunofluorescent imaging in Chapter 2.....	46
<b>Table 2.3.</b> Chemicals, commercial kits, and other critical reagents used in Chapter 2.....	47
<b>Table 3.1.</b> Antibodies used for flow cytometry in Chapter 3.....	96
<b>Table 3.2.</b> Antibodies used for immunofluorescent imaging in Chapter 3.....	97
<b>Table 3.3.</b> Chemicals, commercial kits, and other critical reagents used in Chapter 3.....	97
<b>Table 3.4.</b> Mouse strains used in Chapter 3.....	98
<b>Table 3.5.</b> Modified Racine scale used to quantify seizure behavior in Figure 3.9.....	98

# Chapter 1: Introduction

## 1.1 OVERVIEW

Brain injury results in an inflammatory response that initially amplifies damage, causing secondary injury, before transitioning to a wound healing response at later timepoints. Understanding this process and how different immune cells and signals can modulate inflammatory versus reparative outcomes is crucial to design therapies that ameliorate human CNS injuries and associated morbidities. The aims of this thesis were as follows:

- 1) Determine how lymphocytes modulate seizure susceptibility after TBI, described in Chapter 2.
- 2) Delineate the function of type 2 innate lymphoid cells (ILC2s) in the wound healing response to ischemic stroke, described in Chapter 3.
- 3) Review and organize the known mechanisms of crosstalk between the nervous system and type 2 immunity and how these interactions influence physiology and disease, described in Chapter 4.

## **1.2 CNS INJURIES AND RELATED SEQUALAE**

CNS injury is a leading cause of mortality and morbidity worldwide due to the limited capacity for adult CNS regeneration and the lack of effective treatments to stop or reverse damage. Injuries to the CNS can take on a variety of different forms and severities depending on the cause, location, and extent of the injury but are generally categorized into: strokes (including ischemic and hemorrhagic sub-types), traumatic brain injuries (TBIs, including head impacts, concussions, and blast/projectile injuries), and spinal cord injury (SCI). CNS damage often decreases quality of life and causes many long-lasting physical and mental sequelae, including mobility issues, cognition (impaired attention and executive dysfunction), amnesia, acceleration of aging-associated cognitive decline, fatigue, personality changes (e.g., impulsivity, aggression), seizures, and depression.<sup>1,2</sup> While little can be done to prevent the primary injury, especially in the case of TBI and SCI which are often accidental, treatments can and have been developed to treat sequelae following CNS damage. Increasing our understanding how immune cells and signals modulate the response to injury and related sequelae can help us generate additional therapies for human patients by identifying beneficial wound healing and reparative pathways to augment or detrimental, damage-exacerbating pathways to inhibit.

## **1.3 IMMUNE RESPONSES TO STERILE BRAIN INJURIES**

Regardless of the initial cause of the injury, CNS damage initiates a stereotyped sterile inflammatory cascade. Primary injury leads either to direct cell death via lysis or mechanical forces or indirect death via hypoxia or nutrient stress, as well as the disruption of the blood-brain barrier. Dead and dying cells release damage-associated molecular patterns (DAMPs) to signal to the immune system that tissue injury has occurred. DAMPs include nuclear alarmins, like IL-33 and HMGB1, heat shock proteins, extracellular nucleic acids, and extracellular adenosine triphosphate (ATP). DAMPs are quickly sensed by nearby microglia, the resident macrophage of the brain, or astrocytes who express pattern recognition receptors (PRRs), such as toll-like receptors (TLRs), NOD-like receptors (NLRs), scavenger receptors, and purinergic receptors,

which recognize DAMPs. Signaling downstream of PRRs initiates gene transcription, inflammasome activation, and secretion of pro-inflammatory cytokines and chemokines, such as IL-1 $\beta$ , IL-6, IL-18, TNF $\alpha$ , CCL2, and CXCL1. These molecules signal to other nearby glia and endothelial cells, which amplify the cascade and recruit patrolling myeloid cells such as neutrophils and classical monocytes to the damaged tissue. These myeloid cells become activated and phagocytose dead cells and debris, while also releasing additional inflammatory mediators such as reactive oxygen species (ROS) and nitric oxide (NO), which can cause additional secondary damage and complement activation. As the magnitude of this initial response wanes, neutrophils die off and monocytes differentiate into macrophages. Monocyte-derived macrophages and activated microglia continue to phagocytose material and begin to express reparative growth factors and anti-inflammatory molecules, such as brain-derived neurotrophic factor (BDNF), insulin-like growth factor 1 (IGF-1), IL-10, and transforming growth factor beta (TGF- $\beta$ ), which act to halt excess inflammation and promote wound healing and growth programs. The immune response ultimately concludes with the formation of glial and fibroblastic scars around the damaged tissue in order to seal off the injured area from remaining healthy parenchyma and re-establish the barriers between the CNS and the periphery.<sup>1</sup> In later stages of the response, adaptive T lymphocytes are recruited to the injured site, which occurs through both antigen-dependent and -independent mechanisms, where they take up residence and patrol for future perturbations.<sup>1,3</sup>

#### **1.4 'FLAVORS' OF LYMPHOCYTE RESPONSES**

Immune responses can be broadly categorized by the upstream activators to which they respond and the downstream signals and effector functions they elicit. While this is an oversimplification and substantial plasticity exists within and between these 'flavors' of immune responses,<sup>4</sup> it remains an effective and useful way to conceptualize the components of the immune system and understand their prototypical functions.

Type 1 immunity responds to intracellular pathogens, such as viruses and intracellular bacteria, as well as cancer. Type 1 immunity is triggered by signals generated by innate immune cells (e.g., DCs, macrophages) generated after encounters with intracellular pathogens or stressed cells, such as IL-12 and IL-15. The cellular components of this branch of immunity include CD8<sup>+</sup> T cells, natural killer (NK) cells, ILC1s, and Th1s, which all express the lineage-defining transcription factor Tbet. Once activated, these type 1 lymphocytes produce cytokines and/or mediate cytotoxicity against infected, stressed, or cancerous cells. The major effector cytokine of type 1 immunity is IFN $\gamma$ , which promotes macrophage activation, cellular defense programs against viruses, and reinforces this type 1 program by polarizing naive CD4<sup>+</sup> T cells towards a Th1 fate in secondary lymphoid organs.<sup>4,5</sup>

Type 2 immunity is the branch of the immune system that responds to large extracellular parasites (such as helminths and mites), protists, and allergens. Type 2 immune cells are activated by alarmins such as IL-33, IL-25, and thymic stromal lymphopoietin (TSLP) that are released after tissue damage caused by parasite infection or allergic irritation. Alarmins activate type 2 lymphocytes that include ILC2s and Th2s, defined by expression of the transcription factor GATA-3. Once activated, type 2 lymphocytes produce the effector cytokines IL-4, IL-5, and IL-13, which promote eosinophil recruitment, reinforce the type 2 program during T cell priming, promote alternative activation of macrophages, and mediate tissue remodeling processes.<sup>5,6</sup>

Type 3/17 immunity responds to extracellular bacteria and fungi and is activated downstream of signals such as IL-1 $\beta$  and IL-23. Components of this branch of immunity include Th17s and ILC3s, which produce IL-17A, IL-17F, and IL-22 upon activation. These cytokines mediate upregulation of anti-microbial peptides, induce chemokines that recruit neutrophils, and promote epithelial repair and regeneration. Type 3/17 is particularly important at barrier sites such as the skin and mucosal surfaces like the gut, where there is increased microbial burden.<sup>5</sup>

In this thesis, the type 1 and type 2 immune responses to CNS injury will be investigated.

## **Chapter 2: Thalamic type 1 lymphocytes and interferon- $\gamma$ (IFN $\gamma$ ) restrict seizure susceptibility following traumatic brain injury (TBI)**

### **2.1 ABSTRACT**

Traumatic brain injury (TBI) is a leading cause of mortality and disability worldwide. One such TBI-related sequela is post-traumatic epilepsy (PTE), in which patients develop seizures months to years after injury. The processes responsible for the development of PTE remain poorly defined, but emerging work suggest that the thalamus, the relay center of the brain that undergoes secondary damage after cortical TBI, may be involved. TBI also involves immune responses and the recruitment of peripheral immune cells to the site(s) of injury, but it is also unknown how the immune system influences the development of seizure susceptibility after brain damage. In this study, we characterize the identities and kinetics of lymphocytic infiltrates into the cortex and thalamus using a mouse model of cortical TBI. We identify a population of IFN $\gamma$ -producing type 1 lymphocytes that take up residence within the thalamus over the weeks following injury, where they elicit an IFN $\gamma$  response in microglia and neurons. Depletion of one type of lymphocyte, CD4<sup>+</sup> T cells, protected from TBI-induced seizure susceptibility that was associated with a reciprocal increase in other non-CD4<sup>+</sup> thalamic type 1 lymphocytes and highly phagocytic disease-associated microglia (DAMs). This allowed us to identify IFN $\gamma$  as a putative regulator of seizure development. We find that a single dose of IFN $\gamma$  prior to seizure assessment was sufficient to dramatically reduced TBI-induced seizure incidence, severity, and mortality. This work identifies IFN $\gamma$  as an inhibitor of TBI-associated seizure susceptibility, which could have therapeutic implications for patients suffering from PTE.

## 2.2 INTRODUCTION

Traumatic brain injury (TBI) is a leading cause of morbidity and mortality worldwide. It is estimated that between 24–69 million people worldwide<sup>7,8</sup> and 5.3 million people in the US<sup>2</sup> suffer from TBI, with an additional 1.7 million people affected by TBI in the US every year.<sup>1</sup> TBI comprises a heterogeneous group of brain injuries, both in etiology (e.g., concussions, blunt-force impacts, blast or projectile injuries) and severity (mild to extreme), contributing to the difficulties in measuring its incidence in the human population.<sup>1</sup> Primary injury results in the initiation of a sterile inflammatory response within the brain, as dead and dying cells release alarmins that signal to resident microglia to initiate inflammatory cascades. Circulating myeloid cells, such as neutrophils and monocytes, are recruited to the injured tissue and further amplify the immune response, which can cause secondary injuries. Later phases of the immune response involve microglial and macrophage phagocytosis of cellular debris, the recruitment of adaptive T cells, and the formation of an astrocytic scar around the damaged tissue.<sup>1</sup>

TBI can cause a variety of long-lasting physical and mental sequelae, including mobility issues, fatigue, amnesia, cognitive decline, and depression.<sup>1,2</sup> Post-traumatic epilepsy (PTE) is one such sequela that affects roughly 20% of patients with severe TBI and accounts for ~5% of all epilepsy cases worldwide (~3.5 million people).<sup>9</sup> The exact mechanisms underlying the development of PTE are unknown, but it is believed that epileptogenesis occurs following a latent period (ranging from months to years after TBI) during which damage and inflammation cause maladaptive structural reorganization of neural circuits that ultimately results in hyperexcitable or hypersynchronous neuronal activity.<sup>9,10</sup> PTE is often associated with the hippocampus,<sup>9</sup> but emerging studies illustrate the importance of the thalamus in this process.<sup>11–13</sup>

The thalamus is often conceptualized as the ‘relay center’ of the brain, in which many different sensory pathways (e.g., vision, audition, touch) converge and information is radiated out to the cerebral cortex. In reality, the thalamus receives more synaptic input back from the cortex than it sends, and these reciprocal corticothalamic circuits are critical for sensory processing,

cognition, and sleep.<sup>14</sup> After primary cortical TBIs, secondary damage occurs in the physically distant but functionally connected thalamus as thalamic neurons that innervate the damaged cortex degenerate and die, potentially via axonal severing and excitotoxicity.<sup>11,15,16</sup> The thalamus is associated with seizures because thalamic neurons that fire tonically that can undergo a switch to a synchronous burst firing mode, which can then propagate to other brain regions due to thalamus's widespread connections. Secondary thalamic damage after TBI can aggravate this process, as loss of thalamic neurons and associated gliosis cause alterations in these circuits.<sup>12,17</sup>

One of the immune cell types that infiltrate the brain after TBI are T cells. T cells are adaptive lymphocytes that respond to self or foreign antigens through recognition of peptide-bound major histocompatibility (MHC) molecules via their T cell receptor (TCR). T cells undergo priming by antigen-presenting cells in secondary lymphoid organs, such as the spleen and lymph nodes, after which they can traffic to and enter peripheral organs. Many recent mouse studies have identified T cells that infiltrate and take up residency within the CNS after viral infection,<sup>18–20</sup> autoimmune encephalitis,<sup>21,22</sup> cancer,<sup>23</sup> aging,<sup>24</sup> and injury,<sup>3,25,26</sup> and T cell populations have also been identified that accumulate in the human brain and cerebrospinal fluid during health<sup>27</sup> and disease.<sup>28</sup> While brain-infiltrating T cells have been well characterized, the precise functions of these cells within the brain and how they impact neurological sequelae, particularly after TBI, remain poorly defined.

Here, we characterize the lymphocytic infiltrate into the cortex and thalamus following the controlled cortical impact (CCI) mouse model of TBI. We identify a population of T cells that infiltrate into the thalamus with slower kinetics after injury, mirror the timeline of secondary thalamic damage and gliosis. We identify these T cells as IFN $\gamma$ -producing type 1 lymphocytes, which induce a thalamic sub-region-specific IFN $\gamma$  response in microglia and neurons. Surprisingly, we determine that CD4<sup>+</sup> T cells promote seizure susceptibility after TBI by locally inhibiting other non-CD4<sup>+</sup> type 1 lymphocytes and reactive microglia in the thalamus. We also reveal that



treatment with IFN $\gamma$  alone can reduce seizure susceptibility after TBI, which may have implications for treating PTE in humans and reducing seizure severity.

## 2.3 RESULTS

### 2.3.1 Type 1 lymphocyte infiltrates persist in the thalamus several weeks after TBI.

Using the controlled cortical impact (CCI) model of TBI, we previously characterized a secondary injury that occurs within the ipsilateral thalamus consisting of gliosis and immune cell infiltrates (**Figure 2.1.A**).<sup>17</sup> To further characterize the identity and kinetics of thalamic immune cell infiltrates, we used high-dimensional flow cytometric analysis (gating schematic shown in **Figure 2.2.A**). We identified a prominent population of non-B lymphocytes that infiltrated the ipsilateral thalamus with different kinetics as compared with the perilesional cortex: an initial wave of lymphocytes infiltrated the cortex and peaked in magnitude at ~14 days post injury (dpi), while a secondary wave of lymphocytes infiltrated the thalamus at later time points, peaking around 30-40dpi (**Figures 2.1.B-C**). Both these lymphocyte populations waned by ~80dpi but remained elevated compared to sham controls (**Figures 2.1.B-C**). These lymphocytes included CD8<sup>+</sup> T cells, CD4<sup>+</sup> FoxP3<sup>-</sup> conventional T cells (T<sub>conv</sub>), and NK/ILC1s (NK1.1<sup>+</sup>), which all followed similar infiltration kinetics (**Figure 2.1.D-E; 2.2.B,D**). The thalamus was dominated by CD8<sup>+</sup> T cells at later timepoints, while the relative proportion of these lymphocytes was similar in the cortex over time (**Figure 2.1.F, I**). A small number of regulatory T cells (T<sub>regs</sub>; CD4<sup>+</sup> FoxP3<sup>+</sup>) were also observed in both the cortex and thalamus, while B cells were minimally present in these brain regions (**Figure 2.1.F, I; 2.2.B,D**). In contrast, lymphocyte infiltration into the ipsilateral hippocampus was minimal and lymphocytes within the hippocampus were sparse compared to the cortex and thalamus (**Figure 2.2F-G**). These data indicate that after TBI immune cells primarily infiltrate into the cortex and thalamus, and not the hippocampus, and that infiltration into the cortex versus thalamus follows different kinetics.

We next interrogated the flavor of the brain-infiltrating lymphocytes we observed after TBI. NK/ILC1s and CD8<sup>+</sup> T cells, observed in both the cortex and thalamus, expressed the defining type 1 transcription factor Tbet (**Figure 2.2.C,E**), as expected. We interrogated the flavor of the CD4<sup>+</sup> T<sub>conv</sub> cells in the cortex and thalamus and observed that, across both of these brain regions and across all time points, the CD4<sup>+</sup> T<sub>conv</sub> cells preferentially expressed Tbet over GATA-3 or ROR $\gamma$ t, indicating that these cells were also of a type 1 flavor (**Figures 2.1.G-H, J-K; 2.2.C,E**). Thus, most TBI-induced brain-infiltrating lymphocytes were type 1 lymphocytes with the capacity to produce interferon- $\gamma$  (IFN $\gamma$ ).

We further immunophenotyped these lymphocytes for expression of memory and tissue-residency markers. Across both subacute and chronic time points (7–35dpi), over 90% of thalamic CD8<sup>+</sup> and CD4<sup>+</sup> T cells expressed the memory marker CD44 without expression of the circulatory marker CD62L (**Figure 2.3.A-D**). Additionally, the majority (>80%) of thalamic T cells at all time points expressed the tissue residency marker CD69 (**Figure 2.2.A-D**), which inhibits the egress of lymphocytes from tissues into the circulation, consistent with existing literature.<sup>18,19,21,22,27,29</sup> A small subset of thalamic CD8<sup>+</sup> T cells (~10–20%) and CD4<sup>+</sup> T cells (~20–30%) co-expressed CD103, another tissue residency marker present on a subset of brain-infiltrating T cells.<sup>18,19,21,22,27</sup> Cortical and thalamic T cells expressed similar levels of these markers (i.e., CD44<sup>+</sup> CD62L<sup>-</sup> CD69<sup>+</sup> CD103<sup>±</sup>), which was distinct from circulating T cells within the blood (**Figure 2.2.E-G**). These data suggest the T cells that infiltrate the brain after TBI express markers of tissue residency.

Next, we used confocal microscopy to define the spatial positioning of T cells within the thalamus after TBI. We observed a population of T cells (CD45<sup>+</sup> CD3 $\epsilon$ <sup>+</sup> cells) within the ipsilateral thalamus at 21dpi that were increased compared to sham-injured brains (**Figure 2.1.L**). We quantified the distribution of T cells within the thalamus and determined that T cells were elevated in the reticular nucleus (nRT), ventral posterolateral (VPL), and ventral posteromedial (VPM) thalamus after 21dpi, with a trending increase in the lateral posterior/lateral dorsal (LP/LD,

“visual”) thalamus (**Figure 2.1.M**). In contrast, T cells did not increase in the ventral anterolateral (VAL) thalamus, a motor region not directly connected to the injured somatosensory cortex (**Figure 2.1.M**). T cells were modestly enriched in the VPL compared to the nRT and VPM (**Figure 2.1.M-N**). We also confirmed that many of these thalamic T cells expressed the type 1 transcription factor Tbet that licenses IFN $\gamma$  production within lymphocytes<sup>30</sup> at 30dpi using *Tbx21<sup>zsGreen</sup>* reporter mice<sup>31</sup> (**Figure 2.2.H**). These data suggest that TBI elicits a type 1 immune response within the brain, consisting of Tbet<sup>+</sup> tissue resident memory T cells, that initially infiltrate the perilesional cortex followed by the ipsilateral thalamus, mirroring the kinetics of damage to each brain region, and remain increased at both sites up to several months post injury.

### **2.3.2 IFN $\gamma$ is elevated in the thalamus following TBI and is produced primarily by infiltrating CD8<sup>+</sup> T Cells.**

Given that type 1 immune responses classically involve IFN $\gamma$  production, we next characterized the expression of IFN $\gamma$  after TBI. We first measured the levels of IFN $\gamma$  within the ipsilateral cortex, hippocampus, and thalamus after TBI. The concentration of IFN $\gamma$  within the thalamus increased from 7 to 35dpi and IFN $\gamma$  was more concentrated within the thalamus as compared with the cortex or hippocampus (**Figure 2.4.A-D**). IL-13, a type 2 cytokine, and IL-2, a growth/survival factor for T cells, did not change over the time points tested or between brain regions (**Figure 2.5.A-C**). We next interrogated the cellular source of IFN $\gamma$  after TBI using *ex vivo* stimulation and flow cytometry (gating strategy in **Figure 2.5.D**). At 4–6 weeks post-injury, IFN $\gamma$ <sup>+</sup> cells were observed within the ipsilateral thalamus, while IL-5/13<sup>+</sup> and IL-17A<sup>+</sup> cells were sparse (**Figure 2.4.E-G**). CD8<sup>+</sup> T cells were the largest producers of IFN $\gamma$  4–6 weeks post TBI (**Figure 2.4.H-I; 2.5.E-G**) and CD8<sup>+</sup> T cells constituted ~80–90% of all IFN $\gamma$ <sup>+</sup> cells in the thalamus, while CD4<sup>+</sup> T cells accounted for the remaining ~10–20% (**Figure 2.4.J-K**). IFN $\gamma$  was also the dominant lymphocyte-derived cytokine in the cortex and hippocampus, with CD8<sup>+</sup> T cells accounting for

~90% of IFN $\gamma$ <sup>+</sup> cells across all brain regions (**Figure 2.5.H-J**). These data demonstrate that type 1 lymphocytes, in particular CD8<sup>+</sup> T cells, produce the effector cytokine IFN $\gamma$  after TBI, and that this IFN $\gamma$  production is enriched within the ipsilateral thalamus.

We next examined the spatial response to TBI within the thalamus using confocal microscopy. Consistent with our previous work,<sup>17</sup> we observed gliosis within the ipsilateral thalamus 7–8 weeks after TBI (**Figure 2.6.A**). The density of reactive astrocytes (GFAP<sup>+</sup>) and microglia (Iba1<sup>+</sup>) was elevated within nRT, VPL, and LP/LD thalamus, demonstrating increased astrocytic and microglial activation within these thalamic subregions after TBI (**Figure 2.6.B-C**). In contrast, an unrelated region, the ventral anterolateral (VAL) thalamus associated with motor function, was not gliotic, demonstrating subregional specificity of the thalamic response to cortical damage (**Figure 2.6.A-C**). Additionally, we confirmed that cortical injury led to thalamic neuron loss, with a decrease in NeuN density within the LP/LD thalamus and a trending decrease within the VPL (**Figure 2.7.A-B**).<sup>17</sup>

### **2.3.3 TBI induces a subregion-specific IFN $\gamma$ response within the ipsilateral thalamus.**

Given the increased IFN $\gamma$  within the thalamus after TBI (**Figure 2.4**), we next explored if the expression of interferon-stimulated genes (ISGs) were also elevated. We observed a marked increase in the expression of class II MHC (MHC-II, I-A/I-E) within the nRT and VPL thalamus, but not the VPM or VAL (**Figure 2.6.D,F**). Additionally, we observed an increase in total STAT1 expression after TBI across the thalamus (**Figure 2.6.E,G**). The expression of these ISGs was restricted to the damaged hemisphere, with minimal staining in the contralateral thalamus (although MHC-II was also expressed by border-associated macrophages (BAMs) within the pial membrane and choroid plexus across both hemispheres) (**Figure 2.7.C-D**). To determine which cell types were responding to IFN $\gamma$ , we analyzed the co-expression of STAT1 with microglia (Iba1<sup>+</sup>) or neurons (NeuN<sup>+</sup>). We observed higher densities of interferon-responsive microglia (STAT1<sup>+</sup>

Iba1<sup>+</sup>) within the VPL and LP/LD thalamus, with ~60% of microglia expressing STAT1 in these regions (**Figure 2.6H-J**). Interferon-responsive neurons (STAT1<sup>+</sup> NeuN<sup>+</sup>) were most abundant in the VPL, VPM, and LD/LP, with ~20% of neurons in these regions expressing STAT1 (**Figure 2.6H-K; 2.7.E**). The majority (~80%) of STAT1 in the nRT, VPL, and LP/LD was expressed by microglia while STAT1 was equally expressed by microglia and neurons in the VPM (**Figure 2.6.L**), suggesting that interferon-responsive neurons were relatively enriched within the VPM compared to other thalamic regions. This is consistent with our previously published single nuclear RNA sequencing data,<sup>17</sup> which shows elevated expression of the IFN $\gamma$  receptor subunits *Ifngr1* and *Ifngr2* within microglia and excitatory neurons (**Figure 2.7.F-G**). Together, these data reveal a subregion-specific interferon response within the ipsilateral thalamus after TBI, with microglia and neurons responding to these signals in different subregions.

#### **2.3.4 CD4<sup>+</sup> T cell depletion recues TBI-induced seizure susceptibility and increases disease-associated microglia (DAMs) and type 1 lymphocytes in the ipsilateral thalamus.**

Next, we interrogated the impact of T cells on seizure susceptibility, a common neurological sequela after TBI. We first targeted CD4<sup>+</sup> T cells using an antibody-mediated depletion approach: mice that received sham or TBI surgery were injected with an anti-CD4 antibody or isotype control 3 hours after surgery, and then every 4 days until 12dpi (**Figure 2.8.A**). To assess seizure susceptibility, mice were challenged with pentylenetetrazol (PTZ), a GABA<sub>A</sub> receptor antagonist that is commonly used to induce seizures in mice.<sup>32,33</sup> Mice were given a sensitizing dose of PTZ 4 weeks after injury, and then given challenged again at 5 weeks post injury, at which point seizure behavior was recorded and scored on a modified Racine scale (**Figure 2.8.A**). As expected, a greater proportion of mice who experienced TBI had generalized tonic-clonic (GTC) seizures than sham controls. Interestingly, injured mice treated with anti-CD4 antibodies were protected from TBI-induced seizure susceptibility, as a significantly smaller proportion of these mice experienced GTC seizures than isotype-treated controls (**Figure 2.8B**).

Additionally, injured mice treated with anti-CD4 antibodies also had a significant reduction in the duration of their GTC seizures (Racine stage 5), compared to isotype-treated injured mice (**Figure 2.8.C**). We did not observe any significant differences in the PTZ-induced mortality or seizure frequency of anti-CD4 treated mice (**Figure 2.9.A-C**) or in the duration of or latency to any of the other Racine stages (**Figure 2.9.D-K**). Importantly, CD4<sup>+</sup> T cells were significantly depleted with anti-CD4 antibody treatment as expected (**Figure 2.8.D**). Together, these data indicate that depletion of CD4<sup>+</sup> T cells rescues TBI-induced seizure susceptibility, suggesting that CD4<sup>+</sup> T cells promote seizure susceptibility after TBI.

To gain unbiased information on how CD4<sup>+</sup> T cells may be influencing thalamic microglia, we performed single cell RNA sequencing (scRNAseq) on CD11b<sup>+</sup> myeloid cells isolated from the thalami of anti-CD4-treated TBI mice, along with isotype-treated sham and TBI controls, at 14dpi. scRNAseq data was quality controlled by filtering on unique reads per cell, genes per cell, and percent mitochondrial RNA, and contaminating astrocytes (*Slc1a3*<sup>+</sup>) and oligodendrocytes (*Mbp*<sup>+</sup>) were excluded from downstream analysis of *Hexb*<sup>+</sup> myeloid cells (**Figure 2.10.A-F**). UMAP clustering on filtered myeloid cells revealed several microglial clusters, along with a BAM cluster (**Figure 2.8.E**). Among microglia, there were two disease-associated microglia (DAM) clusters, an interferon-responsive cluster (“IFN”), a cluster enriched for neuronal transcripts (“neuro”), a proliferative cluster (“Cyc”), and several homeostatic populations that were grouped into 2 homeostatic clusters (“H1, H2”) based on their similarities within the clustering tree (**Figure 2.8.E, 2.10.G**). DAM clusters differentially upregulated several canonical DAM genes, including *Itgax*, *Cd9*, *CD63*, *Trem2*, *ApoE*, and *Spp1*, with reduced expression of homeostatic genes such as *P2ry12* (**Figure 2.8.G, 2.10.H**). DAM clusters had higher expression of DAM signature genes (top 25 differentially expressed DAM genes from Keren-Shaul, et al., 2017),<sup>34</sup> and the DAM2 cluster had higher expression of Stage 2 DAM signature genes,<sup>34</sup> confirming their identities as Stage 1 (DAM1) and Stage 2 (DAM2) DAMs (**Figure 2.10.J-K**). The IFN cluster differentially expressed several interferon-response genes, such as *Iffit3*, *Isg15*, and *Stat1* (**Figure 2.8.G, 2.10.H**), and

had the most elevated module score for signature genes of type 1 interferon-responsive microglia (IRMs).<sup>35</sup> Microglia within DAM1, DAM2, and IFN clusters were rare in sham, isotype-treated mice, but dramatically increased in frequency with TBI (**Figure 2.8.F,H**), indicating these thalamic populations expanded with injury. Anti-CD4 treatment further increased the frequency of DAM1, DAM2, and IFN clusters (**Figure 2.8.F,H**), suggesting CD4<sup>+</sup> T cell depletion increased the abundance of these microglial states.

Since we observed multiple lines of evidence for robust IFN $\gamma$  secretion and downstream response in the thalamus after TBI, we next sought to determine if IFN $\gamma$  was contributing to any of the microglial states that were increased after TBI. To do so, we performed bulk RNA sequencing on cortical microglia that were treated *in vivo* with IFN $\gamma$ : naive mice were injected intracerebroventricularly (i.c.v) with IFN $\gamma$  or PBS vehicle control, and cortical microglia were isolated for RNA sequencing 24 hours after injection (**Figure 2.10.M**). Compared to PBS-treated controls, IFN $\gamma$ -treated microglia upregulated several canonical ISGs, including MHC-II genes (*H2-Aa*, *H2-Ab1*, *H2-Eb1*), MHC-I genes (*H2-D1*, *H2-K1*, *B2m*), *Cxcl9*, *Irf1*, and *Ifitm3* (**Figure 2.10.N**). Applying these IFN $\gamma$  signature genes to our scRNAseq data as a module score, we observed increased IFN $\gamma$  scores within DAM1, DAM2, and IFN clusters, as well as the BAM and cycling clusters (**Figure 2.10.O**), suggesting that IFN $\gamma$  may be responsible for partially driving both the DAM and IFN-responsive microglial states. . In support of this, gene ontology (GO) analysis revealed that “response to type II interferon” was significantly elevated within the DAM2 cluster (**Figure 2.10.I**). Furthermore, when looking at the IFN $\gamma$  module score between treatment conditions, we observed that DAM1, DAM2, and IFN microglia had higher IFN $\gamma$  scores after TBI compared to sham controls (**Figure 2.8.I**), suggesting that the increased thalamic IFN $\gamma$  after TBI is driving these microglial states. Moreover, we observed an additional increase in the IFN $\gamma$  score of DAM2 microglia (and trending increase in DAM1 microglia) with anti-CD4 treatment, compared

to isotype-treated TBI controls (**Figure 2.8.I**), suggesting that anti-CD4 treatment may be further increasing IFN $\gamma$  signaling within stage 2 DAMs in the thalamus after TBI.

To validate our scRNAseq data, we confirmed our observations at the protein level with flow cytometry. Consistent with our scRNAseq data, we observed an increase in the frequency of CD11c<sup>+</sup> CLEC7A<sup>+</sup> microglia (DAMs) within the thalamus 14 days after TBI; the frequency of CD11c<sup>+</sup> CLEC7A<sup>+</sup> microglia was further increased with anti-CD4 treatment (**Figure 2.8.J-K**, gating strategy in **Figure 2.11.A**). Additionally, the median fluorescence intensity (MFI) of CLEC7A, a DAM marker and ISG,<sup>34,36,37</sup> was increased on thalamic microglia from anti-CD4 treated mice compared to isotype treated controls after TBI (**Figure 2.8.L**). This pattern was also observed when using a different set of DAM markers, CD11c<sup>+</sup> and CD9<sup>+</sup> (**Figure 2.8.M**), confirming that anti-CD4 treatment increased the frequency of thalamic DAMs. Importantly, this pattern was only observed within thalamic microglia: DAMs were modestly increased in the cortex and hippocampus with TBI, but no difference was observed with anti-CD4 treatment in these brain regions (**Figure 2.11.E-F, J-K**).

We also explored the impacts of CD4<sup>+</sup> T cell depletion on other brain-infiltrating lymphocytes at 14dpi. In the thalamus, when CD4<sup>+</sup> T cells were depleted with anti-CD4 treatment (**Figure 2.8.D**), we observed an increase in the number of total type 1 lymphocytes (Thy1.2<sup>+</sup> Tbet<sup>+</sup> cells) (**Figure 2.8.N-O**). This included an additional increase in thalamic NK/ILC1s (**Figure 2.8.P, 2.11.B**) and a trending increase in thalamic CD8<sup>+</sup> T cells (**Figure 2.8Q, 2.11.C**), suggesting that CD4<sup>+</sup> T cells typically inhibit the abundance of these other type 1 lymphocytes within the thalamus. Anti-CD4 treatment resulted in global loss of CD4<sup>+</sup> T cells in the cortex, hippocampus, and blood (**Figure 2.11.G,L,O**). Cortical NK/ILC1s and CD8<sup>+</sup> T cells were not impacted by anti-CD4 treatment (**Figure 2.11.H-I**), while hippocampal NK/ILC1s were also elevated without impacts on CD8<sup>+</sup> T cells (**Figure 2.11.M-N**). Importantly, CD4 depletion did not impact the concentration of circulating immune cells, including NK/ILC1s, CD8<sup>+</sup> T cells, CD11b<sup>+</sup> myeloid cells, B cells, or  $\gamma\delta$  T



cells (**Figure 2.11.P-T**). This suggests that the majority of the impact of anti-CD4 treatment are restricted to the brain, particularly in the thalamus and partially in the hippocampus, where CD4 depletion resulted in a reciprocal increase in other non-CD4<sup>+</sup> type 1 lymphocytes.

Together, these data illustrate that CD4<sup>+</sup> T cell depletion causes an increase in thalamic type 1 lymphocytes and a local hyper-IFN $\gamma$  response, which signals to thalamic microglia and drives them to a stage 2 DAM state, which is ultimately protective against seizures. This supports a model in which thalamic CD4<sup>+</sup> T cells typically promote susceptibility to TBI-induced seizures through inhibition of non-CD4<sup>+</sup> type 1 lymphocytes (NK/ILC1s, CD8<sup>+</sup> T cells) and DAMs.

### **2.3.5 IFN $\gamma$ treatment reduces TBI-induced seizure susceptibility.**

Given the association of increased IFN $\gamma$  and protection from seizures after TBI, we next directly examined the impact of exogenous IFN $\gamma$  on seizure susceptibility. We induced TBI and waited 4 weeks to give mice a sensitizing dose of PTZ, as before. However, one day prior to the second dose of PTZ and seizure assessment, we treated mice with either a high dose of IFN $\gamma$  intraperitoneally (i.p.) (10  $\mu$ g/mouse) or PBS vehicle (**Figure 2.12.A**). As expected, the proportion of PBS-treated injured mice who experience one or more GTC seizure was markedly elevated compared to naive controls (**Figure 2.12.B**). Interestingly, mice that received IFN $\gamma$  were protected from TBI-induced seizures, as a smaller proportion of these mice experienced GTC seizures compared to PBS-treated controls (**Figure 2.12.B**). Moreover, IFN $\gamma$ -treated injured mice were also significantly protected from PTZ-induced mortality, as a smaller proportion of this cohort died within 20 minutes after PTZ injection compared to PBS-treated injured controls (**Figure 2.12.C**). IFN $\gamma$ -treated mice also had shorter GTC seizures and overall less severe seizure behavior, as quantified by the maximum Racine score reached by each mouse (**Figure 2.12.D-G**). IFN $\gamma$ -treated injured mice spent less time in Racine stages 2–7 compared to PBS-treated injured controls, although the latency to each stage was unaffected (**Figure 2.11.I-J**). Thus, IFN $\gamma$  pre-treatment

just 24 hours prior to seizure challenge was sufficient to reduce the incidence, duration, and severity of seizures after TBI, as well as seizure associated mortality.

## 2.4 DISCUSSION

Here, we identify and characterize a thalamic immune response after cortical TBI that consists of type 1 IFN $\gamma$ -producing Tbet<sup>+</sup> tissue resident memory lymphocytes, including CD8<sup>+</sup> and CD4<sup>+</sup> T cells, in accordance with recent studies.<sup>3</sup> The accumulation of these lymphocytes in the thalamus weeks after TBI results in a local IFN $\gamma$  response primarily in microglia and/or macrophages that at least partially drives them into a highly phagocytic DAM phenotype. Ablation of CD4<sup>+</sup> T cells surprisingly rescued TBI-induced seizure susceptibility by unleashing other non-CD4<sup>+</sup> type 1 lymphocytes and their IFN $\gamma$  production that further promoted DAMs within the thalamus. Strikingly, a single dose of IFN $\gamma$  was sufficient to reduce the incidence, duration, and severity of seizures after TBI, suggesting that IFN $\gamma$  is a direct modulator of TBI-induced seizure susceptibility.

Brain-infiltrating and residing lymphocyte populations have been described in multiple models of disease, infection, and pathology. However, the cellular and molecular factor(s) that drive the accumulation of these lymphocytes remain unclear. It is well documented that T cells must first undergo nodal priming and licensing in order to cross the blood-brain barrier (BBB) and enter the brain parenchyma.<sup>38</sup> Are the thalamic T cells observed after TBI primed and licensed for thalamic entry, or do they passively accumulate through local BBB leakage? If they are primed and licensed for entry, what (auto)antigens do they recognize, and are they clonally distinct from the pool of cortex-infiltrating T cells? A recent study in a mouse model of spinal cord injury revealed that CNS-infiltrating T cells are clonally expanded cells that recognize CNS autoantigens (in particular, myelin basic protein) released into the periphery after damage.<sup>3</sup> Single cell TCR sequencing of thalamic T cells after TBI would help to determine if these T cells are also clonally

expanded in response to autoantigens. Additionally, the factors driving the accumulation of these T cells to specific thalamic subregions (e.g., VPL thalamus) remain unknown. Several chemokines have been identified that recruit T cells to the CNS in other contexts. For example, microglial-derived CCL2 and CCL8 recruit CD8<sup>+</sup> T cells to the brain in a mouse model of radiation-induced brain injury.<sup>25</sup> Additionally, microglial-derived CXCL16 recruits and maintains CXCR6-expressing brain-resident CD8<sup>+</sup> T cells in mouse models of Alzheimer's disease<sup>39</sup> and viral encephalitis.<sup>40</sup> Fibroblasts are also a potential source of T cell-recruiting chemokines, as fibroblast-derived CCL19 and CCL21 recruits CD8<sup>+</sup> T cells during viral neuroinflammation.<sup>41</sup> In our model, DAMs express a variety of putative T cell recruiting chemokines, including CCL2, CCL5, CCL12, and CXCL16, which raises the possibility that DAMs may directly recruit T cells to areas of damage within the brain – a hypothesis that requires further investigation. Identification of the axes driving recruitment and maintenance of thalamic T cells after TBI may allow for precise therapeutic targeting of this population.

Despite these advances, several caveats and unanswered questions remain. While our data suggests that CD4<sup>+</sup> depletion preferentially impacts the thalamus after TBI (as minimal effects were seen in the blood and cortex), we cannot rule out effects on T cell priming in secondary lymphoid organs. Additionally, anti-CD4 treatment depletes both CD4<sup>+</sup> T<sub>conv</sub> and CD4<sup>+</sup> T<sub>reg</sub> cells. T<sub>reg</sub> cells are well described to inhibit various immune responses, and – despite a scarcity of Tregs within the injured thalamus (**Figure 2.1E, 2.2D**) – the ablation of T<sub>reg</sub>s may be responsible for the reciprocal increased in type 1 lymphocytes observed with anti-CD4 treatment, potentially via enhanced nodal priming mechanisms. Additionally, the role of DAMs after TBI remains poorly defined. DAMs have increased phagocytic and lysosomal processing capabilities, which may mediate enhanced clearing of debris and/or synapses and have context-dependent effects on the progression of neurological diseases.<sup>42</sup> The abundance of DAMs has been anticorrelated with seizure severity<sup>43</sup> and a Th1-IFN $\gamma$ -microglia axis was reported during treatment of gliomas with checkpoint blockade that promoted microglial phagocytosis and subsequent tumor control.<sup>23</sup> We

also observed a population of phagocytic DAMs that were driven (in part) by IFN $\gamma$  in the thalamus, further increased with anti-CD4 treatment and its associated increase in IFN $\gamma$  signaling, and anticorrelated with seizure severity (**Figure 2.8**). Together, this suggests that DAMs and their phagocytic function (driven at least in part by IFN $\gamma$ ) help to restrict seizure susceptibility, although additional work is needed to describe the targets of DAM-mediated phagocytosis in this context.

While IFN $\gamma$  has previously been reported to impact brain physiology, including social and anxiety-like behavior,<sup>44,45</sup> the mechanism by which IFN $\gamma$  mediates its anti-seizure effects requires additional research. The short timeframe in which IFN $\gamma$  was able to prevent seizures (24 hours) argues for a rapid mechanism. A growing body of literature suggests that IFN $\gamma$  is able to directly signal to neurons to increase inhibitory tone. IFN $\gamma$  has been reported to increase inhibition of neurons in the rodent cortex and hippocampus, potentially by promoting surface expression and phosphorylation of GABA receptors.<sup>46-49</sup> Additionally, a previous study identified inhibitory neurons as the population that directly responds to IFN $\gamma$  via STAT1 to mediate impacts on social behavior and demonstrated the ability of IFN $\gamma$  to restrict severity of and latency to seizures in resting mice.<sup>45</sup> IFN $\gamma$  signaling directly to neurons to quickly enhance inhibition and thereby prevent seizures is an appealing hypothesis, bolstered by reports of IFN $\gamma$  receptor expression at synapses where downstream signaling may mediate rapid, transcription-independent effects.<sup>49-51</sup> On the other hand, microglia have higher expression of the IFN $\gamma$  receptor in our snRNAseq data (**Figure 2.7F-G**), the majority of STAT1<sup>+</sup> cells are microglia across most thalamic subregions (**Figure 2.6.H-L**) and STAT1<sup>+</sup> microglia are known to have increased phagocytic capacities that may impact synapse or neuronal engulfment.<sup>35,52,53</sup> An interplay between neurons and microglia is also a possibility, as IFN $\gamma$  signaling via STAT1 in neurons has previously been reported to recruit microglia (via CCL2) which in turn mediate synaptic modifications.<sup>54</sup> Future work must dissect the roles of IFN $\gamma$  signaling to neurons versus microglia in the context of TBI using cell-type specific deletion of the IFN $\gamma$  receptor (i.e., *Syn1<sup>cre</sup>;Ifngr1<sup>Flox</sup>* versus *Cx3cr1<sup>creER</sup>;Ifngr1<sup>Flox</sup>*).

Regardless of its exact anti-seizure mechanism, IFN $\gamma$  is an appealing therapeutic candidate for the treatment of seizures. Our work reveals that TBI not only elicits a pro-inflammatory immune response that causes additional immunopathology (as is traditionally thought), but also actively recruits lymphocytes to damaged areas to produce cytokines that restrict seizure development. Additional research is needed to understand the regulation of the IFN $\gamma$  response in the thalamus in order to understand what other factor(s) may be able to enhance this signaling axis. Promoting these aspects of the immune response to TBI would be a novel approach to treat PTE patients and deserves further investigation. Additionally, the impact of IFN $\gamma$  on other forms of epilepsy should be explored to determine if IFN $\gamma$  is able to limit seizures in additional disease contexts.

## 2.5 FIGURES

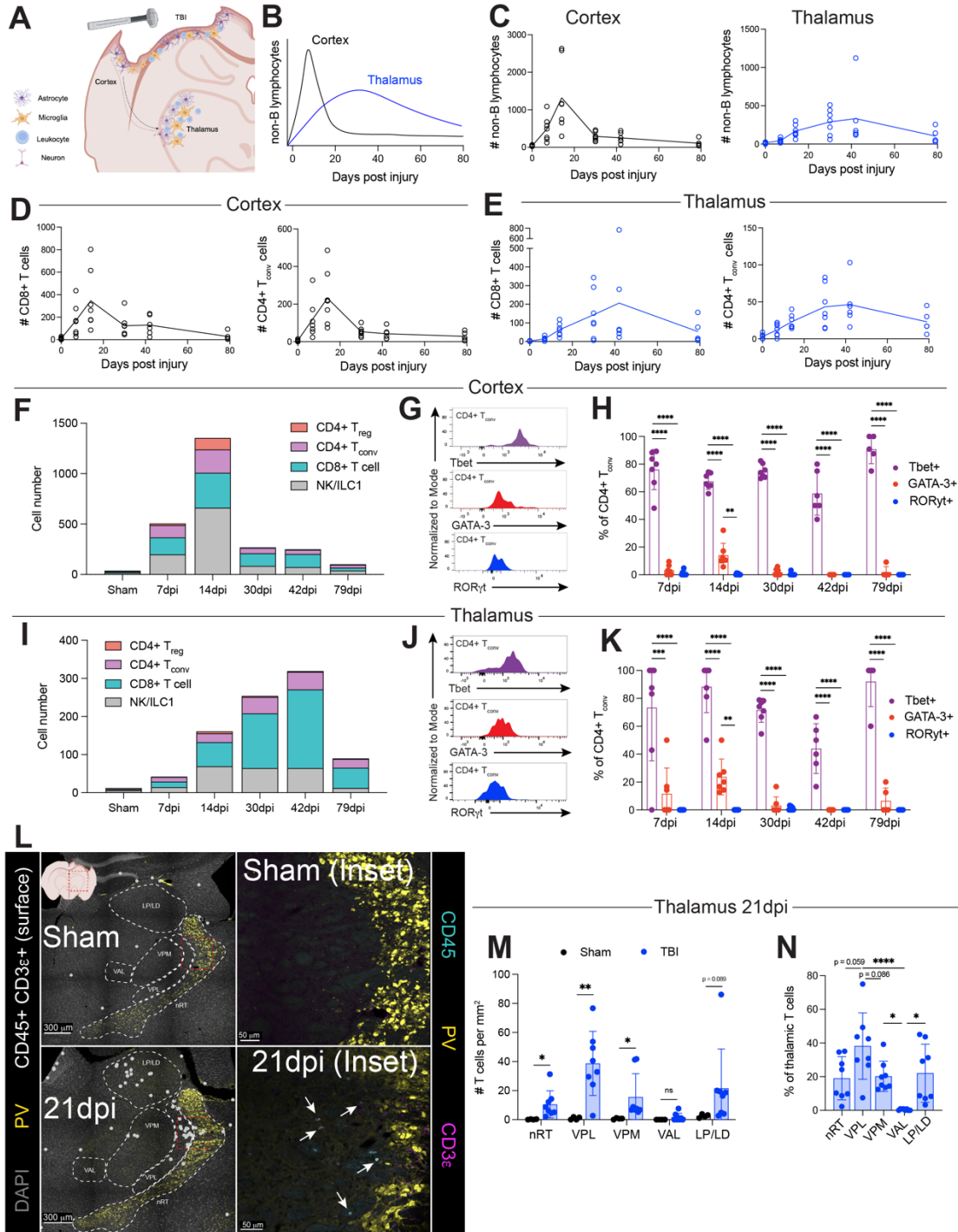


**Figure 2.1. Type 1 lymphocytes infiltrate the thalamus with different kinetics than the cortex following TBI, persisting for several weeks.**

A) Schematic of controlled cortical impact (CCI) model of TBI approximately 30 days post injury (dpi), depicting cortical and thalamic gliosis (astrocytes and microglia) and immune infiltrates (leukocytes) across a coronal section of the murine brain.

(Figure caption continued on next page)

(Figure caption continued from following page)

- B) Schematic depicting kinetics of non-B lymphocyte infiltration into cortex (black line) and thalamus (blue line) following TBI.
- C) Quantification of non-B lymphocyte ( $CD45^+ CD11b^- CD19^- Thy1.2^+$ ) cell numbers via flow cytometry in perilesional cortex (left, black) and ipsilateral thalamus (right, blue) after TBI. Mice per timepoint: sham (0dpi), 7dpi, 14dpi, 30dpi n=7; 42dpi n=6; 79dpi n=5. See Figure S1A for gating strategy.
- D) Quantification of  $CD8^+$  T cell (left) and  $CD4^+ FoxP3^- T_{conv}$  cell (right) numbers via flow cytometry in the perilesional cortex across a timecourse following TBI. Mice per timepoint: sham (0dpi), 7dpi, 14dpi, 30dpi n=7; 42dpi n=6; 79dpi n=5.
- E) Quantification of  $CD8^+$  T cell (left) and  $CD4^+ FoxP3^- T_{conv}$  cell (right) numbers via flow cytometry in the ipsilateral thalamus across a timecourse following TBI. Mice per timepoint: sham (0dpi), 7dpi, 14dpi, 30dpi n=7; 42dpi n=6; 79dpi n=5.
- F) Quantification of NK/ILC1,  $CD8^+$  T,  $CD4^+ FoxP3^- T_{conv}$ , and  $CD4^+ FoxP3^+ T_{reg}$  cell numbers via flow cytometry in the perilesional cortex across a timecourse after TBI. Data represents means. Mice per timepoint: sham (0dpi), 7dpi, 14dpi, 30dpi n=7; 42dpi n=6; 79dpi n=5.
- G) Representative histograms of Tbet, GATA-3, and  $ROR\gamma_t$  expression within cortical  $CD4^+ FoxP3^- T_{conv}$  cells 7 days after TBI.
- H) Quantification of Tbet<sup>+</sup>, GATA-3<sup>+</sup>, and  $ROR\gamma_t^+$  frequencies within cortical  $CD4^+ FoxP3^- T_{conv}$  cells across timecourse following TBI. Mice per timepoint: sham (0dpi), 7dpi, 14dpi, 30dpi n=7; 42dpi n=6; 79dpi n=5. One-way ANOVA with Tukey's multiple comparisons test within each timepoint.
- I) Quantification of NK/ILC1,  $CD8^+$  T,  $CD4^+ FoxP3^- T_{conv}$ , and  $CD4^+ FoxP3^+ T_{reg}$  cell numbers via flow cytometry in the ipsilateral thalamus across a timecourse after TBI. Data represents means. Mice per timepoint: sham (0dpi), 7dpi, 14dpi, 30dpi n=7; 42dpi n=6; 79dpi n=5.
- J) Representative flow histograms of Tbet, GATA-3, and  $ROR\gamma_t$  expression within thalamic  $CD4^+ FoxP3^- T_{conv}$  cells 30 days after TBI.
- K) Quantification of Tbet<sup>+</sup>, GATA-3<sup>+</sup>, and  $ROR\gamma_t^+$  frequencies within thalamic  $CD4^+ FoxP3^- T_{conv}$  cells across timecourse following TBI. Mice per timepoint: sham (0dpi), 7dpi, 14dpi, 30dpi n=7; 42dpi n=6; 79dpi n=5. One-way ANOVA with Tukey's multiple comparisons test within each timepoint.
- L) Representative confocal images of thalami from sham (top) or TBI (21dpi, bottom) mice, highlighting T cells (white circles,  $CD45^+ CD3\epsilon^+$  surface reconstruction) and thalamic subregions (white dashed lines). Parvalbumin (PV, yellow) is included to highlight the reticular thalamic nucleus (nRT). Insets (red dashed lines, right) depict native CD45 (cyan), PV (yellow), and CD3 $\epsilon$  (magenta) stains.
- M) Quantification of T cells ( $CD45^+ CD3\epsilon^+$  cells) normalized per area of thalamic subregions or from sham versus TBI (21dpi) mice. Sham n=4; TBI n=8. Two-way ANOVA with Šidák's multiple comparisons test.
- N) Quantification of T cells ( $CD45^+ CD3\epsilon^+$  cells) normalized per area of thalamic subregions from TBI (21dpi) mice. n=8. One-way ANOVA with Tukey's multiple comparisons test.
- O) Percentage of total thalamic T cells ( $CD45^+ CD3\epsilon^+$  cells) found within each thalamic subregion from TBI (21dpi) mice. n=8. One-way ANOVA with Tukey's multiple comparisons test.
- Data are mean  $\pm$  SD. Data points represent biological replicates (individual mice). Statistics: ns = not significant, \*p < 0.05, \*\*p < 0.01, \*\*\*p < 0.001, \*\*\*\*p < 0.0001.

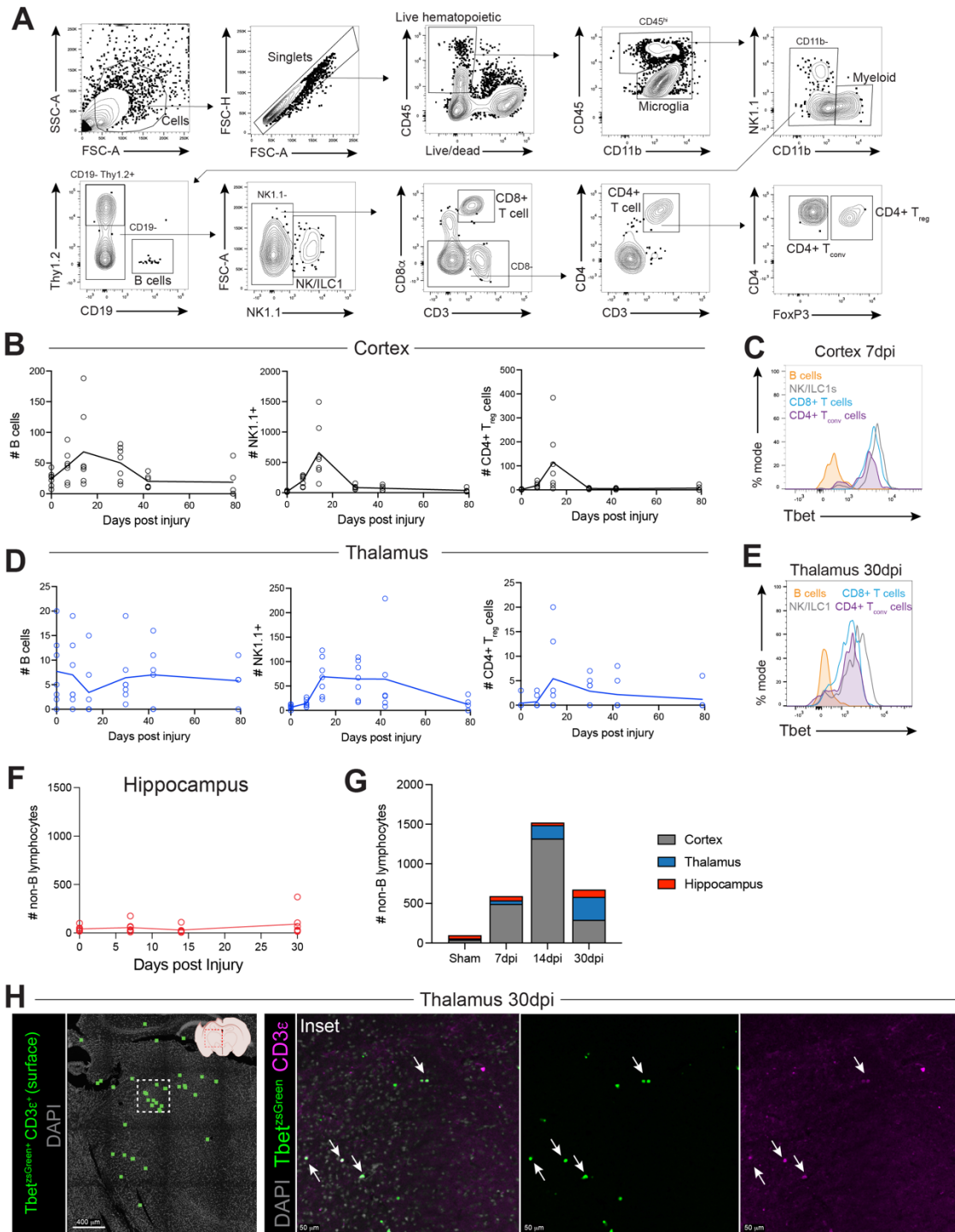


**Figure 2.2. Minimal lymphocyte infiltration into the hippocampus following TBI.**

A) Gating strategy used to identify brain-infiltrating lymphocytes for Figure 1. Representative flow plots are from cortical samples at 7dpi.

B) Quantification of B cells (left), NK/ILC1s (middle), and CD4<sup>+</sup> FoxP3<sup>+</sup> T<sub>regs</sub> cell numbers via flow cytometry in the perilesional cortex across a timecourse following TBI. Mice per timepoint: sham (0dpi), 7dpi, 14dpi, 30dpi n=7; 42dpi n=6; 79dpi n=5.

(Figure caption continued on next page)



*(Figure caption continued from previous page)*

- C) Representative flow histograms depicting Tbet expression in B cells, NK/ILC1s, CD8<sup>+</sup> T cells, and CD4<sup>+</sup> FoxP3<sup>-</sup> T<sub>conv</sub> cells from the cortex at 7dpi, demonstrating productive Tbet staining in type 1 lymphocytes but not B cells.
- D) Quantification of B cells (left), NK/ILC1s (middle), and CD4<sup>+</sup> FoxP3<sup>+</sup> T<sub>regs</sub> (right) cell numbers via flow cytometry in the ipsilateral thalamus across a timecourse following TBI. Mice per timepoint: sham (0dpi), 7dpi, 14dpi, 30dpi n=7; 42dpi n=6; 79dpi n=5.
- E) Representative flow histograms depicting Tbet expression in B cells, NK/ILC1s, CD8<sup>+</sup> T cells, and CD4<sup>+</sup> FoxP3<sup>-</sup> T<sub>conv</sub> cells from the thalamus at 30dpi, demonstrating productive Tbet staining in type 1 lymphocytes but not B cells.
- F) Quantification of non-B lymphocyte (CD45<sup>+</sup> CD11b<sup>-</sup> CD19<sup>-</sup> Thy1.2<sup>+</sup>) cell numbers via flow cytometry in the ipsilateral hippocampus after TBI. n = 7 mice per timepoint.
- G) Quantification of non-B lymphocyte (CD45<sup>+</sup> CD11b<sup>-</sup> CD19<sup>-</sup> Thy1.2<sup>+</sup>) cell numbers via flow cytometry in the perilesional cortex, ipsilateral hippocampus, and ipsilateral thalamus after TBI. Data represents means. n = 7 mice per timepoint.
- H) Representative confocal image (left) of the thalamus from Tbet<sup>zsGreen</sup> reporter mice highlighting Tbet<sup>+</sup> T cells (green squares, Tbet<sup>+</sup> CD3ε<sup>+</sup> surface reconstruction). Insets (right) depict merged and separated native Tbet and CD3ε signals.

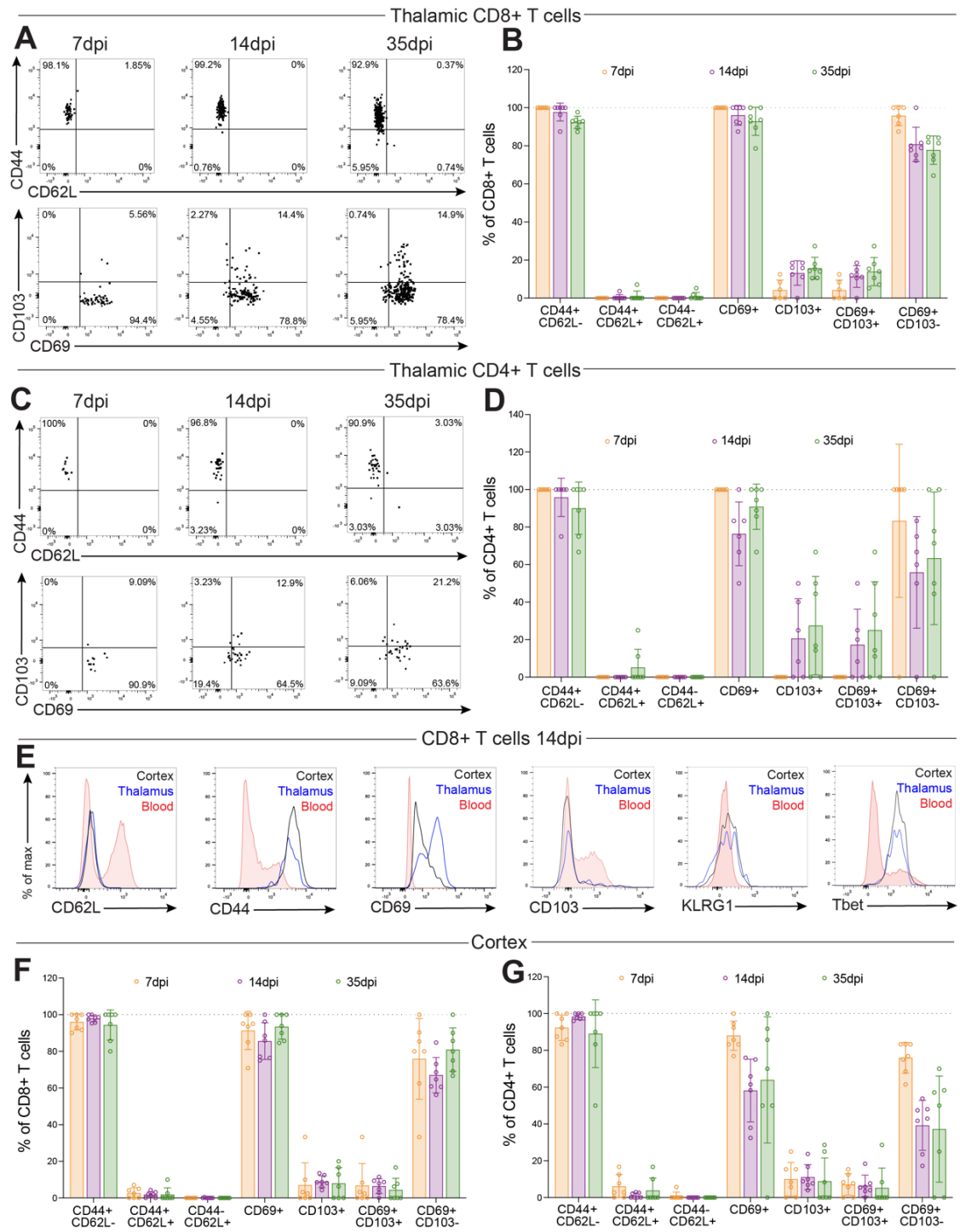


**Figure 2.3. Brain-infiltrating lymphocytes have a tissue-resident memory phenotype.**

A) Concatenated flow plots of thalamic CD8<sup>+</sup> T cells at 7, 14, and 35dpi depicting expression of CD44, CD62L, CD69, and CD103.

B) Quantification of CD44, CD62L, CD69, and CD103 expression within thalamic CD8<sup>+</sup> T cells at 7, 14, and 35dpi, displayed as frequency of CD8<sup>+</sup> T cells at each timepoint. Mice per timepoint: 7dpi n=6; 14dpi n=7; 35dpi n=7.

(Figure caption continued on next page)

*(Figure caption continued from previous page)*

- C) Concatenated flow plots of thalamic CD4<sup>+</sup> T cells at 7, 14, and 35dpi depicting expression of CD44, CD62L, CD69, and CD103.
- D) Quantification of CD44, CD62L, CD69, and CD103 expression within thalamic CD4<sup>+</sup> T cells at 7, 14, and 35dpi, displayed as frequency of CD4<sup>+</sup> T cells at each timepoint. Mice per timepoint: 7dpi n=6; 14dpi n=7; 35dpi n=7.
- E) Representative flow histograms depicting expression of CD62L, CD44, CD69, CD103, KLRG1, and Tbet within cortical (black), thalamic (blue), and blood (red) CD8<sup>+</sup> T cells at 14dpi.
- F) Quantification of CD44, CD62L, CD69, and CD103 expression within cortical CD8<sup>+</sup> T cells at 7, 14, and 35dpi, displayed as frequency of CD8<sup>+</sup> T cells at each timepoint. n=7 mice per timepoint.
- G) Quantification of CD44, CD62L, CD69, and CD103 expression within cortical CD4<sup>+</sup> T cells at 7, 14, and 35dpi, displayed as frequency of CD4<sup>+</sup> T cells at each timepoint. n=7 mice per timepoint.

Data are mean ± SD. Data points represent biological replicates (individual mice).

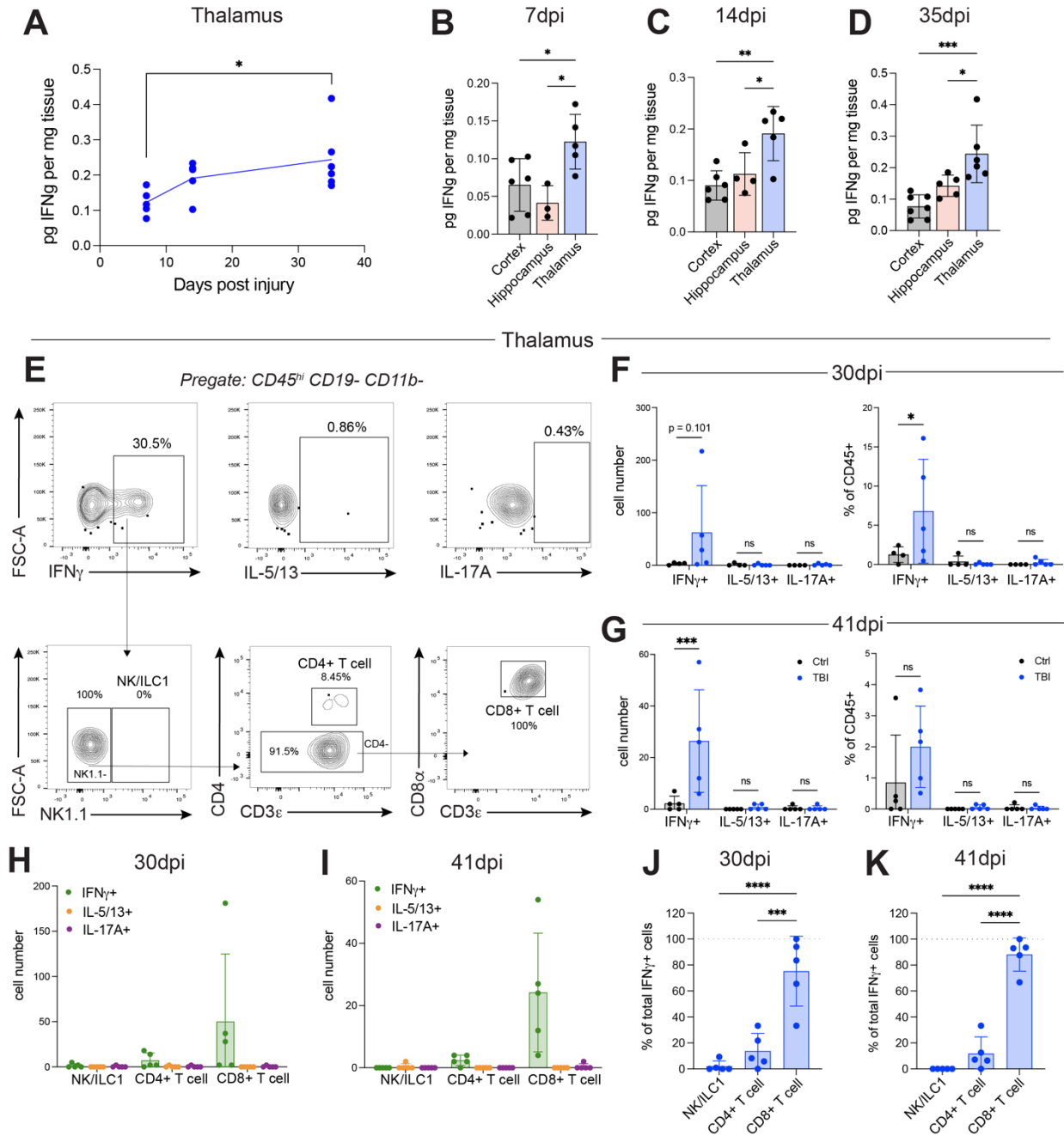


**Figure 2.4. IFN $\gamma$  is elevated in the thalamus following TBI and is produced primarily by infiltrating CD8+ T Cells.**

A) Quantification of IFN $\gamma$  within the ipsilateral thalamus at 7, 14, and 35dpi via Luminex on micro-dissected homogenates, normalized per mg of tissue. Mice per timepoint: 7dpi n = 5; 14dpi n = 5; 35dpi n = 6. One-way ANOVA with Tukey's multiple comparisons test.

B) Quantification of IFN $\gamma$  within the perilesional cortex, ipsilateral hippocampus, and ipsilateral thalamus at 7dpi via Luminex on micro-dissected homogenates, normalized per mg of tissue. Mice per brain region: cortex n=6; hippocampus n=3; thalamus n=5. One-way ANOVA with Tukey's multiple comparisons test.

(Figure caption continued on next page)

(Figure caption continued from previous page)

- C) Quantification of IFN $\gamma$  within the perilesional cortex, ipsilateral hippocampus, and ipsilateral thalamus at 14dpi via Luminex on micro-dissected homogenates, normalized per mg of tissue. Mice per brain region: cortex n=6; hippocampus n=4; thalamus n=5. One-way ANOVA with Tukey's multiple comparisons test.
- D) Quantification of IFN $\gamma$  within the perilesional cortex, ipsilateral hippocampus, and ipsilateral thalamus at 35dpi via Luminex on micro-dissected homogenates, normalized per mg of tissue. Mice per brain region: cortex n=7; hippocampus n=5; thalamus n=6. One-way ANOVA with Tukey's multiple comparisons test.
- E) Representative flow plots depicting IFN $\gamma$ , IL-5/13, and IL-17A expression (top row) within thalamic CD45<sup>hi</sup> CD11b<sup>-</sup> CD19<sup>-</sup> cells at 41dpi following *ex vivo* stimulation. IFN $\gamma$ <sup>+</sup> cells are further gated into NK/ILC1s, CD4<sup>+</sup> T cells, and CD8<sup>+</sup> T cells (bottom row), depicting the relative abundance of these cell types within the total IFN $\gamma$ <sup>+</sup> pool.
- F) Quantification of total IFN $\gamma$ <sup>+</sup>, IL-5/13<sup>+</sup>, and IL-17A<sup>+</sup> cells within the thalamus of sham or TBI mice 30dpi, depicted as cell numbers (left) and frequency of total CD45<sup>+</sup> cells (right). Mice per condition: sham n=4; TBI n=5. Two-way ANOVA with Šidák's multiple comparisons test.
- G) Quantification of total IFN $\gamma$ <sup>+</sup>, IL-5/13<sup>+</sup>, and IL-17A<sup>+</sup> cells within the thalamus of sham or TBI mice 41dwpi, depicted as cell numbers (left) and frequency of total CD45<sup>+</sup> cells (right). n=5 mice per condition. Two-way ANOVA with Šidák's multiple comparisons test.
- H) Quantification of IFN $\gamma$ <sup>+</sup>, IL-5/13<sup>+</sup>, and IL-17A<sup>+</sup> NK/ILC1, CD4<sup>+</sup> T, and CD8<sup>+</sup> T cell numbers within the thalamus at 30dpi. TBI n=5 mice.
- I) Quantification of IFN $\gamma$ <sup>+</sup>, IL-5/13<sup>+</sup>, and IL-17A<sup>+</sup> NK/ILC1, CD4<sup>+</sup> T, and CD8<sup>+</sup> T cell numbers within the thalamus at 41dwpi. TBI n=5 mice.
- J) Quantification of frequency of NK/ILC1, CD4<sup>+</sup> T cells, and CD8<sup>+</sup> T cells within total IFN $\gamma$ <sup>+</sup> cells within the thalamus at 30dpi. Mice per condition: sham n=4; TBI n=5. One-way ANOVA with Tukey's multiple comparisons test. TBI n=5 mice.
- K) Quantification of frequency of NK/ILC1, CD4<sup>+</sup> T cells, and CD8<sup>+</sup> T cells within total IFN $\gamma$ <sup>+</sup> cells within the thalamus at 30dpi. TBI n=5 mice. One-way ANOVA with Tukey's multiple comparisons test.

Data are mean  $\pm$  SD. Data points represent biological replicates (individual mice). Statistics: ns = not significant, \*p < 0.05, \*\*p < 0.01, \*\*\*p < 0.001, \*\*\*\*p < 0.0001.

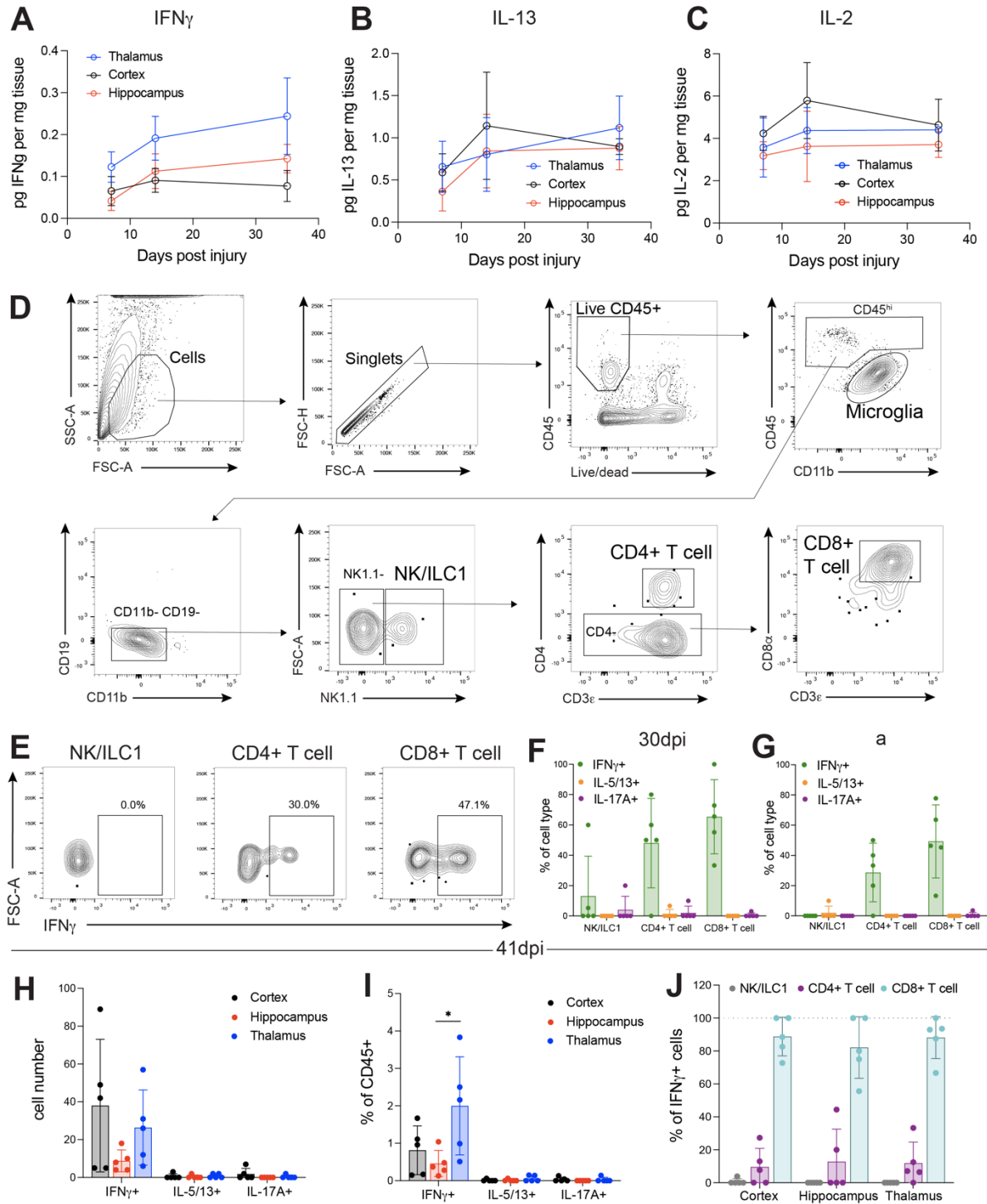


**Figure 2.5. CD8+ T Cells produce IFN $\gamma$  across brain regions following TBI.**

- A) Quantification of IFN $\gamma$  within the perilesional cortex, ipsilateral hippocampus, and ipsilateral thalamus at 7, 14, and 35dpi via Luminex on micro-dissected homogenates, normalized per mg of tissue.
- B) Quantification of IL-13 within the perilesional cortex, ipsilateral hippocampus, and ipsilateral thalamus at 7, 14, and 35dpi via Luminex on micro-dissected homogenates, normalized per mg of tissue. (Figure caption continued on next page)

(Figure caption continued from previous page)

- C) Quantification of IL-2 within the perilesional cortex, ipsilateral hippocampus, and ipsilateral thalamus at 7, 14, and 35dpi via Luminex on micro-dissected homogenates, normalized per mg of tissue.
- D) Gating strategy used to identify brain-infiltrating lymphocytes for cytokine quantification following *ex vivo* stimulation (in Figure 2). Representative flow plots are from cortical samples at 41dpi.
- E) Representative flow plots depicting IFN $\gamma$  expression within thalamic NK/ILC1s, CD4<sup>+</sup> T cells, and CD8<sup>+</sup> T cells at 41dpi.
- F) Quantification of the frequency of IFN $\gamma$ , IL-5/13, and IL-17A expression within NK/ILC1s, CD4<sup>+</sup> T cells, and CD8<sup>+</sup> T cells at 30dpi. TBI n=5 mice.
- G) Quantification of the frequency of IFN $\gamma$ , IL-5/13, and IL-17A expression within NK/ILC1s, CD4<sup>+</sup> T cells, and CD8<sup>+</sup> T cells at 41dpi. TBI n=5 mice.
- H) Quantification of total IFN $\gamma$ <sup>+</sup>, IL-5/13<sup>+</sup>, and IL-17A<sup>+</sup> cell numbers within the perilesional cortex, ipsilateral hippocampus, and ipsilateral thalamus by flow cytometry at 41dpi. n=5 mice per brain region.
- I) Quantification of total IFN $\gamma$ <sup>+</sup>, IL-5/13<sup>+</sup>, and IL-17A<sup>+</sup> frequencies (within the total CD45<sup>+</sup> pool) in the perilesional cortex, ipsilateral hippocampus, and ipsilateral thalamus by flow cytometry at 41dpi. One-way ANOVA with Tukey's multiple comparisons test within each cytokine. n=5 mice per brain region.
- J) Quantification of frequency of NK/ILC1, CD4<sup>+</sup> T cells, and CD8<sup>+</sup> T cells within total IFN $\gamma$ <sup>+</sup> cells in the perilesional cortex, ipsilateral hippocampus, and ipsilateral thalamus by flow cytometry at 41dpi. n=5 mice per brain region.

Data are mean  $\pm$  SD. Data points represent biological replicates (individual mice). Statistics: \*p < 0.05.

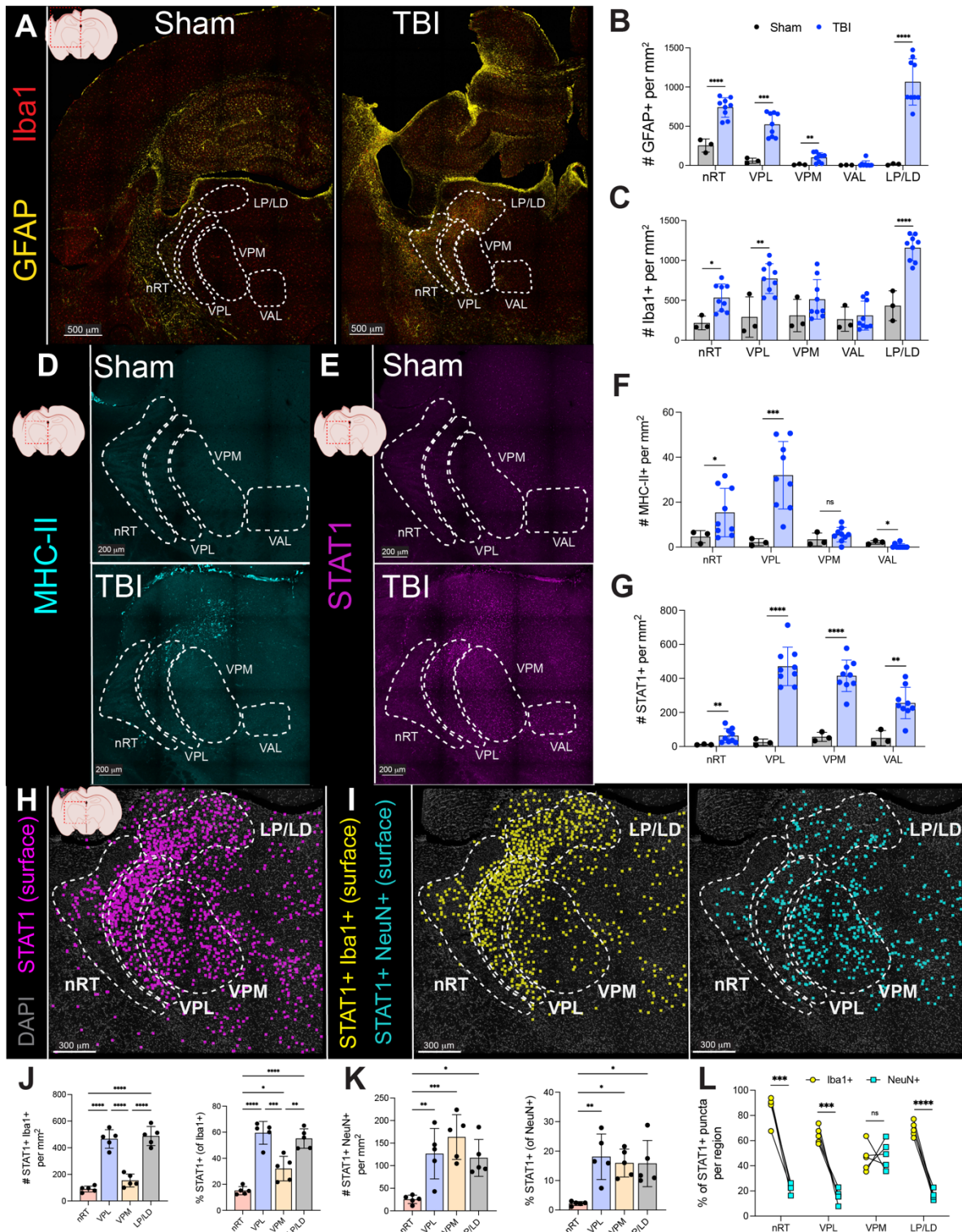


**Figure 2.6. TBI induces a subregion-specific IFN $\gamma$  response within the ipsilateral thalamus.**

A) Representative confocal images of coronal brain sections from sham and TBI mice 7-8wpi depicting GFAP and Iba1 staining in the damaged hemisphere. Thalamic subregions are outlined in dotted white lines.

(Figure caption continued on next page)



(Figure caption continued from previous page)

- B) Quantification of GFAP<sup>+</sup> cell density within thalamic subregions in sham and TBI mice 7-8wpi. Mice per group: sham n=3; TBI n=7. Unpaired Student's t test within each subregion.
- C) Quantification of Iba1<sup>+</sup> cell density within thalamic subregions in sham and TBI mice 7-8wpi. Mice per group: sham n=3; TBI n=7. Unpaired Student's t test within each subregion.
- D) Representative confocal images thalami from sham and TBI mice 7-8wpi depicting MHC-II staining. Thalamic subregions are outlined in dotted white lines.
- E) Representative confocal images thalami from sham and TBI mice 7-8wpi depicting STAT1 staining. Thalamic subregions are outlined in dotted white lines.
- F) Quantification of MHC-II<sup>+</sup> cell density within thalamic subregions in sham and TBI mice 7-8wpi. Mice per group: sham n=3; TBI n=7. Unpaired Student's t test within each subregion.
- G) Quantification of STAT1<sup>+</sup> cell density within thalamic subregions in sham and TBI mice 7-8wpi. Mice per group: sham n=3; TBI n=7. Unpaired Student's t test within each subregion.
- H) Representative confocal image of thalamus after TBI (7-8wpi) depicting distribution of STAT1<sup>+</sup> cells (magenta squares, surface reconstruction). Thalamic subregions are outlined in dotted white lines.
- I) Representative confocal image of thalamus after TBI (7-8wpi) depicting distribution of STAT1<sup>+</sup> Iba1<sup>+</sup> cells (yellow squares, surface reconstruction, left) and STAT1<sup>+</sup> NeuN<sup>+</sup> cells (cyan squares, surface reconstruction, right). Thalamic subregions are outlined in dotted white lines.
- J) Quantification of STAT1<sup>+</sup> Iba1<sup>+</sup> cells across thalamic subregions after TBI (7-8wpi), shown as cell density (left) or frequency of total Iba1<sup>+</sup> (right) within each subregion. One-way ANOVA with Tukey's multiple comparisons test.
- K) Quantification of STAT1<sup>+</sup> NeuN<sup>+</sup> cells across thalamic subregions after TBI (7-8wpi), shown as cell density (left) or frequency of total NeuN<sup>+</sup> (right) within each subregion. One-way ANOVA with Tukey's multiple comparisons test.
- L) Quantification of frequency of Iba1<sup>+</sup> and NeuN<sup>+</sup> cells within total STAT1<sup>+</sup> puncta for each thalamic subregion after TBI (7-8wpi). Paired Student's t test within each subregion.

Data are mean ± SD. Data points represent biological replicates (individual mice). Thalamic subregions: reticular nucleus (nRT), ventral posterolateral (VPL), ventral posteromedial (VPM), ventral anterolateral (VAL), and lateral posterior/lateral dorsal (LP/LD). Statistics: ns = non-significant, \*p < 0.05, \*\*p < 0.01, \*\*\*p < 0.001, \*\*\*\*p < 0.0001.

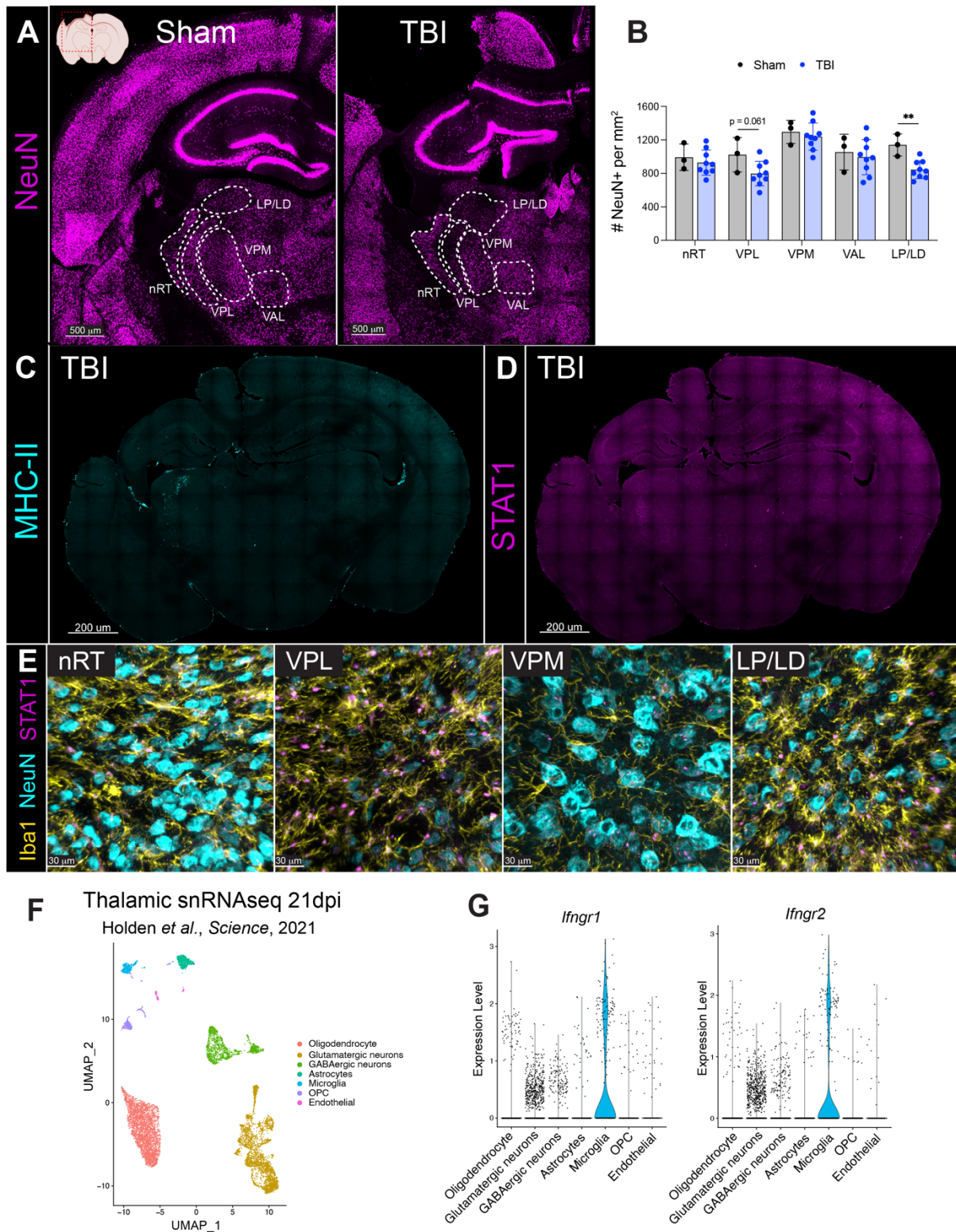


**Figure 2.7. Neuronal loss observed after TBI and additional thalamic ISG imaging.**

A) Representative confocal images of coronal brain sections from sham and TBI mice 7-8wpi depicting NeuN staining in the damaged hemisphere. Thalamic subregions are outlined in dotted white lines.

(Figure caption continued on next page)

(Figure caption continued from previous page)

- B) Quantification of NeuN<sup>+</sup> cell density within thalamic subregions in sham and TBI mice 7-8wpi. Mice per group: sham n=3; TBI n=7. Unpaired Student's t test within each subregion.
  - C) Representative confocal image of entire coronal brain section depicting MHC-II staining across both damaged (left) and contralateral (right) hemispheres 7-8wpi.
  - D) Representative confocal image of entire coronal brain section depicting STAT1 staining across both damaged (left) and contralateral (right) hemispheres 7-8wpi.
  - E) Representative confocal images depicting native Iba1, NeuN, and STAT1 staining across thalamic subregions after TBI (7-8wpi).
  - F) UMAP clustering of single nuclear RNA sequencing (snRNAseq) data from sham and injured thalami 21dpi from Holden et al, *Science*, 2021. Cell cluster assignments are as depicted in the original publication.<sup>17</sup>
  - G) Expression of *Ifngr1* and *Ifngr2* across cell types in snRNAseq data in (F) depicting enriched expression of these transcripts in microglia and glutamatergic (excitatory) neurons.
- Data are mean ± SD. Data points represent biological replicates (individual mice). Thalamic subregions: reticular nucleus (nRT), ventral posterolateral (VPL), ventral posteromedial (VPM), ventral anterolateral (VAL), and lateral posterior/lateral dorsal (LP/LD). Statistics: \*\*p < 0.01.

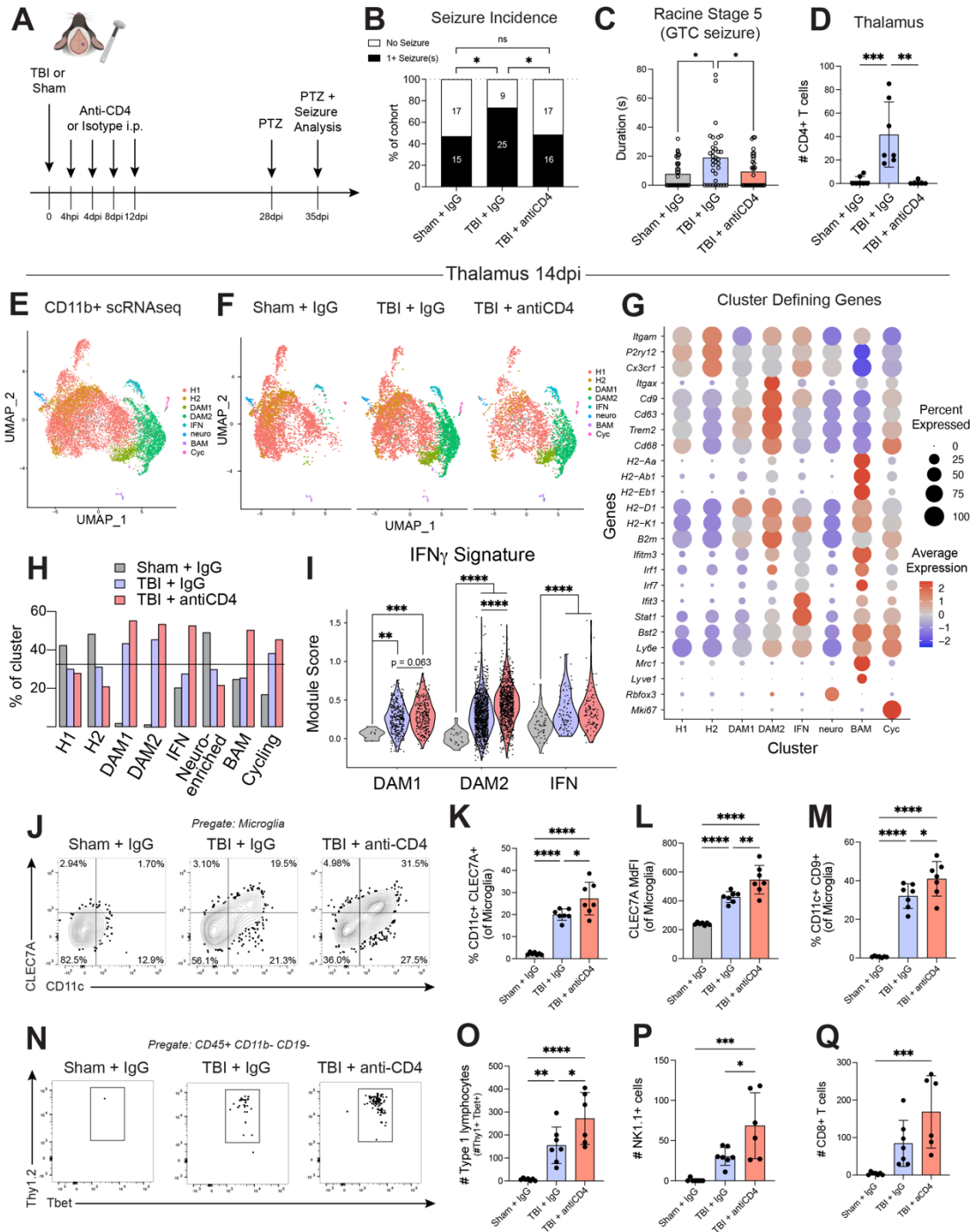


**Figure 2.8. CD4<sup>+</sup> T cell depletion recues TBI-induced seizure susceptibility and increases disease-associated microglia (DAMs) and type 1 lymphocytes in the ipsilateral thalamus.**

A) Schematic depicting anti-CD4 antibody (or IgG2b isotype) treatment following sham or TBI surgeries and pentylene tetrazol (PTZ) dosing regimen to assess seizure susceptibility. Mice were initially treated with antibodies (250 µg/mouse i.p.) 3 hours after surgery, and then every 4 days for a total of 4 doses. Mice were given a sensitizing dose of PTZ (45 mg/kg i.p.) at 4 weeks post injury, and then given a challenge of PTZ at 5 weeks post injury when point seizure behavior was recorded and quantified. (Figure caption continued on next page)

(Figure caption continued from previous page)

- B) Quantification of seizure incidence in sham+IgG, TBI+IgG, and TBI+anti-CD4 treated groups, depicted as percentage of each cohort that experience one or more generalized tonic-clonic (GTC) seizures (black bars). Numbers within bar graph represent number of mice in each group that experienced 0 or 1+ GTC seizures. Mice per condition: sham+IgG n=32, TBI+IgG n=34, TBI+anti-CD4 n=33. Fisher's exact tests.
- C) Quantification of GTC seizure duration (Racine Stage 5) in sham+IgG, TBI+IgG, and TBI+anti-CD4 treated groups. Mice per condition: sham+IgG n=32, TBI+IgG n=34, TBI+anti-CD4 n=33. Kruskal-Wallis test with Dunn's multiple comparisons test.
- D) Quantification by flow cytometry of CD4<sup>+</sup> T cells in the thalamus of sham+IgG, TBI+IgG, and TBI+anti-CD4 treated mice at 14dpi demonstrating efficient depletion of CD4<sup>+</sup> T cells with anti-CD4 treatment.
- E) Unsupervised clustering (UMAP plot) of single cell RNA sequencing (scRNAseq) data from CD11b<sup>+</sup> microglia/myeloid cells pooled from sham+IgG, TBI+IgG, and TBI+anti-CD4 conditions and colored by cluster (resolution=0.5). Cells were categorized into homeostatic microglia (H1, H2), disease-associated microglia (DAM1, DAM2), interferon-responsive microglia (IFN), microglia enriched for neuronal transcripts (neuro), border-associated macrophages (BAM), and proliferative microglia (Cyc).
- F) UMAP plot of scRNAseq data from CD11b<sup>+</sup> microglia/myeloid cells, showing 2,500 cells per condition (sham+IgG, TBI+IgG, and TBI+anti-CD4) and colored by cluster as in (E).
- G) Expression of cluster defining genes across clusters in scRNAseq data from (E,F). Data represents RNA counts and is depicted as percent of cluster expressing each gene (circle size) and relative averaged expression (heatmap color).
- H) Quantification of the frequency of each cluster (out of total myeloid cells) within each condition (sham+IgG, TBI+IgG, and TBI+anti-CD4). Clusters are normalized so that equal contribution from each sample would be shown by 3 bars at 33% (black line).
- I) IFN $\gamma$  module score per cell from DAM1, DAM2, and IFN clusters split by sham+IgG, TBI+IgG, and TBI+anti-CD4 conditions. IFN $\gamma$  module score is based on differentially upregulated genes from microglia treated *in vivo* with IFN $\gamma$  (see Figure S5M-O). Kruskal-Wallis test within each cluster.
- J) Representative flow plots depicting CD11c and CLEC7A expression within thalamic microglia (CD45<sup>lo</sup> CD11b<sup>+</sup> CD64<sup>+</sup> CX3CR1<sup>+</sup>) from Sham+IgG, TBI+IgG, and TBI+anti-CD4 treated mice 14dpi. See gating strategy in Figure S7A.
- K) Frequency of CD11c<sup>+</sup> CLEC7A<sup>+</sup> microglia within total thalamic microglia from Sham+IgG, TBI+IgG, and TBI+anti-CD4 treated mice 14dpi.
- L) Median fluorescence intensity (MdfI) of CLEC7A within thalamic microglia from Sham+IgG, TBI+IgG, and TBI+anti-CD4 treated mice 14dpi.
- M) Frequency of CD11c<sup>+</sup> CD9<sup>+</sup> microglia within total thalamic microglia from Sham+IgG, TBI+IgG, and TBI+anti-CD4 treated mice 14dpi.
- N) Representative flow plots depicting Thy1.2<sup>+</sup> Tbet<sup>+</sup> type 1 lymphocytes in the thalamus of Sham+IgG, TBI+IgG, and TBI+anti-CD4 treated mice 14dpi.
- O) Quantification of Thy1.2<sup>+</sup> Tbet<sup>+</sup> type 1 lymphocyte cell numbers in the thalamus of Sham+IgG, TBI+IgG, and TBI+anti-CD4 treated mice 14dpi.
- P) Quantification of NK/ILC1 cell numbers in the thalamus of Sham+IgG, TBI+IgG, and TBI+anti-CD4 treated mice 14dpi.
- Q) Quantification of CD8<sup>+</sup> T cell numbers in the thalamus of Sham+IgG, TBI+IgG, and TBI+anti-CD4 treated mice 14dpi.

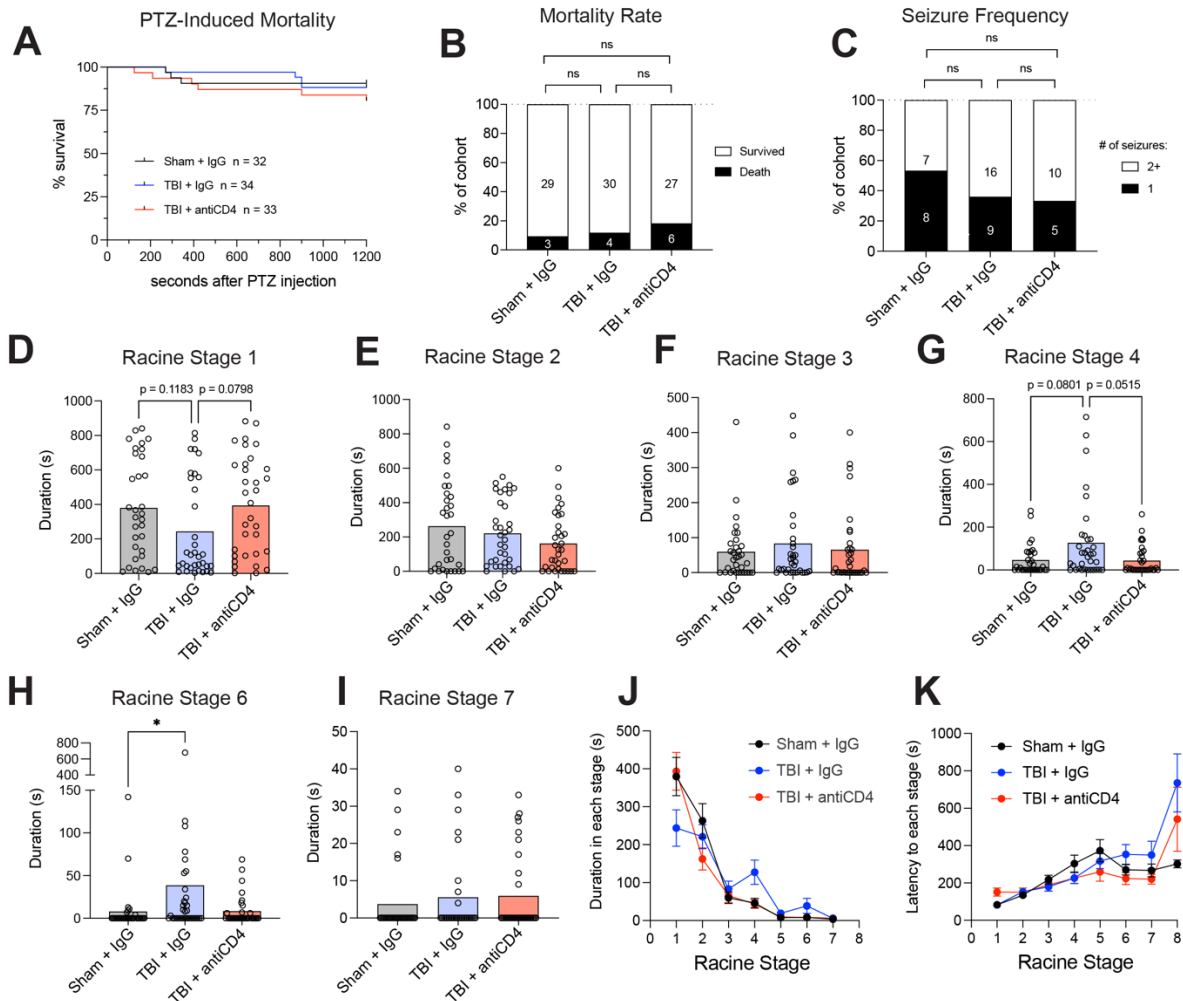


**Figure 2.9. CD4<sup>+</sup> T cell depletion does not impact PTZ-induced mortality, seizure frequency, or latency to Racine stages after TBI.**

- A) Survival curve depicting percentage of surviving Sham+IgG, TBI+IgG, and TBI+anti-CD4 mice after PTZ challenge (at 5wpi).
- B) Quantification of mortality rate after PTZ challenge (at 5wpi) in Sham+IgG, TBI+IgG, and TBI+anti-CD4 groups depicted as percentage of each cohort that died (black bars). Numbers within bar graph represent number of mice in each group that died or survived. Fisher's exact tests.
- C) Quantification of mortality rate after PTZ challenge (at 5wpi) in Sham+IgG, TBI+IgG, and TBI+anti-CD4 groups depicted as percentage of each cohort that experience 1 (black bars) or 2+ (white bars) seizures. Fisher's exact tests.
- D) Duration each mouse from indicated groups spent in Racine Stage 1 after PTZ challenge (at 5wpi). Kruskal-Wallis test with Dunn's multiple comparisons test.
- E) Duration each mouse from indicated groups spent in Racine Stage 2 after PTZ challenge (at 5wpi). Kruskal-Wallis test with Dunn's multiple comparisons test.
- F) Duration each mouse from indicated groups spent in Racine Stage 3 after PTZ challenge (at 5wpi). Kruskal-Wallis test with Dunn's multiple comparisons test.
- G) Duration each mouse from indicated groups spent in Racine Stage 4 after PTZ challenge (at 5wpi). Kruskal-Wallis test with Dunn's multiple comparisons test.
- H) Duration each mouse from indicated groups spent in Racine Stage 6 after PTZ challenge (at 5wpi). Kruskal-Wallis test with Dunn's multiple comparisons test.
- I) Duration each mouse from indicated groups spent in Racine Stage 7 after PTZ challenge (at 5wpi). Kruskal-Wallis test with Dunn's multiple comparisons test.
- J) Duration in each stage (s) after PTZ challenge (at 5wpi). Kruskal-Wallis test with Dunn's multiple comparisons test.
- K) Latency to each stage (s) after PTZ challenge (at 5wpi). Kruskal-Wallis test with Dunn's multiple comparisons test.
- (Figure caption continued on next page)

*(Figure caption continued from previous page)*

- H) Duration each mouse from indicated groups spent in Racine Stage 6 after PTZ challenge (at 5wpi). Kruskal-Wallis test with Dunn's multiple comparisons test.
- I) Duration each mouse from indicated groups spent in Racine Stage 7 after PTZ challenge (at 5wpi). Kruskal-Wallis test with Dunn's multiple comparisons test.
- J) Quantification of duration in all Racine stages of mice from indicated groups after PTZ challenge (at 5wpi).
- K) Quantification of latency to each Racine stage of mice from indicated groups after PTZ challenge (at 5wpi).

For (D-I), data are means. For (J-K), data are means  $\pm$  SEM. Data points represent biological replicates (individual mice). Mice per condition (pooled from 2 independent experiments): sham+IgG n=32, TBI+IgG n=34, TBI+anti-CD4 n=33. Statistics: ns=not significant, \*p < 0.05.

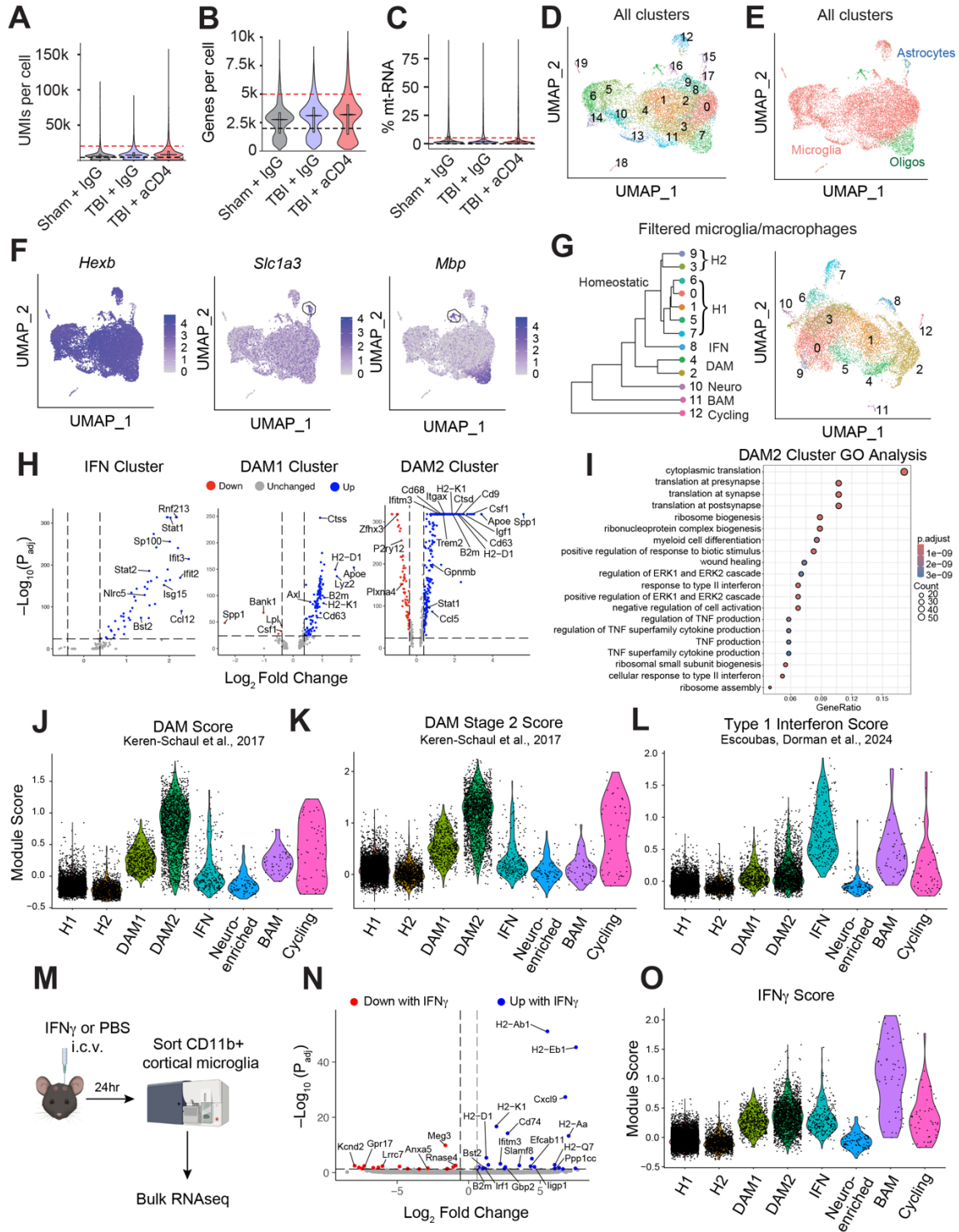


**Figure 2.10. Quality controls metrics and cell type assignment of scRNAseq data.**

A) Violin plot showing scRNAseq unique molecular identifier (UMI) counts per cell across conditions and filtering thresholds (4,000–20,000 UMI counts/cell).

B) Violin plot showing scRNAseq gene counts per cell across conditions and filtering thresholds (2,000–5,000 genes/cell).

C) Violin plot showing scRNAseq percentage of mitochondrial genes (mt-RNA) per cell across conditions and filtering thresholds (% mt-RNA < 5%). (Figure caption continued on next page)



(Figure caption continued from previous page)

- D) Unsupervised clustering (UMAP plot) of filtered cells (using thresholds in A–C) shown with a clustering resolution of 1. Further filtering of non-microglial cells was done using this clustering resolution.
- E) Cell type assignment shown on UMAP plot from D. Cells were further filtered by *Mbp* expression, with all cells having a normalized *Mbp* expression > 2 removed from downstream analyses.
- F) Selection of genes used to filter for microglia: *Hexb*, *Slc1a3* (GLAST, expressed by astrocytes), and *Mbp* (myelin basic protein, expressed by oligodendrocytes). Black lines indicate clusters (7, 15) removed from downstream analysis.
- G) Clustering tree and UMAP plot for re-clustered microglia after removal of contaminating astrocytes and oligodendrocytes (clustering resolution = 0.5). Clusters 0/6/1/5/7 and 3/9 were combined into homeostatic clusters "H1" and "H2" respectively due to fewer than 10 upregulated genes identified in clusters 5,6,7, and 9.
- H) Volcano plots depicting differentially expressed genes (DEGs) for the IFN-responsive ("IFN") cluster (8), DAM Stage 1 ("DAM1") cluster (4), and DAM Stage 2 ("DAM2") cluster (2), compared to average expression of all other clusters. Labelled genes are from the top 20 genes by log fold change. DEG thresholds:  $p_{\text{adj}} < 10^{-25}$ ,  $|\text{FC}| > 1.3$ .
- I) Gene ontology (GO) analysis of differentially upregulated genes from the 'DAM2' cluster, as depicted in (H).
- J) Violin plot showing DAM module score across scRNAseq clusters using the top 30 DEGs by log fold change defining DAMs (from Keren-Shaul et. al. 2017)<sup>34</sup> and corresponding assignment of DAM1 and DAM2 cluster identities.
- K) Violin plot showing DAM Stage 2 module score across scRNAseq clusters using the top 30 DEGs by log fold change defining Stage 2 DAMs (from Keren-Shaul et. al. 2017)<sup>34</sup> and corresponding assignment of DAM1 and DAM2 cluster identities.
- L) Violin plot showing type 1 interferon module score across scRNAseq clusters using the DEGs defining type 1 interferon-responsive microglia (IRMs, from Escoubas, Dorman et. al. 2024)<sup>35</sup> and corresponding assignment of IFN cluster identity.
- M) Schematic depicting experimental design of IFN $\gamma$  (or PBS vehicle) intracerebroventricular (i.c.v.) injections and subsequent sorting of cortical microglia (CD45<sup>lo</sup> CD11b<sup>+</sup>) 4 hours after injection for bulk RNA sequencing.
- N) Volcano plot depicting DEGs in cortical microglia 4 hours after *in vivo* treatment with IFN $\gamma$ , as compared to PBS-treated controls (as shown in M). DEG thresholds:  $p_{\text{adj}} < 0.05$ ,  $|\text{FC}| > 1.5$ .
- O) Violin plot showing IFN $\gamma$  module score across scRNAseq clusters using the genes differentially upregulated in cortical microglia 4 hours after *in vivo* IFN $\gamma$  treatment (blue genes highlighted in N), demonstrating elevated IFN $\gamma$  signatures in DAM1, DAM2, IFN, BAM, and cycling microglial clusters.

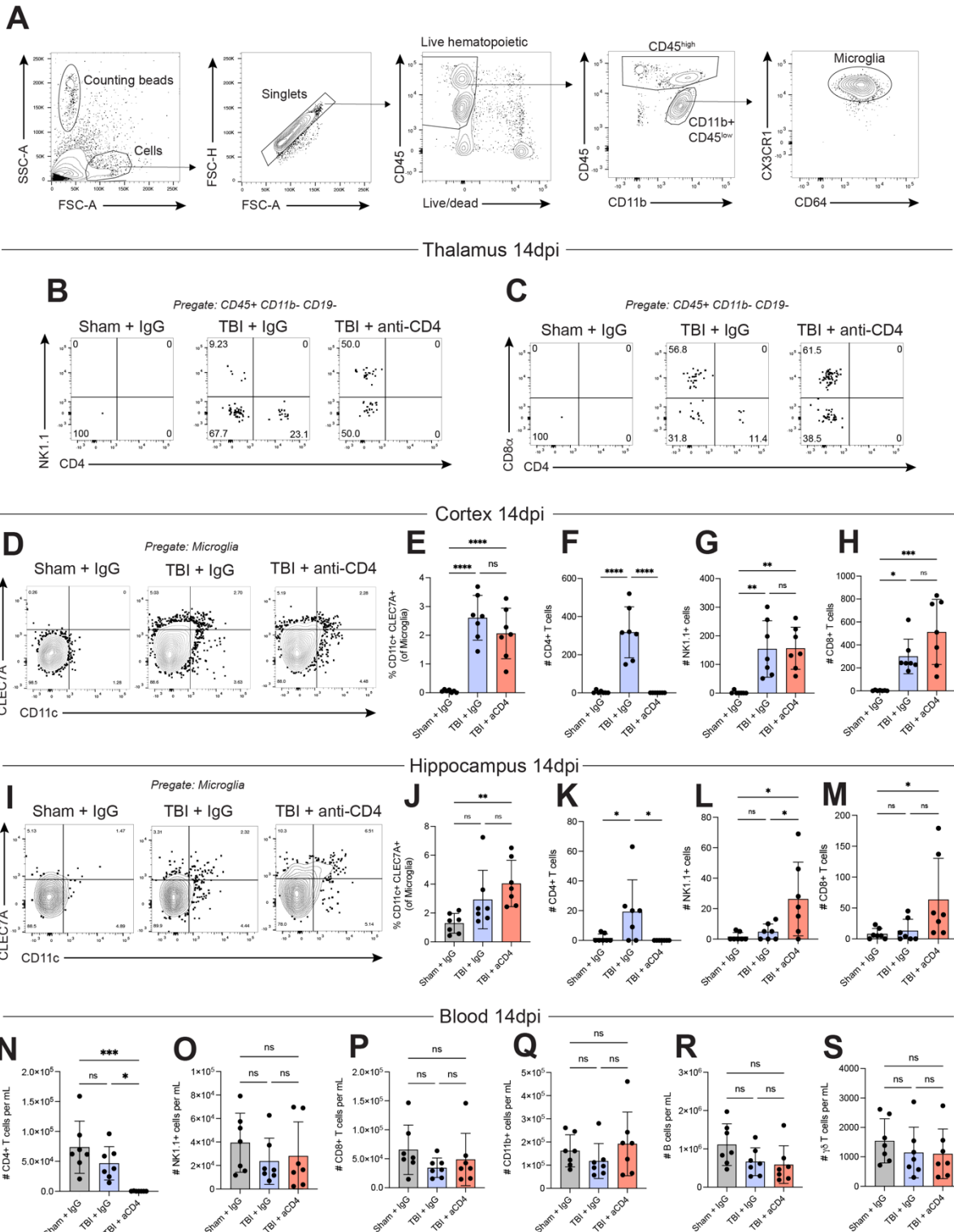


**Figure 2.11. CD4<sup>+</sup> T cell depletion does not impact DAMs and type 1 lymphocytes in other brain regions or in circulation.**

A) Gating strategy used to identify microglia across brain regions for subsequent DAM marker expression analysis. Representative flow plots are from the cortex at 14dpi.

(Figure caption continued on next page)

(Figure caption continued from previous page)

- B) Representative flow plots from the ipsilateral thalami of Sham+IgG, TBI+IgG, and TBI+anti-CD4 treated mice at 14dpi showing CD4<sup>+</sup> cell depletion and NK1.1<sup>+</sup> cell expansion with anti-CD4 treatment.
- C) Representative flow plots from the ipsilateral thalami of Sham+IgG, TBI+IgG, and TBI+anti-CD4 treated mice at 14dpi showing CD4<sup>+</sup> cell depletion and CD8 $\alpha$ <sup>+</sup> cell expansion with anti-CD4 treatment.
- D) Representative flow plots depicting CD11c and CLEC7A expression within perilesional cortical microglia (CD45<sup>lo</sup> CD11b<sup>+</sup> CD64<sup>+</sup> CX3CR1<sup>+</sup>) from Sham+IgG, TBI+IgG, and TBI+anti-CD4 treated mice 14dpi.
- E) Frequency of CD11c<sup>+</sup> CLEC7A<sup>+</sup> microglia within total cortical microglia from Sham+IgG, TBI+IgG, and TBI+anti-CD4 treated mice 14dpi.
- F) Quantification via flow cytometry of CD4<sup>+</sup> T cell numbers in the perilesional cortex from Sham+IgG, TBI+IgG, and TBI+anti-CD4 mice at 14dpi.
- G) Quantification via flow cytometry of NK/ILC1 cell numbers in the perilesional cortex from Sham+IgG, TBI+IgG, and TBI+anti-CD4 mice at 14dpi.
- H) Quantification via flow cytometry of CD8<sup>+</sup> T cell numbers in the perilesional cortex from Sham+IgG, TBI+IgG, and TBI+anti-CD4 mice at 14dpi.
- I) Representative flow plots depicting CD11c and CLEC7A expression within ipsilateral hippocampal microglia (CD45<sup>lo</sup> CD11b<sup>+</sup> CD64<sup>+</sup> CX3CR1<sup>+</sup>) from Sham+IgG, TBI+IgG, and TBI+anti-CD4 treated mice 14dpi.
- J) Frequency of CD11c<sup>+</sup> CLEC7A<sup>+</sup> microglia within total hippocampal microglia from Sham+IgG, TBI+IgG, and TBI+anti-CD4 treated mice 14dpi.
- K) Quantification via flow cytometry of CD4<sup>+</sup> T cell numbers in the ipsilateral hippocampus from Sham+IgG, TBI+IgG, and TBI+anti-CD4 mice at 14dpi.
- L) Quantification via flow cytometry of NK1.1<sup>+</sup> NK/ILC1 cell numbers in the ipsilateral hippocampus from Sham+IgG, TBI+IgG, and TBI+anti-CD4 mice at 14dpi.
- M) Quantification via flow cytometry of CD8<sup>+</sup> T cell numbers in the ipsilateral hippocampus from Sham+IgG, TBI+IgG, and TBI+anti-CD4 mice at 14dpi.
- N) Quantification via flow cytometry of CD4<sup>+</sup> T cell concentrations in the blood of Sham+IgG, TBI+IgG, and TBI+anti-CD4 mice at 14dpi.
- O) Quantification via flow cytometry of NK1.1<sup>+</sup> NK/ILC1 cell concentrations in the blood of Sham+IgG, TBI+IgG, and TBI+anti-CD4 mice at 14dpi.
- P) Quantification via flow cytometry of CD8<sup>+</sup> T cell concentrations in the blood of Sham+IgG, TBI+IgG, and TBI+anti-CD4 mice at 14dpi.
- Q) Quantification via flow cytometry of CD11b<sup>+</sup> myeloid cell concentrations in the blood of Sham+IgG, TBI+IgG, and TBI+anti-CD4 mice at 14dpi.
- R) Quantification via flow cytometry of CD19<sup>+</sup> B cell concentrations in the blood of Sham+IgG, TBI+IgG, and TBI+anti-CD4 mice at 14dpi.
- S) Quantification via flow cytometry of  $\gamma\delta$  T (CD3<sup>+</sup> TCR $\gamma\delta$ <sup>+</sup>) cell concentrations in the blood of Sham+IgG, TBI+IgG, and TBI+anti-CD4 mice at 14dpi.

Data are mean  $\pm$  SD. Data points represent biological replicates (individual mice). One-way ANOVAs with Tukey's multiple comparisons test. Statistics: ns = non-significant, \*p < 0.05, \*\*p < 0.01, \*\*\*p < 0.001, \*\*\*\*p < 0.0001.

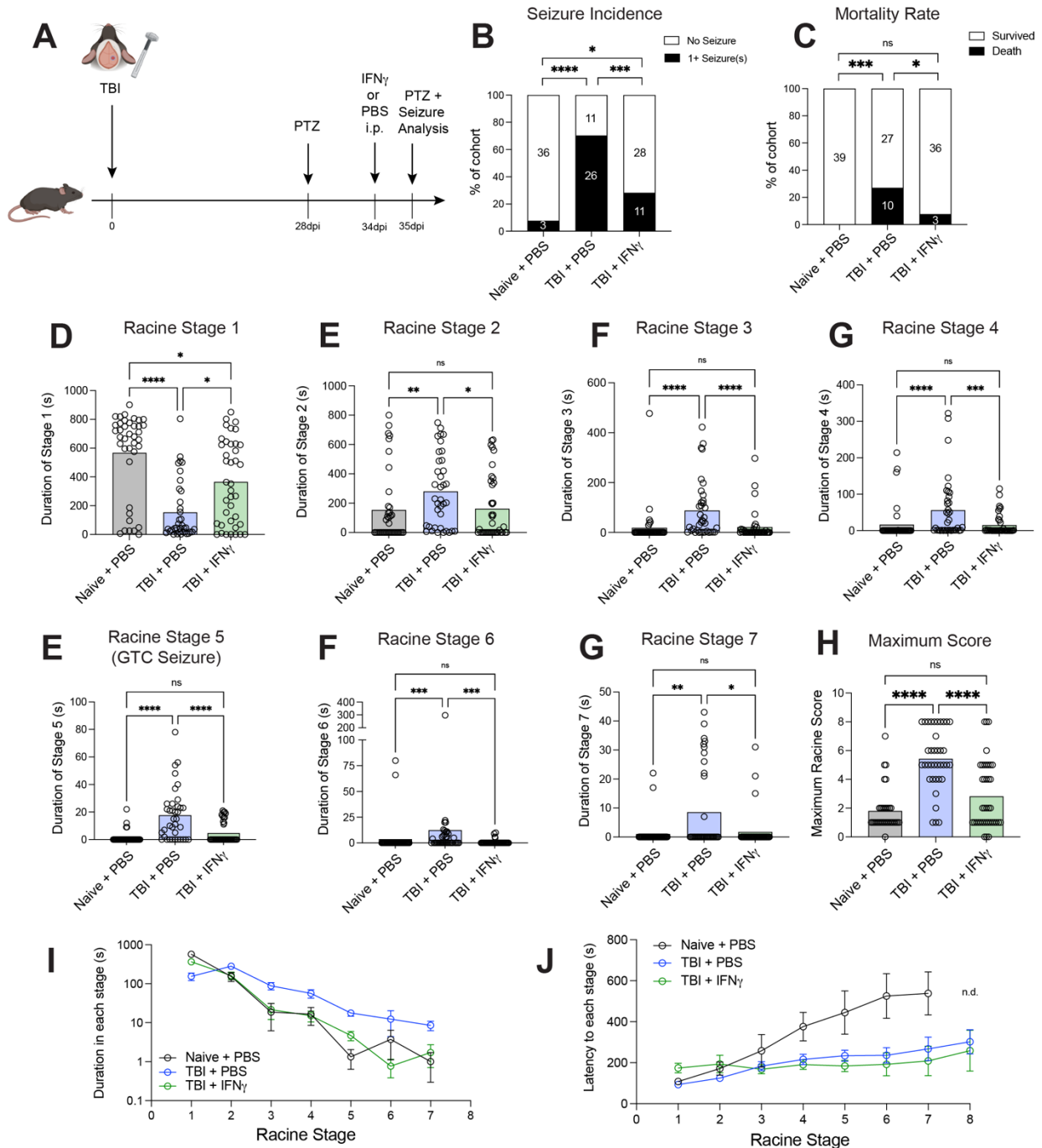


**Figure 2.12. IFN $\gamma$  treatment reduces TBI-induced seizure susceptibility and severity.**

A) Schematic depicting sham or TBI surgeries, followed by IFN $\gamma$  treatment and pentylentetrazol (PTZ) dosing regimen used to assess seizure susceptibility. Mice were given a sensitizing dose of PTZ (45 mg/kg i.p.) at 4 weeks post injury. 24 hours prior to PTZ challenge at 5 weeks, mice were treated with either IFN $\gamma$  (10  $\mu$ g/mouse) i.p. or PBS vehicle. Mice were then given a challenge of PTZ (45 mg/kg i.p.) at 5 weeks post injury, at which point seizure behavior was recorded and quantified.

(Figure caption continued on next page)

(Figure caption continued from previous page)

- B) Percentage of indicated experimental groups that experienced one or more generalized tonic-clonic (GTC) seizures (black bars). Numbers within bar graph represent number of mice in each group that experienced 0 or 1+ GTC seizures. Fisher's exact tests.
- C) Percentage of each indicated group that died (black bars) after PTZ challenge (5wpi). Fisher's exact tests.
- D) Duration of each mouse from indicated groups spent in Racine Stage 1. Kruskal-Wallis test with Dunn's multiple comparisons test.
- E) Duration of each mouse from indicated groups spent in Racine Stage 2 after PTZ challenge (5wpi). Kruskal-Wallis test with Dunn's multiple comparisons test.
- F) Duration of each mouse from indicated groups spent in Racine Stage 3 after PTZ challenge (5wpi). Kruskal-Wallis test with Dunn's multiple comparisons test.
- G) Duration of each mouse from indicated groups spent in Racine Stage 4 after PTZ challenge (5wpi). Kruskal-Wallis test with Dunn's multiple comparisons test.
- H) Duration of each mouse from indicated groups in Racine Stage 5 (GTC seizures) after PTZ challenge (5wpi). Kruskal-Wallis test with Dunn's multiple comparisons test.
- I) Duration of each mouse from indicated groups spent in Racine Stage 6 after PTZ challenge (5wpi). Kruskal-Wallis test with Dunn's multiple comparisons test.
- J) Duration of each mouse from indicated groups spent in Racine Stage 7 after PTZ challenge (5wpi). Kruskal-Wallis test with Dunn's multiple comparisons test.
- K) Maximum Racine Score reached per mouse in indicated groups. Kruskal-Wallis test with Dunn's multiple comparisons test.
- L) Quantification of duration in all Racine stages of mice from indicated groups after PTZ challenge (at 5wpi).
- M) Quantification of latency to each Racine stage of mice from indicated groups after PTZ challenge (at 5wpi).

For C-H, data are mean. For G-H, data are mean  $\pm$  SEM. Data points represent biological replicates (individual mice). Mice per condition (pooled from 2 independent experiments): naive + PBS n=39, TBI + PBS n=37, TBI+ IFN $\gamma$  n=39. Statistics: ns = non-significant, \*p < 0.05, \*\*p < 0.01, \*\*\*p < 0.001, \*\*\*\*p < 0.0001.

**Table 2.1 Antibodies used for flow cytometry in Chapter 2.**

Reagent	Clone	Dilution	Vendor	Catalog #
Fc Block (Rat anti-mouse CD16/CD32)	2.4G2	1:100–1:250	BD Biosciences	553142
FoxP3–AF488	FJK-16s	1:100	eBioscience	53-5773-82
GATA-3–PE	TWAJ	1:100	eBioscience	12-9966-41
CD19–PEDazzle594	6D5	1:400	BioLegend	115554
Tbet–PE-Cy7	4B10	1:100	BioLegend	25-5825-80
ROR $\gamma$ t–APC	B2D	1:100	eBioscience	17-6981-82
CD3–AF700	17A2	1:200	BioLegend	100216
Thy1.2 (CD90.2)–BV421	53-2.1	1:400	BioLegend	140327
CD11b–BV605	M1/70	1:400	BD Biosciences	563015
NK1.1–BV650	PK136	1:400	BioLegend	108736
CD4–BV711	RM4-5	1:200	BioLegend	100557
CD8 $\alpha$ –BV785	53-6.7	1:200	BioLegend	100750
CD45–BUV395	30-F11	1:400	BD Biosciences	564279
TCR $\gamma$ $\delta$ –PerCP-Cy5.5	GL3	1:200	BioLegend	118118
CD69–FITC	H1.2F3	1:100	BioLegend	104505
CD62L–PerCP-Cy5.5	MEL-14	1:200	BioLegend	104431
CD8 $\alpha$ –Pacific Blue	5H10	1:200	Invitrogen	MCD0828
KLRG1–BV510	2F1/KLRG1	1:200	BioLegend	138421
CD3 $\epsilon$ –BV711	145-2C11	1:200	BD Biosciences	563123
CD44–BV785	IM7	1:400	BioLegend	103041
CD103–BUV737	M290	1:200	BD Biosciences	741739
IFN $\gamma$ –FITC	XMG1.2	1:100	BioLegend	505806
IL-17A–PE-Cy7	TC11-18H10.1	1:100	BioLegend	506922
IL-5–APC	TRFK5	1:100	BioLegend	504306
IL-13–eF660	eBio13A	1:100	eBioscience	50-7133-82
CD3 $\epsilon$ –BV510	145-2C11	1:200	BioLegend	100353
CD11b–FITC	M1/70	1:400	BioLegend	101206
CD369 (Dectin-1/CLEC7A)–APC	RH1	1:200	BioLegend	144305
CD9–BV421	KMC8	1:200	BD Biosciences	564235
CD64–BV605	X54-5/7.1	1:200	BioLegend	139323
CD11c–BV650	N418	1:200	BioLegend	117339
CX3CR1–BV785	SA011F11	1:200	BioLegend	149029
CD45–FITC	30-F11	1:100	BioLegend	103108
CD11b–PE	M1/70	1:100	BioLegend	101208
Ly6C–APC	HK1.4	1:100	BioLegend	128015

**Table 2.2 Antibodies used for immunofluorescent imaging in Chapter 2.**

<b>Reagent</b>	<b>Clone</b>	<b>Dilution</b>	<b>Vendor</b>	<b>Catalog #</b>
Rat anti-GFAP	2.2B10	1:1000	Invitrogen	13-0300
Rabbit anti-Iba1	Polyclonal	1:1000	Wako	019-19741
Chicken anti-NeuN	Polyclonal	1:500	Millipore Sigma	ABN91
Rat anti-MHC-II (I-A/I-E)	M5/114.15.2	1:500	eBioscience	14-5321-82
Rabbit anti-STAT1	D1K9Y	1:200	Cell Signaling Technology	14994S
Mouse anti-Parvalbumin (PV)	PARV-19	1:1000	Sigma Aldrich	P3088-100UL
Guinea Pig anti-Iba1	Gp311H9	1:1000	Synaptic Systems	234 308
Syrian hamster anti-CD3 $\epsilon$	500A2	1:200	BD Biosciences	553238
Rat anti-CD45-AF488	30-F11	1:200	BioLegend	103122
Goat anti-rat AF488	Polyclonal	1:1000	Invitrogen	A11006
Goat anti-rabbit AF555	Polyclonal	1:1000	Invitrogen	A21429
Goat anti-chicken AF647	Polyclonal	1:1000	Invitrogen	A21449
Goat anti-rat AF555	Polyclonal	1:1000	Invitrogen	A21434
Goat anti-rabbit AF647	Polyclonal	1:1000	Invitrogen	A21245
Goat anti-guinea pig AF888	Polyclonal	1:1000	Invitrogen	A11073
Goat anti-chicken AF405+	Polyclonal	1:1000	Invitrogen	A48260
Goat anti-hamster AF647	Polyclonal	1:1000	Invitrogen	A21451
Goat anti-mouse AF555	Polyclonal	1:1000	Invitrogen	A21424

**Table 2.3. Chemicals, commercial kits, and other critical reagents used in Chapter 2.**

Reagent	Dilution	Vendor	Catalog #
Fixable Viability Dye eFlour 780	1:1000	eBioscience	65-0865-18
Draq7	1:1000	BioLegend	424001
Cell Stimulation Cocktail (500X)	1:500	Cytek	TNB-4975
Brefeldin A Solution (1000X)	1:1000	eBioscience	00-4506-51
Heparin sodium salt	—	Sigma	H3393
PharmLyse (100X)	1:100	BD Biosciences	555899
Percoll	22%	GE Healthcare	17-0891-01
FoxP3/Transcription Factor Staining Buffer Set	—	eBioscience	00-5523-00
BD Cytofix/Cytoperm Fixation/Permeabilization Kit	—	BD Biosciences	554714
CountBright Absolute Counting Beads, for flow cytometry	—	Invitrogen	C36950
RIPA Buffer (10X)	1:10	Cell Signaling Technology	9806
Phenylmethylsulfonyl fluoride (PMSF)	1:200 from 200X stock	Cell Signaling Technology	8553S
Pierce BCA Protein Assay Kit	—	Thermo Scientific	23225
CD11b MACS Beads	—	Miltenyi Biotech	130-097-142
MACS LS Columns	—	Miltenyi Biotech	130-042-401
Fluoromount G with DAPI	—	Southern Biotech	0100-20
Fluoromount G	—	Southern Biotech	0100-01
Pentylentetrazole (PTZ)	—	Tocris	2687/1G
Recombinant mouse IFN $\gamma$ (carrier free)	—	BioLegend	575308
Mouse IFN $\gamma$ Recombinant Protein	—	Gibco	PMC4034



## 2.6 MATERIALS AND METHODS

### Mice

All experiments were conducted per protocols approved by the Institutional Animal Care and Use Committee at the University of California, San Francisco and Gladstone Institutes. Precautions were taken to minimize stress and the number of animals used in each set of experiments. Male and female (6-8 weeks old) C57BL/6J mice (JAX#000664) were purchased and used for most experiments. Male mice were used for all flow, imaging, and seizure experiments, while both male and female mice were used for scRNAseq. Mice weighed 22-28 g at the time of surgery. For specific experiments, *Tbx21<sup>zsGreen</sup>* reporter mice were used (MGI #5690118).<sup>31</sup>

### Controlled cortical impact (CCI) surgeries

Controlled cortical impact (CCI) was induced in the somatosensory cortex as previously described.<sup>17</sup> Briefly, in isoflurane-anesthetized adult mice, a 3-mm diameter craniotomy was performed over the right somatosensory (S1) cortex (centered at -1 mm posterior from Bregma, 3 mm lateral). TBI was performed with a CCI device (Impact One Stereotaxic Impactor for CCI, Leica Microsystems) equipped with a metal piston using the following parameters: 3 mm tip diameter, 18° angle, 0.8 mm depth from the dura, 3 m/s velocity, and 300 ms dwell time. Sham mice received identical anesthesia and scalp incision but received a sham craniotomy of 3-mm diameter (in which the drill bit was used to trace a craniotomy on the skull without the forming of a bone flap), and the injury was not delivered.

### PTZ Challenge and Seizure Analysis

To determine the seizure susceptibility of mice with TBI in a high throughput manner, we assessed behavioral seizures induced by intraperitoneally (i.p.) injection of proconvulsive agent pentylenetetrazol (PTZ; 45 mg/kg). PTZ dose was selected based on prior studies for C57BL6 mice in our group and others.<sup>32,33</sup> Four weeks after TBI/sham surgery mice received the first dose

of PTZ (45 mg/kg) (priming dose, without video recording). One week after the first dose of PTZ injection, the second dose of 45mg/kg PTZ was administered, and mice were video-recorded for 15 minutes after PTZ. The video recording was analyzed off-line for incidence of generalized tonic-clonic (GTC) seizure, mortality rate and seizure severity using the modified Racine scale<sup>55</sup> which scored behavioral seizures into: Stage 0 = normal behavior; 1 = immobility; 2 = generalized spasm, tremble, or twitch; 3 = tail extension; 4 = forelimb clonus; 5 = generalized tonic-clonic activity; 6 = bouncing or running seizures; 7 = full tonic extension; 8 = death.

### **In vivo antibody-mediated depletion**

Rat anti-mouse CD4 antibodies (250 µg, clone GK1.5, BioXCell) and the corresponding isotype control rat IgG2b antibodies (250 µg, clone LTF-2, BioXCell) were diluted in sterile PBS buffer (BioXCell) immediately prior to i.p. injection 3 hours after mice underwent TBI/sham surgeries. Both antibody-treated cohort and isotype control-treated cohort received booster doses every 4 days (250 µg, sterile PBS) for two constitutive weeks to maintain CD4 T cell depletion.

### **In vivo cytokine treatment**

Recombinant mouse IFN $\gamma$  (carrier-free, BioLegend) was reconstituted in sterile double distilled water and freshly diluted in 1X Dulbecco's Phosphate Buffered Saline (DPBS) before treatment. IFN $\gamma$  (10 µg per animal in volume of 200 µl) were injected i.p. 24 hours before PTZ challenge recording. The control TBI or sham animals were treated with 200 µl of DPBS.

### **Blood collection for flow cytometry**

Mice were deeply anesthetized with isoflurane. Blood was collected via cardiac puncture with an insulin syringe and thoroughly mixed with 0.3 mL of a 5 U/mL heparin sodium salt (Sigma) solution in 1X DPBS to prevent coagulation. Blood isolates were then pelleted (500xg for 5 min) and subjected to two rounds of red blood cell lysis (1X Pharm-Lyse solution; BD) prior to antibody staining for flow cytometry. Final cell counts were normalized to the volume of blood collected from each mouse.

### **Brain dissociation for flow cytometry**

Mice were deeply anesthetized with isoflurane and perfused with 10-15 mL of ice cold 1X PBS via the left ventricle (after blood collection, see above). The brain was dissected from the skull and three 1mm coronal sections were cut using a brain matrix. Perilesional cortex, ipsilateral hippocampus, and ipsilateral thalamus were micro-dissected under a dissection microscope from these sections and separately collected into 2 mL of iMED (isolation medium: 1X HBSS (without calcium or magnesium) supplemented with 15 mM HEPES and 0.6% glucose). Brain samples were then homogenized to yield microglia and other immune cells, as previously described.<sup>56</sup> Briefly, brain samples were mechanically dissociated in a 2 cm<sup>3</sup> glass dounce homogenizer in iMED on ice, filtered through a 70 µm cell strainer, and washed twice. Samples were centrifuged at 220xg for 10 min at 4°C and then resuspended in a 22% Percoll solution (GE Healthcare) with a PBS layer floated on top. Samples were centrifuged at 950xg for 20 min (acceleration=4, brake=0) and the supernatant layers were discarded to remove myelin and debris. Cell pellets were resuspended prior to antibody staining for flow cytometry.

### **Staining for flow cytometry**

For myeloid/microglia panels, single cell suspensions were first incubated in FACS Wash Buffer (FWB, 1X DPBS (pH 7.4) with 3% (v/v) heat-inactivated FBS and 0.05% NaN<sub>3</sub>) containing 5% (v/v) normal rat serum and Fc Block (2.4G2, 1:250, BD Biosciences) for 20 min at 4°C. Cells were pelleted at 1200rpm for 2 min and resuspended in FWB containing surface antibodies for 45min at 4°C. Cells were washed and resuspended with FWB prior to analysis.

For lymphocyte panels involving transcription factor staining, single cell suspensions were first incubated with a viability dye (Fixable Viability Dye eFluor780, eBioscience), Fc Block (2.4G2, 1:100, BD Biosciences), and surface antibodies diluted in 1X DPBS for 45-60 min at 4°C. Cells were washed with FWB and then fixed and permeabilized overnight at 4°C using the FoxP3/transcription factor Staining Buffer Set (eBioscience). Cells were washed with 1X PermBuffer (eBioscience) and stained with intracellular antibodies for 60 min at 4°C. Cells were

washed again with 1X PermBuffer and then resuspended in FWB prior to analysis. Any experiments that included anti-CD4 treated mice were stained with an anti-CD4 clone (RM4-5) different than the clone used for *in vivo* CD4 depletion (GK1.5) to avoid epitope masking.

For cytokine staining, cells were first stimulated *ex vivo* with PMA (phorbol 12-myristate 13-acetate) and ionomycin. Single cell suspensions were resuspended in complete RPMI (1X RPMI 1640 supplemented with 10% (v/v) heat-inactivated FBS, 1% (v/v) penicillin/streptomycin, 1% (v/v) Glutamax, 1 mM sodium pyruvate, 10 mM HEPES, 10 mM non-essential amino acids, and 55  $\mu$ M  $\beta$ -mercaptoethanol) containing 1X Tonbo Cell Stimulation Cocktail (Cytex) and 1X Brefeldin A (BFA, eBioscience) for 3 hours in a 37°C / 5% CO<sub>2</sub> incubator. Cells were washed with FWB and stained with a viability dye (Fixable Viability Dye eFluor780, eBioscience), Fc Block (2.4G2, 1:100, BD Biosciences), and surface antibodies diluted in 1X DPBS for 45-60 min at 4°C. Cells were then washed and fixed and permeabilized for 20 min at 4°C using the Cytotfix/Cytoperm Fixation/ Permeabilization Kit (BD Biosciences). Cells were washed with 1X PermBuffer (BD Biosciences) and stained with intracellular antibodies overnight at 4°C. Cells were washed again with 1X PermBuffer (BD Biosciences) and then resuspended in FWB prior to analysis.

Prior to data collection, counting beads (CountBright Absolute Counting Beads, Invitrogen) were added to each sample and samples were filtered through a 40  $\mu$ m cell strainer. Flow cytometric data was collected on a BD Fortessa and data analysis was performed using FlowJo software (BD).

### **Staining for immunofluorescent imaging**

Mice were deeply anesthetized with isoflurane and perfused with 10-15 mL of ice cold 1X PBS via the left ventricle, followed by 10 mL of 4% (w/v) paraformaldehyde (PFA) diluted in 1X PBS. Brains were dissected out and fixed overnight at 4°C in 4% PFA/PBS. Brains were then washed in PBS and placed in 30% (w/v) sucrose for cryopreservation for a minimum of 2 days.

Brains were then frozen in OCT and stored at  $-80^{\circ}\text{C}$  until sectioning into  $40\ \mu\text{m}$  sections using a cryostat (Leica).  $40\ \mu\text{m}$  sections were then stored in 1X PBS containing 0.05%  $\text{NaN}_3$  at  $4^{\circ}\text{C}$ .

Brain sections were stained in 24 well plates and first blocked in 0.5 mL/well Block/Stain Solution (1X PBS containing 5% (v/v) normal goat serum and 0.4% (v/v) Triton X-100) for 1 hour at room temperature (RT). Sections were then stained overnight at  $4^{\circ}\text{C}$  with primary antibodies diluted in 0.25 mL/well Block/Stain Solution on a plate shaker ( $\sim 90\text{rpm}$ ). Sections were washed four times with PBS-T (0.05% (v/v) Triton X-100 in 1X PBS) for 5 min each at RT ( $\sim 90\text{rpm}$ ) and then stained with secondary antibodies in 0.5 mL/well Block/Stain Solution for 1.5–2hrs at RT ( $\sim 90\text{rpm}$ ). Sections were washed three times with PBS (5 min each at RT,  $\sim 90\text{rpm}$ ) before mounting in Fluoromount G with or without DAPI (Southern Biotech). Any antibodies directly conjugated to fluorophores were incubated with primary antibodies overnight.

### **Confocal Imaging and Image Analysis**

Stained sections were imaged with a Nikon A1R laser scanning confocal microscope (with 405, 488, 561, and 650 laser lines). Large tiled images of hemi-brains were collected using a 16X/0.8 NA Plan Apo water-immersion objective with 512 resolution, 1 frame/s scanning speed, 2x line averaging, and  $4\ \mu\text{m}$  Z-steps. Higher magnification images of thalami were collected using a 25X/1.1 NA Plan Apo water-immersion objective with 1024 resolution, 0.5 frame/s scanning speed, 2x line averaging, and  $2\ \mu\text{m}$  Z-steps. Images were rendered into three dimensions and quantitatively analyzed using Bitplane Imaris v9.5.1 software (Andor Technology PLC). 3D reconstructions of each channel were generated and quantified using the Imaris surface function, thresholded on signal intensity, volume, DAPI-intensity, as previously described.<sup>26,57,58</sup> Thalamic subregions were manually traced based off of NeuN staining, and quantification of cells per region were normalized to the cross-sectional area of each subregion. 2 technical replicates (independent sections) were imaged and averaged per mouse.

## **Brain tissue homogenization and cytokine measurement**

Mice were deeply anesthetized with isoflurane and perfused with 10-15 mL of ice cold 1X PBS via the left ventricle. The brain was dissected from the skull and three 1mm coronal sections were cut using a brain matrix. Perilesional cortex, ipsilateral hippocampus, and ipsilateral thalamus were micro-dissected under a dissection microscope from these sections, snap frozen on dry ice, and stored at -80°C. Tissue samples were thawed on ice, weighed, and transferred to a 2 mL tube pre-filled with 3.0 mm high-impact zirconium beads (Benchmark Scientific). 1X RIPA Buffer (Cell Signaling Technology) supplemented with 1 mM PMSF (Cell Signaling Technology) was added to each tube at a ratio of 1 mL per 100 mg of tissue per manufacturer's recommendations. Samples were lysed and homogenized on a Precellys Evolution Touch Homogenizer (Bertin Technologies) on the standard mouse setting (2x30s at 6500rpm) at 4°C. Crude lysates were centrifuged at 10,000xg for 10min at 4°C and the clarified supernatant was collected. Total protein content of each homogenate was quantified using the Pierce BCA Protein Assay Kit (Thermo Scientific) and homogenates were stored at -80C. Homogenates were then normalized to 2mg/mL total protein and sent to Eve Technologies on dry ice. Eve Technologies performed Luminex multiplex cytokine measurement to quantify cytokine concentrations in the homogenates using the Mouse High-Sensitivity T Cell 18-Plex Discovery Assay (MDHSTC18) Array. Total cytokine quantities were back-calculated from the concentration of each sample and normalized to the weight of the original brain tissue sample.

## **CD11b<sup>+</sup> cell isolation and single cell RNA sequencing (scRNAseq)**

For microglial isolation for downstream RNA-sequencing, cells were isolated as described previously<sup>56</sup>. Briefly, the right (ipsilateral) thalami from four mice per condition (two male and two female) were dissected on ice, pooled, and mechanically dissociated using a glass tissue homogenizer in isolation medium (1X HBSS, 15 mM HEPES, 0.6% glucose, 1 mM EDTA). Cells were filtered through 70 µm cell strainers and then centrifuged at 300xg for 10 minutes at 4°C before being resuspended in 22% Percoll (GE Healthcare) and centrifuged at 950xg for 20

minutes (acceleration=4, brake=0) in order to remove myelin and cellular debris. Pelleted microglia were then resuspended in staining media (1X PBS, 0.5% BSA, 2 mM EDTA) and incubated with CD11b MACS beads (Miltenyi Biotech, 1:50) for 15 minutes at 4°C. Cells were washed with staining buffer, pelleted at 300xg for 5 minutes at 4°C, and reconstituted in 500  $\mu$ L staining buffer. Microglia were isolated as described in the manual for MACS LS columns (Miltenyi Biotech) and collected in staining buffer without EDTA, pelleted at 300xg for 5 minutes at 4°C, and counted on a hemocytometer. 15,000-20,000 cells were diluted in 30  $\mu$ L in a BSA-coated plate for 10X sequencing.

Approximately 40,000 cells were loaded into each well of Chromium Chip G (v3.1) on the Chromium X, libraries were prepared in-house as described in the 10x Manual, and libraries were sequenced on three lanes of the NovaSeq SP100 at the UCSF CAT core.

### **scRNAseq data analysis**

Sequenced samples were processed using the Cell Ranger 2.1 pipeline (built on the STAR aligner)<sup>59</sup> and aligned to the GRCm38 (mm10) mouse reference genome. Clustering and differential expression analysis were conducted using Seurat version 3.1.4. Sequencing scripts can be found at [https://github.com/lcdorman/Paz\\_MG\\_TBI](https://github.com/lcdorman/Paz_MG_TBI), and original data can be found on GEO [submission in progress]. Cells were identified as “female” or “male” based on their expressions of the genes *Xist*, *Tsix*, *Ddx3y*, and *Eif2s3y*; any cells expressing at least one count of *Xist* or *Tsix* and no counts of *Ddx3y/Eif2s3y* were labelled female, while all others were labeled male. Counts were then normalized using `sctransform`, regressing out percent mitochondrial RNA and total genes per cell. The top 2000 most variable genes were used to calculate 50 principal components, and the top 30 PCs were used for nearest neighbor, UMAP, and cluster calculations (resolution = 1). Contaminating celltypes were identified through expression of *Slc1a3* and *Mbp*, and all cells with normalized expression of *Mbp* > 2 were removed. Microglia were then re-normalized and clustered as described above, with a resolution of 0.5. Two sets of most closely related homeostatic clusters (0/1/5/6/7 and 3/9) were combined due to <10 upregulated genes

(log fold change > 0.2, adjusted p-value <  $10^{-8}$ ). Differential gene expression between clusters were calculated using the MAST test in Seurat. Volcano plots were generated using the EnhancedVolcano package in R, with gene labels chosen from the top differentially expressed genes. Cutoffs were set at log fold change 0.37 (30% increase) and  $p_{\text{adj}}$  smaller than  $10^{-25}$ . A disease-associate microglia (DAM) signature score was generated using the top 25 differentially upregulated genes in DAMs in Keren-Shaul et al., 2017 ( $p < 0.001$ , ranked by logFC) and the *AddModuleScore* function in Seurat.<sup>34</sup> A type 1 interferon-responsive microglia (IRM) signature score was generated using the genes differentially expressed by the IRM cluster (cluster 8) in Escoubas, Dorman et al., 2024 ( $p < 0.01$ ,  $\log_2\text{FC} > \log_2(1.5)$ ) and the *AddModuleScore* function in Seurat.<sup>35</sup> Gene ontology analysis was performed using the ClusterProfiler R package for gene set testing (*enrichGO* function).<sup>60</sup> Bar plots depicting relative cluster frequency were created using ggplot2 in R. A table was made of cells per cluster per sample, either for the whole microglial data set or divided by sex. Cell numbers were normalized by sample by dividing each entry by the total number of cells for that sample and multiplying by 100. Percents per cluster were then calculated by dividing the normalized cell numbers by the total number of cells in that cluster and multiplying by 100.

### **Stereotactic i.c.v. Injection, Microglial Isolation, and Bulk RNA sequencing**

Brain injections were performed with a Kopf stereotaxic apparatus (David Kopf, Tujunga, CA) and a microdispensing pump (World Precision Instruments) holding a Hamilton Syringe (model 701 RN, 10 microliter) with a beveled glass needle (~50 micron outer diameter). For intraventricular (i.c.v.) injections into juveniles (P9), mice were anesthetized with 1.5% isoflurane at an oxygen flow rate of 1L/min, head-fixed with a stereotaxic frame (for juveniles, size P11), and treated with ophthalmic eye ointment. Fur was shaved and the incision site was sterilized with 70% ethanol and Betadine prior to surgical procedures. Subcutaneous 0.5% lidocaine was administered at the incision site and lack of reflex response was checked. Body temperature was maintained throughout surgery using a heating pad. After incision, a hole was drilled in the skull



and 500 nL of recombinant mouse IFN $\gamma$  (diluted to 0.2 mg/mL in PBS, Gibco) or PBS was injected (from lambda: 3 mm AP, 1.5 mm ML, -2 mm DV) at a rate of 250 nL/min. The needle was held in place for 5 minutes to allow diffusion and then slowly removed. The incision was closed and mice were allowed to fully recover with heat. Buprenorphine (Henry Schein Animal Health) was administered (0.1 mg/kg) according to approved protocols (briefly, mice were dosed prior to surgery, 4-8h later, and the next morning if needed by intraperitoneal injection).

Approximately 22h later, mice were euthanized and microglia were isolated from cortex, as described previously.<sup>56</sup> 2 females and 1 male mice were used per condition, aged P10 at collection. Cells were stained with CD45–FITC (1:100, BioLegend), CD11b–PE (1:100, BioLegend), and Ly6C–APC (1:100, BioLegend). CD45<sup>lo</sup> CD11b<sup>+</sup> Ly6C<sup>-</sup> microglia were sorted on a BD Aria III sorter into RLT plus buffer (QIAGEN). RNA was isolated from 60,000-100,000 microglia per mouse with the RNeasy® Plus Micro kit (Qiagen). Quality and concentration were determined with the Agilent RNA 6000 Pico kit on a Bioanalyzer (Agilent). All samples had an RNA Integrity Number (RIN) >7. cDNA and libraries were made using the Lexogen QuantSeq 3' mRNA-seq FWD library prep kit and quality was assessed by Agilent High Sensitivity DNA kit on a Bioanalyzer (Agilent). Pooled libraries were RNA sequenced on an Illumina HiSeq 4000 single-end for 65 cycles (SE65) yielding 50-70 million reads per sample. Quality of reads was evaluated using FastQC (<http://www.bioinformatics.babraham.ac.uk/projects/fastqc>), all samples passed quality control, and reads were aligned to mm10 (GRCm38; retrieved from Ensembl, version September 2017) using STAR (version 2.5.4b)<sup>59</sup> with '-outFilterMultimapNmax 1' to only keep reads that map one time to the reference genome. Mapped reads were counted using HTSeq (version 0.9.0)<sup>61</sup> and DESeq2 package (version 1.24.0)<sup>62</sup> was used to normalize the raw counts and perform differential gene expression analysis.

## **Chapter 3: Defining the impact of type 2 innate lymphoid cells (ILC2s) on the recovery from brain injury.**

### **3.1 ABSTRACT**

Adult brain injuries such as ischemic stroke are a leading cause of morbidity and mortality worldwide due to the limited capacity for adult brain regeneration and the lack of effective therapies to improve outcomes. While classical inflammation after brain injuries can be detrimental, type 2 immune responses are protective in this context: the type 2 cytokines Interleukin-33 (IL-33) and IL-13 have been shown to limit brain damage, yet the mechanism for this effect, including the sources and targets of these signals, is poorly defined. Group 2 innate lymphoid cells (ILC2s) are innate lymphocytes that reside in the meninges adjacent to the brain and are known to participate in wound healing processes and produce IL-13 in response to IL-33. This study explores the hypothesis that IL-33 released after brain damage activates ILC2s to produce IL-13 and regulate microglia and infiltrating myeloid cells, thereby promoting recovery from CNS injury. Using a mouse model of ischemic stroke, we find that meningeal ILC2s are activated after brain injury and may regulate cortical inhibitory synapse numbers. Despite this, we find that ILC2s largely do not regulate microglia or infiltrating myeloid or lymphoid cells and do not impact lesion size, gliosis, fibrosis, seizure susceptibility, or sensorimotor behavior in our model of brain damage. We also define the ontogeny of infiltrating myeloid cells and the role of monocyte trafficking and IL-4/13 signaling in generating alternatively activated macrophages and promoting wound healing.

### 3.2 INTRODUCTION

Ischemic stroke is a leading cause of morbidity and mortality worldwide, with increased prevalence in adult and elderly populations. Because there are currently no effective treatments that promote neuroprotection and functional recovery after CNS injury, it is imperative to increase mechanistic understanding of the wound healing response to brain damage.<sup>1,63,64</sup> Ischemic stroke is characterized by the disruption of blood flow to the brain, causing downstream hypoxia, nutrient stress, and subsequent rapid cell death.<sup>63,64</sup> After primary CNS damage, signals released from dead cells initiate sterile inflammatory cascades that recruit peripheral immune cells, including neutrophils and monocytes, which in turn cause secondary injury. The resolution phase is characterized by wound healing programs in microglia and macrophages and glial and fibrotic scar formation.<sup>1,26,63,64</sup> While classical inflammation can drive secondary damage after CNS injury, type 2 'allergic' immunity is largely protective, acting primarily during the recovery phase. The type 2 cytokines Interleukin-33 (IL-33) and IL-13 are protective after stroke and other brain injuries and mediate this effect by inducing alternative activation of microglia and macrophages, reducing lesion size, and accelerating motor recovery.<sup>65-75</sup> However, the precise mechanism(s) by which these cytokines act, including their cellular sources and targets, remains unknown.

Group 2 innate lymphoid cells (ILC2s) are tissue-resident lymphocytes that participate in type 2 immune responses against parasites and allergens, as well as wound healing and tissue remodeling processes.<sup>4,76</sup> Unlike T cells that respond to specific antigens, ILC2s respond to generic stimuli that are released after tissue perturbation and damage.<sup>4,76,77</sup> Interleukin-33 (IL-33) is a well characterized and potent activator of ILC2s that is sequestered in the nucleus at steady state but released after tissue damage.<sup>76-79</sup> Upon activation, ILC2s proliferate and produce canonical type 2 cytokines, such as IL-5 and IL-13.<sup>4,76</sup> IL-5 promotes eosinophil expansion, while IL-13 is the main effector cytokine that has pleiotropic effects across many cell types, including alternatively activating macrophages and promoting reparative growth programs.<sup>4,76,80-83</sup>

The meninges are a thin connective tissue that surrounds the CNS and act as a barrier with the periphery, consisting of three layers: the dura, arachnoid, and pial membranes.<sup>84,85</sup> Recent literature has identified numerous resident lymphocyte subsets in the dural meninges, including CD4<sup>+</sup> T cells,  $\gamma\delta$  T cells, and ILCs, and has shown that lymphocyte-derived cytokines can impact memory, learning, and social behavior in mice.<sup>45,84–92</sup> ILC2s are present in the meninges<sup>90</sup> and have been implicated in protection against aging-associated cognitive decline<sup>91</sup> and regulation of inhibitory synapse maturation during postnatal development,<sup>92</sup> suggesting they are a relevant lymphocyte population that can impact brain physiology. ILC2s also expand after spinal cord injury,<sup>90</sup> intracerebral hemorrhage,<sup>93</sup> and stroke (via the middle cerebral artery occlusion model, MCAO)<sup>94</sup> and can promote recovery when adoptively transferred,<sup>90,94</sup> but the details of their endogenous function and regulation after cortical damage are not yet known.

Immune cell tissue niches regulate the localization and activity of tissue-resident immune cells.<sup>95–97</sup> Our group has recently described a perivascular ILC2 tissue niche within the adventitia, the outermost layer of large blood vessels.<sup>95–98</sup> In the lung, ILC2s closely associate with Adventitial Fibroblasts (AFs), a specialized subset of perivascular fibroblasts that promote ILC2 activation via IL-33 during parasitic worm infection.<sup>57,98</sup> Similar fibroblast subsets in the adipose tissue promote ILC2 activation via IL-33.<sup>99,100</sup> The meninges is also rich in heterogenous fibroblasts,<sup>26,101</sup> which were recently described to support a meningeal T cell immunosurveillance niche.<sup>102</sup> Meningeal fibroblasts locally regulate other lymphocyte populations under neuroinflammatory settings,<sup>41,103,104</sup> suggesting that they may also locally regulate ILC2s after brain injury.

Given that IL-33 is released after CNS injury and IL-33, meningeal ILC2s, and IL-13 have all been implicated in improving outcomes after stroke, we hypothesized that IL-33 released from meningeal fibroblasts activates ILC2s to produce IL-13 and regulate microglia and infiltrating myeloid cells, thereby promoting recovery from CNS injury. In this study, we explored this hypothesis using the photothrombotic (PT) damage of ischemic stroke in the mouse somatosensory (S1) cortex.<sup>105,106</sup> We first characterized this model, including the kinetics of

myeloid cell infiltration after CNS damage and the ontogeny of these myeloid cells using a genetic fate mapping strategy. We next used genetic reporters to characterize the activation of meningeal ILC2s following PT injury and their localization to IL-33<sup>+</sup> meningeal fibroblasts. To determine the impacts of IL-33 signaling in ILC2s after PT stroke, we generated a conditional knockout model in which the IL-33 receptor, ST2, is deleted from ILC2s (ILC2<sup>ΔST2</sup> mice). We explored the downstream phenotypes of ILC2<sup>ΔST2</sup> mice after PT stroke, including the regulation of myeloid and lymphoid cells in the meninges and cortex, the extent of damage and gliosis in the brain, changes in synapse numbers in the cortex and functionally connected thalamus, and alterations in seizure susceptibility and sensorimotor behavior. We find that, although ILC2s are moderately activated after PT damage and may promote cortical inhibitory synapse numbers, IL-33 signaling in ILC2s in this context largely does not impact cortical wound healing or behavior. Although additional research will be needed to test the roles of ILC2s in other CNS injury models (e.g., MCAO, TBI, meningitis) and validate these findings, this study advances our mechanistic understanding of sterile damage responses in the CNS and challenges literature identifying ILC2s as a promising population to target for the treatment of human brain injuries.

### **3.3 RESULTS**

#### **3.3.1 Myeloid cells infiltrate and expand in the brain following PT injury**

To investigate the role of ILC2s in the response to CNS injury, we utilized the well-defined photothrombotic (PT) model of ischemic stroke.<sup>105,106</sup> This model involves performing stereotactic survival surgery on anesthetized mice in order to induce an ischemic injury in a cortical region of interest, which in our case was the primary somatosensory (S1) cortex. Briefly, a fiber optic white light is placed onto the intact cranium over the S1 cortex and mice are injected intraperitoneally (i.p.) with a photoreactive dye (Rose Bengal) that initiates thrombosis in the cortical microvasculature upon exposure to high-intensity white light (**Figure 3.1.A**). Sham control

mice are subjected to the same surgical procedure and dye injection but are not exposed to the fiber optic light. The PT model induces ischemia in the region exposed to the fiber optic cable, causing hypoxia and subsequent cell death, and results in circular lesions that are grossly visible by 2 days post injury (2dpi) (**Figure 3.1.B**). PT damage models aspects of both ischemic stroke and traumatic brain injury, as the overlaying meningeal membranes are also thrombosed and injured due to their exposure to the light. PT damage recapitulates many established features of CNS injuries, such as the perilesional accumulation of Iba1<sup>hi</sup> microglia by 7-14dpi and the formation of an astrocytic GFAP<sup>+</sup> scar by 14dpi (**Figure 3.1.C**).

To delineate the immune response to PT damage, we used high dimensional flow cytometry to quantify the kinetics of myeloid cell infiltration into the dural meninges and cortex following injury. In the meninges, neutrophils and monocytes infiltrated early, peaking both in numbers and frequency at 1dpi, before gradually decreasing back to resting levels by ~7-14dpi (**Figure 3.1.D-E**). Meningeal macrophages expanded modestly by 7-14dpi, while conventional dendritic cell (cDC) levels remained relatively constant (**Figure 3.1.F-G**). Using a genetic reporter for Arginase 1 (Arg1<sup>YFP</sup> mice),<sup>107</sup> a well-described marker of alternatively activated macrophages, we observed an early expansion of Arg1<sup>YFP+</sup> myeloid (CD11b<sup>+</sup>) cells within the meninges at 1-2dpi that waned in abundance by 7dpi (**Figure 3.1.H**), consistent with many other studies that have observed Arg1<sup>+</sup> alternatively activated macrophages after CNS damage.<sup>66,68,69,72,74</sup> In the brain cortex, the influx of neutrophils and monocytes was slightly delayed, peaking around 2dpi, but remained elevated above baseline levels until at least 21dpi (**Figure 3.1.J-K**). Due to this influx, the frequency of microglia (which constitute ~99% of CD45<sup>+</sup> immune cells in sham mice) decreased 1-2dpi, although microglia expanded numerically by 7dpi (**Figure 3.1.L**). cDCs expanded by 2dpi, remained elevated until ~7-14dpi, and began to wane by 21dpi (**Figure 3.1.M**).

To gain more insight into the ontogeny of these myeloid populations, we generated a CCR2 fate mapping mouse (*Ccr2*<sup>creERT2</sup>; *Rosa26*<sup>LSL-tdTomato(Ai14)</sup>)<sup>108</sup> in which treatment with tamoxifen (TAM) induces permanent recombination and expression of tdTomato in CCR2-expressing cells.

CCR2 is a chemokine receptor highly expressed on classical Ly6C<sup>hi</sup> monocytes but is also expressed by some macrophage and lymphocyte populations.<sup>109</sup> We treated CCR2 fate mapping mice with TAM i.p. 0, 1, and 2dpi to induce tdTomato expression in infiltrating monocytes during this timeframe (matching the kinetics in **Figure 3.1**), and performed a timecourse experiment to track the numbers, identities, and distribution of tdTomato<sup>+</sup> cells after PT injury (**Figure 3.2.A**). In the meninges, a substantial portion (~30%) of immune cells were fate-mapped in sham mice, and the proportion of fate-mapped cells remained relatively constant over the timecourse (**Figure 3.2.B-C**). In contrast, very few cells were labeled in the cortex of sham mice and the frequency of tdTomato<sup>+</sup> cells drastically increased at 2dpi and decreased thereafter (**Figure 3.2.B,D**). The number of fate-mapped cells peaked at 7dpi in the meninges and 2dpi in the cortex, following the expected kinetics of monocyte infiltration into the cortex (**Figure 3.2.C-D**). In the meninges, the majority of fate-mapped cells were macrophages across the timecourse, likely due to resting CCR2 expression in meningeal macrophages (data not shown), although monocytes were also labeled and constituted ~40% of labeled cells at 2dpi (**Figure 3.2.E-F**). The number of labeled-macrophages increased by 7–14dpi, indicating either pre-existing fate-mapped macrophages proliferated or labeled monocytes differentiated into macrophages (**Figure 3.2.E-F**). In the cortex, the vast majority (~90%) of tdTomato<sup>+</sup> cells were monocytes at 2dpi, demonstrating efficient labeling of brain-infiltrating monocytes (**Figure 3.2.G-H**). These labeled monocytes waned numerically by 7dpi, at which point macrophages and cDCs comprised ~40% and ~20% of labeled cells, respectively, suggesting that fate-mapped monocytes differentiated into these populations in the brain (**Figure 3.2.G-H**). By 21dpi, fate-mapped macrophages and cDCs waned in abundance, while microglia accounted for ~30% of fate-mapped cells (**Figure 3.2.G-H**), suggesting monocytes or monocyte-derived cells may ultimately adapt a microglial-like phenotype by late timepoints after injury. Imaging of cortical lesions from fate mapping mice revealed that fate-mapped (tdTomato<sup>+</sup>) cells were present on lesional border by 7dpi, but began to infiltrate the lesion interior by 14–21dpi (**Figure 3.2.I**), indicating that monocyte-derived cells not only line the

cortical lesion but ultimately migrate into its interior. Together, these data illustrate that brain-infiltrating monocytes differentiate into macrophages and cDCs and potentially microglial-like cells that infiltrate the lesion interior after PT stroke.

### 3.3.2 Meningeal ILC2s colocalize with IL-33<sup>+</sup> fibroblasts and are activated after PT damage

To determine the localization of ILC2s in the meninges and their upstream cellular regulators, we used confocal microscopy of whole mounted dural meninges from resting adult mice to characterize the meningeal ILC2 niche. To identify ILC2s, we used a well described lineage tracing approach in which IL-5<sup>+</sup> cells permanently express YFP (*Il5<sup>cre</sup>;Rosa26<sup>LSL-YFP</sup>(Ai3)*)<sup>57,80</sup> in conjunction with an IL-33 reporter (*Il33<sup>mCherry</sup>*).<sup>110</sup> Meningeal ILC2s were enriched in perivascular regions, in particular around the large venous sinuses within the dura (**Figure 3.3.A**), suggesting that meningeal ILC2s have an adventitial distribution similar to ILC2s in other organs, such as the lung and liver.<sup>57</sup> Within these perivascular niches, ILC2s were in close proximity to IL-33<sup>+</sup> cells, which primarily marked PDGFR $\alpha$ <sup>+</sup> fibroblasts within the meninges (**Figure 3.3.B**), similar to adventitial fibroblasts in the lung.<sup>57</sup> Using an established co-culture system,<sup>57</sup> meningeal fibroblasts were sufficient to promote ILC2 survival *in vitro* (**Figure 3.3.C**), suggesting that these fibroblasts are capable of regulating ILC2 viability and activation.

The meninges and brain both highly express IL-33 at baseline<sup>66,110,111</sup> and IL-33 is known to be released after CNS injury.<sup>66</sup> To determine if meningeal ILC2s are activated after PT damage, potentially via IL-33 release, we used dual reporter mice for IL-5 (*Il5<sup>RFP</sup>*)<sup>80</sup> and IL-13 (*Il13<sup>huCD4</sup>*)<sup>112</sup> to track endogenous ILC2 cytokine production. As soon as 1dpi, ILC2s upregulated IL-5 and IL-13 expression compared to resting controls, and maintained this elevated level of cytokine production until at least 7dpi (**Figure 3.3D-F**), illustrating that PT damage induces meningeal ILC2 activation. Importantly, this same activation was not observed in CD4<sup>+</sup> T cells within the meninges, as IL-5 and IL-13 expression was not detected in these cells after injury (**Figure 3.3.D**).



Given that ILC2s were activated after PT damage, we next sought to understand the consequences of this activation. To do so, we conditionally deleted expression of the IL-33 receptor ST2 (encoded by *Il1rl1*) from ILC2s using an IL-5<sup>cre</sup> (*Il5<sup>cre</sup>; Il1rl1<sup>Flox</sup>*, hereafter referred to as ILC2<sup>ΔST2</sup> mice),<sup>80,113</sup> thereby preventing IL-33 signaling in ILC2s and their subsequent activation (**Figure 3.3.G**). To validate this model, we used flow cytometry to assess ST2 expression on meningeal ILC2s. In ILC2<sup>ΔST2</sup> mice, meningeal ILC2s had a ~70% reduction in ST2 expression, as compared to cre-negative littermate controls (ILC2<sup>CTRL</sup>), in which ~95% of meningeal ILC2s expressed ST2 (**Figure 3.3.H**). To determine if ILC2s expanded after PT damage and if this expansion was dependent on IL-33 signaling, we subjected ILC2<sup>CTRL</sup> and ILC2<sup>ΔST2</sup> mice to sham or PT damage and analyzed meningeal ILC2 numbers at 14dpi. ILC2 numbers did not significantly change after PT damage and were not different between ILC2<sup>CTRL</sup> and ILC2<sup>ΔST2</sup> mice (**Figure 3.3.I**), indicating that, despite increasing IL-5 and IL-13 production, meningeal ILC2s did not proliferate to a significant degree after PT damage.

### **3.3.3 IL-33 signaling in ILC2s does not impact myeloid or lymphoid populations in the meninges or cortex after PT damage**

To gain unbiased information into the role of activated ILC2s after PT damage, we performed single cell RNA sequencing (scRNAseq) using the 10X platform on meningeal and cortical cells 14 days after PT or sham damage in ILC2<sup>CTRL</sup> and ILC2<sup>ΔST2</sup> mice. We enriched each sample for non-B lymphocytes (CD45<sup>+</sup> CD11b<sup>-</sup> CD19<sup>-</sup>), myeloid cells (CD45<sup>+</sup> CD11b<sup>+</sup>), and fibroblasts (PDGFR $\alpha$ <sup>+</sup> gp38<sup>+</sup>) in order to obtain sufficient numbers of our populations of interest. Overall UMAP clustering identified our expected populations of interest within the meninges, including lymphocytes, myeloid cells, and fibroblasts (**Figure 3.4.A**). When sub-clustering on meningeal lymphocytes, we identified several populations, including: CD4<sup>+</sup> T<sub>conv</sub> cells (*Cd3e<sup>+</sup> Cd4<sup>+</sup> Foxp3<sup>-</sup>*), CD8<sup>+</sup> T cells (*Cd3e<sup>+</sup> Cd8a<sup>+</sup>*), ILC1s (*Cd3e<sup>-</sup> Klrb1c<sup>+</sup> Tbx21<sup>+</sup> Eomes<sup>-</sup>*), NK cells (*Cd3e<sup>-</sup>*

*Klrb1c<sup>+</sup> Tbx21<sup>+</sup> Eomes<sup>+</sup> Itgam<sup>+</sup>*), NKT cells (*Cd3e<sup>+</sup> Klrb1c<sup>+</sup> Tbx21<sup>+</sup>*),  $\gamma\delta$  T cells (*Cd3e<sup>+</sup> Rorc<sup>+</sup> Il17a<sup>+</sup>*), Tregs (*Cd3e<sup>+</sup> Cd4<sup>+</sup> FoxP3<sup>+</sup>*), and ILC2s (*Cd3e<sup>-</sup> Gata3<sup>+</sup> Il5<sup>+</sup> Il13<sup>+</sup>*) (**Figure 3.4.B,D**). While some lymphocyte populations were altered after PT damage (e.g.,  $\gamma\delta$  T cells and Tregs increased in frequency), the frequencies of these populations were largely unaltered in ILC2 <sup>$\Delta$ ST2</sup> mice (**Figure 3.4.C,E**), suggesting IL-33-activated ILC2s do not impact other meningeal lymphocytes.

We also subclustered the meningeal myeloid population and identified many cell types, including several macrophage clusters (*Fcgr1<sup>+</sup> Cx3cr1<sup>+</sup> Mrc1<sup>+</sup>*), neutrophil clusters (*Itgam<sup>+</sup> Ly6g<sup>+</sup>*), monocyte-derived macrophages (moMacs, *Fcgr1<sup>+</sup> Ly6c2<sup>+</sup> Ccr2<sup>+</sup>*), cDC1s (*Xcr1<sup>+</sup> Itgax<sup>+</sup> H2-Ab1<sup>+</sup>*), cDC2s (*Itgam<sup>+</sup> Itgax<sup>+</sup> H2-Ab1<sup>+</sup>*), plasmacytoid DCs (pDCs, *Siglech<sup>+</sup> Ly6c2<sup>+</sup> Itgax<sup>+</sup> H2-Ab1<sup>+</sup>*), migratory DCs (*Itgax<sup>+</sup> H2-Ab1<sup>+</sup> Ccr7<sup>+</sup>*), non-classical monocytes (ncMOs, *Itgam<sup>+</sup> Csf1r<sup>+</sup> Cx3cr1<sup>+</sup>*), mast cells (*Fcer1a<sup>+</sup>*), and several proliferating clusters (*Mki67<sup>+</sup>*) (**Figure 3.4.F,H**). The frequency of many of these myeloid populations were altered with PT stroke in control mice: for example, neutrophils (C3), macrophages (C0,4), and migratory DCs (C9) increased in frequency with stroke (**Figure 3.4.G,I**). In ILC2 <sup>$\Delta$ ST2</sup> mice, several populations were uniquely elevated, including neutrophils (C2,8) and moMacs (C6) (**Figure 3.4.G,I**), indicating that these pro-inflammatory myeloid cells were inappropriately retained in ILC2 <sup>$\Delta$ ST2</sup> mice. These data suggest that IL-33 signaling in ILC2s inhibits these populations and dampens meningeal inflammation after PT injury.

In the cortex, lymphocyte UMAP sub-clustering revealed similar lymphocyte populations as in the meninges (**Figure 3.5.A**). A greater heterogeneity was observed within cortical CD8<sup>+</sup> T cells, with several different clusters of effector (*Eomes<sup>+</sup>*, C2) and tissue-resident (*Cd69<sup>+</sup> C4*, *Itgae<sup>+</sup> C3*) subsets (**Figure 3.5.A,C**). These CD8<sup>+</sup> T cell subsets (C2, C3, C4) were elevated in ILC2 <sup>$\Delta$ ST2</sup> mice (**Figure 3.5.B,D**), suggesting that IL-33 signaling in ILC2s may inhibit the abundance of effector and tissue-resident CD8<sup>+</sup> T cells within the cortex after PT damage. Sub-clustering of cortical microglia revealed several microglial transcriptional states (**Figure 3.5.E**). Microglia subcluster 2, which was elevated in stroke compared to sham mice, was enriched for several

genes expressed by disease-associated microglia (DAMs), including *Itgax*, *Cd9*, *Cd63*, *Trem2*, and *Spp1* (**Figure 3.5.G**).<sup>34</sup> This cluster also had the highest DAM module score based off of the top 25 differentially expressed DAM genes from Keren-Shaul, et al. (2017) (**Figure 3.5.H**).<sup>34</sup> Microglia subcluster 3, however, was enriched for homeostatic genes, such as *P2ry12*, and was uniquely elevated in ILC2<sup>AST2</sup> mice (**Figure 3.5.G,I**). These data suggest a shift towards a DAM phenotype in microglia after PT stroke, but an inappropriate retention of a homeostatic phenotype in ILC2<sup>AST2</sup> mice.

Together, these scRNAseq data indicate that IL-33 signaling in ILC2s may inhibit excessive monocyte and neutrophil accumulation in the meninges, restrict effector and tissue-resident CD8<sup>+</sup> T cells within the cortex, and promote cortical microglial phenotypic polarization after PT damage.

To orthogonally validate our scRNAseq data, we used high dimensional flow cytometry to quantify myeloid populations in ILC2<sup>CTRL</sup> and ILC2<sup>AST2</sup> mice after PT damage. At 2dpi, an early timepoint that captures the majority of myeloid flux into the meninges and brain (**Figure 3.1**), meningeal and cortical myeloid populations, including neutrophils, eosinophils, macrophages/microglia, cDCs, and Arg1+ cells, were unaltered in ILC2<sup>AST2</sup> mice compared to littermate controls (**Figure 3.6.A-K**), indicating that IL-33 signaling in ILC2s does not impact early myeloid cell abundance in the meninges and cortex. At 14dpi, a timepoint matching our scRNAseq data, we observed a significant decrease in meningeal eosinophils in ILC2<sup>AST2</sup> mice (consistent with these mice being heterozygous for *Ii5* due to use of the knock-in/knock-out IL-5<sup>cre</sup>),<sup>80</sup> but no alterations in other neutrophils, macrophages, or other myeloid populations (**Figure 3.6.L-P**), as had been suggested by the scRNAseq data. In the cortex at 14dpi, we observed a trending but nonsignificant increase in neutrophils and classical monocyte abundance in ILC2<sup>AST2</sup> mice over injured controls, but no alternations in total microglial or cDC density (**Figure 3.6.Q-T**). DAMs, as defined by microglia co-expressing the DAM markers CD11c and CD63,<sup>34</sup> were significantly

increased with PT stroke, but were not altered in ILC2<sup>ΔST2</sup> mice (**Figure 3.6.U-V**). Thus, despite our scRNAseq data suggesting otherwise, IL-33 signaling in ILC2s did not restrict the accumulation of pro-inflammatory myeloid populations or promote the abundance of DAMs, suggesting that IL-33 signaling in ILC2s does not impact myeloid populations after PT damage.

We also quantified lymphoid populations in ILC2<sup>CTRL</sup> and ILC2<sup>ΔST2</sup> mice 14 days after PT damage using flow cytometry. The numbers of meningeal CD4<sup>+</sup> T cells, CD8<sup>+</sup> T cells, NK/ILC1s (NK1.1<sup>+</sup>), and B cells were unaltered with PT stroke or in ILC2<sup>ΔST2</sup> mice (**Figure 3.7.A-D**). The vast majority (>80%) of both CD4<sup>+</sup> and CD8<sup>+</sup> T cells in the meninges were CD44<sup>+</sup> CD62L<sup>-</sup>, indicating prior antigen experience, and ~40% of these cells had a tissue-resident memory phenotype (CD44<sup>+</sup> CD69<sup>+</sup>); however, the expression of these markers was not altered with PT injury or with IL-33 signaling deficiency in ILC2s (**Figure 3.7.E-J**). In the cortex, lymphocytes, including CD4<sup>+</sup> T cells, CD8<sup>+</sup> T cells, and NK/ILC1s, were increased with PT stroke, as expected, but unaltered in ILC2<sup>ΔST2</sup> mice (**Figure 3.7.K-N**). The vast majority (>80%) of CD4<sup>+</sup> and CD8<sup>+</sup> T cells in the cortex were again CD44<sup>+</sup> CD62L<sup>-</sup>, indicating prior antigen experience, and ~20% of CD4<sup>+</sup> T cells and ~40% of CD8<sup>+</sup> T cells had a tissue-resident memory phenotype (CD44<sup>+</sup> CD69<sup>+</sup>) (**Figure 3.7.O-T**). However, the expression of these markers was again unaltered in ILC2<sup>ΔST2</sup> mice (**Figure 3.7.O-T**). These data indicate that IL-33 signaling in ILC2s did not impact the accumulation of tissue-resident memory T cells in either the meninges or cortex, as had been suggested by our scRNAseq data.

### **3.3.4 IL-33 signaling in ILC2s does not impact lesion size or gliosis after PT damage**

To determine if IL-33 signaling in ILC2s impacted healing of the cortical lesion after PT stroke, we performed immunohistochemical analyses of the lesions from ILC2<sup>CTRL</sup> and ILC2<sup>ΔST2</sup> mice 14 days after PT damage. ILC2<sup>CTRL</sup> and ILC2<sup>ΔST2</sup> brain samples were blinded and serially sectioned, at which point the slides with the maximum cross-sectional lesion area were chosen

for staining and imaging (2 technical replicates per mouse). Maximal cross-sectional lesion sizes were not different between ILC2<sup>CTRL</sup> and ILC2<sup>ΔST2</sup> mice (**Figure 3.8.A-B**). Additionally, the areas covered by reactive astrocytes (GFAP<sup>+</sup>), activated microglia/macrophages (Iba1<sup>+</sup>), or fibrosis-related extracellular matrix (ER-TR7<sup>+</sup>) were not different between ILC2<sup>CTRL</sup> and ILC2<sup>ΔST2</sup> mice (**Figure 3.8.C-E**). In addition to primary lesions in the cortex, the PT damage model also induces secondary damage and gliosis in the functionally connected ventrobasal (VB) thalamus, which receives synaptic input from dead or damaged S1 cortical neurons.<sup>14,17</sup> The mean fluorescence intensity (MFI) of GFAP or Iba1 were elevated in the ipsilateral VB thalamus compared to the contralateral (uninjured) VB thalamus, confirming that PT damage induced thalamic gliosis, but were not different between ILC2<sup>CTRL</sup> and ILC2<sup>ΔST2</sup> mice (**Figure 3.8.F-H**). Together, these data reveal that IL-33 signaling in ILC2s does not impact the extent of cortical damage, cortical and thalamic gliosis, or lesional fibrosis after PT damage.

### **3.3.5. IL-33 signaling in ILC2s promotes cortical inhibitory synapse numbers after PT injury**

We next explored the impacts of IL-33 signaling in ILC2s on cortical and thalamic synapses. Our group has recently shown that ILC2s regulate the formation of cortical inhibitory synapses during postnatal development via IL-13 signaling to interneurons,<sup>92</sup> suggesting that synapses may be a relevant downstream target of ILC2s activated after injury. Using immunohistochemistry and high-magnification confocal imaging, we quantified synapses by staining for pre- and post-synaptic markers and quantifying the number of colocalized puncta, as previously described.<sup>92,114,115</sup> Inhibitory (GABAergic) synapses were marked by VGAT (vesicular GABA transporter) on the pre-synapse and Gephyrin (a structural protein that stabilizes GABA receptors) on the post-synapse (**Figure 3.8.I,M**). Excitatory (glutamatergic) synapses were identified by VGLUT1 (vesicular glutamate transporter 1) on the pre-synapse and Homer1 (a post-synaptic density protein) on the post-synapse. At 14dpi, ILC2<sup>ΔST2</sup> mice had a reduction in inhibitory,

but not excitatory, synapses in layer 2 (L2) of the perilesional cortex (**Figure 3.8.J-K**). To determine if these alterations in synapses affected neuronal firing rates, we performed whole cell patch-clamp electrophysiology of L2 cortical neurons to measure the rate of miniature inhibitory postsynaptic currents (mIPSCs). While the frequency of mIPSCs in the cortex was unaltered with PT stroke, the frequency of mIPSCs was reduced in ILC2<sup>ΔST2</sup> mice (**Figure 3.8.L**), consistent with the observed loss of inhibitory synapses (**Figure 3.8.J**). We also quantified synapses in the functionally connected VB thalamus. At 14dpi, there was a trending but nonsignificant reduction in inhibitory synapses and no difference in excitatory synapses in the ipsilateral VB thalamus of ILC2<sup>ΔST2</sup> mice (**Figure 3.8.N-O**). We measured miniature excitatory postsynaptic currents (mEPSCs) in the VB thalamus and observed increased mEPSCs with PT stroke and a trending but nonsignificant increase in mEPSCs in ILC2<sup>ΔST2</sup> mice (**Figure 3.8.P**), suggesting a trend towards hyper-excitability in the ipsilateral thalamus after injury. Together, these data indicate that IL-33 signaling in ILC2s promotes inhibitory synapse numbers in the perilesional cortex, thereby maintaining a proper balance of inhibitory signals and preventing hyperexcitability. These effects may also partially be at play in the VB thalamus, as trends towards hyperexcitability were also observed in this region in ILC2<sup>ΔST2</sup> mice.

### **3.3.6 IL-33 signaling in ILC2s does not impact seizure susceptibility, cognition, or sensorimotor behaviors after PT stroke**

Given that IL-33 signaling in ILC2s promotes inhibition in the cortex and may restrict corticothalamic hyperexcitability, we next explored if ILC2<sup>ΔST2</sup> mice had altered susceptibility to chemical-induced seizures. Increased susceptibility to seizures is a common sequela of human patients who experience CNS injuries, such as TBI, and is associated with imbalances of excitation and inhibition within the brain.<sup>9</sup> To assess seizure susceptibility, we induced sham or PT injury in ILC2<sup>CTRL</sup> and ILC2<sup>ΔST2</sup> mice and treated them with pentylenetetrazol (PTZ) according

to two different paradigms. In the first paradigm, mice were treated with 50 mg/kg PTZ i.p. at 14dpi, at which seizure behavior was quantified (**Figure 3.9.A**). After PT injury, ILC2<sup>AST2</sup> mice displayed a trending but nonsignificant increase in the number, duration, and incidence of generalized tonic-clonic (GTC) seizures in this paradigm (**Figure 3.9.B-D**). In the second paradigm, mice were first treated with a sensitizing dose of PTZ at 14dpi (45 mg/kg i.p.), followed by a challenge dose one week later at 21dpi (45 mg/kg i.p.), at which point seizure behavior was quantified according to the modified Racine scale (**Figure 3.9.E, Table 3.5**). The number and incidence of GTC seizures, as well as the duration of mice within each Racine stage, were unaltered in ILC2<sup>AST2</sup> mice compared to littermate ILC2<sup>CTRL</sup> mice in this second paradigm (**Figure 3.9.F-H**). Thus, according to these PTZ challenge paradigms, IL-33 signaling in ILC2s does not significantly impact seizure susceptibility following PT stroke.

To determine if any other behaviors were altered by IL-33 signaling in ILC2s, we subjected ILC2<sup>CTRL</sup> and ILC2<sup>AST2</sup> mice to an array of cognitive and sensorimotor assays both prior to PT stroke induction and 14 days after PT stroke. Because the same cohort of mice were subjected to these assays twice, we cannot conclude if behavioral effects seen after stroke are due to brain damage or re-testing bias. Regardless, after injury ILC2<sup>CTRL</sup> and ILC2<sup>AST2</sup> mice moved the same amount in the open-field test, spent similar fractions of time in the open arm of the elevated plus maze, differentially recognized incongruent objects to the same extent (object congruence test), reacted similarly to painful stimuli (hot plate test), nested similarly, had similar abilities to stay on a rotating rod (rotarod), and inhibited their startle response to a loud noise to a similar extent after hearing a softer noise beforehand (pre-pulse inhibition test) (**Figure 3.9.I-L, N-P**). ILC2<sup>AST2</sup> mice had a trending but nonsignificant increase in the number of entries made into each arm of the Y maze, compared to littermate ILC2<sup>CTRL</sup> mice, suggesting a modest trend towards hyperactive behavior (**Figure 3.9.M**). Overall, no behaviors were significantly altered in ILC2<sup>AST2</sup> mice after PT damage, indicating that IL-33 signaling in ILC2s does not impact these behaviors after injury.

### 3.3.7 Meningeal Arg1 expression partially depends on monocyte trafficking and IL-4/13 signaling, while cortical Arg1 expression is fully dependent on monocyte trafficking

Since IL-33 signaling in ILC2s did not impact Arg1 expression in myeloid cells at 2dpi (**Figure 3.6.F,K**), we next explored what other pathways may promote the expansion of this population. As shown in **Figure 3.1**, classical monocytes traffic into the meninges and cortex following PT damage. Classical monocytes are highly plastic cells that are recruited to peripheral tissues during inflammation where they differentiate into macrophages or DCs in accordance with local tissue signals that shape their ultimate phenotype.<sup>116</sup> Since the kinetics of monocyte infiltration closely mirrors the kinetics of Arg1<sup>+</sup> myeloid abundance after PT damage, monocytes and their progeny may be responsible for the emergence of this population. Additionally, IL-4 and IL-13 are also known to polarize macrophages towards an alternatively activated phenotype, including upregulation of Arg1 expression.<sup>81</sup> To determine if monocytes or IL-4/13 signaling were involved in the emergence of Arg1<sup>+</sup> myeloid cells after PT stroke, we used global CCR2-deficient (*Ccr2*<sup>-/-</sup>) mice, which are deficient in circulating classical monocytes,<sup>117</sup> or global IL-4R $\alpha$ -deficient (*Il4ra*<sup>-/-</sup>) mice, which are deficient in both IL-4 and IL-13 signaling.<sup>118</sup> In the meninges at 2dpi, both *Ccr2*<sup>-/-</sup> and *Il4ra*<sup>-/-</sup> mice had a modest reduction in the frequencies of Arg1<sup>+</sup> CD11b<sup>+</sup> myeloid cells compared to wild-type mice (**Figure 3.10.A-B**). As expected, *Ccr2*<sup>-/-</sup> mice had a trending reduction in meningeal Ly6C<sup>hi</sup> monocytes, whereas *Il4ra*<sup>-/-</sup> mice did not (**Figure 3.10.C**). These data indicate that both CCR2-dependent monocyte trafficking and IL-4/13 signaling partially contribute to the Arg1<sup>+</sup> population in the meninges, suggesting there are redundancies in this pathway and that both monocyte-derived cells and pre-existing meningeal myeloid cells can upregulate Arg1. In the cortex, *Ccr2*<sup>-/-</sup> mice had a dramatic reduction in Arg1<sup>+</sup> CD11b<sup>+</sup> myeloid cells, while this population was unaltered in *Il4ra*<sup>-/-</sup> mice, compared to wild-type (**Figure 3.10.D-E**). *Ccr2*<sup>-/-</sup> mice also had a dramatic reduction in Ly6C<sup>hi</sup> monocytes within the cortex, while *Il4ra*<sup>-/-</sup> mice did not (**Figure 3.10.F**). These data indicate that, in contrast to the meninges, Arg1 upregulation in the



cortex is almost entirely dependent on CCR2-mediated monocyte infiltration and independent of IL-4/13 signaling.

### **3.3.8 Monocyte infiltration modestly limits cortical damage but does not impact fibrosis after PT stroke, while IL-4/13 is dispensable for both**

To determine if CCR2-dependent monocyte trafficking or IL-4/13 signaling and their associated effects on early Arg1 expression impacted wound healing or lesional fibrosis after PT stroke, we quantified the lesion size and fibrotic area of *Ccr2*<sup>-/-</sup> and *Il4ra*<sup>-/-</sup> mice 14dpi. *Ccr2*<sup>-/-</sup> mice had slightly larger cortical lesions compared to wild-type mice at 14dpi, although this was quite variable across mice (**Figure 3.10.G-H**). *Il4ra*<sup>-/-</sup> lesions areas were not different from wild-type lesion areas at this timepoint (**Figure 3.10.G-H**). These data indicate that CCR2-dependent monocyte trafficking into the brain partially helps to restrict cortical damage after PT stroke, while IL-4/13 signaling does not play a significant role in this process. *Ccr2*<sup>-/-</sup> and *Il4ra*<sup>-/-</sup> mice did not have different levels of fibrosis compared to wild-type mice at 14dpi, as quantified by the area ER-TR7 staining (which marks Collagen VI)<sup>119</sup> (**Figure 3.10.I-J**). This indicates that CCR2-dependent monocyte trafficking and IL-4/13 signaling do not impact lesional fibrosis after PT injury.

## **3.4 DISCUSSION**

In this study, we tested our primary hypothesis that meningeal ILC2s are activated by IL-33 released after PT injury to produce IL-13, which in turn regulates microglia and macrophages to promote wound healing. We found that ILC2s resided within the meninges in close proximity to IL-33-expressing fibroblasts that were capable of supporting them *in vitro* and determined that ILC2s became activated after PT stroke by upregulating the effector type 2 cytokines IL-5 and IL-13. We were ultimately unable to demonstrate that this activation was IL-33-dependent, as ST2-deficient ILC2s (in ILC2<sup>ΔST2</sup> mice) did not have altered expansion after PT damage (and wild-type ILC2s also did not numerically expand). Our scRNAseq data suggested that IL-33 signaling in

ILC2s restricted pro-inflammatory meningeal myeloid populations (neutrophils and monocyte-derived macrophages) and cortical tissue-resident memory CD8<sup>+</sup> T cells while promoting appropriate polarization of homeostatic microglia towards a DAM phenotype. However, we were ultimately unable to validate this data at the protein level by flow cytometry, as mice with ST2-deficient ILC2s did not have altered meningeal and cortical myeloid and lymphoid populations, or cortical DAMs. IL-33 signaling in ILC2s also did not impact downstream wound healing, gliotic, or fibrotic responses, nor did it affect seizure susceptibility, cognition, or sensorimotor behavior. The only phenotype affected by IL-33 signaling in ILC2s was the abundance of inhibitory synapses in the perilesional cortex, which had modest trending impacts on corticothalamic hyperexcitability, as assessed by electrophysiology. This result is corroborated by a recent study from our groups that identified a role for ILC2-derived IL-13 in regulating cortical inhibitory synapses during postnatal development via direct signaling to interneurons.<sup>92</sup> Our data suggests that this same circuit may be reactivated in tissue remodeling contexts in adulthood, such as after CNS injury; however, additional work is needed to validate this finding and determine if deletion of IL-4R $\alpha$  from interneurons (VGAT<sup>cre</sup>;IL4ra<sup>Flox</sup>)<sup>92</sup> recapitulates the loss of inhibitory synapses observed with ST2-deficient ILC2s. Overall, our study argues for a mild role for ILC2s in the response to brain injury, in which they may help to maintain neuronal inhibition and prevent local hyperexcitability.

Our results were surprising, given the growing body of literature that describes IL-33, ILC2s, and IL-13 as regulators of the healing response to CNS injury. Other groups have reported that ILC2s are beneficial after spinal cord injury (SCI),<sup>90</sup> intracerebral hemorrhage,<sup>93</sup> and the middle cerebral artery occlusion model (MCAO) of ischemic stroke.<sup>94</sup> There are many potential explanations for these discrepancies. First, we used a different model of brain damage – photothrombotic (PT) stroke – than these other studies. While PT stroke is minimally invasive, highly reproducible, and less variable compared to other stroke models (such as MCAO),<sup>105,106,120</sup> PT stroke induces milder damage to a smaller overall brain volume and thus causes fewer behavioral alterations: of the sensorimotor behavioral abnormalities reported after PT damage,

most are mild and occur only in the first few days after damage.<sup>121–123</sup> PT stroke is also an imperfect model of human ischemic stroke. While human strokes typically involve incomplete blockage of an upstream cerebral artery followed by reperfusion and secondary injury, PT stroke induces permanent thrombosis in capillaries in the brain and overlying meninges, resulting in no reperfusion injury and minimal regions of partial ischemia (lesional penumbras).<sup>105</sup> Additional research should determine the role of ILC2s in a more severe and physiologically relevant model of brain damage such as transient MCAO (tMCAO) or the CCI model of TBI; it is possible the meningeal ILC2s have greater reparative roles in these models, potentially due to larger quantities of IL-33 released after more significant injuries that are known to impact sensorimotor behavior.

Additionally, other groups used more generic and imprecise tools to ablate ILC2s, such as *Rag2<sup>-/-</sup>;Il2rg<sup>-/-</sup>* mice<sup>94</sup> (which lack all adaptive and innate lymphocytes) or anti-Thy1.2 treatment<sup>93,94</sup> (which systemically ablates all lymphocytes, as well as other Thy1<sup>+</sup> cells), potentially accounting for their greater observed effects on the endogenous type 2 response. In contrast, our study used a much more specific genetic tool, the IL-5<sup>cre</sup>, which specifically targets IL-5<sup>+</sup> ILC2s and some Th2s.<sup>57,58,80</sup> Moreover, we specifically deleted the IL-33 receptor ST2 from ILC2s using IL-5<sup>cre</sup>, instead of depleting the entire cell population (although similar results were observed in IL-5<sup>cre</sup>; R26<sup>DTA</sup> mice, data not shown). While we were able to achieve efficient deletion of ST2 from meningeal ILC2s (**Figure 3.3H**), the use of this more subtle genetic manipulation may have hindered us from observing the true functions of ILC2s after PT damage, especially if any were IL-33-independent. Future work should test the role of ILC2s in more severe damage models (tMCAO, CCI) using broader ILC2-depletion strategies (e.g., *IL-5<sup>cre</sup>; R26<sup>DTA</sup>, Nmur1<sup>cre</sup>;R26<sup>DTA</sup>*) to validate our findings in this study and help resolve this discrepancy with existing literature.

During our study of the ILC2 response to PT stroke, we also deeply characterized the myeloid cell infiltrates into the meninges and cortex after damage. We performed monocyte fate mapping using *Ccr2<sup>creERT2</sup>; R26<sup>LSL-tdTomato</sup>* mice, which allowed us to observe monocyte-derived macrophages, cDCs, and microglia-like cells in the cortex after injury (**Figure 3.2**). While this data

is corroborated by other lineage tracing studies using similar tools,<sup>124,125</sup> monocytes are a notoriously difficult population to target specifically and CCR2, while highly expressed on classical monocytes, is also expressed by a variety of macrophage, dendritic cell, and activated T cell populations.<sup>109</sup> Indeed, we observed substantial CCR2 fate mapping in sham-injured meninges due to steady state expression of CCR2 by a subset of meningeal macrophages (**Figure 3.2.B,E**), complicating interpretations of our data within the meninges. Thus, the fate-mapped cells in our study may not all be monocyte-derived and should therefore be cautiously interpreted and orthogonally validated, potentially via adoptive transfer or parabiosis studies.

We also observed an intriguing Arg1<sup>+</sup> myeloid population that emerged early (1-2 dpi) after injury (**Figure 3.1.H-I**). While ILC2s did not impact this population (**Figure 3.6**), CCR2-dependent trafficking partially or fully contributed to the emergence of this population in the meninges and cortex, respectively, which correlated with levels of classical monocytes (**Figure 3.10.A-F**). Thus, our data argues that monocytes and/or monocyte-derived cells are a key component of this Arg1<sup>+</sup> population, which has been reported to have wound healing functions after CNS injury.<sup>66,68,69,72,74</sup> IL-4/13 signaling, a known upstream regulator of Arg1 expression,<sup>81</sup> only contributed to Arg1 upregulation in the meninges, but not the cortex (**Figure 3.10.A-F**). Several unanswered questions remain. If ILC2s do not influence the meningeal Arg1<sup>+</sup> pool, what is the relevant source of IL-4/13 that partially drives this phenotype? Eosinophils or mast cells are putative candidates. At what point during monocyte differentiation does IL-4/13 act to induce Arg1? In the brain, what signal(s) is/are driving Arg1 expression in monocytes? Additional work is needed to address these open questions in order to understand the mechanisms regulating this reparative myeloid population and design therapies that can drive this population in human patients.

### 3.5 FIGURES

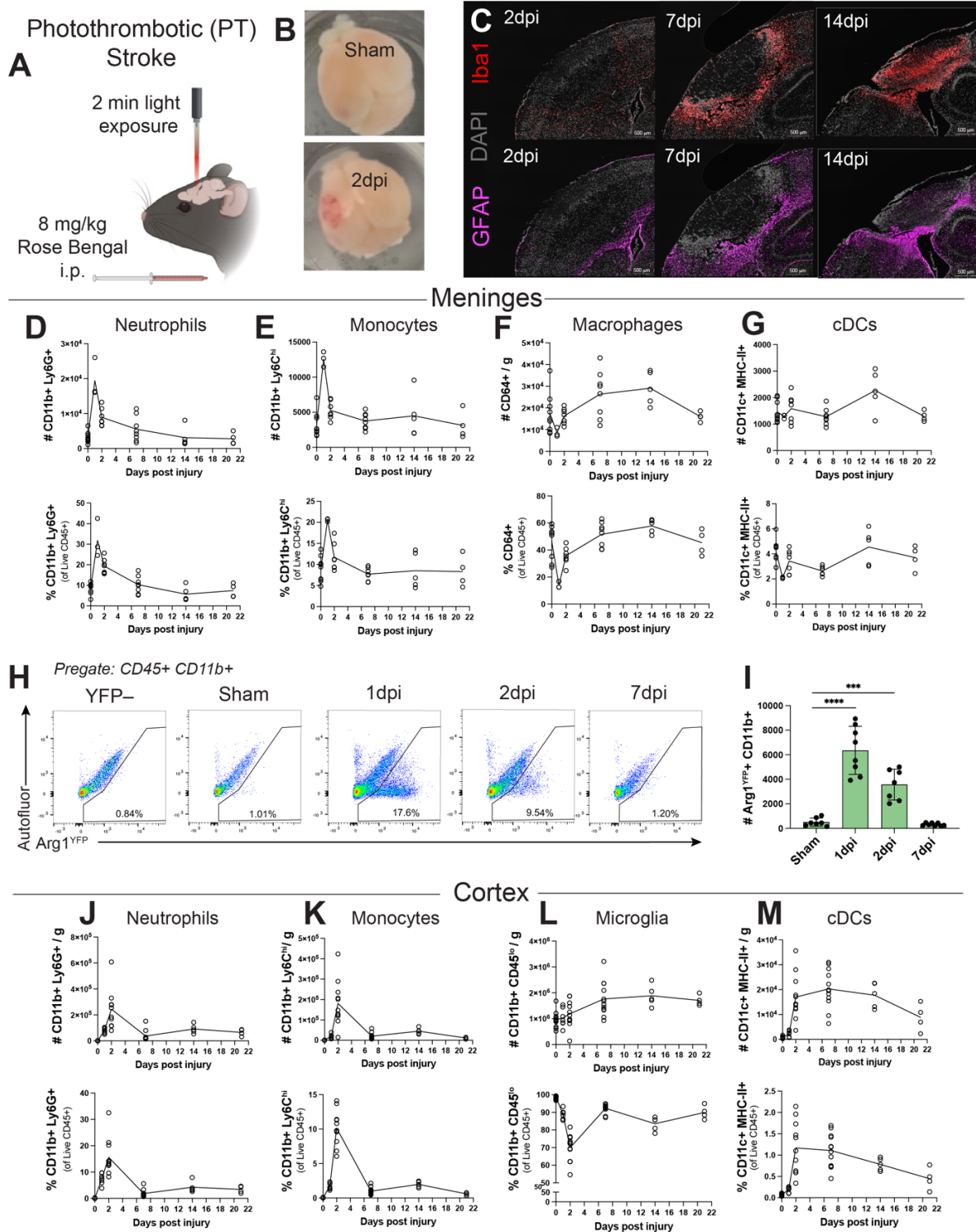


**Figure 3.1. Characterization of myeloid infiltrate kinetics in the meninges and cortex following PT damage.**

A) Schematic depicting photothrombotic (PT) stroke surgical model. See Methods for details. (Figure caption continued on the next page)

(Figure caption continued from the previous page)

- B) Pictures of representative sham and PT damaged brains at 2pi.
  - C) Representative images depicting Iba1 (microglia/macrophage) and GFAP (reactive astrocyte) staining over timecourse following PT damage.
  - D) Quantification of meningeal neutrophils (CD11b<sup>+</sup> Ly6G<sup>+</sup>) by cell number (top) and frequency of live CD45<sup>+</sup> cells (bottom) across timecourse following PT damage.
  - E) Quantification of meningeal classical monocytes (Ly6G<sup>-</sup> CD11b<sup>+</sup> Ly6C<sup>hi</sup>) by cell number (top) and frequency of live CD45<sup>+</sup> cells (bottom) timecourse following PT damage.
  - F) Quantification of meningeal macrophages (Ly6G<sup>-</sup> Ly6C<sup>-</sup> CD64<sup>+</sup>) by cell number (top) and frequency of live CD45<sup>+</sup> cells (bottom) timecourse following PT damage.
  - G) Quantification of meningeal conventional dendritic cells (cDCs) (Ly6G<sup>-</sup> Ly6C<sup>-</sup> CD64<sup>-</sup> CD11c<sup>+</sup> MHC-II<sup>+</sup>) by cell number (top) and frequency of live CD45<sup>+</sup> cells (bottom) timecourse following PT damage.
  - H) Representative flow cytometry plots depicting Arg1<sup>YFP</sup> expression within total meningeal myeloid (CD45<sup>+</sup> CD11b<sup>+</sup>) cells over timecourse following PT damage. Autofluorescence (in PerCP-Cy5.5 channel) is shown on y-axis to reveal true Arg1<sup>YFP</sup> signal. Arg1<sup>YFP</sup><sup>-</sup> (WT) mouse is including as a gating control.
  - I) Quantification of meningeal CD11b<sup>+</sup> Arg1<sup>YFP</sup><sup>+</sup> cell numbers, as gated in (H), over timecourse following PT damage. One-way ANOVA with Tukey's multiple correction's test.
  - J) Quantification of cortical neutrophils (CD11b<sup>+</sup> Ly6G<sup>+</sup>) by cell number per gram (top) and frequency of live CD45<sup>+</sup> cells (bottom) timecourse following PT damage.
  - K) Quantification of cortical classical monocytes (CD11b<sup>+</sup> Ly6G<sup>-</sup> Ly6C<sup>hi</sup>) by cell number per gram (top) and frequency of live CD45<sup>+</sup> cells (bottom) timecourse following PT damage.
  - L) Quantification of cortical microglia (CD11b<sup>+</sup> CD45<sup>lo</sup>) by cell number per gram (top) and frequency of live CD45<sup>+</sup> cells (bottom) timecourse following PT damage.
  - M) Quantification of cortical cDCs (Ly6G<sup>-</sup> Ly6C<sup>-</sup> CD64<sup>-</sup> CD11c<sup>+</sup> MHC-II<sup>+</sup>) by cell number per gram (top) and frequency of live CD45<sup>+</sup> cells (bottom) timecourse following PT damage.
- Data are mean (± SD). Data points represent biological replicates (individual mice). Statistics: \*\*\*p < 0.001, \*\*\*\*p < 0.0001.

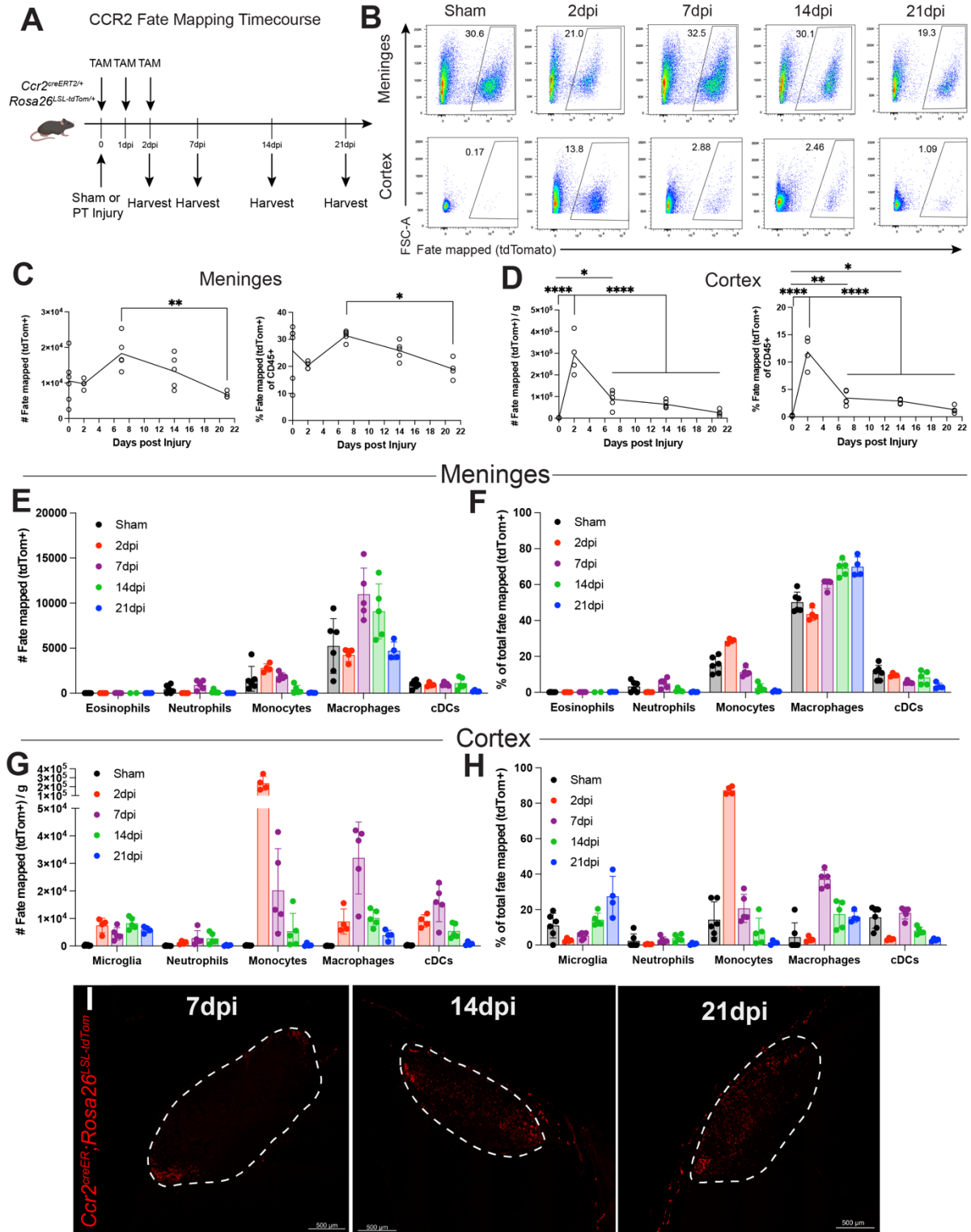


**Figure 3.2. CCR2 fate-mapping demonstrates monocyte differentiation into macrophages and cDCs within the cortex following PT injury.**  
*(Figure caption continued on the next page)*

(Figure caption continued from the previous page)

- A) Schematic depicting CCR2 fate mapping experiment. *Ccr2<sup>creERT2/+</sup>;Rosa26<sup>LSL-tdTomato (Ai14)/+</sup>* mice were treated with tamoxifen (2 mg/mouse) on 0, 1, and 2dpi and harvested over the indicate timecourse following PT damage.
- B) Representative flow plots depicting fate mapped cells (Ai14, tdTomato) within total CD45<sup>+</sup> cells in the meninges (top row) and cortex (bottom row) over timecourse following PT damage.
- C) Quantification of total meningeal fate mapped cells (Ai14<sup>+</sup>) by cell numbers (left) and frequency of live CD45<sup>+</sup> cells (right) over timecourse following PT injury. One-way ANOVA with Tukey's multiple comparisons test.
- D) Quantification of total cortical fate mapped cells (Ai14<sup>+</sup>) by cell numbers (left) and frequency of live CD45<sup>+</sup> cells (right) over timecourse following PT injury. One-way ANOVA with Tukey's multiple comparisons test.
- E) Number of fate-mapped (Ai14<sup>+</sup>) eosinophils, neutrophils, monocytes, macrophages, and cDCs within the meninges over timecourse following PT injury.
- F) Percentage of each cell type within total meningeal fate-mapped (Ai14<sup>+</sup>) cells for each timepoint following PT injury.
- G) Number of fate-mapped (Ai14<sup>+</sup>) eosinophils, neutrophils, monocytes, macrophages, and cDCs within the cortex over timecourse following PT injury.
- H) Percentage of each cell type within total cortical fate-mapped (Ai14<sup>+</sup>) cells for each timepoint following PT injury.
- I) Representative images depicting fate-mapped (Ai14<sup>+</sup>) cells within cortical lesions from each indicated timepoint following PT injury.

Data are mean ( $\pm$  SD). Data points represent biological replicates (individual mice). Statistics: \*p < 0.05, \*\*p < 0.01, \*\*\*p < 0.001, \*\*\*\*p < 0.0001.



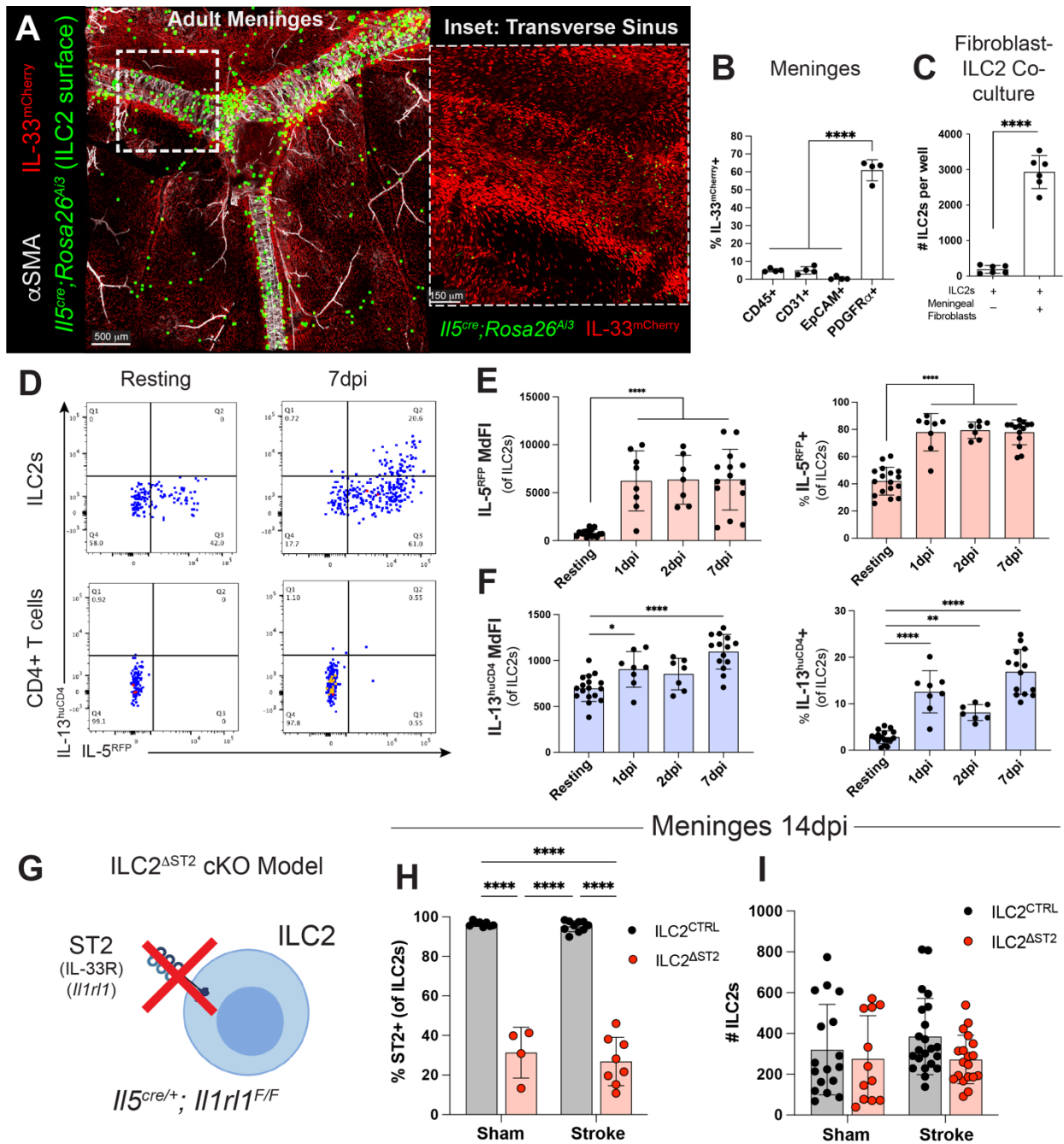


**Figure 3.3. Meningeal ILC2s closely localize to IL-33<sup>+</sup> fibroblasts and produce IL-5 and IL-13 following PT damage.**

A) Representative confocal image of whole mounted dural meninges from resting adult *I15<sup>cre/+</sup>; Rosa26<sup>LSL-YFP (Ai13)/+</sup>; I133<sup>mCherry/+</sup>* reporter mouse depicting distribution of ILC2s (YFP<sup>+</sup>) and IL-33<sup>+</sup> cells (mCherry<sup>+</sup>) along dural sinuses (marked by  $\alpha$  smooth muscle actin,  $\alpha$ SMA). ILC2 surface is shown as green squares to illustrate their distribution across the meninges. Inset depicts native staining around one arm of the transverse dural sinus. (Figure caption continued on the next page)

(Figure caption continued from the previous page)

- B) Percentage of immune (CD45<sup>+</sup>), endothelial (CD31<sup>+</sup>), epithelial (EpCAM<sup>+</sup>), and fibroblast (PDGFR $\alpha$ <sup>+</sup>) cells that are IL-33<sup>mCherry+</sup> from resting adult meninges, quantified via flow. One-way ANOVA with Tukey's multiple comparisons test.
- C) Number of ILC2s per well recovered from 5 day cultured with confluent meningeal fibroblasts (PDGFR $\alpha$ <sup>+</sup> gp38<sup>+</sup>) or media alone. Pooled data from 2 experiments. Each dot represents one well (technical replicates). Unpaired 2-tailed *t*-test.
- D) Representative flow plots depicting IL-5<sup>RFP</sup> and IL-13<sup>huCD4</sup> reporter expression from resting controls (left column) or 7dpi (right column) in ILC2s (CD45<sup>+</sup> Lin<sup>-</sup> Thy1.2<sup>+</sup> Arg1<sup>YFP+</sup>, top row) and CD4<sup>+</sup> T cells (CD45<sup>+</sup> CD3<sup>+</sup> CD4<sup>+</sup>) from the meninges.
- E) Quantification of IL-5<sup>RFP</sup> reporter expression in meningeal ILC2s (CD45<sup>+</sup> Lin<sup>-</sup> Thy1.2<sup>+</sup> Arg1<sup>YFP+</sup>) by median fluorescence intensity (MdfI, left) or percent positivity (right). One-way ANOVA with Tukey's multiple comparisons test.
- F) Quantification of IL-13<sup>huCD4</sup> reporter expression in meningeal ILC2s (CD45<sup>+</sup> Lin<sup>-</sup> Thy1.2<sup>+</sup> Arg1<sup>YFP+</sup>) by median fluorescence intensity (MdfI, left) or percent positivity (right). One-way ANOVA with Tukey's multiple comparisons test.
- G) Schematic depicting ILC2 <sup>$\Delta$ ST2</sup> conditional knockout (cKO) genetic mouse model. *Il5*<sup>cre/+</sup>; *Il1rl1*<sup>F/F</sup> have ST2 (IL-33R, *Il1rl1*) deleted on ILC2s.
- H) Percentage of meningeal ILC2s expressing ST2 in ILC2 <sup>$\Delta$ ST2</sup> mice or littermate ILC2<sup>CTRL</sup> mice 14 days after PT or sham injury as quantified by flow cytometry, depicting ~70% deletion of ST2 on ILC2s in ILC2 <sup>$\Delta$ ST2</sup> mice. Two-way ANOVA with Tukey's multiple comparison's test.
- I) Number of meningeal ILC2s (CD45<sup>+</sup> Lin<sup>-</sup> Thy1<sup>+</sup> GATA-3<sup>+</sup>) in ILC2 <sup>$\Delta$ ST2</sup> mice or littermate ILC2<sup>CTRL</sup> mice 14 days after PT or sham injury as quantified by flow cytometry. Two-way ANOVA with Tukey's multiple comparison's test.

Data are mean ( $\pm$  SD). Data points represent biological replicates (individual mice), unless otherwise noted. Statistics: \**p* < 0.05, \*\**p* < 0.01, \*\*\**p* < 0.001, \*\*\*\**p* < 0.0001.

Meninges scRNAseq 14dpi

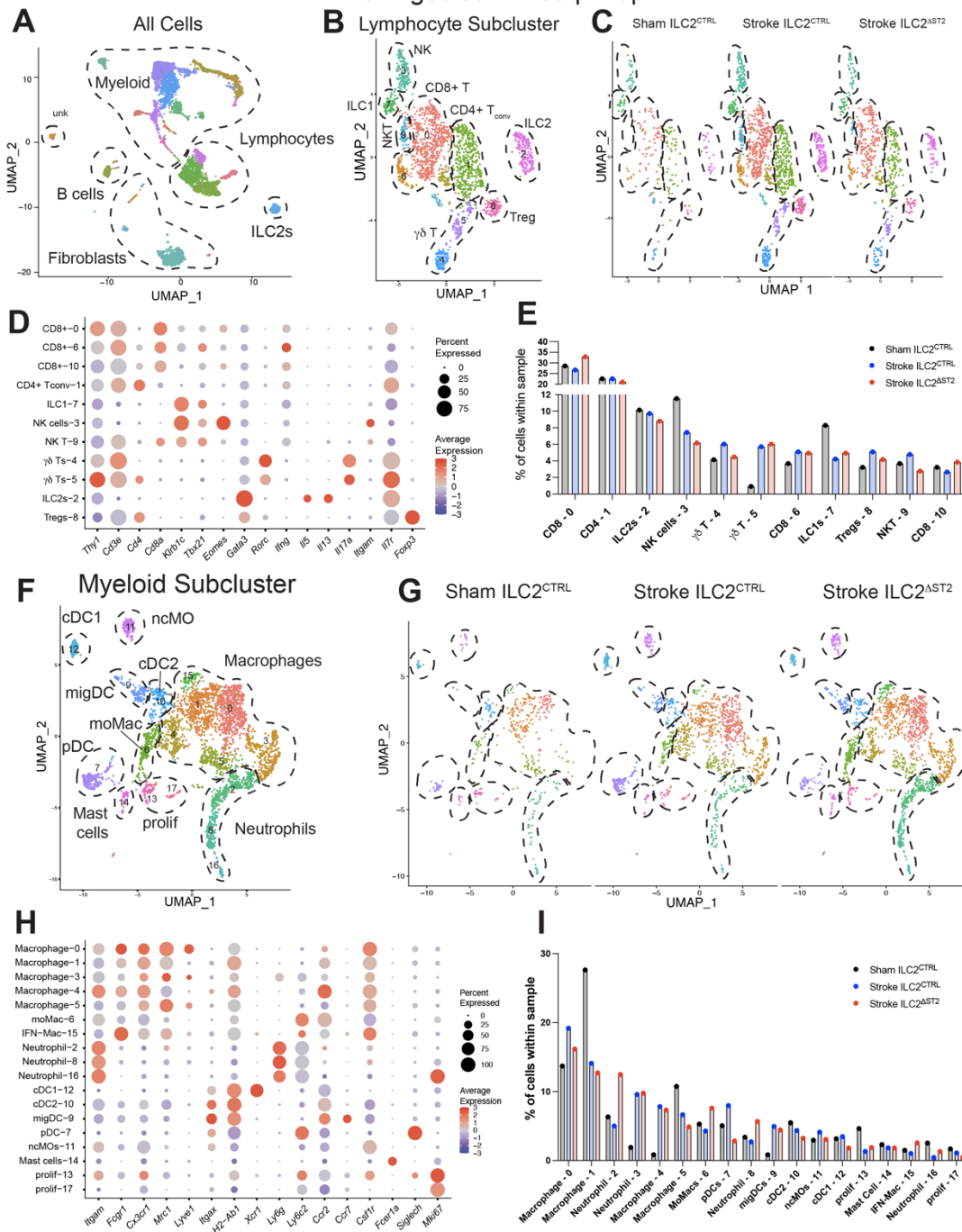


**Figure 3.4. Meningeal single cell RNA sequencing (scRNAseq) reveals potential retention of pro-inflammatory myeloid cells in ILC2<sup>ΔST2</sup> mice 14 days after PT injury.**

A) Overall UMAP clustering of meningeal scRNAseq data after quality control filtering, depicting clusters corresponding to myeloid cells, non-B lymphocytes, ILC2s, B cells, and fibroblasts.  
 B) UMAP sub-clustering of meningeal lymphocyte scRNAseq data, depicting clusters corresponding to indicated lymphocyte cell types.  
 (Figure caption continued on the next page)

*(Figure caption continued from the previous page)*

- C) UMAP sub-clustering of lymphocyte scRNAseq data as in (B) split by experimental condition.
- D) Expression of meningeal lymphocyte sub-cluster defining genes depicted as percent of each cluster expressing each gene (circle size) and relative average expression (heatmap color).
- E) Percentage of each lymphocyte cluster within total cells of each experimental condition.
- F) UMAP sub-clustering of meningeal myeloid scRNAseq data, depicting clusters corresponding to indicated myeloid cell types.
- G) UMAP sub-clustering of myeloid scRNAseq data as in (F) split by experimental condition.
- H) Expression of meningeal myeloid sub-cluster defining genes depicted as percent of each cluster expressing each gene (circle size) and relative average expression (heatmap color).
- I) Percentage of each myeloid cluster within total cells of each experimental condition.

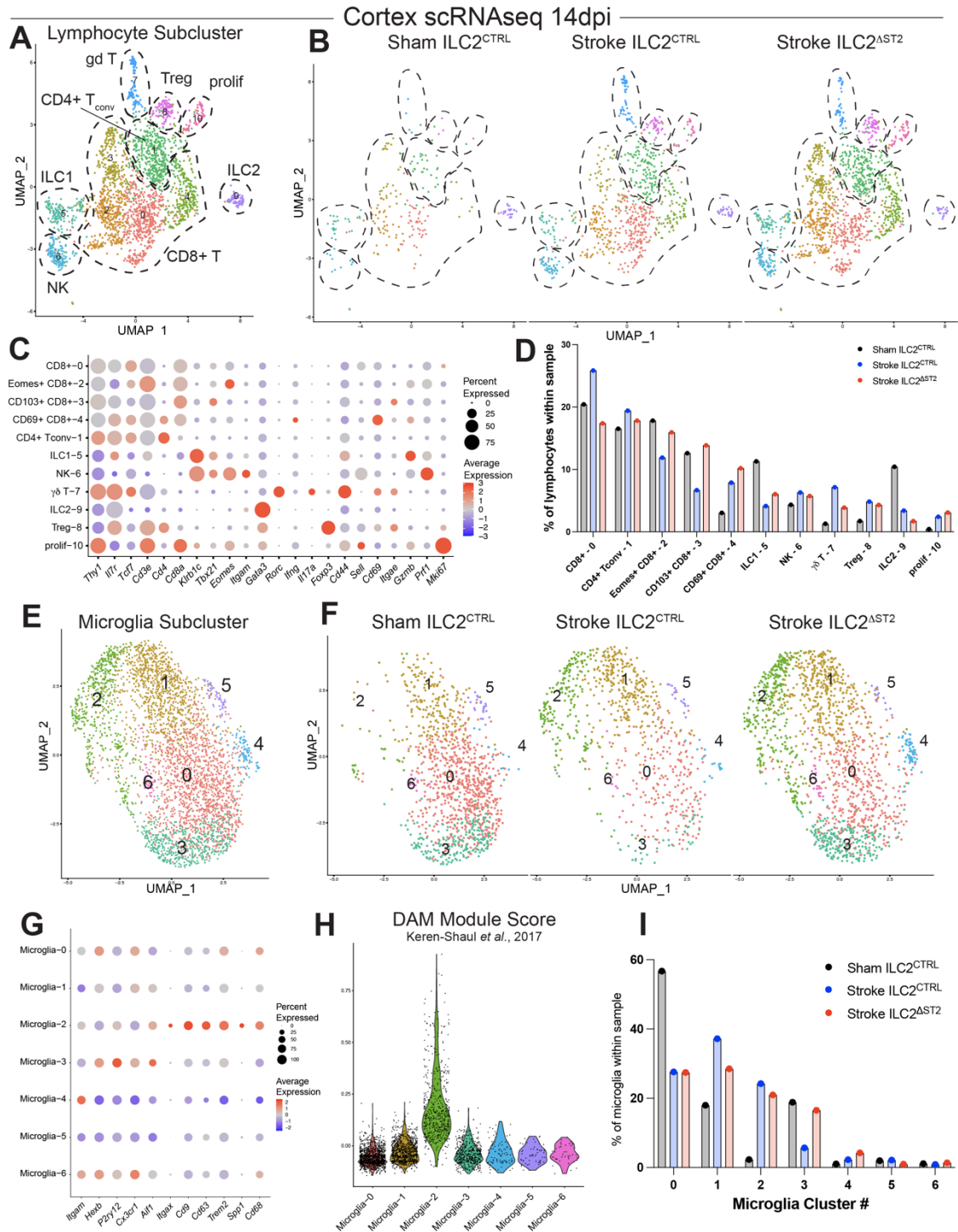


**Figure 3.5. Cortical single cell RNA sequencing (scRNAseq) reveals potential retention of tissue-resident CD8<sup>+</sup> T cells and inappropriate microglial phenotypic polarization in ILC2<sup>ΔST2</sup> mice 14 days after PT injury.**

A) UMAP sub-clustering of cortical lymphocyte scRNAseq data, depicting clusters corresponding to indicated lymphocyte cell types.

B) UMAP sub-clustering of cortical scRNAseq data as in (A) split by experimental condition. (Figure caption continued on the next page)

*(Figure caption continued from the previous page)*

- C) Expression of cortical lymphocyte sub-cluster defining genes depicted as percent of each cluster expressing each gene (circle size) and relative average expression (heatmap color).
- D) Percentage of each lymphocyte cluster within total cells of each experimental condition.
- E) UMAP sub-clustering of cortical microglia scRNAseq data.
- F) UMAP sub-clustering of microglia scRNAseq data as in (E) split by experimental condition.
- G) Expression of cortical microglia sub-cluster defining genes depicted as percent of each cluster expressing each gene (circle size) and relative average expression (heatmap color).
- H) Violin plot depicting disease-associated microglia (DAM) module score (based off of top 25 differentially upregulated DAM genes)<sup>34</sup> for each microglial subcluster.
- I) Percentage of each microglial subcluster within total microglial of each experimental condition.

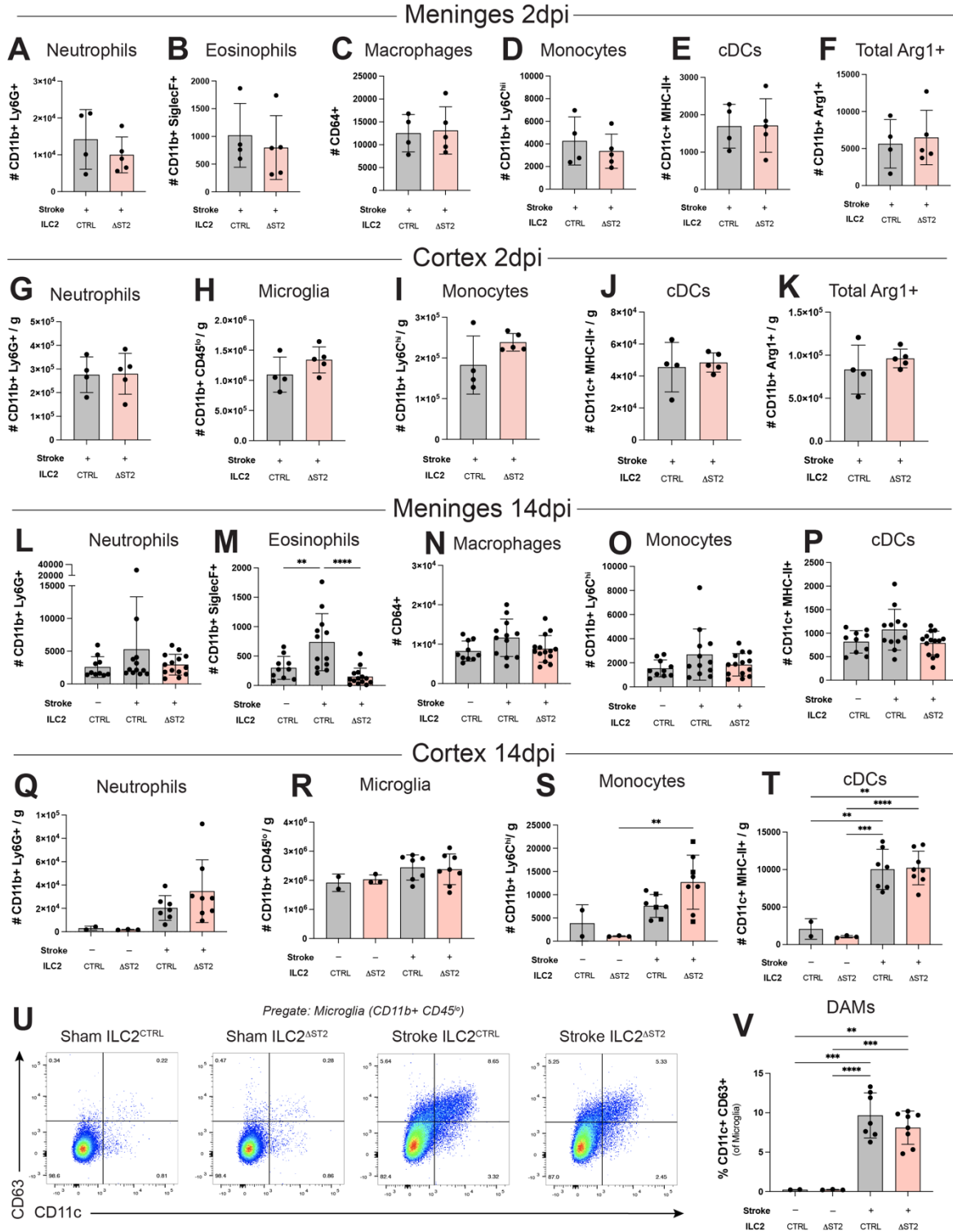


**Figure 3.6. IL-33 signaling in ILC2s does not impact meningeal or cortical myeloid population abundance 2 or 14 days after PT injury.**

A) Number of meningeal neutrophils (CD11b<sup>+</sup> Ly6G<sup>+</sup>) in ILC2<sup>ΔST2</sup> or ILC2<sup>CTRL</sup> littermates 2dpi.  
 B) Number of meningeal eosinophils (CD11b<sup>+</sup> SigF<sup>+</sup>) in ILC2<sup>ΔST2</sup> or ILC2<sup>CTRL</sup> littermates 2dpi.  
 (Figure caption continued on the next page)

(Figure caption continued from the previous page)

- C) Number of meningeal macrophages (CD64<sup>+</sup>) in ILC2<sup>ΔST2</sup> or ILC2<sup>CTRL</sup> littermates 2dpi.
- D) Number of meningeal monocytes (CD11b<sup>+</sup> Ly6C<sup>hi</sup>) in ILC2<sup>ΔST2</sup> or ILC2<sup>CTRL</sup> littermates 2dpi.
- E) Number of meningeal cDCs (CD11c<sup>+</sup> MHC-II<sup>+</sup>) in ILC2<sup>ΔST2</sup> or ILC2<sup>CTRL</sup> littermates 2dpi.
- F) Number of total meningeal Arg1<sup>+</sup> myeloid cells (CD11b<sup>+</sup> Arg1<sup>+</sup>) in ILC2<sup>ΔST2</sup> or ILC2<sup>CTRL</sup> littermates 2dpi.
- G) Number/gram of cortical neutrophils (CD11b<sup>+</sup> Ly6G<sup>+</sup>) in ILC2<sup>ΔST2</sup> or ILC2<sup>CTRL</sup> littermates 2dpi.
- H) Number/gram of cortical microglia (CD11b<sup>+</sup> CD45<sup>lo</sup>) in ILC2<sup>ΔST2</sup> or ILC2<sup>CTRL</sup> littermates 2dpi.
- I) Number/gram of cortical monocytes (CD11b<sup>+</sup> Ly6C<sup>hi</sup>) in ILC2<sup>ΔST2</sup> or ILC2<sup>CTRL</sup> littermates 2dpi.
- J) Number/gram of cortical cDCs (CD11c<sup>+</sup> MHC-II<sup>+</sup>) in ILC2<sup>ΔST2</sup> or ILC2<sup>CTRL</sup> littermates 2dpi.
- K) Number/gram of total cortical Arg1<sup>+</sup> myeloid cells (CD11b<sup>+</sup> Arg1<sup>+</sup>) in ILC2<sup>ΔST2</sup> or littermate ILC2<sup>CTRL</sup> mice 2dpi.
- L) Number of meningeal neutrophils (CD11b<sup>+</sup> Ly6G<sup>+</sup>) in sham or PT-injured ILC2<sup>ΔST2</sup> and ILC2<sup>CTRL</sup> littermates 14dpi.
- M) Number of meningeal eosinophils (CD11b<sup>+</sup> SigF<sup>+</sup>) in sham or PT-injured ILC2<sup>ΔST2</sup> and ILC2<sup>CTRL</sup> littermates 14dpi. One-way ANOVA with Tukey's multiple comparisons test.
- N) Number of meningeal macrophages (CD64<sup>+</sup>) in sham or PT-injured ILC2<sup>ΔST2</sup> and ILC2<sup>CTRL</sup> littermates 14dpi.
- O) Number of meningeal monocytes (CD11b<sup>+</sup> Ly6C<sup>hi</sup>) in sham or PT-injured ILC2<sup>ΔST2</sup> and ILC2<sup>CTRL</sup> littermates 14dpi.
- P) Number of meningeal cDCs (CD11c<sup>+</sup> MHC-II<sup>+</sup>) in sham or PT-injured ILC2<sup>ΔST2</sup> and ILC2<sup>CTRL</sup> littermates 14dpi.
- Q) Number per gram of cortical neutrophils (CD11b<sup>+</sup> Ly6G<sup>+</sup>) in sham or PT-injured ILC2<sup>ΔST2</sup> and ILC2<sup>CTRL</sup> littermates 14dpi.
- R) Number per gram of cortical microglia (CD11b<sup>+</sup> CD45<sup>lo</sup>) in sham or PT-injured ILC2<sup>ΔST2</sup> and ILC2<sup>CTRL</sup> littermates 14dpi.
- S) Number per gram of cortical monocytes (CD11b<sup>+</sup> Ly6C<sup>hi</sup>) in sham or PT-injured ILC2<sup>ΔST2</sup> and ILC2<sup>CTRL</sup> littermates 14dpi. One-way ANOVA with Tukey's multiple comparisons test.
- T) Number per gram of cortical cDCs (CD11c<sup>+</sup> MHC-II<sup>+</sup>) in sham or PT-injured ILC2<sup>ΔST2</sup> and ILC2<sup>CTRL</sup> littermates 14dpi. One-way ANOVA with Tukey's multiple comparisons test.
- U) Representative flow plots depicting CD11c and CD63 expression within cortical microglia from sham or PT-injured ILC2<sup>ΔST2</sup> and ILC2<sup>CTRL</sup> littermates 14dpi.
- V) Percentage of cortical microglia that are CD11c<sup>+</sup> CD63<sup>+</sup> (DAMs, as gated in U) from sham or PT-injured ILC2<sup>ΔST2</sup> and ILC2<sup>CTRL</sup> littermates 14dpi. One-way ANOVA with Tukey's multiple comparisons test.

Data are mean ± SD. Data points represent biological replicates (individual mice). Statistics: \*\*p < 0.01, \*\*\*p < 0.001, \*\*\*\*p < 0.0001.



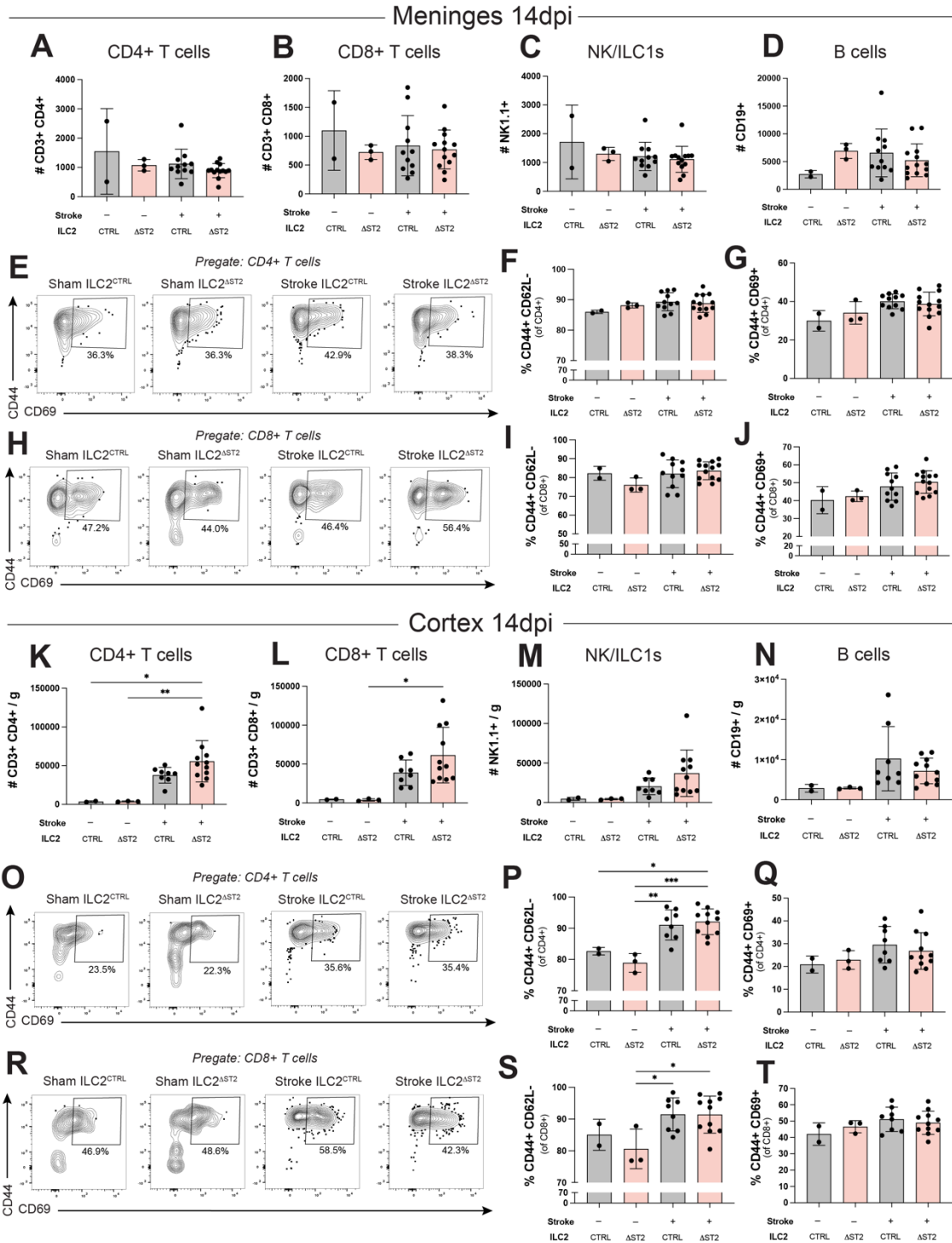


**Figure 3.7. IL-33 signaling in ILC2s does not impact meningeal or cortical lymphocyte population abundance or expression of tissue-residency markers 14 days after PT injury.**

A) Number of meningeal CD4+ T cells (CD3<sup>+</sup> CD4<sup>+</sup>) in sham or PT-injured ILC2<sup>ΔST2</sup> and ILC2<sup>CTRL</sup> littermates 14dpi.

B) Number of meningeal CD8+ T cells (CD3<sup>+</sup> CD8<sup>α</sup>+) in sham or PT-injured ILC2<sup>ΔST2</sup> and ILC2<sup>CTRL</sup> littermates 14dpi.

(Figure caption continued on the next page)

(Figure caption continued from the previous page)

- C) Number of meningeal NK/ILC1s (NK1.1<sup>+</sup>) in sham or PT-injured ILC2<sup>ΔST2</sup> and ILC2<sup>CTRL</sup> littermates 14dpi.
- D) Number of meningeal B cells (CD19<sup>+</sup>) in sham or PT-injured ILC2<sup>ΔST2</sup> and ILC2<sup>CTRL</sup> littermates 14dpi.
- E) Representative flow plots depicting CD69 and CD44 expression within meningeal CD4<sup>+</sup> T cells from sham or PT-injured ILC2<sup>ΔST2</sup> and ILC2<sup>CTRL</sup> littermates 14dpi.
- F) Percentage of meningeal CD4<sup>+</sup> T cells that are CD44<sup>+</sup> CD62L<sup>-</sup> from sham or PT-injured ILC2<sup>ΔST2</sup> and ILC2<sup>CTRL</sup> littermates 14dpi.
- G) Percentage of meningeal CD4<sup>+</sup> T cells that are CD44<sup>+</sup> CD69<sup>+</sup> (as gated in E) from sham or PT-injured ILC2<sup>ΔST2</sup> and ILC2<sup>CTRL</sup> littermates 14dpi.
- H) Representative flow plots depicting CD69 and CD44 expression within meningeal CD8<sup>+</sup> T cells from sham or PT-injured ILC2<sup>ΔST2</sup> and ILC2<sup>CTRL</sup> littermates 14dpi.
- I) Percentage of meningeal CD8<sup>+</sup> T cells that are CD44<sup>+</sup> CD62L<sup>-</sup> from sham or PT-injured ILC2<sup>ΔST2</sup> and ILC2<sup>CTRL</sup> littermates 14dpi.
- J) Percentage of meningeal CD8<sup>+</sup> T cells that are CD44<sup>+</sup> CD69<sup>+</sup> (as gated in H) from sham or PT-injured ILC2<sup>ΔST2</sup> and ILC2<sup>CTRL</sup> littermates 14dpi.
- K) Number per gram of cortical CD4<sup>+</sup> T cells (CD3<sup>+</sup> CD4<sup>+</sup>) in sham or PT-injured ILC2<sup>ΔST2</sup> and ILC2<sup>CTRL</sup> littermates 14dpi. One-way ANOVA with Tukey's multiple comparisons test.
- L) Number per gram of cortical CD8<sup>+</sup> T cells (CD3<sup>+</sup> CD8α<sup>+</sup>) in sham or PT-injured ILC2<sup>ΔST2</sup> and ILC2<sup>CTRL</sup> littermates 14dpi. One-way ANOVA with Tukey's multiple comparisons test.
- M) Number per gram of cortical NK/ILC1s (NK1.1<sup>+</sup>) in sham or PT-injured ILC2<sup>ΔST2</sup> and ILC2<sup>CTRL</sup> littermates 14dpi.
- N) Number per gram of cortical B cells (CD19<sup>+</sup>) in sham or PT-injured ILC2<sup>ΔST2</sup> and ILC2<sup>CTRL</sup> littermates 14dpi.
- O) Representative flow plots depicting CD69 and CD44 expression within cortical CD4<sup>+</sup> T cells from sham or PT-injured ILC2<sup>ΔST2</sup> and ILC2<sup>CTRL</sup> littermates 14dpi.
- P) Percentage of cortical CD4<sup>+</sup> T cells that are CD44<sup>+</sup> CD62L<sup>-</sup> from sham or PT-injured ILC2<sup>ΔST2</sup> and ILC2<sup>CTRL</sup> littermates 14dpi. One-way ANOVA with Tukey's multiple comparisons test.
- Q) Percentage of cortical CD4<sup>+</sup> T cells that are CD44<sup>+</sup> CD69<sup>+</sup> (as gated in E) from sham or PT-injured ILC2<sup>ΔST2</sup> and ILC2<sup>CTRL</sup> littermates 14dpi.
- R) Representative flow plots depicting CD69 and CD44 expression within cortical CD8<sup>+</sup> T cells from sham or PT-injured ILC2<sup>ΔST2</sup> and ILC2<sup>CTRL</sup> littermates 14dpi.
- S) Percentage of cortical CD8<sup>+</sup> T cells that are CD44<sup>+</sup> CD62L<sup>-</sup> from sham or PT-injured ILC2<sup>ΔST2</sup> and ILC2<sup>CTRL</sup> littermates 14dpi. One-way ANOVA with Tukey's multiple comparisons test.
- T) Percentage of cortical CD8<sup>+</sup> T cells that are CD44<sup>+</sup> CD69<sup>+</sup> (as gated in H) from sham or PT-injured ILC2<sup>ΔST2</sup> and ILC2<sup>CTRL</sup> littermates 14dpi.

Data are mean ± SD. Data points represent biological replicates (individual mice). Statistics: \*p < 0.05, \*\*p < 0.01, \*\*\*p < 0.001.

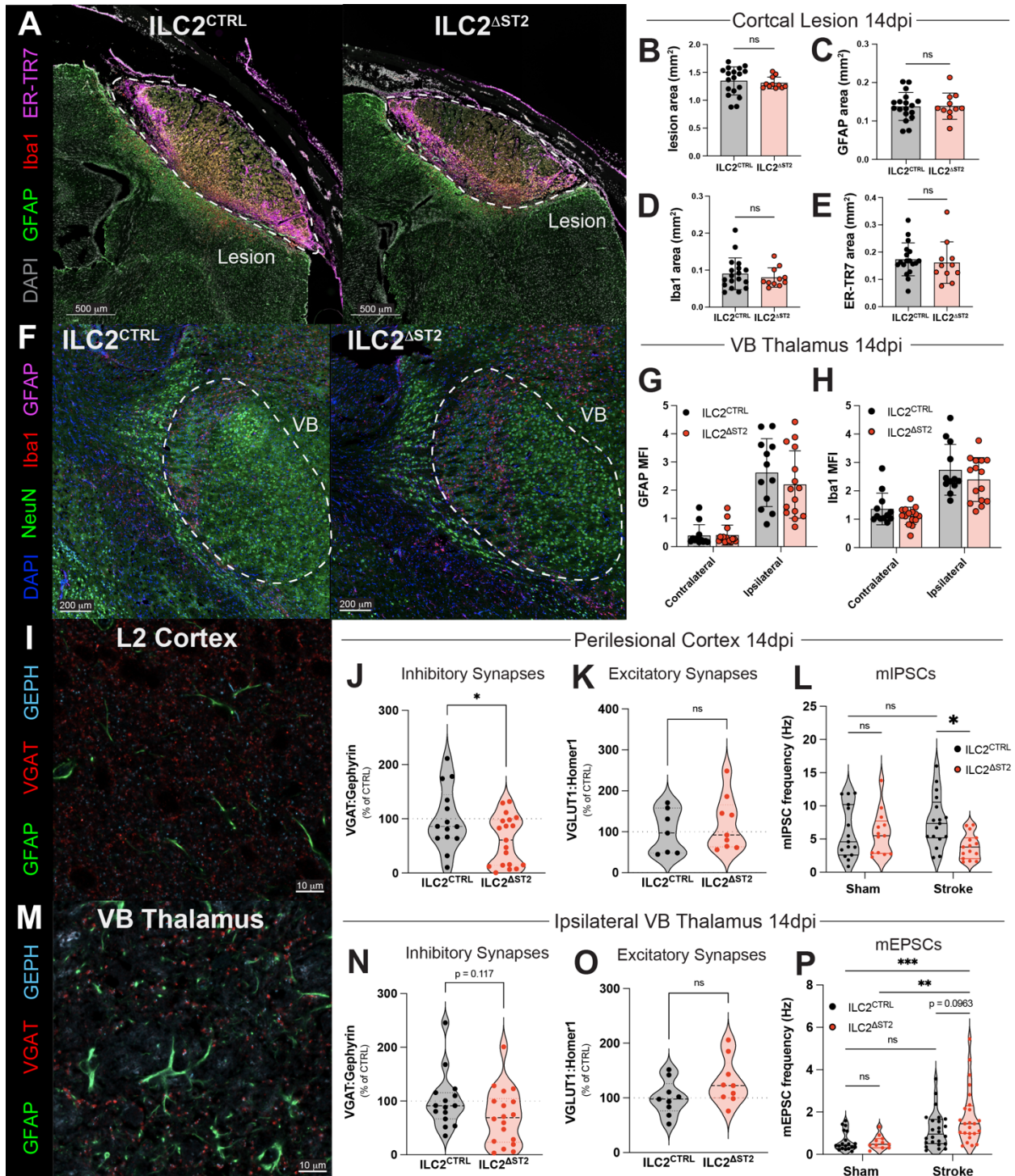


**Figure 3.8. IL-33 signaling in ILC2s promotes cortical inhibitory synapse numbers but does not impact cortical lesion size, gliosis, or fibrosis.**

A) Representative maximal cross-sectional area images of cortical lesions in ILC2<sup>ΔST2</sup> and ILC2<sup>CTRL</sup> littermates 14dpi, depicting GFAP (reactive astrocyte), Iba1 (microglia/macrophages), ER-TR7 (collagen VI), and DAPI (nuclei) staining.

B) Maximal cross-sectional lesional area from ILC2<sup>CTRL</sup> and ILC2<sup>ΔST2</sup> mice 14dpi. Unpaired 2-tailed t-test. (Figure caption continued on the next page)

*(Figure caption continued from the previous page)*

- C) Lesional GFAP<sup>+</sup> area from ILC2<sup>CTRL</sup> and ILC2<sup>AST2</sup> mice 14dpi. Unpaired 2-tailed t-test.
- D) Lesional Iba1<sup>+</sup> area from ILC2<sup>CTRL</sup> and ILC2<sup>AST2</sup> mice 14dpi. Unpaired 2-tailed t-test.
- E) Lesional ER-TR7<sup>+</sup> area from ILC2<sup>CTRL</sup> and ILC2<sup>AST2</sup> mice 14dpi. Unpaired 2-tailed t-test.
- F) Representative images of ipsilateral ventrobasal (VB) thalamus in ILC2<sup>AST2</sup> and ILC2<sup>CTRL</sup> littermates 14dpi, depicting NeuN (neuronal cell bodies), Iba1 (microglia/macrophages), GFAP (reactive astrocytes), and DAPI (nuclei) staining.
- G) Quantification of GFAP mean fluorescence intensity (MFI) within contralateral or ipsilateral VB thalamus from ILC2<sup>CTRL</sup> and ILC2<sup>AST2</sup> mice 14dpi.
- H) Quantification of Iba1 mean fluorescence intensity (MFI) within contralateral or ipsilateral VB thalamus from ILC2<sup>CTRL</sup> and ILC2<sup>AST2</sup> mice 14dpi.
- I) Representative field of view (FOV) within layer 2 (L2) of the perilesional cortex depicting staining for GFAP, VGAT (vesicular GABA transporter), and GEPH (Gephyrin).
- J) Quantification of inhibitory (VGAT:Gephyrin) synapses in perilesional L2 cortex in ILC2<sup>CTRL</sup> and ILC2<sup>AST2</sup> mice 14dpi, normalized to average of control (100%). Unpaired 2-tailed t-test.
- K) Quantification of excitatory (VGLUT1:Homer1) synapses in perilesional L2 cortex in ILC2<sup>CTRL</sup> and ILC2<sup>AST2</sup> mice 14dpi, normalized to average of control (100%). Unpaired 2-tailed t-test.
- L) Frequency of miniature inhibitory postsynaptic currents (mIPSCs) in L2 perilesional cortex from sham or PT-injured ILC2<sup>CTRL</sup> and ILC2<sup>AST2</sup> mice 14dpi. Two-way ANOVA with Tukey's multiple comparisons test.
- M) Representative field of view (FOV) within ipsilateral VB thalamus depicting staining for GFAP, VGAT (vesicular GABA transporter), and GEPH (Gephyrin).
- N) Quantification of inhibitory (VGAT:Gephyrin) synapses in ipsilateral VB thalamus in ILC2<sup>CTRL</sup> and ILC2<sup>AST2</sup> mice 14dpi, normalized to average of control (100%). Unpaired 2-tailed t-test.
- O) Quantification of excitatory (VGLUT1:Homer1) synapses in ipsilateral VB thalamus in ILC2<sup>CTRL</sup> and ILC2<sup>AST2</sup> mice 14dpi, normalized to average of control (100%). Unpaired 2-tailed t-test.
- P) Frequency of miniature excitatory postsynaptic currents (mEPSCs) in ipsilateral VB thalamus from sham or PT-injured ILC2<sup>CTRL</sup> and ILC2<sup>AST2</sup> mice 14dpi. Two-way ANOVA with Tukey's multiple comparisons test.

Data are mean ( $\pm$  SD). Data points in (B-D, G-H) represent individual brain sections (2 brain sections per mouse). Data points in (J-K, N-O) represent individual mice. Data points in (L, P) represent individual cells. Statistics: ns=not significant, \* $p < 0.05$ , \*\* $p < 0.01$ , \*\*\* $p < 0.001$ .

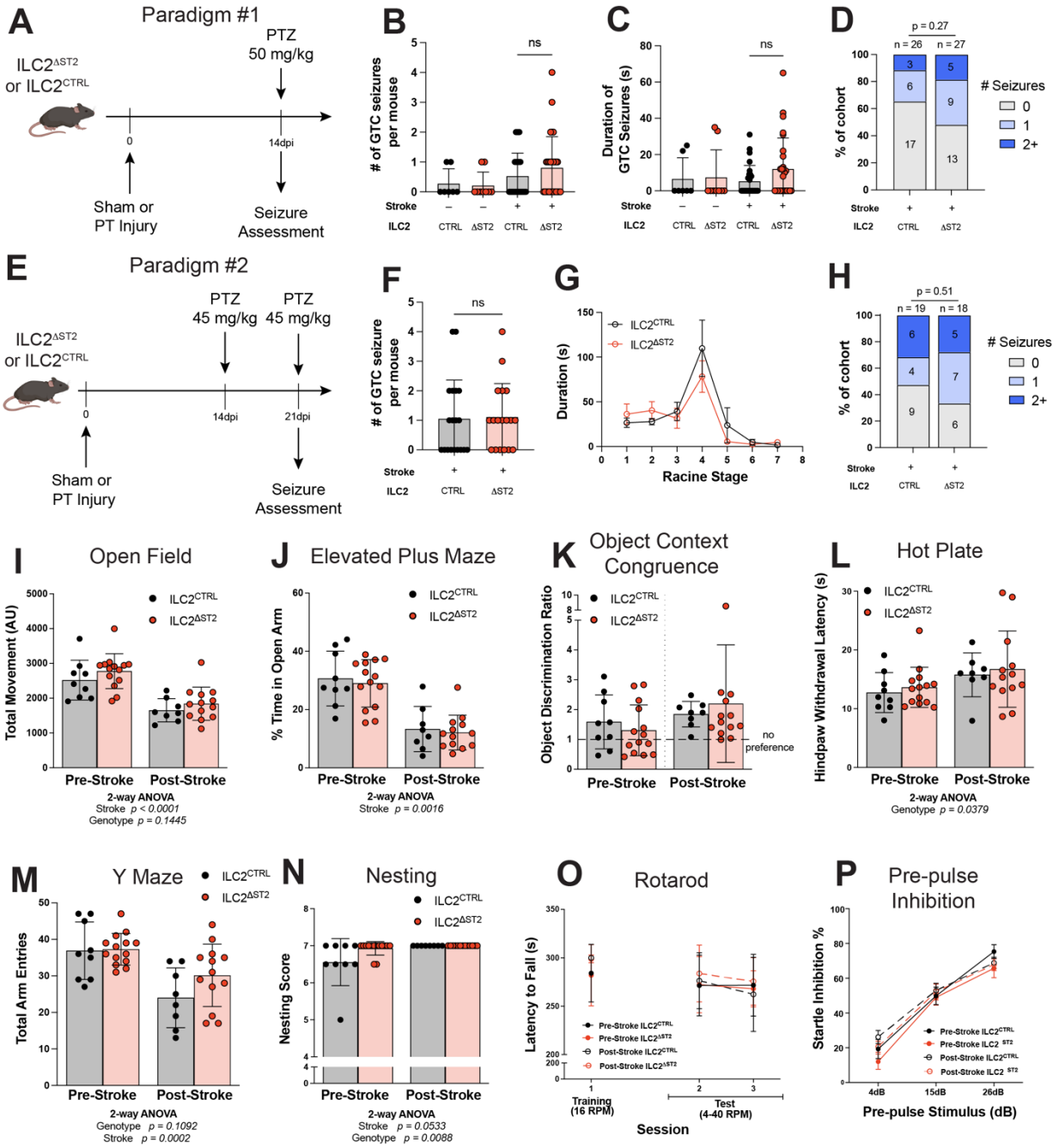


**Figure 3.9. IL-33 signaling in ILC2s does not impact seizure susceptibility or other behaviors after PT damage.**

- A) Schematic depicting paradigm #1 for seizure assessment. Mice are given sham or PT injury and injected with 50 mg/kg pentylenetetrazol (PTZ) at 14dpi, followed by seizure assessment.
- B) Number of generalized tonic-clonic (GTC) seizures in sham or PT-injured ILC2<sup>CTRL</sup> and ILC2<sup>ΔST2</sup> mice challenged via paradigm #1. Kruskal-Wallis test with Dunn's multiple comparisons test.
- C) Duration of generalized tonic-clonic (GTC) seizures in sham or PT-injured ILC2<sup>CTRL</sup> and ILC2<sup>ΔST2</sup> mice challenged via paradigm #1. Kruskal-Wallis test with Dunn's multiple comparisons test. (Figure caption continued on the next page)

(Figure caption continued from the previous page)

- D) Percentage of PT-injured ILC2<sup>CTRL</sup> and ILC2<sup>AST2</sup> mice experiencing 0, 1, or 2+ GTC seizures following paradigm #1. Fisher's exact test comparing 0 or 1+ seizures.
- E) Schematic depicting paradigm #2 for seizure assessment. Mice are given sham or PT injury and injected with 45 mg/kg PTZ at 14dpi, and again at 21dpi, followed by seizure assessment.
- F) Number of generalized tonic-clonic (GTC) seizures in PT-injured ILC2<sup>CTRL</sup> and ILC2<sup>AST2</sup> mice challenged via paradigm #2. Mann-Whitney U test.
- G) Duration of PT-injured ILC2<sup>CTRL</sup> and ILC2<sup>AST2</sup> mice in each Racine Stage following PTZ challenge via paradigm #2. Data are means  $\pm$  SEM. See **Table 4.5** for Racine scoring details.
- H) Percentage of PT-injured ILC2<sup>CTRL</sup> and ILC2<sup>AST2</sup> mice experiencing 0, 1, or 2+ GTC seizures following paradigm #2. Fisher's exact test comparing 0 or 1+ seizures.
- I) Total movement of ILC2<sup>CTRL</sup> and ILC2<sup>AST2</sup> mice before and 14d after PT stroke, as quantified by the open field test. Two-way ANOVA.
- J) Percentage of the time ILC2<sup>CTRL</sup> or ILC2<sup>AST2</sup> mice spent in the open arms of the elevate plus maze before and 14d after PT stroke. Two-way ANOVA.
- K) Object discrimination ratio of ILC2<sup>CTRL</sup> and ILC2<sup>AST2</sup> mice before and 14d after PT stroke, as quantified by the object context congruence test.
- L) Latency of time before ILC2<sup>CTRL</sup> and ILC2<sup>AST2</sup> mice withdrew hindpaws from painful hot plate stimulus before and 14d after PT stroke. Two-way ANOVA.
- M) Total number of entries into each arm of the Y maze that ILC2<sup>CTRL</sup> and ILC2<sup>AST2</sup> mice made before and 14d after PT stroke. Two-way ANOVA.
- N) Nesting score for each ILC2<sup>CTRL</sup> or ILC2<sup>AST2</sup> mouse before and 14d after PT stroke, as quantified by overnight nesting test. Two-way ANOVA.
- O) Latency of each ILC2<sup>CTRL</sup> or ILC2<sup>AST2</sup> mouse to fall off of the rotarod during training (static rotation) and test trials (accelerating rotation), both before and 14d after PT stroke.
- P) Percentage that each ILC2<sup>CTRL</sup> or ILC2<sup>AST2</sup> mouse inhibited their startle response to the indicated pre-pulse stimuli prior to a 120dB loud stimulus, both before and 14d after PT stroke. Data are mean  $\pm$  SD, unless otherwise noted. Data points represent biological replicates (individual mice). Statistics: ns = not significant.

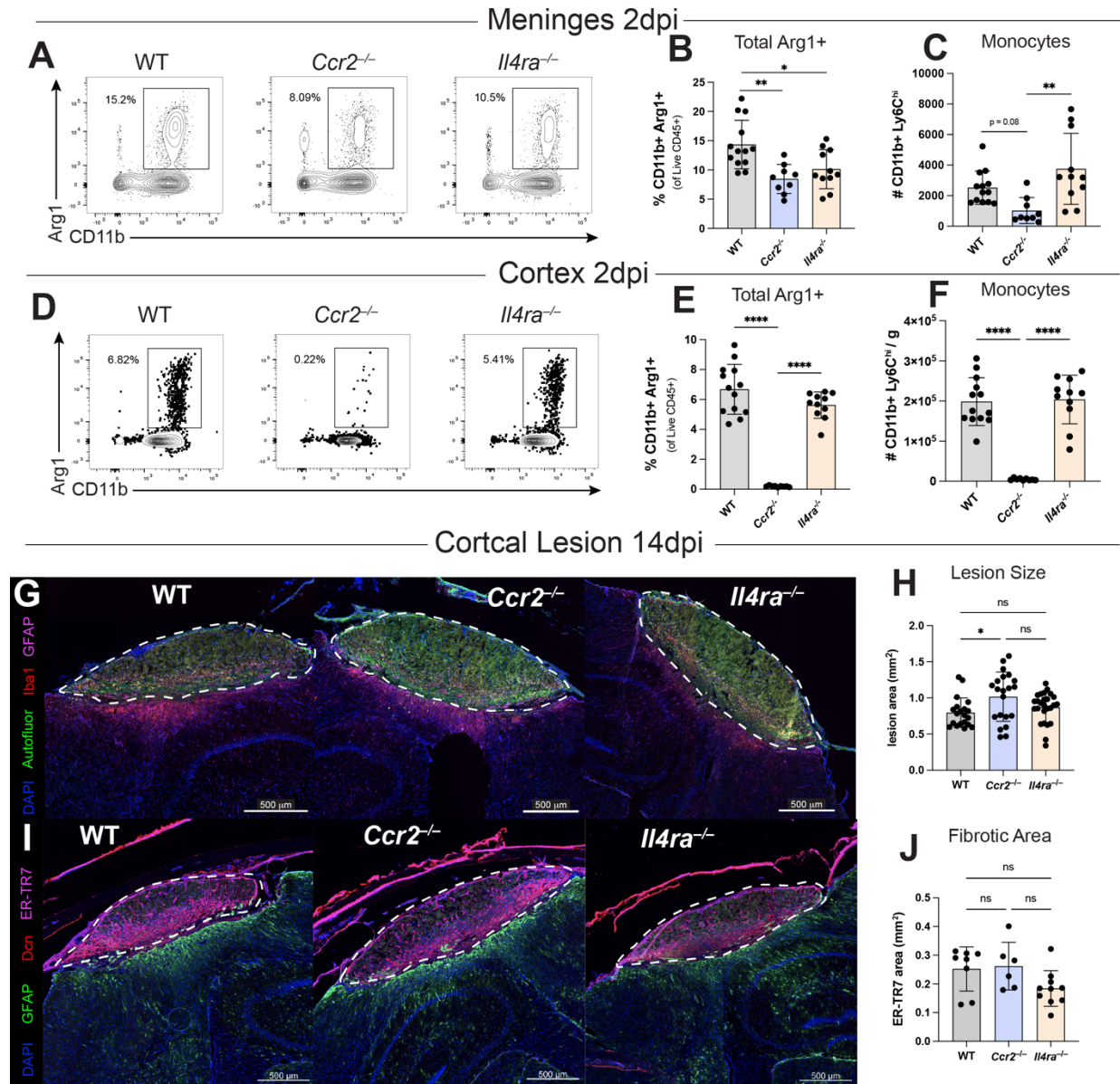


**Figure 3.10. CCR2-dependent monocyte trafficking contributes to Arg1<sup>+</sup> myeloid and limits cortical damage after PT damage.**

- A) Representative flow plots depicting CD11b and Arg1 expression within total CD45<sup>+</sup> meningeal immune cells in wild-type (WT), *Ccr2*<sup>-/-</sup>, and *Il4ra*<sup>-/-</sup> at 2dpi.
- B) Percentage of total live CD45<sup>+</sup> meningeal immune cells that are CD11b<sup>+</sup> Arg1<sup>+</sup> in WT, *Ccr2*<sup>-/-</sup>, and *Il4ra*<sup>-/-</sup> at 2dpi. One-way ANOVA with Tukey's multiple comparisons test.
- C) Number of classical monocytes (CD11b<sup>+</sup> Ly6C<sup>hi</sup>) in the meninges of WT, *Ccr2*<sup>-/-</sup>, and *Il4ra*<sup>-/-</sup> 2dpi. One-way ANOVA with Tukey's multiple comparisons test.
- D) Representative flow plots depicting CD11b and Arg1 expression within total CD45<sup>+</sup> cortical immune cells in WT *Ccr2*<sup>-/-</sup>, and *Il4ra*<sup>-/-</sup> at 2dpi.
- E) Percentage of total live CD45<sup>+</sup> cortical immune cells that are CD11b<sup>+</sup> Arg1<sup>+</sup> in WT, *Ccr2*<sup>-/-</sup>, and *Il4ra*<sup>-/-</sup> at 2dpi. One-way ANOVA with Tukey's multiple comparisons test.
- F) Number per gram of classical monocytes (CD11b<sup>+</sup> Ly6C<sup>hi</sup>) in the cortex of WT, *Ccr2*<sup>-/-</sup>, and *Il4ra*<sup>-/-</sup> 2dpi. One-way ANOVA with Tukey's multiple comparisons test
- (Figure caption continued on the next page)

(Figure caption continued from the previous page)

- G) Representative maximal cross-sectional area images of cortical lesions in WT, *Ccr2*<sup>-/-</sup>, and *Il4ra*<sup>-/-</sup> mice at 14dpi, depicting GFAP (reactive astrocyte), Iba1 (microglia/ macrophages), and DAPI (nuclei) staining.
- H) Maximal cross-sectional lesional area from WT, *Ccr2*<sup>-/-</sup>, and *Il4ra*<sup>-/-</sup> mice at 14dpi. Data points represent individual brain sections (2 sections per mouse). One-way ANOVA with Tukey's multiple comparisons test.
- I) Representative cross-sectional area images of cortical lesions in WT, *Ccr2*<sup>-/-</sup>, and *Il4ra*<sup>-/-</sup> mice at 14dpi, depicting GFAP (reactive astrocyte), Decorin (Dcn, ECM molecule), ER-TR7 (Collagen VI), and DAPI (nuclei) staining.
- J) Lesional ER-TR7<sup>+</sup> area from WT, *Ccr2*<sup>-/-</sup>, and *Il4ra*<sup>-/-</sup> mice at 14dpi. Data points represent individual brain sections (2 sections per mouse). One-way ANOVA with Tukey's multiple comparisons test.

Data are mean ( $\pm$  SD). Data points represent biological replicates (individual mice) unless otherwise specified. Statistics: ns=not significant, \*p < 0.05, \*\*p < 0.01, \*\*\*\*p < 0.0001.



**Table 3.1. Antibodies used for flow cytometry in Chapter 3.**

Reagent	Clone	Dilution	Vendor	Catalog #
Fc Block (Rat anti-mouse CD16/CD32)	2.4G2	1:100–1:250	BD Biosciences	553142
KLRG1–FITC	2F1/KLRG1	1:400	BioLegend	138410
TCR $\gamma\delta$ –PerCP–Cy5.5	GL3	1:200	BioLegend	118118
CD19–PEDazzle594	6D5	1:400	BioLegend	115554
ST2–FITC	DJ8	1:200	MD Bioproducts	101001F
ST2–PE	DJ8	1:400	MD Bioproducts	101001PE
FoxP3–PE–Cy7	FJK-16s	1:100	eBioscience	25-5773-82
GATA-3–eF660	TWAJ	1:100	eBioscience	50-9966-42
CD3–AF700	17A2	1:200	BioLegend	100216
CD90.2 (Thy1.2)–BV421	53-2.1	1:400	BioLegend	140327
CD11b–BV605	M1/70	1:400	BD Biosciences	563015
NK1.1–BV650	PK136	1:400	BioLegend	108736
CD4–BV711	RM4-5	1:200	BioLegend	100557
CD8 $\alpha$ –BV785	53-6.7	1:200	BioLegend	100750
CD45–BUV395	30-F11	1:400	BD Biosciences	564279
CD69–FITC	H1.2F3	1:100	BioLegend	104505
CD62L–PE	MEL-14	1:200	BioLegend	104407
CD44–PE–Cy7	IM7	1:400	BioLegend	103030
CD25–PerCP–Cy5.5	PC61	1:200	BioLegend	102030
KLRG1–PE–Cy7	2F1/KLRG1	1:400	BioLegend	138416
huCD4–biotin	RPA-T4	1:100	BioLegend	300504
KLRG1–PerCP–Cy5.5	2F1/KLRG1	1:200	BioLegend	138417
CD127 (IL-7R $\alpha$ )–AF647	A7R34	1:200	BioLegend	135019
Ly6C–FITC	HK1.4	1:400	BioLegend	128005
CD206–PE–Cy7	C026C2	1:200	BioLegend	141719
CD11b–FITC	M1/70	1:400	BioLegend	101206
CD63–PE	NVG-2	1:200	BioLegend	143904
CD9–BV421	KMC8	1:200	BD Biosciences	564235
CD64–BV605	X54-5/7.1	1:200	BioLegend	139323
CD11c–BV650	N418	1:200	BioLegend	117339
CX3CR1–BV785	SA011F11	1:200	BioLegend	149029
MHC-II (I-A/I-E)–BUV737	M5/114.15.2	1:400	BD Biosciences	748845
Thy1.2–FITC	53-2.1	1:400	BD Biosciences	553004
MerTK–PerCP–eF710	DS5MMER	1:200	eBioscience	46-5751-80
CD172a (SIRP $\alpha$ )–PE	P84	1:200	eBioscience	12-1721-80
CD11c–PE–Cy7	N418	1:200	BioLegend	117318
CD64–AF647	X54-5/7.1	1:200	BD Biosciences	558539
Ly6G–APC–Cy7	1A8	1:200	BioLegend	127624
CD11b–Pacific Blue	M1/70	1:400	BioLegend	101224
Ly6C–BV605	HK1.4	1:200	BioLegend	128035
CD192 (CCR2)–BV711	475301	1:200	BD Biosciences	747964
Siglec F–BV786	E50-2440	1:200	BD Biosciences	740956
Ly6G–AF488	1A8	1:200	BioLegend	127626
Ly6C–PerCP–Cy5.5	HK1.5	1:200	BioLegend	128011
Arg1–APC	A1exF5	1:100	eBioscience	17-3697-82
CD31–AF488	390	1:400	BioLegend	102414
Podoplanin (gp38)–PE–Cy7	8.1.1	1:200	BioLegend	127412
CD140a (PDGFR $\alpha$ )–APC	APA5	1:200	BioLegend	135908
CD326 (EpCAM)–APC–Fire750	G8.8	1:200	BioLegend	118230

Reagent	Clone	Dilution	Vendor	Catalog #
Sca-1–BV711	D7	1:200	BioLegend	108131
CD45–PerCPCy5.5	30-F11	1:200	BioLegend	103132

**Table 3.2. Antibodies used for immunofluorescent imaging in Chapter 3.**

Reagent	Clone	Dilution	Vendor	Catalog #
Rat anti-GFAP	2.2B10	1:1000	Invitrogen	13-0300
Chicken anti-GFAP	Polyclonal	1:200	Invitrogen	PA1-10004
Rabbit anti-Iba1	Polyclonal	1:1000	Wako	019-19741
Chicken anti-NeuN	Polyclonal	1:500	Millipore Sigma	ABN91
Chicken anti-GFP/YFP	Polyclonal	1:200	Aves	GFP-1020
$\alpha$ SMA–eF660	1A4	1:300	eBioscience	50-9760-82
Rabbit anti-VGAT	Polyclonal	1:2000	Synaptic Systems	131003
Mouse anti-Gephyrin	mAb7a	1:300	Synaptic Systems	147021
Guinea Pig anti-VGLUT1	Polyclonal	1:5000	Millipore Sigma	AB5905
Rabbit anti-Homer1	Polyclonal	1:200	Synaptic Systems	160 003
Rat anti-Col VI (ER-TR7)	ER-TR7	1:200	Novus Biologicals	NB100-64932
Goat anti-Decorin (Dcn)	Polyclonal	1:200	Novus Biologicals	AF1060
Goat anti-chicken AF488	Polyclonal	1:500–1:1000	Invitrogen	A11039
Donkey anti-chicken CF488A	Polyclonal	1:500–1:1000	Sigma-Aldrich	SAB4600031-250UL
Donkey anti-rabbit AF555	Polyclonal	1:500–1:1000	Invitrogen	A31572
Donkey anti-goat AF555	Polyclonal	1:500–1:1000	Invitrogen	A32758
Donkey anti-rat AF647	Polyclonal	1:500–1:1000	abcam	ab150155
Goat anti-rat AF488	Polyclonal	1:500–1:1000	Invitrogen	A11006
Goat anti-rabbit AF555	Polyclonal	1:500–1:1000	Invitrogen	A21429
Goat anti-mouse AF647	Polyclonal	1:500–1:1000	Invitrogen	A21236
Goat anti-chicken AF405+	Polyclonal	1:500–1:1000	Invitrogen	A48260
Goat anti-guinea pig AF647	Polyclonal	1:500–1:1000	Invitrogen	A21450

**Table 3.3. Chemicals, commercial kits, and other critical reagents used in Chapter 3.**

Reagent	Dilution	Vendor	Catalog #
Fixable Viability Dye eFlour 780	1:1000	eBioscience	65-0865-18
Draq7	1:1000	BioLegend	424001
DAPI (4',6-Diamidino-2-phenylindole dihydrochloride)	1:1000 from 2 mg/mL stock	Sigma-Aldrich	D9542-10MG
Fluoromount G with DAPI	—	Southern Biotech	0100-20
Fluoromount G	—	Southern Biotech	0100-01
Streptavidin–APC	1:400	BioLegend	405207
Percoll	22%	GE Healthcare	17-0891-01
FoxP3/Transcription Factor Staining Buffer Set	—	eBioscience	00-5523-00
BD Cytotfix/Cytoperm Fixation/Permeabilization Kit	—	BD Biosciences	554714
CountBright Absolute Counting Beads, for flow cytometry	—	Invitrogen	C36950
Pentylene tetrazole (PTZ)	—	Tocris	2687/1G
Histodenz	—	Sigma-Aldrich	D2158-100g
Rose Bengal	—	Sigma-Aldrich	330000-1G
Tamoxifen	—	Sigma-Aldrich	T5648

**Table 3.4. Mouse strains used in Chapter 3.**

Strain	Source	Identifier
Wild-type B6 (C57BL/6J)	Bred in house from mice obtained from JAX.	JAX# 000664
IL-33 <sup>mCherry</sup> ( <i>Il33<sup>H2B-mCherry</sup></i> )	Vainchtein et al. 2018 (110)	Courtesy of Mucosal Immunology Study Team (MIST)
Rosa26 <sup>LSL-YFP</sup> (Ai3) (B6.Cg-Gt(ROSA)26Sor <sup>tm3(CAG-EYFP)Hze/J</sup> )	Madisen et al. 2010 (126)	JAX# 007903
Rosa26 <sup>LSL-tdTomato</sup> (Ai14) (B6.Cg-Gt(ROSA)26Sortm14(CAG-tdTomato)Hze/J)	Madisen et al. 2010 (126)	JAX# 007914
Arg1 <sup>YFP</sup> (C.129S4(B6)-Arg1 <sup>tm1.1Lky/J</sup> )	Reese et al. 2007 (127)	JAX# 015858
IL-13 <sup>huCD4</sup> (B6.129S4(C)-Il13 <sup>tm2.1Lky/J</sup> )	Liang et al. 2012 (112)	JAX# 031367
IL-5 <sup>Cre-RFP</sup> (B6(C)-Il5tm1.1(icre)Lky/J)	Nussbaum et al. 2013 (80)	JAX# 030926
ST2 <sup>Flox</sup> ( <i>Il1rl1<sup>flox</sup></i> )	Chen et al. 2015 (113)	<i>In progress</i>
<i>Il4ra</i> <sup>-/-</sup> ( <i>Il4ra<sup>tm1Fbb</sup></i> )	Mohrs et al. 1999 (118)	MGI: 2657172
<i>Ccr2</i> <sup>-/-</sup> ( <i>Ccr2<sup>RFP/RFP</sup></i> ) (B6.129(Cg)- <i>Ccr2<sup>tm2.1ffc/J</sup></i> )	Saederup et al. 2010 (117)	JAX# 017586
<i>Ccr2</i> <sup>creERT2</sup> ( <i>Ccr2<sup>tm1(cre/ERT2,mKate2)Arte</sup></i> )	Croxford et al., 2015 (108)	MGI: 6314378

**Table 3.5. Modified Racine scale used to quantify seizure behavior in Figure 3.9.**

Racine Stage	Behavior
0	Baseline behavior (exploratory, rearing)
1	Sudden behavioral arrest, immobility
2	Myoclonic jerks, mild
3	Myoclonic jerks, moderate to severe, with stiffened/extended tail
4	Partial body clonus, forelimb or hindlimb
5	Generalized tonic-clonic (GTC) seizure, with loss of posture/control
6	Severe GTC seizure with wild running, jumping, or vocalizations
7	Tonic full-body extension
8	Respiratory arrest and death

### 3.6 MATERIALS AND METHODS

#### Mice

All mouse strains were bred and maintained in the specific pathogen-free animal facility in University of California, San Francisco, and all animal protocols were approved by and in accordance with the guidelines established by the Institutional Animal Care and Use Committee and Laboratory Animal Resource Center. All experiments were performed using used 8-15 week old adult male and female mice. All experiments of  $n > 5$  were analyzed for sex-specific trends, and none were evident unless specifically noted. Littermate controls were used for all experiments when feasible, and all mice were backcrossed  $>10$  generations on a C57BL/6 background unless otherwise indicated. The mouse strains used are shown in **Table 4**. For experiments involving inducible cre lines (e.g., creERT2), mice were injected i.p. with 2 mg of Tamoxifen (Sigma) dissolved in corn oil (Sigma) (100  $\mu$ L from a 20 mg/mL stock solution) per timepoint.

#### Photothrombotic (PT) Injury Survival Surgeries

PT injury surgeries were performed as previously described.<sup>26,128–130</sup> Mice are anesthetized via isoflurane inhalation and weighed, and their head is fixed in a stereotax (Kopf Instruments) while their body is warmed by a heating pad. Anesthesia is verified by absence of pedal reflex. The scalp is shaved and sterilized using 70% ethanol and betadine, and ophthalmic ointment is placed on the eyes. Mice are given a subcutaneous injection of 0.5% lidocaine in sterile saline ( $<7$ -8mg/kg) under the scalp skin for local analgesia. An incision is made along the midline of the scalp skin to expose the cranium, and the periosteum is removed. After bregma is visualized, the (x,y) coordinates (3.0 mm, -0.5mm) for the right somatosensory cortex (S1) are measured relative to bregma using the stereotax. A 3 mm diameter fiber optic cable connected to a 150W white light illuminator (Dolan-Jenner Fiber-Lite MI-152) is positioned directly over the S1 cortex on the intact cranium and fixed in position. Mice are then given 8 mg/kg Rose Bengal (Sigma) (from a freshly made 1 mg/mL solution in sterile saline) via i.p. injection and the dye is allowed to circulate for 1 minute. At this time, the light is turned on to maximum intensity for 2

minutes to induce dye photoexcitation and photothrombotic damage. Sham surgeries involve all procedures listed above except for light exposure. Following the procedure, nylon sutures and veterinary-grade surgical glue are used to close the scalp. Mice are treated with 0.05 mg/kg buprenorphine HCl s.c. (diluted in sterile saline) and allowed to fully recover on a heating pad before returning to standard housing racks. Mice are treated again with 0.05 mg/kg buprenorphine i.p. 4–8 hours after surgery, and again the following morning (~24 hours post-surgery). Mice will be then closely monitored for signs of pain the next afternoon (~36 hours post-surgery) and the following day (~48 hours post surgery), per approved animal protocols.

### **Meningeal dissociation for flow cytometry**

Mice were euthanized with CO<sub>2</sub> and perfused with 10-15 mL of cold 1X DPBS via the left ventricle. Horizontal cuts were made to remove the skullcap which was placed in ice cold 1X DPBS after removal of the brain. Under a dissecting microscope, the dural meninges were quickly removed by gentle scraping using fine forceps and collected into 1 mL of ice-cold digestion buffer (RPMI with 10% (v/v) heat-inactivated FBS, 80 µg/mL DNase I (Roche), and 0.2 wU/mL Liberase TM (Roche)) in a 24 well plate. Meninges were enzymatically digested at 37°C with shaking at ~200 RPM for 30 min. After gentle trituration with a P1000 pipette, meninges and digestion buffer were passed through a 70-µm cell strainer; remaining tissue was firmly pressed through the filter in a circular motion using a wide tip plastic plunger from a 1 mL syringe. The strainer was flushed with FACS Wash Buffer (FWB, 1X DPBS (pH 7.4) with 3% (v/v) heat-inactivated FBS and 0.05% NaN<sub>3</sub>) and collected into a 15 mL conical tube. Cells were pelleted at 1500rpm for 5 min at 4°C and resuspended in FWB for downstream applications.

### **Brain dissociation for flow cytometry**

Mice were euthanized with CO<sub>2</sub> and perfused with 10-15 mL of ice-cold 1X PBS via the left ventricle. The brain was removed from the skullcap and two coronal cuts were made 2mm away from either edge of the cortical using a brain matrix and razor blade. Perilesional cortex was micro-dissected under a dissection microscope from these sections and collected into 2 mL of

iMED (isolation medium: 1X HBSS (without calcium or magnesium) supplemented with 15 mM HEPES and 0.6% glucose). Brain samples were weighed and then homogenized to yield microglia and other immune cells, as previously described.<sup>131</sup> Briefly, brain samples were mechanically dissociated in a 2 cm<sup>3</sup> glass dounce homogenizer in iMED on ice, filtered through a 70 µm cell strainer, and washed twice with iMED. Samples were centrifuged at 220xg for 10 min at 4°C and then resuspended in a 22% Percoll solution (GE Healthcare) with a PBS layer floated on top. Samples were centrifuged at 950xg for 20 min (acceleration=4, brake=0) and the supernatant layers were discarded to remove myelin and debris. Cell pellets were resuspended prior to antibody staining for flow cytometry. Cell numbers calculated from flow cytometric data were normalized to the weight of the original cortical sample.

### **Staining for flow cytometry**

For myeloid/DAM panels, single cell suspensions were first blocked in FWB containing 5% (v/v) normal rat serum and Fc Block (2.4G2, 1:250, BD Biosciences) for 20 min at 4°C. Cells were pelleted at 1200rpm for 2 min and resuspended in FWB containing surface antibodies and viability dye for 45min at 4°C. Cells were washed and resuspended with FWB prior to analysis.

For panels involving intracellular Arg1 staining, single cell suspensions were first blocked in FWB containing 5% (v/v) normal rat serum and Fc Block (2.4G2, 1:250, BD Biosciences) for 20 min at 4°C. Cells were pelleted at 1200rpm for 2 min and resuspended in FWB containing surface antibodies for 45min at 4°C. Cells were then washed and fixed/permeabilized for 20 min at 4°C using the Cytofix/Cytoperm Fixation/Permeabilization Kit (BD Biosciences). Cells were washed with 1X PermBuffer (BD Biosciences) and stained with intracellular antibodies overnight at 4°C. Cells were pelleted at 2000rpm for 4min at 4°C, washed twice with 1X PermBuffer (BD Biosciences), and then resuspended in FWB prior to analysis.

For lymphocyte panels involved IL-5 and IL-13 reporters (i.e. *Il5<sup>RFP</sup>* and *Il13<sup>huCD4</sup>*), cell suspensions were incubated with a viability dye (Fixable Viability Dye eFluor780, eBioscience), Fc block (2.4G2, 1:100), and surface antibodies (including anti-humanCD4-biotin) diluted in PBS

for 60 min at 4°C. Cells were washed in FWB and then incubated with streptavidin-APC (1:400) for 20 min at 4°C. Samples were then washed and resuspended in FWB prior to analysis.

For lymphocyte panels only involving surface staining, single cell suspensions were first incubated with a viability dye, Fc Block (2.4G2, 1:100, BD Biosciences), and surface antibodies diluted in 1X DPBS for 45 min at 4°C. Samples were then washed and resuspended in FWB prior to analysis.

For lymphocyte panels involving transcription factor staining, single cell suspensions were first incubated with a viability dye (Fixable Viability Dye eFluor780, eBioscience), Fc Block (2.4G2, 1:100, BD Biosciences), and surface antibodies diluted in 1X DPBS for 45-60 min at 4°C. Cells were washed with FWB and then fixed/permeabilized overnight at 4°C using the FoxP3/transcription factor Staining Buffer Set (eBioscience). Cells were washed with 1X PermBuffer (eBioscience) and stained with intracellular antibodies for 60 min at 4°C. Cells were washed again with 1X PermBuffer and then resuspended in FWB prior to analysis.

All staining for flow took place in a 96 well V-bottom plate in 50 µL. Prior to data collection, counting beads (CountBright Absolute Counting Beads, Invitrogen) were added to each sample and samples were filtered through a 40 µm cell strainer. Flow cytometric data was collected on a BD Fortessa and data analysis was performed using FlowJo software (BD).

### **Whole-mount meningeal staining and imaging**

Mice were euthanized with CO<sub>2</sub> and perfused via the left ventricle with 10-15 mL of ice-cold 1X PBS followed by 10 mL of 4% (w/v) paraformaldehyde (PFA, Thermo Scientific). Skullcaps containing dural/arachnoid meninges were separated from the brain/pial membrane and post-fixed in 4% PFA overnight at 4°C with shaking (90 rpm). Skullcaps/meninges were washed with 1X PBS and then incubated in Blocking/Permeabilization Buffer (0.3% (v/v) Triton X-100, 5% (v/v) fetal bovine serum (FBS), 0.5% (w/v) bovine serum albumin (BSA), and 0.05% NaN<sub>3</sub> (w/v) in PBS) for at least one overnight at 4°C (90 rpm). Skullcaps/meninges were then

incubated with primary antibodies in Staining Solution (0.15% (v/v) Triton X-100, 7.5% (v/v) FBS, 0.75% (w/v) BSA, and 0.075% (w/v) NaN<sub>3</sub> in PBS) for three days at 4°C (90 rpm). Skullcaps/meninges were washed three times in PBS-T (1X PBS with 0.15% Triton X-100) for 30 min each at 4°C (90 rpm) and incubated with secondary antibodies in Staining Solution overnight at 4°C. Skullcaps/meninges were washed three times in PBS-T for 30 min each and then incubated with directly conjugated antibodies in Staining Solution overnight at 4°C (90 rpm). Skullcaps/meninges were again washed three times in PBS-T for 30 min each and then stained in DAPI (2 µg/mL in PBS) for 30-60 min at 4°C (90 rpm), and rinsed in 1X PBS. Meninges were then dissected out of skullcaps under a dissecting microscope in a PBS bath and whole-mounted onto glass slides. Residual PBS was wicked away and replaced with RIMS (Refractive Index Matching Solution: 80% (w/v) Histodenz in 1X PBS, 0.01% (w/v) NaN<sub>3</sub>, 0.1% (v/v) Tween20). Meninges were covered with a glass coverslip, sealed with nail polish, and allowed to clear at least one day prior to imaging.

### **Immunofluorescent staining of brain tissue**

For imaging of intact cortical lesions (containing lesions, meninges, and cranium), mice were euthanized with CO<sub>2</sub> and perfused via the left ventricle with 10-15 mL of ice-cold 1X PBS followed by 10 mL of 4% (w/v) PFA (Thermo Scientific). Skulls (containing intact brain, meninges, and cranium) were fixed in 4% PFA overnight at 4°C with shaking (90 rpm). Skulls were then washed with 1X PBS and decalcified in 0.3M EDTA (VWR) for 1 week at 4°C with shaking (90 rpm). Skulls were then incubated in 30% (w/v) sucrose for at least one day at 4°C with shaking (90 rpm) for cryopreservation. Skulls were frozen in O.C.T. (Fisher Scientific) on dry ice and stored at -80°C until sectioning. Skulls were sectioned on a cryostat (Leica) into 14 µm sections which were immediately mounted on SuperFrost Plus glass slides (Fisher Scientific). Slide-mounted sections were stored at -80°C until staining. For lesion size analysis, the 2 slides with the maximal cross sectional lesion area were chosen and the experimenter was blinded to genotype



throughout the entire sectioning, staining, and imaging process. When stained, slide-mounted sections were thawed, rehydrated with 1X PBS, and blocked/permeabilized for 1 hour at RT in Block/Stain Solution (1X PBS with 0.4% (v/v) TritonX-100 and 5% (v/v) horse serum). Samples were incubated with primary antibodies diluted in Block/Stain Solution for 1 hour at RT or overnight at 4°C. Samples were washed three times in Slide Wash Buffer (1X PBS with 0.05% TritonX-100) for 5 min at RT with shaking (~90rpm) and incubated in secondary antibodies diluted 1:500 in Block/Stain solution for 45-60 min at RT. Samples were washed again washed three times in Slide Wash and mounted in DAPI Fluoromount-G (Southern Biotech). Slides were allowed to cure overnight in the dark prior to imaging.

For imaging of synapses, mice were euthanized with CO<sub>2</sub> and perfused via the left ventricle with 10-15 mL of ice-cold 1X PBS followed by 10 mL of 4% (w/v) PFA (Thermo Scientific). Brains were dissected out and fixed for only 4 hours in 4% PFA at 4°C with shaking (90 rpm). Brains were then washed with 1X PBS and incubated in 30% (w/v) sucrose for at least one day at 4°C with shaking (90 rpm) for cryopreservation. Brains were frozen in O.C.T. (Thermo Scientific) on dry ice and stored at -80°C prior to sectioning into 40 µm sections that were collected and stored in 1X PBS containing 0.05% (w/v) NaN<sub>3</sub>. Antigen retrieval was performed in 0.01M sodium citrate pH=6 at 95°C for 5 min, cooled at room temperature for 5 min in solution, and washed three times in PBS. Sections were blocked for one hour at room temperature in Block/Stain Solution (1X PBS with 0.4% (v/v) high-purity Surfact-Amps TritonX-100 and 5% (v/v) normal goat serum), and then stained overnight with primary antibody mix in Block/Staining Solution at 4°C with shaking (90 rpm). Sections were washed three times in PBS-T (0.05% Triton X-100 in 1X PBS) and stained with secondary antibody diluted 1:1000 in Staining Solution for 1.5 hours at RT with shaking (90 rpm). Secondary antibody solutions were centrifuged at 15,000xg for 3 min in 1.5 mL tubes prior to staining to remove any aggregates. Sections were washed three times in

PBS-T and mounted onto slides with Fluoromount-G with or without DAPI (Southern Biotech). Slides were allowed to cure overnight in the dark prior to imaging.

### **Image Acquisition**

For lesion size, gliosis, and fibrosis quantification (14  $\mu\text{m}$  sections), tiled widefield images were taken using a Zeiss Axio Imager.M2 widefield epifluorescent microscope with a 10X/0.3 air objective. Only 1 Z stack was collected per image.

For whole mounted meninges, tiled confocal images were taken using a Nikon A1R laser scanning confocal microscope (with 405, 488, 561, and 650 laser lines) and a 16X/0.8 NA Plan Apo water-immersion objective with 512 resolution, 1 frame/s scanning speed, 2x line averaging, and 4  $\mu\text{m}$  Z-steps. Images were rendered into three dimensions and quantitatively analyzed using Bitplane Imaris v9.5.1 software (Andor Technology PLC). 3D reconstructions of each channel were generated using the Imaris surface function, thresholded on signal intensity, volume, DAPI-intensity, and sphericity (for ILC2s).

For synapse imaging, brain sections were imaged on a Zeiss LSM 800 confocal microscope with a 63X/1.4 NA Plan-Apochromat oil-immersion objective with the following acquisition parameters: field size = 101.4 mm x 101.4 mm (10,281.96 mm<sup>2</sup>); pixel size = ~0.08 mm (1200x1200 pixels); scan speed = 4; line averaging = 4x; 16 bit. Power, master gain, and digital gain were adjusted for individual experiments and kept consistent within an experiment. Single optical sections were acquired at a consistent depth of 5 mm below the surface to reduce variability of signal. Images were taken in either L2 of the perilesional S1 cortex or in the ipsilateral ventrobasal thalamus, as determined by NeuN staining.

### **Lesion Size, Fibrosis, and Gliosis Quantification**

Lesional analysis was performed as previously described.<sup>26</sup> Briefly, lesion sizes were calculated in ImageJ by tracing lesional borders, as defined by ER-TR7 and GFAP staining. Fibrotic (ER-TR7<sup>+</sup>) or gliotic (GFAP<sup>+</sup>, Iba1<sup>+</sup>) areas were determined by thresholding the relevant channel in ImageJ, using a consistent threshold for each image except for cases of exceptionally

high tissue background. The percentage of lesional area covered by the thresholded area was calculated in Image J, and thresholded areas were calculated by multiplying this percent by the lesional area for each section. 2 technical replicates (independent brain sections) were collected per mouse and averaged. After data analysis was finished, data was unblinded.

### **Synapse Quantification**

The ImageJ2 plugin PunctaAnalyzer v2 was used to quantify the numbers of synaptic puncta and the colocalization of presynaptic and postsynaptic marker channels, as described previously.<sup>92,115,132</sup> Pre- and post-synaptic marker pairs for inhibitory (VGAT and Gephyrin) and excitatory (VGLUT1 and Homer1) synapses were used. Background subtraction (rolling ball size 25-50 pixels) was applied, and threshold set to the max tail of the intensity histogram per channel for each image. 2-3 FOVs were acquired per region per brain slice and 2 slices were acquired per mouse. Puncta counts were normalized to the mean of the controls within each experiment.

### **Meningeal fibroblast-ILC2 co-cultures**

Meningeal fibroblast and ILC2 were co-cultured using a modified protocol from Dahlgren et al., 2019.<sup>57</sup> For fibroblast isolation, single cell suspensions of meningeal cells were generated and stained with surface antibodies as described above. Meningeal fibroblasts (CD45<sup>-</sup> CD31<sup>-</sup> EpCAM<sup>-</sup> PDGFR $\alpha$ <sup>+</sup> gp38<sup>+</sup>) were sorted on a FACS AriaII (BD) into fibroblast medium (1X DMEM supplemented with 10% heat-inactivated FBS, 1X Glutamax, and 1% penicillin/streptomycin). Meningeal fibroblasts were plated at 15,000 cells/well in a flat-bottom 96-well plate in fibroblast medium and culture for 7 days until confluency.

ILC2s were isolated from the lung as previously described.<sup>57,58</sup> Briefly, IL-5 lineage tracker mice (*Il5<sup>cre</sup>; Rosa26<sup>LSL-tdTom(Ai14)</sup>*) were treated every other day with recombinant carrier-free murine IL-33 (BioLegend) to expand ILC2s *in vivo*. 48 hours after the last dose of IL-33, lungs from these mice were isolated and dissociated on the “lung1” program of a GentleMacs tissue dissociator (Miltenyi Biotech). Lungs were digested in 1X HBSS containing 0.2 wU/mL Liberase TM (Roche) and 40 mg/mL DNase I (Roche) for 30 min at 37°C with shaking (200 rpm). Samples were then

homogenized with the GentleMacs “lung2” program, filtered through 70mm cell strainers, washed, and subjected to red blood cell lysis (1X Pharm-Lyse solution; BD Biosciences). Lung samples were stained with surface antibodies for 45 min in FWB, washed, and sorted on a FACSAriaII (BD). ILC2s were sorted as CD45<sup>+</sup> Lineage<sup>-</sup> CD3e<sup>-</sup> CD4<sup>-</sup> IL-5<sup>cre;tdTomato+</sup> into fibroblast medium. 7,500 ILC2s were added per well containing meningeal fibroblasts that had been culturing for 7 days (after removal of half of the existing conditioned medium). ILC2s cultured in the same plate in fibroblast medium alone served as negative controls. Co-cultures were analyzed after 5 days of culture by flow cytometry and the number of remaining live ILC2s (CD45<sup>+</sup>) per well were quantified.

### **scRNAseq data acquisition and analysis**

For single cell RNA sequencing (scRNAseq), single cell suspensions of meningeal and brain samples from ILC2<sup>CTRL</sup> and ILC2<sup>ΔST2</sup> mice were generated and stained with surface antibodies for flow cytometry as described above. 1 male and 2 female mice were used per condition and pooled together prior to staining. Samples were split in half for fluorescence-activated cell sorting (FACS) on a FACSAria Fusion (BD). From one half, lymphocytes (CD45<sup>+</sup> CD11b<sup>-</sup> CD19<sup>-</sup>), myeloid cells (CD11b<sup>+</sup>), and fibroblasts (PDGFRα<sup>+</sup> gp38<sup>+</sup>) were sorted, while total live cells (DAPI<sup>-</sup>) cells were sorted from the other half. Within each condition, all of the sorted lymphocytes were pooled with each proportions of sorted myeloid cells, fibroblasts, and total live cells such that the total number of cells per sample was approximately 16,000 (final breakdown: ~15% lymphocytes, ~28% myeloid cells, ~28% fibroblasts, ~28% total live cells per sample). Approximately 16,000 cells per condition were loaded into each well of Chromium Chip G (v3.1) on the Chromium X, libraries were prepared in-house as described in the 10X Manual, and libraries were sequenced on three lanes of the NovaSeq SP100 at the UCSF CAT core.

Sequenced samples were processed using the Cell Ranger 2.1 pipeline (built on the STAR aligner)<sup>59</sup> and aligned to the GRCm38 (mm10) mouse reference genome. Clustering and

differential expression analysis were conducted using Seurat version 3.12. Sequencing scripts can be found at <https://github.com/lcdorman/scrnaseq/tree/master/Rmd>, and original data can be found on GEO [submission in progress]. Briefly, cells with high mitochondrial gene expression and low or high UMI and feature counts were filtered out from downstream analysis using the following parameters: UMIs/cell: 1000-10000, features/cell: 500-3000, and 0-15% mitochondrial genes. Seurat's *SCTransform* function was used to normalize data, select variable features for dimensionality reduction (with the removal of certain sex-related and mitochondrial genes), and scale data. Principle components were calculated using Seurat's *RunPCA* function, followed by graph-based clustering using Seurat's *FindNeighbors* (dims =1:30) and *FindClusters* (res = 0.6) functions and 2D visualization using Seurat's *RunUMAP* function (dims = 1:30). *FindAllMarkers* (test.use = MAST) was used to find differentially expressed genes in each cluster and clusters were annotated using select marker genes. Additional feature plots, UMAP plots, dot plots, and heatmaps were generated using Seurat and ggplot2. Myeloid cells and lymphocytes were subset and reclustered as above: meningeal lymphocytes (res=0.6), meningeal myeloid cells (res = 0.9), cortical lymphocytes (res=0.6), cortical microglia (res=0.5). For microglia, a disease-associated microglia (DAM) signature score was generated using the top 25 differentially upregulated genes in DAMs in Keren-Shaul et al., 2017 (p<0.001, ranked by logFC) and the *AddModuleScore* function in Seurat.<sup>34</sup> Relative abundance across time was calculated for each lymphocyte and macrophage/myeloid subcluster after normalizing for the total number of cells within each condition.

### **Seizure induction and quantification**

Seizure induction and quantification were performed as previously described.<sup>115</sup> For each experiment, a fresh solution of pentylenetetrazol (PTZ, Tocris) was prepared by dissolving PTZ in normal saline. Depending on the paradigm used, mice were injected with either 45 or 50 mg/kg of PTZ (see Figure 9A,E). Each animal was placed in the center of a transparent cage and allowed to adjust to the new environment for 10 minutes. PTZ was injected i.p. and seizure behaviors

were video recorded for 20 minutes. Video clips were analyzed to measure the number of as generalized tonic-clonic (GTC) seizures per mouse, the duration of these seizures, and the latency to seizure onset. For mice in paradigm #2 (**Figure 9.E**), the duration of and latency to each Racine stage was quantified (see **Table 5** for details of Racine scoring). More than 10s between two GTCs was considered as two separate events. All experiments were conducted in the same conditions between 1 PM and 5 PM, and the experimenter was blinded to genotype throughout data collection and analysis.

### **Whole cell patch-clamp electrophysiology**

Brain slices were prepared as previously described.<sup>111,115</sup> Briefly, 250- $\mu$ m-thick horizontal slices including thalamus were prepared in ice-cold sucrose cutting solution containing 234 mM sucrose, 2.5 mM KCl, 1.25 mM NaH<sub>2</sub>PO<sub>4</sub>, 10 mM MgSO<sub>4</sub>, 0.5 mM CaCl<sub>2</sub>, 26 mM NaHCO<sub>3</sub>, and 10 mM glucose, equilibrated with 95% O<sub>2</sub> and 5% CO<sub>2</sub>, pH 7.4, using a Leica VT1200 vibrating microtome (Leica Microsystems). Slices were incubated initially at 32–34°C for an hour and then at room temperature in artificial cerebrospinal fluid containing 126 mM NaCl, 2.5 mM KCl, 1.25 mM NaH<sub>2</sub>PO<sub>4</sub>, 1 mM MgCl<sub>2</sub>, 2 mM CaCl<sub>2</sub>, 26 mM NaHCO<sub>3</sub>, and 10 mM glucose, equilibrated with 95% O<sub>2</sub> and 5% CO<sub>2</sub>, pH 7.4.

Recordings were performed as previously described.<sup>111,115</sup> Briefly, recording electrodes made of borosilicate glass had a resistance 3–5 M $\Omega$  when filled with intracellular solution containing 115 mM potassium gluconate, 11 mM KCl, 1 mM MgCl<sub>2</sub>, 1 mM CaCl<sub>2</sub>, 10 mM HEPES, and 11 mM EGTA, 2 mM K<sub>2</sub>ATP, 0.1% biocytin, pH adjusted to 7.35 with KOH (286 mOsm) for miniature excitatory postsynaptic current (mEPSC) recording or 129 mM CsCl, 5 mM QX-314Cl, 2 mM MgCl<sub>2</sub>, 10mM HEPES, and 10 mM EGTA, 4 mM MgATP, 0.1% biocytin, pH adjusted to 7.38 with CsOH (288 mOsm) for miniature inhibitory postsynaptic currents (mIPSC) recording. Series resistance was monitored in all recordings, and the recordings were excluded from analysis if the series resistance was >25 M $\Omega$  or varied by >20%. Recordings were obtained using a MultiClamp 700B (Molecular Devices), digitized (Digidata 1550B; Molecular Devices), and acquired at 20 kHz

using the pClamp 10 software (Molecular Devices). Recordings were performed in a voltage clamp mode at a holding potential of  $-70$  mV and obtained from visually identified neurons in the perilesional somatosensory cortex (L2) or ventrobasal thalamus for 10 min. In the presence of  $0.5$   $\mu$ M tetrodotoxin,  $50$   $\mu$ M picrotoxin (P1675; Sigma-Aldrich) or  $50$   $\mu$ M D(-)-2-amino-5-phosphonopentanoic acid (5AP; HB0225; Hello Bio) and  $20$   $\mu$ M 6,7-Dinitroquinoxaline-2,3(1H,4H)-dione (DNQX, D0540; Sigma- Aldrich) were used to isolate mEPSCs or mIPSCs, respectively. Recordings were analyzed using ClampFit (Molecular Devices) and MiniAnalysis (Synaptosoft).

### **Behavioral analyses**

All behavioral experiments were performed and quantified by the Gladstone Institutes Behavioral Core (San Francisco, CA) per standard operating protocols. After confirming no sex differences were present, data from each sex was pooled together for visualization in this manuscript.

## **Chapter 4: Cross-regulatory interactions between the nervous system and Type 2 immunity**

### **4.1 ABSTRACT**

Interactions between the nervous and immune systems are critical to healthy physiology and are altered in many human diseases. This review covers recent work defining how the nervous system can both regulate and be regulated by type 2 immune responses, the branch of the immune system that responds to allergens, parasites, and toxins. Many of the major players in type 2 immune responses, including type 2 lymphocytes and cytokines, mast cells, and IgE, have been implicated in neuronal function and behavior. Conversely, neurons in both the central peripheral nervous systems can impact type 2 immune responses and behaviors relevant to allergy, such as food avoidance. Defining this complex circuitry and its molecular intermediates in physiology may reveal type 2 immunomodulators that can be harnessed for therapeutic benefit in neurologic diseases including Alzheimer's Disease, brain injury, and neurodevelopmental disorders. Conversely, modulation of the nervous system may be an important adjunct to treating immunologic disorders including atopic dermatitis, asthma, and food allergy.



## 4.2 INTRODUCTION

The nervous system encodes data in the synaptic connections between neurons that build functional neuronal circuits. In contrast, the immune system encodes information in cells that can move throughout the entire body. The innate immune system responds to patterns of tissue injury, infection, and remodeling, whereas the adaptive immune system targets an array of self and foreign antigens. Both the nervous and immune systems are shaped by experience and exposures to promote host survival and include a diversity of cellular and functional types. For many years, the complexity of neuroscience and immunology hampered intellectual cross-talk, but the past few years has led to a renaissance of work at the interface of these two key organizers of health and disease.

A particular challenge in understanding the neuroimmune interface is that both the nervous and immune systems have tremendous cellular and molecular diversity. For example, immune responses can be broadly categorized into ‘flavors’ optimized for different classes of pathogens. In this review, we will focus on how the nervous system interacts with one of these flavors – Type 2 immunity – the branch of the immune system that responds to infectious parasites, allergens, irritants, and toxins. Healthy type 2 immune responses require a coordinated response across the body, recruiting necessary immune cells to the infected or injured tissue concurrent with behavioral changes that modify the risk of future exposure and further organ injury.<sup>6</sup> Here we review recent studies showing that molecules associated with type 2 immune responses also impact the nervous system. We also review work demonstrating that the nervous system modulates the magnitude and impact of type 2 immune responses and allergy-related behaviors (**Figure 4.1**). In each of these settings, we discuss how type 2 immune signaling may be linked to a variety of diseases. These include brain disorders like brain injury and Alzheimer’s Disease, as well as allergic diseases such as atopic dermatitis, asthma, and food allergy.

Throughout this review, we will highlight two central questions. First, why do allergic immune pathways directly impact the brain? Are these a built-in system to shape behavioral

responses that are relevant to allergic immunity, or simply a co-opted pathway that reutilizes conserved molecules in a different context? Secondly, how critical is the peripheral nervous system in regulating allergic physiology and pathology? Is it a partial modulator or a critical regulator, and to what extent can it be harnessed for therapeutic benefit? Defining the answer to these questions will be critical to guiding therapies designed to modulate this neuro – type 2 immune interface across CNS diseases and peripheral allergic disorders. This review will focus on advances in the past three to five years that address these questions.

#### **4.3 COMPONENTS OF TYPE 2 IMMUNITY AND THE NERVOUS SYSTEM**

Type 2 immunity is activated to contain large extracellular parasites such as helminths (worms), protozoa, and mites.<sup>6,83</sup> Parasites are tissue-invasive organisms, potentially accounting for the well known roles of type 2 cells and cytokine signals in tissue remodeling and repair. These tissue-reparative functions are also integrated into mammalian biology that is beyond traditional settings of infection, including early organ development (modeling) and responses to sterile injury.<sup>133,134</sup> Prominent upstream actors of type 2 responses are the ‘alarmins’. Interleukin 33 (IL-33) is one such alarmin, an IL-1 family member widely expressed in structural cells (e.g. subsets of fibroblasts, epithelial cells, endothelial cells) that is sequestered in the nucleus under steady-state conditions. Upon tissue damage or stress, IL-33 is released into the interstitial fluid and signals to cells expressing its cognate receptor IL-33R, a dimer of IL-1RL1 (also known as ST2) and IL-1RAP, and drives proliferation, activation, and cytokine production.<sup>78</sup> IL-25 and Thymic Stromal Lymphopoietin (TSLP) are also critical initiators of type 2 immunity, signaling via their receptors IL-17RB and TSLPR, respectively.<sup>6</sup>

Type 2 immunity drives classic ‘weep and sweep’ responses at barrier tissues (skin, intestine, respiratory tract) and systemic and local adaptive type 2 memory, including CD4+ T helper type 2 (Th2) cell generation and IgE production and binding to mast cells, which together mediate quicker responses to future insults.<sup>6</sup> IL-4, IL-5, IL-9, IL-13, and amphiregulin are key

cytokine mediators of type 2 immunity. IL-13 in particular signals to diverse tissue immune, epithelial, endothelial, and structural cells (fibroblasts, mural cells, muscle cells) to propagate the immune response, promote tissue remodeling and mucous production, and regulate wound repair.<sup>76,134</sup> Type 2 innate lymphoid cells (ILC2) are early responders to alarmins, enriched at epithelial-rich barrier tissues and structural fibroblast-dense borders across the body, including the lung, skin, intestine, and brain meninges.<sup>76</sup> ILC2 alarmin receptor expression is associated with residence within a specific organ and topographic niche (e.g., IL-18R in skin, IL-17RB in gut, and IL-33R in border and adventitial niches across organs), but can be dynamically regulated during inflammation.<sup>57,135</sup> ILC2s are therefore poised to rapidly respond to the local release of alarmins and produce the 'effector' type 2 cytokines IL-5 and IL-13. Th2 cells respond to specific antigens via their T cell receptor (TCR), but once generated can take up residence in the tissues and cooperate with ILC2, including responding directly to alarmins.<sup>6,76</sup> Mast cells are tissue-resident granulocytes that express IL-33R and the high-affinity IgE receptor, FcεRI. Mast cells degranulate upon crosslinking of FcεRI-bound IgE molecules to cognate allergens, releasing histamine, eicosanoids (prostaglandins, leukotrienes) and proteases, and later cytokines such as IL-4/13, that are responsible for anaphylaxis (vasodilation, erythema, urticaria) and participate in many other types of allergic responses. Allergic diseases such as atopic dermatitis, allergic asthma, and food allergy are associated with a break in tolerance to commensal, environmental, or food antigens that drives maladaptive and chronic type 2 immune responses with associated tissue irritation, hyperreactivity, and – in severe cases – anaphylaxis.<sup>83</sup>

The nervous system is broadly divided into the Central Nervous System (CNS), including the brain and spinal cord, and the Peripheral Nervous System (PNS). Information in the CNS is encoded within the synaptic connections between neurons and the ultimate circuit patterns these create. These neurons are broadly classified as excitatory or inhibitory based on the neurotransmitter they produce: excitatory neurons produce glutamate (glutamatergic), while inhibitory neurons produce gamma aminobutyric acid (GABA, GABAergic) or, less commonly,

glycine (glycinergic). More globally, brain function can be tuned via neuromodulatory neurons that release non-synaptic neurotransmitters, such as serotonin, acetylcholine, norepinephrine, and dopamine, often in synchrony with neurons in the sympathetic and parasympathetic nervous systems, which are part of the PNS. In addition to their primary neurotransmitter, neurons often express neuropeptides (e.g., CGRP, NMU, Substance P), which adds specificity to their function.

The PNS consists of all neurons that extend outside the brain and spinal cord. Sensory neurons transmit afferent information about touch, temperature, proprioception, pain, and itch to the brain via sensory nerves. Sensory neurons have cell bodies in dorsal root ganglia (DRGs) along the spinal cord or the jugular/nodose ganglia of the vagus nerve and some cranial nerves. Analogous to the neuromodulatory neurons within the brain, autonomic neurons exist entirely outside the brain, and consist of the sympathetic, parasympathetic, and enteric nervous systems. The sympathetic nervous system promotes the “fight or flight” response via local release of neuromodulators including norepinephrine, which increase heart rate and dilate blood vessels and bronchioles. The parasympathetic nervous system, via release of acetylcholine, promotes the “rest and digest” response by reducing heart rate, constricting peripheral blood vessels, and promoting digestion of food. In addition to its sensory roles, the vagus nerve is also the major parasympathetic efferent from the brainstem to the rest of the body. The Enteric Nervous System (ENS) is a self contained nervous system acting through many of the same neurotransmitters described above that is specific to the small and large intestines, and is reviewed elsewhere.<sup>136,137</sup>

#### **4.4 TYPE 2 IMMUNE REGULATION OF THE BRAIN**

Cytokines are critical messengers in neuroimmune communication and coordination. Neurons express various cytokine receptors, enabling them to directly respond to local immune cues (**Figure 4.2**). Growing evidence demonstrates that type 2 cytokines can impact early life brain physiology, CNS injury, and disease, through both direct signaling to neurons and indirect mechanisms. Type 2 cytokines also signal to peripheral neurons throughout the body and relay

this inflammatory information back to the CNS. Type 2 cytokine signaling within the CNS and across the PNS present interesting similarities and differences that reveal key insights into how these neuroimmune circuits mediate homeostasis across the body.

#### 4.4.1 CNS Development, Synapses, and Cognition

Type 2 cytokines can impact brain physiology and behavior by modulating synaptic formation and neural circuit maturation both in development and in adulthood. Both the upstream initiator cytokine IL-33 and effector cytokines IL-4 and IL-13 have been implicated in these contexts, although they appear to have different functions and targets: IL-33 primarily signals to myeloid cells such as microglia to promote tissue remodeling, indirectly impacting synapse numbers, while IL-4/13 signal directly to neurons to mediate synaptic changes.

During postnatal development, IL-33 is expressed primarily by astrocytes, and deficiency of IL-33 (*Il33*<sup>-/-</sup> mice) or conditional deletion of its receptor in microglia and other myeloid cells (*Cx3cr1*<sup>creERT2</sup>;*Il1rl1*<sup>fl/fl</sup>) led to excess excitatory synapses in spinal cord and thalamus, as quantified by immunohistochemistry.<sup>110</sup> This resulted in lowered seizure thresholds as assessed via pentylenetetrazole (PTZ) challenge.<sup>138</sup> A parallel study found similar synaptic effects in the cortex, as well as increased susceptibility to kainic acid-induced seizures.<sup>139</sup> In both cases, conditional deletion experiments (using pan-myeloid *Cx3cr1*<sup>creER</sup>) suggest that IL-33 signaled directly to ST2 on microglia and myeloid cells.<sup>110,138,139</sup> Mechanistically, IL-33 signaling on microglia increased phagocytosis and promoted elimination of excitatory synapses, visualized using immunohistochemistry, in a manner that partly depended on expression of the pattern recognition receptors MARCO and TLR2.<sup>138,139</sup>

In the adult hippocampus, a key region for memory encoding, IL-33 was detected via a genetic reporter in neurons. In adulthood, loss of neuronal IL-33 or its receptor on microglia surprisingly led to fewer dendritic spines, a proxy for excitatory synapses,<sup>140</sup> whereas viral IL-33 delivery increased dendritic spines, consistent with another study.<sup>141</sup> These apparently contradictory results in development versus adulthood may reflect the role of IL-33 in promoting

microglial remodeling of the extracellular matrix (ECM), which has age-dependent impacts on synapses.<sup>140</sup> Regardless, in all of the above studies, the homeostatic role of IL-33 appears to act more like other IL-1 family members in promoting activation of myeloid cells, rather than its role in regulating downstream cytokines like IL-4/13, and thus may not fit into the classical model of type 2 allergic immunity.

In contrast to IL-33, IL-4 and IL-13 are the ultimate effector cytokines of type 2 immune responses. IL-4/13 may modulate synaptic development and cognition via a very different mechanism: by directly signaling to neurons that express their shared receptor, IL-4R $\alpha$ . Earlier studies reported that T cell-depleted and *Il4*<sup>-/-</sup> mice have deficits in learning and memory, which could be rescued by adoptive transfer of wild-type bone marrow or T cells.<sup>142</sup> These deficits were later phenocopied in *Il13*<sup>-/-</sup> and *Il4ra*<sup>-/-</sup> mice.<sup>143,144</sup> However, IL-4R $\alpha$  is widely expressed across brain regions and both neuronal and non-neuronal cells,<sup>92,145,146</sup> raising the question of which cell types are sensing these cytokines.

Several recent studies suggest that IL-4/13 signals directly to inhibitory interneurons. Interneurons are critical to brain function that act as the “regulatory T cells of the nervous system” by shutting down activating signals, thereby enhancing the most robust signals while suppressing noise.<sup>147</sup> Conditional deletion of IL-4R $\alpha$  in inhibitory neurons (via *Gad2*<sup>cre</sup>) phenocopied memory deficits (contextual fear memory) seen in T cell-deficient mice, implicating direct IL-4R $\alpha$  signaling to inhibitory neurons.<sup>148</sup> Studies of IL-4/13 signaling in the hippocampus, also point towards impacts on inhibitory neuron function. Using slice electrophysiology to acutely measure synaptic firing, deletion of *Il4ra* from all neurons (*Syn1*<sup>cre</sup>) but not excitatory neurons (*Camk2a*<sup>cre</sup>) led to reduced excitatory and inhibitory synapse frequency and alterations in overall excitability patterns. *Syn1*<sup>cre</sup>;*Il4ra*<sup>fl/fl</sup> mice also had fewer presynaptic vesicles (by electron microscopy), demonstrating that IL-4 or IL-13 can directly influence the release of neurotransmitters from neurons that mediate memory encoding. This study also showed that neuronal loss of IL-4R $\alpha$  led to deficits in anxiety-like behavior and contextual fear learning.<sup>145</sup> Application of IL-4 or IL-13 to cultured neurons

(typically a mixture of excitatory and inhibitory subtypes) acutely regulated protein phosphorylation, including neurotransmitter receptors,<sup>146,149</sup> and similar studies in human cultured neurons showed impacts on gene expression and synaptic firing.<sup>145</sup> Taken together, these studies strongly argue for a role of IL-4/13 signaling in directly modulating neuronal function.

Importantly, some of these impacts of IL-4/13 signaling on inhibitory neurons may be particularly critical during early development of the brain, when the innate immune system is predominant, and suggest that meningeal lymphocytes are an important source of IL-13. Using sensitive lineage reporters in mice, IL-13 was detected in ILC2s which populated the brain meninges over the first 15 days of life and produced IL-13 in an early postnatal wave (P5-15). Mice with an ILC2 deficiency (IL-5<sup>cre</sup>;R26<sup>DTA</sup>) or loss of inhibitory neuron-specific IL-4R $\alpha$  (Vgat<sup>Cre</sup>;Il4ra<sup>Flox</sup>) had reduced inhibitory synapse numbers in early life (P15-P30) and altered social behavior that persisted into adulthood despite a normalization of synapse numbers. These effects were not observed in mice with loss of IL-4R $\alpha$  in microglial and myeloid cells (Cx3cr1<sup>creERT2</sup>;Il4ra<sup>Flox</sup>).<sup>92</sup>

Despite these strongly concordant data, some areas of discrepancy remain. One important area has to do with the cellular sources of IL-4/13. Several studies suggest that lymphocytes are an important source, including T cells in adulthood<sup>142,148</sup> and ILC2 during development.<sup>92</sup> This raises the question of how these lymphocyte-derived signals are able to cross the blood brain barrier to access CNS neurons. Given emerging evidence that the blood-brain barrier (BBB) is a dynamic structure that can be selectively permeable<sup>150</sup> and the meningeal membranes contain pores that allow passage of small molecules across the blood-CSF barrier,<sup>151</sup> studies in the coming years may help to resolve this key point. Alternatively, groups have reported that IL-13 may be locally produced by neurons within the adult CNS and that postsynaptic neurons express its receptor IL-13R $\alpha$ 1,<sup>149</sup> although sensitive lineage reporters did not indicate any CNS sources of IL-13, at least in development.<sup>92</sup> Other studies have reported IL-4R $\alpha$  expression at presynaptic terminals in both mice and humans, using super resolution and electron

microscopy.<sup>145</sup> This would suggest the unexpected hypothesis that IL-13 signaling can act as a classical neurotransmitter, an idea that requires further investigation.

A more modest area of discrepancy relates to behavioral impacts: some studies observed impacts on contextual learning,<sup>145,148</sup> whereas others did not,<sup>152</sup> although behavioral outcomes can vary substantially due to differences in experimental design. Finally, IL-4 may signal to microglia in certain contexts, as it was reported that IL-4 inhibits microglial-dependent remodeling of granule cells in the cerebellum during postnatal development, resulting in hyperactive behaviors in mice that were dependent on direct IL-4 signaling in microglia (Cx3cr1<sup>creERT2</sup>;Il4ra<sup>Flox</sup>).<sup>153</sup> Taken together these studies strongly argue that type 2 cytokines signal impact synapse function and behavior, raising the question of how this signaling may be altered in the setting of type 2 challenges, like allergy, injury, and parasitic infection.

#### 4.4.2 CNS Injury

Type 2 immune responses modulate tissue repair and remodeling in peripheral tissues,<sup>134</sup> and the same is true in the CNS after damage. The alarmin IL-33 is widely expressed in the CNS, particularly in astrocytes and oligodendrocytes<sup>110,140</sup>, and is released after spinal cord injury (SCI).<sup>154</sup> Global deficiency of IL-33 or its receptor ST2 (*Il33*<sup>-/-</sup> or *Il1rl1*<sup>-/-</sup> mice) resulted in larger lesions and functional deficits in mice after SCI, ischemic stroke via the middle cerebral artery occlusion (MCAO) model, or traumatic brain injury (TBI) via the controlled cortical impact (CCI) model.<sup>154–156</sup> These works clearly demonstrate a role for IL-33 signaling after CNS injury; however, IL-33 is an IL-1 family member with well-described roles in direct modulation of microglia (and macrophage) function, including in development and aging.

Although IL-33 can signal directly to multiple immune cell types, ILC2s and subsets of 'type 2-like' tissue regulatory T cells (Tregs) express particularly high levels of IL-33R and the type 2 transcription factor GATA3, which themselves can coordinate downstream macrophage responses. Indeed, *Il33*<sup>-/-</sup> mice have reduced alternatively activated macrophages, defined by



Arg1 and CD206 expression, after SCI and stroke (MCAO),<sup>154,156</sup> while *Il33*<sup>-/-</sup> and *Il1rl1*<sup>-/-</sup> mice had fewer Tregs after stroke (MCAO) or TBI (CCI).<sup>155,157</sup> Adoptively transferred ST2-sufficient Tregs, but not ST2-deficient Tregs, survived in the brain and reduced astrogliosis after MCAO, suggesting direct IL-33 signaling in Tregs is important for their protective function after injury.<sup>157</sup> Meningeal and CNS-associated ILC2 also expand after spinal cord injury, stroke (MCAO), and intracerebral hemorrhage in mice.<sup>93,94,154</sup> Depletion of ILC using genetic (*Rag*<sup>-/-</sup>;*Il2rg*<sup>-/-</sup> mice) or antibody-mediated (anti-Thy1.2) approaches was associated with larger lesions after injury,<sup>93,94</sup> while adoptive transfer of ILC2 reduced lesion sizes.<sup>90</sup> Conversely, treatment with exogenous IL-33 increased Arg1+ macrophages<sup>158,159</sup> and ILC2s,<sup>93</sup> reduced lesion sizes, and improved functional outcomes following SCI and MCAO.<sup>94,155,158-160</sup> Together, these results suggest key roles for IL-33 signaling after CNS injury, acting at least in part via ILC2 and type 2-like Treg. Roles for CNS injury-associated IL-33 signaling on additional cell types, including mast cells, other lymphocytes (e.g., NK cells, CD8+ T cells), and microglia/macrophages, are likely but remain poorly defined.

With CNS injury, type 2 lymphocytes may also exert beneficial effects via multiple mechanisms, including IL-4 and IL-13: ILC2 upregulated IL-4 and IL-13 expression after stroke (MCAO) and SCI, respectively.<sup>90,94</sup> These type 2 effector cytokines have, in turn, been shown to impact CNS damage. *Il4*<sup>-/-</sup> mice had increased lesion sizes and worsened neurological scores after stroke (MCAO).<sup>161</sup> Treatment of mice with exogenous IL-13 decreased lesion size, rescued motor deficits, and increased Arg1+ macrophages after stroke (MCAO) or TBI.<sup>74,162-164</sup> Together, these data suggest that the IL-33/ST2 and IL-4/IL-13/IL-4R $\alpha$  axes are important for limiting the extent of damage after CNS injury, and these effects are mediated by ILC2, Treg, and/or alternatively activated microglia and macrophages. Future work is required to elucidate the precise cellular targets and mechanisms through which IL-33 and IL-4/13 mediate their functional impacts on CNS damage.

#### 4.4.3 Alzheimer's Disease and Aging

As human lifespan increased over the past century, rates of Alzheimer's Disease have also risen sharply, affecting one in nine individuals over the age of 65. Alzheimer's is the most common neurodegenerative disease and is characterized by progressive loss of memory and cognitive ability associated with the pathological accumulation of extracellular beta-amyloid plaques and subsequently tau fibrils within neurons.<sup>165</sup> Of note, most mouse models used to study Alzheimer's are pure models of amyloid deposition, as mice do not spontaneously develop tau fibrils. Nevertheless, given recent clinical studies showing modest benefit of anti-amyloid therapies in humans, these studies are likely to be relevant to human disease.

Type 2 immunity is implicated in both Alzheimer's and normal aging. ILC2 accumulated in the meninges and choroid plexus (CP) of aged mice,<sup>166</sup> and T cells in the CP acquired Th2 properties during aging, increasing their IL-4 and CCL11 expression while decreasing IFN $\gamma$  production.<sup>167</sup> ILC2 were reduced and functionally deficient in IL-5 production in the APP/PS1 model mouse model of amyloid pathology.<sup>168</sup> Treatment of AD-model or aged mice with type 2 cytokines may partly reverse amyloid pathology: Viral overexpression of IL-4 or injection of IL-4/IL-13 into the CNS reduced gliosis and amyloid-beta deposition in the APP/PS1 and APP23 mouse models, respectively, while improving spatial learning and memory (assessed via the Morris Water Maze).<sup>169,170</sup> Adoptive transfer of ILC2 or treatment with exogenous IL-33 or IL-5 rescued the cognitive function of aged mice and Alzheimer's mouse models, possibly by inhibiting pro-inflammatory CD8<sup>+</sup> T cells and their TNF $\alpha$  production and by promoting hippocampal neurogenesis.<sup>166,168</sup> These data suggest that cognitive decline associated with Alzheimer's and aging is, at least in part, driven by a reduction in type 2 cytokine signaling, in particular IL-4 and IL-5. Treatment with these cytokines may be a promising therapeutic intervention to ameliorate cognition in aged humans and those suffering from Alzheimer's.

IL-33 treatment may also improve cognition and memory in amyloid models, but this again appears to act like other IL-1 family cytokines by directly promoting the phagocytic function of

myeloid cells. IL-33 improved performance on a spatial memory task in APP/PS1 mice by reducing amyloid beta (A $\beta$ ) deposition and promoting its phagocytic clearance by microglia.<sup>122,123</sup> Levels of soluble ST2 (sST2), a splice variant and decoy receptor of ST2 that inhibits IL-33 signaling, are also correlated with AD severity: individuals that have the ApoE4 genotype that bear a genetic variant of an *IL1RL1* enhancer that reduces sST2 levels have a reduced AD risk, which was corroborated by mouse studies showing that sST2 levels modulate microglial phagocytosis and clearance of A $\beta$ .<sup>173</sup> Additional work is required to understand the mechanisms by which type 2 cytokines are reduced in aging and AD, the sources and targets of these signals, and the mechanism by which they promote learning and memory retention.

#### 4.4.4 Cytokine signaling in the periphery

Some of the biggest strides in peripheral neuroimmunology research have been in the skin, where signaling from type 2 cytokines and upstream alarmins were shown to regulate itch across various dermatitis models. For example, the pruritogenic cytokine IL-31, an upstream regulator of allergic phenotypes, has long been linked to itch associated with atopic dermatitis.<sup>174</sup> Th2 cells are one immune source of IL-31, with overexpression of *Il31* in T cells being sufficient to induce spontaneous itch and dermatitis in mice.<sup>175</sup> A subset of DRG neurons controls this itching behavior: IL-31 drives ERK1/2 phosphorylation and firing of IL-31R<sup>+</sup> sensory neurons that innervate the skin. These sensory neurons express the classic cation channels TRPV1 and TRPA1, and consequently *Trpv1*<sup>-/-</sup> or *Trpa1*<sup>-/-</sup> mice have significantly reduced IL-31-mediated itch.<sup>176</sup> Interestingly, despite reduced scratching, *Il31*<sup>-/-</sup> mice actually had higher numbers of IL-4/IL-13-producing Th2 cells, skin IL-4Ra<sup>+</sup> macrophages, and serum IgE during house dust mite (HDM)-induced allergic dermatitis. Instead, selective *Il31ra* ablation in sensory neurons (*Advillin*<sup>cre</sup>; *Il31ra*<sup>fl/fl</sup>) increased Th2 abundance upon HDM exposure.<sup>177</sup> These findings collectively suggest that IL-31 acts on skin sensory neurons not only to drive itch, but also to limit excessive type 2 inflammation during chronic dermatitis.

Older studies suggest that IL-33 and TSLP contribute to various models of itch and pain, although it is unclear whether these alarmins directly signal to neurons or indirectly via immune cells.<sup>178–180</sup> During allergic conjunctivitis, IL-33 recruited ST2<sup>+</sup> Th2 cells. Immunohistochemical staining revealed axonal elongation of neurons in the conjunctiva, a phenotype that has been associated with injury responses and can contribute to chronic hypersensitivity. Adoptive transfers of ovalbumin (OVA)-specific *Il1rl1*<sup>-/-</sup> Th2 cells resulted in fewer scratching bouts and less axonal elongation upon OVA treatment, suggesting that these T cells exacerbated itch via regulation of peripheral nerves in the tissue.<sup>181</sup> The role of IL-33 in immune infiltration also occurs within the PNS itself. In one study exploring the role of TLR2 in pain, treatment of mice with the TLR2 agonist FSL1 led to IL-33 expression in DRG satellite glial cells, as observed via immunofluorescence, resulting in increased macrophage infiltration. Interestingly, intraplantar FSL1 injection triggered IL-33 expression in the DRG. Thus, this study suggests that tissue inflammation could also activate immune responses along the cell bodies of neurons that innervate peripheral organs.<sup>182</sup>

The effector type 2 cytokines IL-4 and IL-13 may directly increase sensory neuron firing during allergic and parasitic responses in the skin. In murine models of atopic dermatitis, Nav1.8<sup>+</sup> sensory nociceptors in the DRG expressed type 2 cytokine receptors, such as IL-4R $\alpha$  and IL-13R $\alpha$ , and administration of IL-4 increased JAK1 phosphorylation and induced neuronal firing, as measured by *ex vivo* calcium imaging.<sup>183</sup> Patients with *JAK1* gain-of-function variants develop atopic dermatitis, yet they can also display systemic allergic phenotypes including asthma and eosinophilia.<sup>184</sup> Therefore, IL-4 signaling to sensory neurons could be relevant in other organs.

In the gut, where enteric infections can drive neuronal death, type 2 cytokines aid in neuroprotection via signaling to immune cells. During infection with the intestinal nematode *Strongyloides venezulensis*, eosinophil-derived IL-4 and IL-13 activated Arg1<sup>+</sup> muscularis macrophages. Mice lacking macrophages, via anti-CSF1R-mediated broad myeloid depletion, or lacking myeloid Arg1 (*Lyz2*<sup>Cre</sup>; *Arg1*<sup>fl/fl</sup>) mice, had fewer enteric neurons after infection. This suggests that IL-4/13 activated Arg1<sup>+</sup> macrophages may limit post-infection neuronal death long-

term, with mice protected from neuronal loss during subsequent infections.<sup>185</sup> It remains unclear whether enteric neurons may also directly respond to IL-4/IL-13 signaling, as in the case of skin sensory neurons.

It is possible that neurons innervating different tissues also differentially respond to type 2 cytokines. For example, unlike the skin, allergic inflammation in the lung may be dependent on JAK1 signaling downstream of other cytokines besides IL-4, as Nav1.8<sup>cre</sup>; Il4ra<sup>Flox</sup> mice displayed no differences to their wild-type counterparts during *Alternaria alternata*-induced allergy. Neuron-intrinsic JAK1 signaling is nevertheless required to regulate the lung allergic response, as Nav1.8<sup>cre</sup>; Jak1<sup>Flox</sup> mice experienced more severe inflammation during papain-induced allergy.<sup>186</sup> This finding suggests that a different signaling pathway is involved in activating neuronal JAK1 during allergic inflammation in the lung. Other JAK1-dependent cytokines, including IL-10 and IFN- $\gamma$ , could trigger sensory neurons in other inflammatory contexts.<sup>187</sup> Indeed, there is a large body of literature on how IFN- $\gamma$ , IL-17, and IL-10, among other cytokines, can shape peripheral neurons, with recent reviews on this topic.<sup>188</sup>

These seminal studies in cytokine-mediated neuroimmune crosstalk focus on cellular interactions within local tissue niches. However, akin to how tissue immune cells bring antigenic signals to lymph nodes, peripheral neurons ultimately relay information to the body's central control system—the brain. Therefore, a new frontier in neuroimmunology lies in uncovering how immune signals in the periphery are conveyed to the brain.

#### 4.5 NEURONAL AND IMMUNE REGULATION OF PHYSIOLOGY AND BEHAVIOR

**Interoception** is the ability of the brain to sense the body's autonomic functions, such as heart rate, respiration, and satiety. Research within the past five years suggests that the brain can also monitor and control the immune system, a concept termed '**immunoception**'.<sup>189–191</sup>

Recent studies have begun to define the brain circuitry that mediates sensing of peripheral immune status, although none of these have focused on Type 2 responses. For example, during

DSS colitis, neurons in the insular cortex (also termed “interoceptive” cortex) were activated, as determined by lineage “trapping” neurons that expressed the immediate early gene *Fos* (*Fos<sup>CreERT2</sup>*). Chemogenetic reactivation of these “trapped” neurons after resolution of inflammation was sufficient to induce IL-6<sup>+</sup> CD4<sup>+</sup> T cells, TNF- $\alpha$ <sup>+</sup> monocytes, and activated  $\gamma\delta$  T cells, partially recapitulating the inflammatory state in the colon that was observed initially during DSS treatment.<sup>192</sup> Afferent sensory neurons in the DRG/spinal cord and vagus nerve deliver sensory information to the brain, including information about inflammation. Vagal and DRG neurons express cytokine receptors and respond to TNF- $\alpha$  and IL-1 $\beta$ .<sup>193</sup> Various studies using murine models of peripheral viral and bacterial infections demonstrated how pro-inflammatory cytokines, including IL-1 $\beta$ , TNF- $\alpha$ , and interferons, trigger hypothalamic activation to induce sickness behavior, which in mice is characterized by reduced motor activity, appetite, and social interaction.<sup>194–198</sup> In a recent example, chemogenetic activation of TRPA1<sup>+</sup> vagal neurons prior to immune challenge, such as lethal LPS injection or intestinal *Salmonella* infection, instead dampened inflammation and increased bacterial dissemination, respectively. Such phenotypes may be potentially mediated by the heterogeneous response of vagal neurons to cytokines.<sup>199</sup> A detailed review on this topic can be found elsewhere.<sup>188</sup>

Unlike sickness behavior, type 2 immune responses may regulate a uniquely allergic response: avoidance of allergens and toxins. Two recent studies showed that exposure to food allergens activates IL-4 secretion and mast cells decorated with antigen-specific IgE in the gut. In parallel, food allergens induced activation of neurons in the brainstem and the amygdala, a brain region important for emotion processing, as measured by expression of the immediate early gene *Fos*. Mast cell-deficient (*Cpa3<sup>Cre</sup>*) mice and chimeric mice reconstituted with hematopoietic cells unable to bind IgE (*Fcer1<sup>-/-</sup>*) had decreased long-term avoidance behavior against the food allergen, suggesting that this behavioral response is in part mediated by mast cell/IgE immune responses.<sup>200,201</sup> Nevertheless, it remains unclear how mast cells and IgE are affecting behavior, as neuronal activation is a broad response that can be induced both directly and indirectly.

Deletion of TRPV1<sup>+</sup> sensory neurons via resiniferatoxin treatment or vagotomy did not rescue this response, suggesting either direct sensing by CNS neurons or a peripheral neuron subset that was not captured in these experiments.<sup>201</sup>

On the other hand, brainstem neurons can receive sensory input about respiratory allergens to control physiological and immune responses to allergy.<sup>202</sup> For example, silencing vagal neurons, in vagotomized, Nav1.8<sup>cre</sup>;DTA, or *Trpv1*-DTR mice, dampened brainstem activity, allergic inflammation, and airway hyperreactivity across various murine respiratory allergy models.<sup>202–204</sup> Specifically, one study used single nuclear RNA sequencing to identify a subset of norepinephrine-producing neurons, marked by *Dbh* expression, in the brainstem that were activated after house dust mite challenge. Viral tracing studies showed that *Dbh*<sup>+</sup> brainstem neurons synapsed on parasympathetic ganglia that innervate the trachea. Depletion of those brainstem neurons via targeted DTA mediated-ablation (via *Dbh*<sup>cre</sup>;DTR mice) dampened airway hyperreactivity after HDM challenge.<sup>202</sup>

A different brainstem region, the lateral parabrachial nucleus, also mediates a key feature of allergic anaphylaxis in mice: hypothermia. In a model of ovalbumin-induced IgE-mediated anaphylaxis, a study showed that mast cell-derived chymase, a protease, activated DRG TRPV1<sup>+</sup> neurons, as measured via calcium imaging. Activation of these sensory neurons correlated with increased *Fos* expression of neurons in the lateral parabrachial nucleus of the brainstem, a region associated with thermoregulation, and subsequently reduced heat generation in brown adipose tissue resulting in hypothermia.<sup>205</sup>

Collectively, these studies show that systemic allergic immune responses modulate neural activity in the brain and allergy-related behavioral and physiological responses, partly mediated by information transmitted from peripheral organs to the brain via the vagus nerve. However, it remains unclear why different allergic contexts induce different behavioral and physiological responses. Therefore, defining which cytokines are relevant in activating vagal and DRG neurons

across allergic contexts, and how these impact neural circuits in the brain, will be important areas for future study.

## 4.6 PERIPHERAL NEURON REGULATION OF TISSUE TYPE 2 IMMUNE RESPONSES

Peripheral nerves release two classes of signaling molecules. Classically, they release neurotransmitters and each individual neuron produces one type of neurotransmitter, which can induce sympathetic (norepinephrine), parasympathetic (acetylcholine), and other responses. These broad physiological categories can be further refined by the co-release of neuropeptides, a class of neurotransmitters made of peptides that can have longer lasting effects. A single neuron can produce different types of neuropeptides, allowing for more complex cell-to-cell signaling. This combinatorial feature of neuropeptide signaling can be conceptually framed as a unique ‘neuropeptide code’. Multiple recent studies have demonstrated that type 2 immune cells express receptors for both neurotransmitters and neuropeptides (**Figure 4.3**).

### 4.6.1 Neurotransmitters: Amplifying immune responses

The sympathetic nervous system mediates “fight or flight” responses via release of catecholamines (dopamine, norepinephrine, and epinephrine), and these same neurotransmitters may broadly suppress type 2 immunity. In contrast, “rest and digest” parasympathetic activation (via acetylcholine) may also promote type 2 reparative and allergic immune responses.

Several studies show that sympathetic activation suppresses ILC2 function. For example, in the lung, dopamine suppressed ILC2 responses by dampening cellular oxidative phosphorylation, and deletion of lung-innervating dopaminergic neurons via intranasal administration of the neurotoxin MPTP (1-methyl-4-phenyl-1,2,3,6-tetrahydropyridine) augmented allergic lung inflammation.<sup>206</sup> Similarly, genetic ablation of tyrosine hydroxylase (TH)-expressing sympathetic neurons by deleting their neurotrophin receptor ( $Th^{Cre}; TrkA^{fl/fl}$ ) led to IL-33-mediated type 2 innate responses upon LPS challenge.<sup>207</sup> Norepinephrine-secreting TH<sup>+</sup> neurons also



innervate adipose tissues, and viral tracing demonstrated that these neurons synapse to the hypothalamic paraventricular nucleus. In this setting, adrenergic neurons were shown by immunohistochemistry to be in close proximity to  $\beta$ 2-adrenergic receptor ( $\beta$ 2AR)-expressing mesenchymal cells. *In vitro* studies suggested that  $\beta$ 2AR agonists drove the secretion of glial-derived neurotrophic factor (GDNF) in these mesenchymal cells, which subsequently triggered ILC2s to release IL-5 and IL-13.<sup>208</sup> ILC2 themselves express  $\beta$ 2AR in the gut, where they colocalize with adrenergic neurons.  $\beta$ 2AR agonists *in vivo* inhibit ILC2 proliferation and effector function, and mice lacking adrenergic signaling in all lymphocytes (*Il7<sup>Cre</sup>;Adrb2<sup>fl/fl</sup>*) had enhanced type 2 inflammation in both gut and lung.<sup>209</sup> Other innate immune cells can express  $\beta$ 2AR: for example, in the gut,  $\beta$ 2AR<sup>+</sup> muscularis macrophages protect enteric neurons from bacterial infection-induced death.<sup>185,210</sup> Overall, this suggests that catecholamines across various tissues dampen type 2 inflammation.

In contrast, acetylcholine, the major neurotransmitter of the parasympathetic nervous system, induces type 2 immune responses. Interestingly, in several settings of type 2 activation, immune cells themselves may contribute to acetylcholine production. Many immune cells express choline acetyltransferase (ChAT), the enzyme catalyzing the rate-limiting step of acetylcholine production. During helminth infection, ILC2 in the lung, gut, and mesenteric lymph nodes produced acetylcholine upon activation by IL-25 and IL-33.<sup>211,212</sup> ILC2 also expressed the acetylcholine receptor (AChR), thus creating an autocrine signaling loop.<sup>212</sup> Accordingly, *Rora<sup>Cre</sup>;Chat<sup>fl/fl</sup>* mice have impaired ILC2 proliferation and activation, resulting in fewer epithelial tuft cells, decreased mucin expression, and impaired helminth expulsion.<sup>211</sup> Both CD4<sup>+</sup> and CD8<sup>+</sup> T cells can express ChAT and secrete acetylcholine.<sup>213</sup> Nevertheless, T cells also respond to acetylcholine signaling in other contexts. During acute pain, glutamatergic neurons from the somatosensory cortex synapse on parasympathetic cholinergic neurons in the vagus nerve that innervate the spleen which subsequently increase splenic Th2 cells. Chronic pain has the opposite effect: GABAergic neurons of the amygdala, identified via a combination of retrograde

viral tracing and GABA immunolabeling, inhibit this same circuit which decreases splenic Th2.<sup>214</sup> These findings indicate that acetylcholine plays a critical role in amplifying type 2 immunity in both an autocrine and neuroimmune paracrine manner.

#### 4.6.2 A neuropeptide code for immune cell modulation

Calcitonin gene-related peptide (CGRP, encoded by *Calca*), a potent vasodilator and modulator of the autonomic nervous system, generally dampens type 2 immunity, although the exact signaling mechanisms may be more complex and context-dependent. As with other neurotransmitters in the PNS, CGRP can be made by both neural and immune cells, and possibly other cell types like pulmonary neuroendocrine cells (PNECs).<sup>181,215,216</sup> In response to IL-33 or helminth infection in the lung, ILC2-derived CGRP acts in an autocrine fashion, dampening ILC2 activation independent of adaptive immunity.<sup>215,217</sup> Neural sources of CGRP can act on ILC2 as well. For example, lung sensory neurons secrete CGRP upon JAK1 activation, resulting in ILC2 suppression and reduced allergic airway inflammation.<sup>218</sup> In contrast, one study reports that CGRP activates and stimulating IL-5 expression of ILC2 *in vitro* and demonstrated via imaging and genetic depletion models that pulmonary neuroendocrine cells (PNEC), a rare epithelial cell type residing at airway branch points, release CGRP and amplified allergic asthma responses.<sup>216</sup> The spatiotemporal dynamics of PNEC-ILC2 crosstalk at the airways may play a role in this amplification loop. In other mucosal organs such as skin and gut, CGRP from sensory nociceptors, enteric neurons, ILC2, and Th2 cells all polarize macrophages towards repair phenotypes, drive mucus production by goblet cells, dampen the immune response against food allergens, dampen type 2 immune recruitment, and attenuate scratching behavior, respectively.<sup>181,219–221</sup>

Whereas CGRP tends to dampen type 2 immunity and may act on multiple flavors of immune response, neuromedin U (NMU) activates ILC2, tissue Th2, and eosinophils, which specifically express the NMU receptor (NMUR1).<sup>222,223</sup> Accordingly, NMU was shown to activate

eosinophils to promote goblet cell differentiation, as eosinophil-specific *Epx<sup>cre</sup>;Nmur1<sup>fl/fl</sup>* mice had fewer small intestinal goblet cells and eosinophils as well as less eosinophil degranulation as observed by electron microscopy.<sup>222,223</sup> Neuron-derived NMU increased during intestinal helminth and protist infection, thereby promoting amphiregulin expression in neighboring IL-25-stimulated ILC2s that further drove eosinophilia and was critical for worm expulsion.<sup>222,224–226</sup> Accordingly, NMUR1 deficiency in eosinophils ultimately resulted in delayed clearance of the intestinal helminth *Nippostrongylus brasiliensis*.<sup>222</sup> In the lung, asthmatic patients displayed increased sputum NMUR1<sup>+</sup> ILC2, suggesting that a similar mechanism to the gut is likely at play.<sup>227</sup> On the other hand, neuromedin B (NMB), a neuropeptide of the same neuromedin family, instead limits the type 2 response during helminth infection. The same study showed that basophils promoted NMB receptor expression in ILC2s, resulting in ILC2 suppression upon NMB exposure.<sup>228</sup> This implies that different neuromedin peptides may be working in conjunction to fine-tune type 2 inflammation at various stages of the immune response. Defining which neurons secrete neuromedins may help to elucidate this highly type 2 specific component of the neuropeptide code.

Finally, other neuropeptides have been shown to modulate the immune response between type 2, type 17, and immunoregulatory phenotypes. For example, Substance P (SP), typically secreted by nociceptors, drives IgE secretion of B cells, amplifies the airway Th2 response, and trigger mast cell degranulation across lung and skin allergy and pain models, respectively.<sup>229–233</sup> On the other hand, a sunburn UV-mediated model of skin damage triggers nociceptor secretion of TFAA4, which instead promotes IL-10 production in dermis-resident macrophages.<sup>234,235</sup> Vasoactive intestinal peptide (VIP), secreted by enteric neurons during feeding, activates neighboring ILC2s as well as ILC3s. Co-signaling with IL-33 or IL-22 further skews ILC activation towards IL-5-secreting ILC2 versus IL-22-producing ILC3, respectively.<sup>236</sup> This observation highlights the fact that many of these neuropeptides work synergistically with local cytokine signaling to amplify the appropriate immune responses during an immune challenge.

Despite recent advances in identifying the neural chemical messengers involved in shaping the immune system, a major outstanding question is which neuronal subsets are producing the relevant neuropeptides. Another important avenue for future study is determining how the neuropeptide code interfaces with cytokine signaling within tissue niches across different allergic contexts to coordinate the immune response over the course of an allergy response. Collectively, unveiling these signaling mechanisms can unlock new therapeutic opportunities for the treatment of autoimmune and neurodegenerative diseases.

#### **4.7 FUTURE DIRECTIONS AND THERAPEUTIC OPPORTUNITIES**

Suppression of type 2 immune responses shows therapeutic benefit for the treatment of allergic diseases, which may act in part via suppressing cytokine signaling in neurons. Targeting of the IL-4/JAK1 signaling axis observed in skin-innervating neurons during chronic itch is a prime success story of neuroimmune therapy. JAK inhibition is now used to treat human patients with chronic idiopathic pruritus (CIP), atopic dermatitis, psoriasis, and other itching diseases and reduce their itching behavior.<sup>183,237</sup> The biologic dupilumab, a human anti-IL-4R $\alpha$  antibody, targets the IL-4/IL-13/IL-4R $\alpha$  axis and may also reduce IL-4/13 signaling in neurons and itch responses. Dupilumab has been approved by the FDA to treat atopic dermatitis and asthma, and is in clinical trials to treat chronic rhinosinusitis with nasal polyps, eosinophilic esophagitis, and allergies.<sup>238</sup> By targeting detrimental neuroimmune axes that go awry during chronic inflammation, we may be able to ameliorate the symptoms and pathology of many type 2-mediated diseases in humans.

Conversely, where type 2 cytokines can boost beneficial functions of distinct cell types, treatment with exogenous type 2 activation may be a promising therapeutic avenue. Treatment with IL-33 promotes the activity of anti-inflammatory ST2<sup>+</sup> Tregs, as well as the phagocytic function of microglia and other myeloid cells, which have both been shown to be beneficial in mouse models of brain injury and AD.<sup>155–158,171,172</sup> Treatment with IL-4/13 has also been shown to ameliorate outcomes after models of CNS damage and AD in mice, potentially via inhibition of

pathologic cytotoxic responses or augmentation of alternatively activated myeloid cells.<sup>74,163,163,164,168</sup> IL-5 treatment has also shown promise for improving cognition of aged mice.<sup>166</sup> While these cytokine treatments experiments have so far been limited to preclinical studies in mice, local overexpression of these cytokines within diseased tissues (possibly via AAVs or local injections) remains a promising potential therapeutic route for the treatment of many CNS injuries and disease states. Moreover, the treatment with neuropeptides (such as NMU) alone or in combination with type 2 cytokines may provide additional specificity to therapeutic responses.

While substantial advances have been made at this type 2 neuroimmune interface, several critical open questions remain. Given that type 2 cytokines can impact synapse maturation and behavior, does exposure to allergies, parasites, and toxins, particularly during critical postnatal development periods, impact brain development and function? If the nervous system is truly necessary for behavioral responses to type 2 challenges, can we modulate the nervous system to prophylactically promote avoidance to allergies or parasitic infections? In addition, the precise anatomical and biochemical mechanisms underlying cytokine signaling in neurons remain unclear. Defining these mechanisms will require deciphering how lymphocyte-derived cytokines gain access to the highly protected brain parenchyma, especially under homeostasis. While recent work has identified small pores in the arachnoid membrane (termed arachnoid cuff exits) that could allow trafficking of cytokines or cells from the dural meninges or periphery into the brain,<sup>151</sup> it is still unclear how specific neuronal subsets in specific regions are exposed to these cytokines. Lastly, neuronal populations across the CNS and PNS respond differently to cytokines. Characterizing the cytokine map of the nervous system and functionally assessing how cytokines alter neuronal firing, as well as the function of supporting cells like astrocytes, oligodendrocytes, microglia, fibroblasts, and endothelial cells, may also be key to better understanding the mechanisms regulating cytokine signaling to neurons.

## 4.8 FIGURES

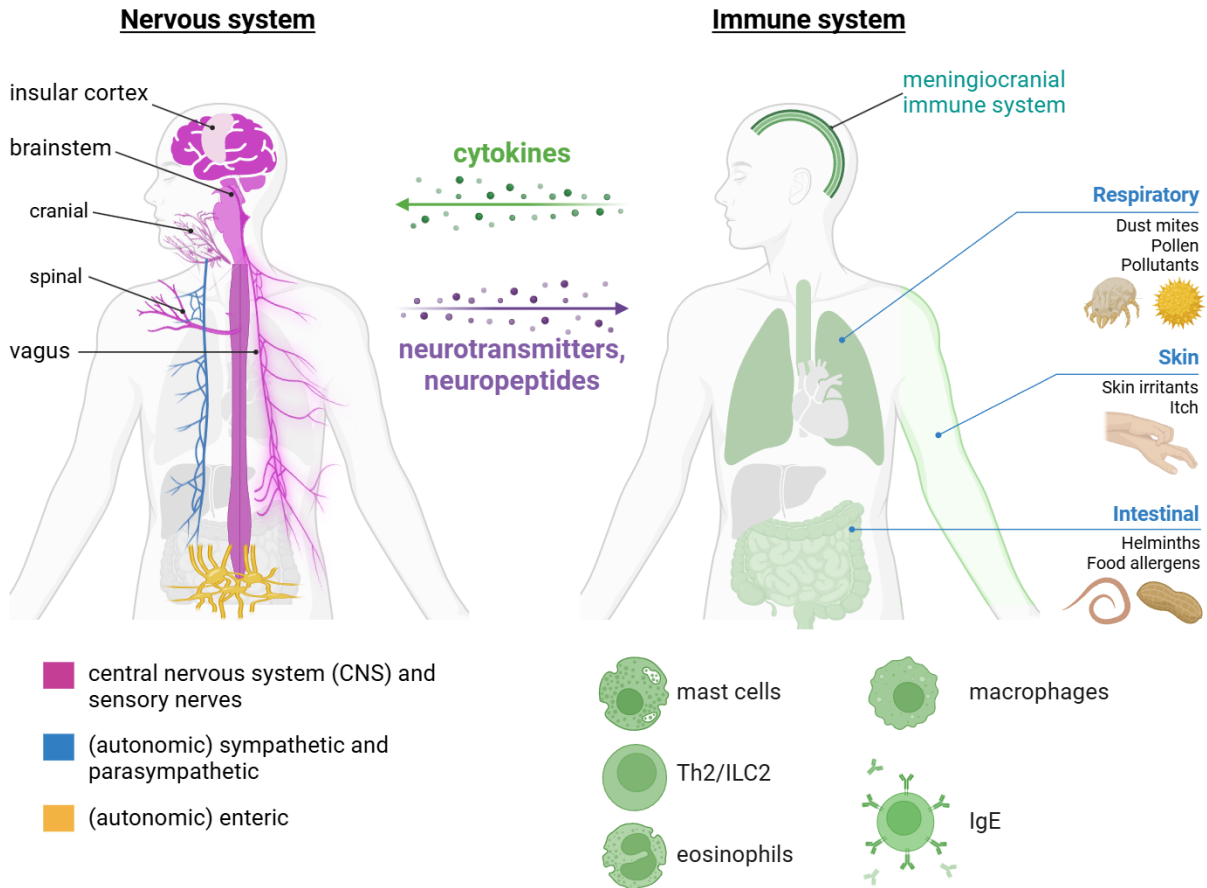


**Figure 4.1: Interactions between the nervous system and type 2 immunity occur across multiple organs depending on the context of allergic triggers or injury.** The nervous system is comprised of the central nervous system and associated sensory nerves (**purple**) and the autonomic nervous system, which includes sympathetic and parasympathetic nerves (**navy**) and the enteric nervous system (**yellow**). The immune system includes cells that span the entire body. Repeated exposure to allergens (**blue**) at mucosal sites (for example lung, skin, gut; **green**) can trigger local type 2 immunity. Type 2 immune cells signal to neurons across the periphery and brain through cytokines, while neurons signal to immune cells via neurotransmitters and neuropeptides.

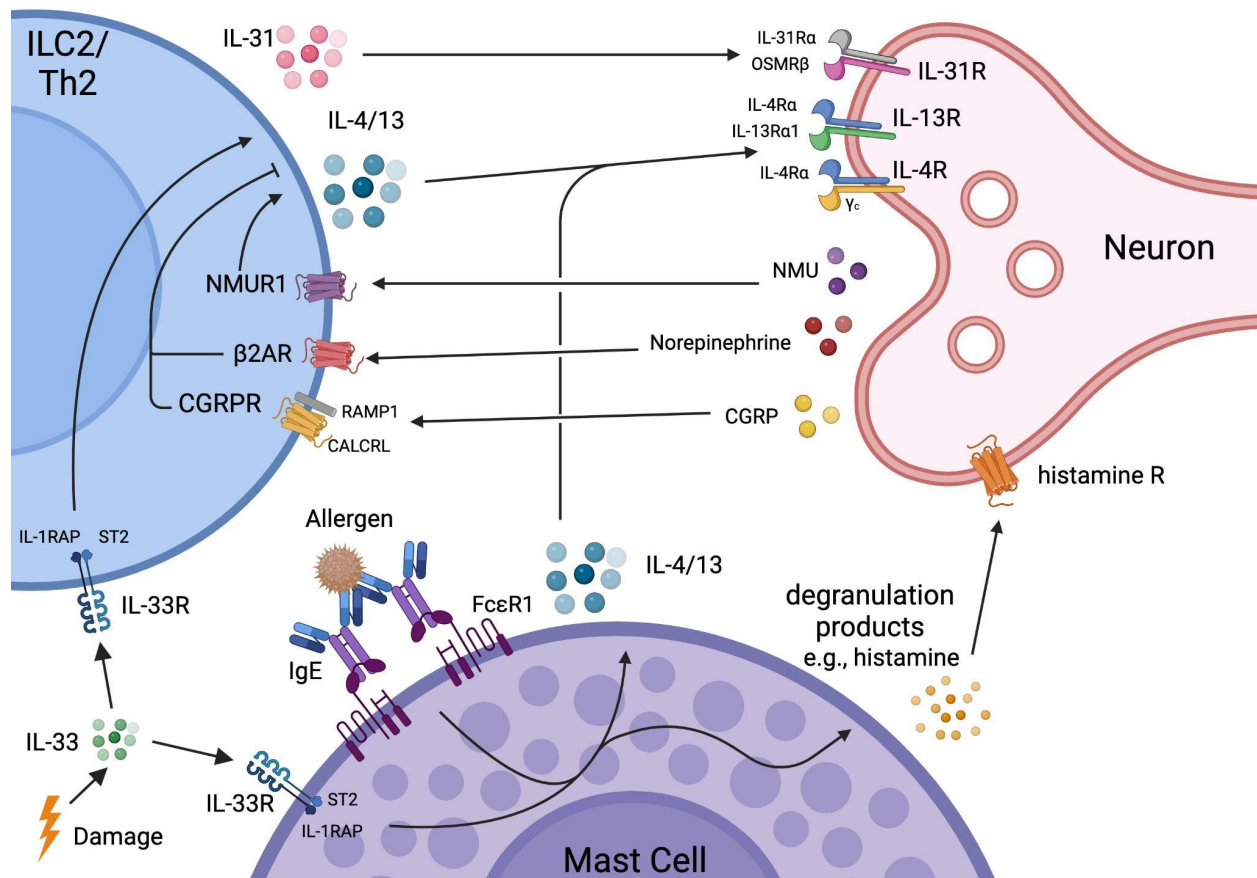


**Figure 4.2: Molecular mechanisms of type 2 neuroimmune crosstalk.** ILC2s/Th2s, mast cells, and neurons all communicate with each other during a type 2 immune response. IL-33, released by tissue damage, activates both ILC2s/Th2s and mast cells, which both can produce IL-4/13. IL-4/13 can in turn signal to neurons. IL-31, which can be produced by Th2s, can trigger neuronal firing and itch responses. Neurons can modulate ILC2/Th2 responses via neurotransmitters and neuropeptides, such as NMU, norepinephrine, and CGRP. Mast cell degranulation products, such as histamine, can also modulate neuronal responses.

## Chapter 5: Closing and Future Directions

In this dissertation, we explore the role of lymphocytes in shaping the recovery process from brain injury. In Chapter 2, we identified IFN $\gamma$ -producing type 1 lymphocytes as a population that can modulate seizure susceptibility following TBI and determined that IFN $\gamma$  has therapeutic potential to restrict post-traumatic epilepsy. In Chapter 3, we determined that ILC2s have minimal impacts on recovery from the photothrombotic model of ischemic stroke, although they are activated and may locally regulate cortical inhibitory synapses. We also delineated the kinetics and ontogeny of brain- and meninges-infiltrating myeloid cells and revealed that classical monocytes contribute to the emergence of alternatively activated macrophages in the brain after PT damage. In Chapter 4, we explored the various mechanisms through which the nervous system and type 2 immunity interact, including how type 2 immune cells shape the nervous system during development and disease, how information about peripheral type 2 immune challenges is relayed to the brain, and how peripheral nerves locally fine tune the activity of type 2 lymphocytes. Together, this work advances our knowledge of neuroimmune interactions, particularly after brain injury, and reveals which lymphocyte populations perform functions relevant for recovery after CNS damage. In doing so, we highlight key pathways that can be harnessed for the treatment of brain damage and their related morbidities in human patients.

Several open questions for future investigation remain. It will be crucial to fully elucidate the mechanism of IFN $\gamma$ 's anti-seizure properties following TBI. Is this rapid effect mediated by direct signaling to neurons? If so, does IFN $\gamma$  signaling in neurons cause canonical STAT1-dependent transcriptional changes, or are these effects mediated by post-translational modifications and/or changes in GABA receptor abundance that mediate local enhanced inhibition? Do microglia play a role in this process by responding to IFN $\gamma$  and increasing DAM and phagocytosis related gene expression? Or, is IFN $\gamma$  signaling required in both cell types to mediate this effect? In what regions of the thalamus is this IFN $\gamma$  signaling required to inhibit seizure



progression? Cell type specific conditional deletion of the IFN $\gamma$  receptor will aid in answering these questions. Further, what dosages of IFN $\gamma$  are required for this effect, and during what timeframe after TBI does IFN $\gamma$  treatment show the most efficacy? Answering these questions will be crucial to assist in better designing therapies that can dose IFN $\gamma$  for maximal therapeutic effect and/or target and overexpress IFN $\gamma$  in the relevant cell types and thalamic regions of interest.

Additionally, further work is required to precisely define the mechanism by which anti-CD4 treatment rescues seizure susceptibility following TBI. Is priming in peripheral secondary lymphoid organs required, and what role to peripheral T<sub>regs</sub> play in this process? Given the reciprocal increase in non-CD4 type 1 lymphocytes seen with anti-CD4 treatment, does depletion of NK cells and CD8+ T cells make seizures more severe after TBI? Future research should test these hypotheses.

Additional questions remain about the mode of entry and trafficking of T cells into the brain after TBI. Given the delayed kinetics of thalamic infiltration, do T cells traffic from the cortex to the ipsilateral thalamus (perhaps via the same axonal tracts through which damage propagates), or do T cells enter the thalamus locally from circulation? What signals are recruiting the T cells to these areas, and who is producing them? Are these T cells clonal populations that have been primed against CNS autoantigens released into the periphery after injury, or are they memory cells that were recruited to sites of inflammation in an antigen-independent manner? How long do these T cells reside within the thalamus, and what cells are sustaining them? Future studies should characterize the thalamic T cell niche and the mechanisms through which these T cells are recruited and sustained in the CNS.

Given that ILC2s mechanistically link together the type 2 cytokines IL-33 and IL-13 that have been shown to promote endogenous wound healing responses to brain and spinal cord injuries, it remains an appealing hypothesis that ILC2s in the adjacent meninges have a role in this process, even though our data largely did not support this model using PT injury. The role of

ILC2s should be assessed in more severe and physiologically relevant models of CNS damage, including tMCAO and TBI, where their function may be more significant. Experimental approaches that are more agnostic to upstream activating cues (i.e., not IL-33-dependent) may be particularly useful in elucidating any true roles of ILC2s after injury.

## REFERENCES

1. Jassam, Y. N., Izzy, S., Whalen, M., McGavern, D. B. & El Khoury, J. Neuroimmunology of Traumatic Brain Injury: Time for a Paradigm Shift. *Neuron* **95**, 1246–1265 (2017).
2. Roozenbeek, B., Maas, A. I. R. & Menon, D. K. Changing patterns in the epidemiology of traumatic brain injury. *Nat. Rev. Neurol.* **9**, 231–236 (2013).
3. Gao, W. *et al.* Engineered T cell therapy for central nervous system injury. *Nature* **634**, 693–701 (2024).
4. Vivier, E. *et al.* Innate Lymphoid Cells: 10 Years On. *Cell* **174**, 1054–1066 (2018).
5. Annunziato, F., Romagnani, C. & Romagnani, S. The 3 major types of innate and adaptive cell-mediated effector immunity. *J. Allergy Clin. Immunol.* **135**, 626–635 (2015).
6. Molofsky, A. B. & Locksley, R. M. The ins and outs of innate and adaptive type 2 immunity. *Immunity* **56**, 704–722 (2023).
7. Dewan, M. C. *et al.* Estimating the global incidence of traumatic brain injury. *J. Neurosurg.* **130**, 1080–1097 (2019).
8. Nguyen, R. *et al.* The International Incidence of Traumatic Brain Injury: A Systematic Review and Meta-Analysis. *Can. J. Neurol. Sci.* **43**, 774–785 (2016).
9. Pease, M. *et al.* Insights into epileptogenesis from post-traumatic epilepsy. *Nat. Rev. Neurol.* **20**, 298–312 (2024).
10. Paz, J. T. & Huguenard, J. R. Microcircuits and their interactions in epilepsy: is the focus out of focus? *Nat. Neurosci.* **18**, 351–359 (2015).
11. Grossman, E. J. & Inglese, M. The Role of Thalamic Damage in Mild Traumatic Brain Injury. *J. Neurotrauma* **33**, 163–167 (2016).
12. Steriade, M. Sleep, epilepsy and thalamic reticular inhibitory neurons. *Trends Neurosci.* **28**, 317–324 (2005).

13. Lindquist, B. E., Timbie, C., Voskobiynyk, Y. & Paz, J. T. Thalamocortical circuits in generalized epilepsy: Pathophysiologic mechanisms and therapeutic targets. *Neurobiol. Dis.* **181**, 106094 (2023).
14. Briggs, F. & Usrey, W. M. Emerging views of corticothalamic function. *Curr. Opin. Neurobiol.* **18**, 403–407 (2008).
15. Ross, D. T. & Ebner, F. F. Thalamic retrograde degeneration following cortical injury: An excitotoxic process? *Neuroscience* **35**, 525–550 (1990).
16. Scott, G. *et al.* Thalamic inflammation after brain trauma is associated with thalamo-cortical white matter damage. *J. Neuroinflammation* **12**, 224 (2015).
17. Holden, S. S. *et al.* Complement factor C1q mediates sleep spindle loss and epileptic spikes after mild brain injury. *Science* **373**, (2021).
18. Urban, S. L. *et al.* Peripherally induced brain tissue–resident memory CD8<sup>+</sup> T cells mediate protection against CNS infection. *Nat. Immunol.* **21**, (2020).
19. Steinbach, K. *et al.* Brain-resident memory T cells represent an autonomous cytotoxic barrier to viral infection. *J. Exp. Med.* **213**, 1571–1587 (2016).
20. Balint, E. *et al.* Bystander activated CD8<sup>+</sup> T cells mediate neuropathology during viral infection via antigen-independent cytotoxicity. *Nat. Commun.* **15**, 896 (2024).
21. Frieser, D. *et al.* Tissue-resident CD8<sup>+</sup> T cells drive compartmentalized and chronic autoimmune damage against CNS neurons. *Sci. Transl. Med.* **14**, eabl6157 (2022).
22. Vincenti, I. *et al.* Tissue-resident memory CD8<sup>+</sup> T cells cooperate with CD4<sup>+</sup> T cells to drive compartmentalized immunopathology in the CNS. *Sci. Transl. Med.* **14**, eabl6058 (2022).
23. Chen, D. *et al.* CTLA-4 blockade induces a microglia-Th1 cell partnership that stimulates microglia phagocytosis and anti-tumor function in glioblastoma. *Immunity* **56**, 2086–2104.e8 (2023).
24. Kaya, T. *et al.* CD8<sup>+</sup> T cells induce interferon-responsive oligodendrocytes and microglia in white matter aging. *Nat. Neurosci.* **25**, 1446–1457 (2022).

25. Shi, Z. *et al.* Microglia drive transient insult-induced brain injury by chemotactic recruitment of CD8+ T lymphocytes. *Neuron* **111**, 696-710.e9 (2023).
26. Ewing-Crystal, N. A. *et al.* Dynamic fibroblast-immune interactions shape wound healing after brain injury. *bioRxiv* 2024.03.13.584873 (2024) doi:10.1101/2024.03.13.584873.
27. Smolders, J. *et al.* Tissue-resident memory T cells populate the human brain. *Nat. Commun.* **9**, 1–14 (2018).
28. Gate, D. *et al.* Clonally expanded CD8 T cells patrol the cerebrospinal fluid in Alzheimer's disease. *Nature* **577**, 399–404 (2020).
29. Pasciuto, E. *et al.* Article Microglia Require CD4 T Cells to Complete the Fetal- to-Adult Transition Microglia Require CD4 T Cells to Complete the Fetal-to-Adult Transition. *Cell* 1–16 (2020) doi:10.1016/j.cell.2020.06.026.
30. Kallies, A. & Good-Jacobson, K. L. Transcription Factor T-bet Orchestrates Lineage Development and Function in the Immune System. *Trends Immunol.* **38**, 287–297 (2017).
31. Zhu, J. *et al.* The Transcription Factor T-bet Is Induced by Multiple Pathways and Prevents an Endogenous Th2 Cell Program during Th1 Cell Responses. *Immunity* **37**, 660–673 (2012).
32. Cho, F. S. *et al.* Enhancing GAT-3 in thalamic astrocytes promotes resilience to brain injury in rodents. *Sci. Transl. Med.* **14**, eabj4310 (2022).
33. Van Erum, J., Van Dam, D. & De Deyn, P. P. PTZ-induced seizures in mice require a revised Racine scale. *Epilepsy Behav.* **95**, 51–55 (2019).
34. Keren-Shaul, H. *et al.* A Unique Microglia Type Associated with Restricting Development of Alzheimer's Disease. *Cell* **169**, 1276-1290.e17 (2017).
35. Escoubas, C. C. *et al.* Type-I-interferon-responsive microglia shape cortical development and behavior. *Cell* **187**, 1936-1954.e24 (2024).

36. de Koning, H. D. *et al.* A comprehensive analysis of pattern recognition receptors in normal and inflamed human epidermis: upregulation of dectin-1 in psoriasis. *J. Invest. Dermatol.* **130**, 2611–2620 (2010).
37. Mata-Martínez, P., Bergón-Gutiérrez, M. & del Fresno, C. Dectin-1 Signaling Update: New Perspectives for Trained Immunity. *Front. Immunol.* **13**, (2022).
38. Korn, T. & Kallies, A. T cell responses in the central nervous system. *Nat. Rev. Immunol.* **17**, 179–194 (2017).
39. Su, W. *et al.* CXCR6 orchestrates brain CD8<sup>+</sup> T cell residency and limits mouse Alzheimer's disease pathology. *Nat. Immunol.* **24**, 1735–1747 (2023).
40. Rosen, S. F. *et al.* Single-cell RNA transcriptome analysis of CNS immune cells reveals CXCL16/CXCR6 as maintenance factors for tissue-resident T cells that drive synapse elimination. *Genome Med.* **14**, 108 (2022).
41. Cupovic, J. *et al.* Central Nervous System Stromal Cells Control Local CD8<sup>+</sup> T Cell Responses during Virus-Induced Neuroinflammation. *Immunity* **44**, 622–633 (2016).
42. Deczkowska, A. *et al.* Disease-Associated Microglia: A Universal Immune Sensor of Neurodegeneration. *Cell* **173**, 1073–1081 (2018).
43. Zheng, Z. *et al.* The effect of dipeptidyl peptidase IV on disease-associated microglia phenotypic transformation in epilepsy. *J. Neuroinflammation* **18**, (2021).
44. Garofalo, S. *et al.* Natural killer cells and innate lymphoid cells 1 tune anxiety-like behavior and memory in mice via interferon- $\gamma$  and acetylcholine. *Nat. Commun.* 2023 141 **14**, 1–15 (2023).
45. Filiano, A. J. *et al.* Unexpected role of interferon- $\gamma$  3 in regulating neuronal connectivity and social behaviour. *Nature* **535**, 425–429 (2016).
46. Janach, G. M. S. *et al.* Interferon- $\gamma$  enhances neocortical synaptic inhibition by promoting membrane association and phosphorylation of GABAA receptors in a protein kinase C-dependent manner. *Brain. Behav. Immun.* **101**, 153–164 (2022).

47. Janach, G. M. S. *et al.* Interferon- $\gamma$  acutely augments inhibition of neocortical layer 5 pyramidal neurons. *J. Neuroinflammation* **17**, 1–12 (2020).
48. Flood, L., Korol, S. V., Ekselius, L., Birnir, B. & Jin, Z. Interferon- $\gamma$  potentiates GABA<sub>A</sub> receptor-mediated inhibitory currents in rat hippocampal CA1 pyramidal neurons. *J. Neuroimmunol.* **337**, 577050 (2019).
49. Clark, D. N., Begg, L. R. & Filiano, A. J. Unique aspects of IFN - $\gamma$ / STAT1 signaling in neurons. *Immunol. Rev.* **311**, 187–204 (2022).
50. Mizuno, T. *et al.* Interferon-gamma directly induces neurotoxicity through a neuron specific, calcium-permeable complex of IFN-gamma receptor and AMPA GluR1 receptor. *FASEB J. Off. Publ. Fed. Am. Soc. Exp. Biol.* **22**, 1797–1806 (2008).
51. Vikman, K., Robertson, B., Grant, G., Liljeborg, A. & Kristensson, K. Interferon-gamma receptors are expressed at synapses in the rat superficial dorsal horn and lateral spinal nucleus. *J. Neurocytol.* **27**, 749–759 (1998).
52. Roy, E. R. *et al.* Concerted type I interferon signaling in microglia and neural cells promotes memory impairment associated with amyloid  $\beta$  plaques. *Immunity* **55**, 879-894.e6 (2022).
53. Zhao, Y. *et al.* STAT1 Contributes to Microglial/Macrophage Inflammation and Neurological Dysfunction in a Mouse Model of Traumatic Brain Injury. *J. Neurosci. Off. J. Soc. Neurosci.* **42**, 7466–7481 (2022).
54. Di Liberto, G. *et al.* Neurons under T Cell Attack Coordinate Phagocyte-Mediated Synaptic Stripping. *Cell* **175**, 458-471.e19 (2018).
55. Roberson, E. D. *et al.* Reducing endogenous tau ameliorates amyloid beta-induced deficits in an Alzheimer's disease mouse model. *Science* **316**, 750–754 (2007).
56. Galatro, T. F., Vainchtein, I. D., Brouwer, N., Boddeke, E. W. G. M. & Eggen, B. J. L. Isolation of microglia and immune infiltrates from mouse and primate central nervous system. in *Methods in Molecular Biology* (2017). doi:10.1007/978-1-4939-6786-5\_23.

57. Dahlgren, M. W. *et al.* Adventitial Stromal Cells Define Group 2 Innate Lymphoid Cell Tissue Niches. *Immunity* **50**, 707-722.e6 (2019).
58. Cautivo, K. M. *et al.* Interferon gamma constrains type 2 lymphocyte niche boundaries during mixed inflammation. *Immunity* **55**, 254-271.e7 (2022).
59. Dobin, A. *et al.* STAR: Ultrafast universal RNA-seq aligner. *Bioinformatics* (2013) doi:10.1093/bioinformatics/bts635.
60. Wu, T. *et al.* clusterProfiler 4.0: A universal enrichment tool for interpreting omics data. *Innov. Camb. Mass* **2**, 100141 (2021).
61. Anders, S., Pyl, P. T. & Huber, W. HTSeq—a Python framework to work with high-throughput sequencing data. *Bioinformatics* **31**, 166–169 (2015).
62. Love, M. I., Huber, W. & Anders, S. Moderated estimation of fold change and dispersion for RNA-seq data with DESeq2. *Genome Biol.* **15**, 550 (2014).
63. Jayaraj, R. L., Azimullah, S., Beiram, R., Jalal, F. Y. & Rosenberg, G. A. Neuroinflammation: Friend and foe for ischemic stroke. *J. Neuroinflammation* **16**, 1–24 (2019).
64. Anrather, J. & Iadecola, C. Inflammation and Stroke: An Overview. *Neurotherapeutics* **13**, 661–670 (2016).
65. Qin, C. *et al.* Dual Functions of Microglia in Ischemic Stroke. *Neurosci. Bull.* **35**, 921–933 (2019).
66. Gadani, S. P., Walsh, J. T., Smirnov, I., Zheng, J. & Kipnis, J. The Glia-Derived Alarmin IL-33 Orchestrates the Immune Response and Promotes Recovery following CNS Injury. *Neuron* **85**, 703–709 (2015).
67. Zhang, S. R. *et al.* IL-33 modulates inflammatory brain injury but exacerbates systemic immunosuppression following ischemic stroke. *JCI Insight* **3**, (2018).
68. Korhonen, P. *et al.* Immunomodulation by interleukin-33 is protective in stroke through modulation of inflammation. *Brain. Behav. Immun.* **49**, 322–336 (2015).



69. Pomeschchik, Y. *et al.* Interleukin-33 treatment reduces secondary injury and improves functional recovery after contusion spinal cord injury. *Brain. Behav. Immun.* **44**, 68–81 (2015).
70. Miao, W. *et al.* IL-13 Ameliorates Neuroinflammation and Promotes Functional Recovery after Traumatic Brain Injury. *J. Immunol.* **204**, 1486–1498 (2020).
71. Luo, Q. *et al.* Interleukin-33 Protects Ischemic Brain Injury by Regulating Specific Microglial Activities. *Neuroscience* **385**, 75–89 (2018).
72. Hamzei Taj, S. *et al.* Targeted intracerebral delivery of the anti-inflammatory cytokine IL13 promotes alternative activation of both microglia and macrophages after stroke. *J. Neuroinflammation* **15**, 1–17 (2018).
73. Chen, D. *et al.* Interleukin 13 promotes long-term recovery after ischemic stroke by inhibiting the activation of STAT3. *J. Neuroinflammation* **19**, 1–28 (2022).
74. Kolosowska, N. *et al.* Peripheral Administration of IL-13 Induces Anti-inflammatory Microglial/Macrophage Responses and Provides Neuroprotection in Ischemic Stroke. *Neurother. J. Am. Soc. Exp. Neurother.* **16**, 1304–1319 (2019).
75. Xie, D. *et al.* IL-33/ST2 Axis Protects Against Traumatic Brain Injury Through Enhancing the Function of Regulatory T Cells. *Front. Immunol.* **13**, 1–11 (2022).
76. Dahlgren, M. W. & Molofsky, A. B. All along the watchtower: group 2 innate lymphoid cells in allergic responses. *Curr. Opin. Immunol.* **54**, 13–19 (2018).
77. McGinty, J. W. & von Moltke, J. A three course menu for ILC and bystander T cell activation. *Curr. Opin. Immunol.* **62**, 15–21 (2020).
78. Molofsky, A. B., Savage, A. K. & Locksley, R. M. Interleukin-33 in Tissue Homeostasis, Injury, and Inflammation. *Immunity* **42**, 1005–1019 (2015).
79. Cayrol, C. & Girard, J. P. Interleukin-33 (IL-33): A nuclear cytokine from the IL-1 family. *Immunol. Rev.* **281**, 154–168 (2018).

80. Nussbaum, J. C. *et al.* Type 2 innate lymphoid cells control eosinophil homeostasis. *Nature* **502**, 245–248 (2013).
81. Van Dyken, S. J. & Locksley, R. M. Interleukin-4- and Interleukin-13-Mediated Alternatively Activated Macrophages: Roles in Homeostasis and Disease. *Annu. Rev. Immunol.* **31**, 317–343 (2013).
82. Gause, W. C., Wynn, T. A. & Allen, J. E. Type 2 immunity and wound healing: Evolutionary refinement of adaptive immunity by helminths. *Nat. Rev. Immunol.* **13**, 607–614 (2013).
83. Lloyd, C. M. & Snelgrove, R. J. Type 2 immunity: Expanding our view. *Sci. Immunol.* **3**, 1–12 (2018).
84. Rua, R. & McGavern, D. B. Advances in Meningeal Immunity. *Trends Mol. Med.* **24**, 542–559 (2018).
85. Norris, G. T. & Kipnis, J. Immune cells and CNS physiology: Microglia and beyond. *J. Exp. Med.* **216**, 60–70 (2019).
86. Derecki, N. C. *et al.* Regulation of learning and memory by meningeal immunity: a key role for IL-4. *J. Exp. Med.* **207**, 1067–1080 (2010).
87. Brombacher, T. M. *et al.* IL-13–Mediated Regulation of Learning and Memory. *J. Immunol.* **198**, 2681–2688 (2017).
88. Ribeiro, M. *et al.* Meningeal  $\gamma\delta$  T cell-derived IL-17 controls synaptic plasticity and short-term memory. *Sci. Immunol.* **4**, (2019).
89. Alves de Lima, K. *et al.* Meningeal  $\gamma\delta$  T cells regulate anxiety-like behavior via IL-17a signaling in neurons. *Nat. Immunol.* **21**, 1421–1429 (2020).
90. Gadani, S. P., Smirnov, I., Smith, A. T., Overall, C. C. & Kipnis, J. Characterization of meningeal type 2 innate lymphocytes and their response to CNS injury. *J. Exp. Med.* **214**, 285–296 (2017).
91. Fung, I. T. H. *et al.* Activation of group 2 innate lymphoid cells alleviates aging-associated cognitive decline. *J. Exp. Med.* **217**, e20190915 (2020).

92. Barron, J. J. *et al.* Group 2 innate lymphoid cells promote inhibitory synapse development and social behavior. *Science* **386**, eadi1025 (2024).
93. Liu, M. *et al.* Group 2 innate lymphoid cells suppress neuroinflammation and brain injury following intracerebral hemorrhage. *J. Cereb. Blood Flow Metab.* **44**, 355–366 (2024).
94. Zheng, P. *et al.* Group 2 innate lymphoid cells resolve neuroinflammation following cerebral ischaemia. *Stroke Vasc. Neurol.* **8**, 424–434 (2023).
95. Dahlgren, M. W. & Molofsky, A. B. Adventitial Cuffs: Regional Hubs for Tissue Immunity. *Trends Immunol.* **40**, 877–887 (2019).
96. Cautivo, K. M., Steer, C. A. & Molofsky, A. B. Immune outposts in the adventitia: One foot in sea and one on shore. *Curr. Opin. Immunol.* **64**, 34–41 (2020).
97. Sbierski-Kind, J., Mroz, N. & Molofsky, A. B. Perivascular stromal cells: Directors of tissue immune niches. *Immunol. Rev.* **302**, 1–22 (2021).
98. Stenmark, K. R. *et al.* The Adventitia: Essential Regulator of Vascular Wall Structure and Function. *Annu. Rev. Physiol.* **75**, 23–47 (2013).
99. Mahlaköiv, T. *et al.* Stromal cells maintain immune cell homeostasis in adipose tissue via production of interleukin-33. *Sci. Immunol.* **4**, (2019).
100. Rana, B. M. J. *et al.* A stromal cell niche sustains ILC2-mediated type-2 conditioning in adipose tissue. *J. Exp. Med.* jem.20190689 (2019) doi:10.1084/jem.20190689.
101. DeSisto, J. *et al.* Single-Cell Transcriptomic Analyses of the Developing Meninges Reveal Meningeal Fibroblast Diversity and Function. *Dev. Cell* **54**, 43-59.e4 (2020).
102. Rustenhoven, J. *et al.* Functional characterization of the dural sinuses as a neuroimmune interface. *Cell* 1–17 (2021) doi:10.1016/j.cell.2020.12.040.
103. Pikor, N. B., Cupovic, J., Onder, L., Gommerman, J. L. & Ludewig, B. Stromal Cell Niches in the Inflamed Central Nervous System. *J. Immunol.* **198**, 1775–1781 (2017).

104. Pikor, N. B. *et al.* Integration of Th17- and Lymphotoxin-Derived Signals Initiates Meningeal-Resident Stromal Cell Remodeling to Propagate Neuroinflammation. *Immunity* **43**, 1160–1173 (2015).
105. Labat-gest, V. & Tomasi, S. Photothrombotic ischemia: a minimally invasive and reproducible photochemical cortical lesion model for mouse stroke studies. *J. Vis. Exp. JoVE* 1–6 (2013) doi:10.3791/50370.
106. Lee, J. K. *et al.* Photochemically induced cerebral ischemia in a mouse model. *Surg. Neurol.* **67**, 620–625 (2007).
107. Reese, T. A. *et al.* Chitin induces accumulation in tissue of innate immune cells associated with allergy. *Nature* **447**, 92–96 (2007).
108. Croxford, A. L. *et al.* The Cytokine GM-CSF Drives the Inflammatory Signature of CCR2+ Monocytes and Licenses Autoimmunity. *Immunity* **43**, 502–514 (2015).
109. Fujimura, N. *et al.* CCR2 inhibition sequesters multiple subsets of leukocytes in the bone marrow. *Sci. Rep.* **5**, 11664 (2015).
110. Vainchtein, I. D. *et al.* Astrocyte-derived interleukin-33 promotes microglial synapse engulfment and neural circuit development. *Science* **1273**, 1269–1273 (2018).
111. Nguyen, P. T. *et al.* Microglial Remodeling of the Extracellular Matrix Promotes Synapse Plasticity. *Cell* **182**, 1–16 (2020).
112. Liang, H. E. *et al.* Divergent expression patterns of IL-4 and IL-13 define unique functions in allergic immunity. *Nat. Immunol.* **13**, 58–66 (2012).
113. Chen, W. Y., Hong, J., Gannon, J., Kakkar, R. & Lee, R. T. Myocardial pressure overload induces systemic inflammation through endothelial cell IL-33. *Proc. Natl. Acad. Sci. U. S. A.* **112**, 7249–7254 (2015).
114. Stogsdill, J. A. *et al.* Astrocytic neuroligins control astrocyte morphogenesis and synaptogenesis. *Nature* **551**, 192–197 (2017).

115. Han, R. T. *et al.* Microglial pattern recognition via IL-33 promotes synaptic refinement in developing corticothalamic circuits in mice. *J. Exp. Med.* **220**, (2023).
116. Das, A. *et al.* Monocyte and Macrophage Plasticity in Tissue Repair and Regeneration. *Am. J. Pathol.* **185**, 2596 (2015).
117. Saederup, N. *et al.* Selective chemokine receptor usage by central nervous system myeloid cells in CCR2-red fluorescent protein knock-in mice. *PLoS One* **5**, e13693 (2010).
118. Mohrs, M. *et al.* Differences between IL-4- and IL-4 receptor alpha-deficient mice in chronic leishmaniasis reveal a protective role for IL-13 receptor signaling. *J. Immunol. Baltim. Md 1950* **162**, 7302–8 (1999).
119. Schiavinato, A., Przyklenk, M., Kobbe, B., Paulsson, M. & Wagener, R. Collagen type VI is the antigen recognized by the ER-TR7 antibody. *Eur. J. Immunol.* **51**, 2345–2347 (2021).
120. Tuor, U. I., Deng, Q., Rushforth, D., Foniok, T. & Qiao, M. Model of minor stroke with mild peri-infarct ischemic injury. *J. Neurosci. Methods* **268**, 56–65 (2016).
121. Li, H. *et al.* Histological, cellular and behavioral assessments of stroke outcomes after photothrombosis-induced ischemia in adult mice. *BMC Neurosci.* **15**, 58 (2014).
122. Liguz-Leczna, M., Zakrzewska, R., Daniszewska, K. & Kossut, M. Functional assessment of sensory functions after photothrombotic stroke in the barrel field of mice. *Behav. Brain Res.* **261**, 202–209 (2014).
123. Bandet, M. V. & Winship, I. R. Aberrant cortical activity, functional connectivity, and neural assembly architecture after photothrombotic stroke in mice. *eLife* **12**, RP90080 (2024).
124. Chen, H.-R. *et al.* Fate mapping via CCR2-CreER mice reveals monocyte-to-microglia transition in development and neonatal stroke. *Sci. Adv.* **6**, eabb2119 (2020).
125. Yona, S. *et al.* Fate Mapping Reveals Origins and Dynamics of Monocytes and Tissue Macrophages under Homeostasis. *Immunity* **38**, 79–91 (2013).
126. Madisen, L. *et al.* A robust and high-throughput Cre reporting and characterization system for the whole mouse brain. *Nat. Neurosci.* **13**, 133–140 (2010).

127. Reese, T. A. *et al.* Chitin induces accumulation in tissue of innate immune cells associated with allergy. *Nature* **447**, 92–96 (2007).
128. Labat-gest, V. & Tomasi, S. Photothrombotic ischemia: a minimally invasive and reproducible photochemical cortical lesion model for mouse stroke studies. *J. Vis. Exp. JoVE* 50370 (2013) doi:10.3791/50370.
129. Lee, J. K. *et al.* Photochemically induced cerebral ischemia in a mouse model. *Surg Neurol* **67**, 620–5; discussion 625 (2007).
130. Liu, N.-W. *et al.* Evolutional Characterization of Photochemically Induced Stroke in Rats: a Multimodality Imaging and Molecular Biological Study. *Transl. Stroke Res.* **8**, 244–256 (2017).
131. Galatro, T. F., Vainchtein, I. D., Brouwer, N., Boddeke, E. W. G. M. & Eggen, B. J. L. Isolation of Microglia and Immune Infiltrates from Mouse and Primate Central Nervous System. *Methods Mol. Biol.* **1559**, 333–342 (2017).
132. Stogsdill, J. A. *et al.* Astrocytic neuroligins control astrocyte morphogenesis and synaptogenesis. *Nature* **551**, 192–197 (2017).
133. Kotas, M. E. & Locksley, R. M. Why Innate Lymphoid Cells? *Immunity* **48**, 1081–1090 (2018).
134. Gause, W. C., Wynn, T. A. & Allen, J. E. Type 2 immunity and wound healing: Evolutionary refinement of adaptive immunity by helminths. *Nat. Rev. Immunol.* **13**, 607–614 (2013).
135. Ricardo-Gonzalez, R. R. *et al.* Tissue signals imprint ILC2 identity with anticipatory function. *Nat. Immunol.* **19**, 1093–1099 (2018).
136. Sharkey, K. A. & Mawe, G. M. The enteric nervous system. *Physiol. Rev.* **103**, 1487–1564 (2023).
137. Spencer, N. J. & Hu, H. Enteric nervous system: sensory transduction, neural circuits and gastrointestinal motility. *Nat. Rev. Gastroenterol. Hepatol.* **17**, 338–351 (2020).

138. Han, R. T. *et al.* Microglial pattern recognition via IL-33 promotes synaptic refinement in developing corticothalamic circuits in mice. *J. Exp. Med.* **220**, (2023).
139. He, D. *et al.* Disruption of the IL-33-ST2-AKT signaling axis impairs neurodevelopment by inhibiting microglial metabolic adaptation and phagocytic function. *Immunity* **55**, 159-173.e9 (2022).
140. Nguyen, P. T. *et al.* Microglial Remodeling of the Extracellular Matrix Promotes Synapse Plasticity. *Cell* **182**, 388-403.e15 (2020).
141. Wang, Y. *et al.* Astrocyte-secreted IL-33 mediates homeostatic synaptic plasticity in the adult hippocampus. *Proc. Natl. Acad. Sci. U. S. A.* **118**, (2021).
142. Derecki, N. C. *et al.* Regulation of learning and memory by meningeal immunity: a key role for IL-4. *J. Exp. Med.* **207**, 1067–1080 (2010).
143. Brombacher, T. M. *et al.* IL-4R alpha deficiency influences hippocampal-BDNF signaling pathway to impair reference memory. *Sci. Rep.* **10**, 16506 (2020).
144. Brombacher, T. M. *et al.* IL-13-Mediated Regulation of Learning and Memory. *J. Immunol. Baltim. Md 1950* **198**, 2681–2688 (2017).
145. Hanuscheck, N. *et al.* Interleukin-4 receptor signaling modulates neuronal network activity. *J. Exp. Med.* **219**, (2022).
146. Vogelaar, C. F. *et al.* Fast direct neuronal signaling via the IL-4 receptor as therapeutic target in neuroinflammation. *Sci. Transl. Med.* **10**, eaao2304 (2018).
147. Fishell, G. & Kepecs, A. Interneuron Types as Attractors and Controllers. *Annu. Rev. Neurosci.* **43**, 1–30 (2020).
148. Herz, J. *et al.* GABAergic neuronal IL-4R mediates T cell effect on memory. *Neuron* **109**, 3609-3618.e9 (2021).
149. Li, S. *et al.* Interleukin-13 and its receptor are synaptic proteins involved in plasticity and neuroprotection. *Nat. Commun.* **14**, 200 (2023).

150. Yang, A. C. *et al.* Physiological blood–brain transport is impaired with age by a shift in transcytosis. *Nature* 1–6 (2020) doi:10.1038/s41586-020-2453-z.
151. Smyth, L. C. *et al.* Identification of direct connections between the dura and the brain. *Nature* **627**, 165 (2024).
152. Barron, J. J. *et al.* Group 2 innate lymphoid cells promote inhibitory synapse development and social behavior. *BioRxiv Prepr. Serv. Biol.* 2023.03.16.532850 (2023) doi:10.1101/2023.03.16.532850.
153. Guedes, J. R. *et al.* IL-4 shapes microglia-dependent pruning of the cerebellum during postnatal development. *Neuron* **111**, 3435–3449.e8 (2023).
154. Gadani, S. P., Walsh, J. T., Smirnov, I., Zheng, J. & Kipnis, J. The glia-derived alarmin IL-33 orchestrates the immune response and promotes recovery following CNS injury. *Neuron* **85**, 703–709 (2015).
155. Xie, D. *et al.* IL-33/ST2 Axis Protects Against Traumatic Brain Injury Through Enhancing the Function of Regulatory T Cells. *Front. Immunol.* **13**, (2022).
156. Luo, Q. *et al.* Interleukin-33 Protects Ischemic Brain Injury by Regulating Specific Microglial Activities. *Neuroscience* **385**, 75–89 (2018).
157. Ito, M. *et al.* Brain regulatory T cells suppress astrogliosis and potentiate neurological recovery. *Nature* **565**, 246–250 (2019).
158. Pomeshchik, Y. *et al.* Interleukin-33 treatment reduces secondary injury and improves functional recovery after contusion spinal cord injury. *Brain. Behav. Immun.* **44**, 68–81 (2015).
159. Korhonen, P. *et al.* Immunomodulation by interleukin-33 is protective in stroke through modulation of inflammation. *Brain. Behav. Immun.* **49**, 322–336 (2015).
160. Zhang, S. R. *et al.* IL-33 modulates inflammatory brain injury but exacerbates systemic immunosuppression following ischemic stroke. *JCI Insight* **3**, e121560, 121560 (2018).



161. Xiong, X. *et al.* Increased Brain Injury and Worsened Neurological Outcome in Interleukin-4 Knockout Mice After Transient Focal Cerebral Ischemia. *Stroke* **42**, 2026–2032 (2011).
162. Miao, W. *et al.* IL-13 Ameliorates Neuroinflammation and Promotes Functional Recovery after Traumatic Brain Injury. *J. Immunol. Baltim. Md 1950* **204**, 1486–1498 (2020).
163. Chen, D. *et al.* Interleukin 13 promotes long-term recovery after ischemic stroke by inhibiting the activation of STAT3. *J. Neuroinflammation* **19**, (2022).
164. Hamzei Taj, S. *et al.* Targeted intracerebral delivery of the anti-inflammatory cytokine IL13 promotes alternative activation of both microglia and macrophages after stroke. *J. Neuroinflammation* **15**, (2018).
165. Zhang, J. *et al.* Recent advances in Alzheimer's disease: mechanisms, clinical trials and new drug development strategies. *Signal Transduct. Target. Ther.* **9**, 1–35 (2024).
166. Fung, I. T. H. *et al.* Activation of group 2 innate lymphoid cells alleviates aging-associated cognitive decline. *J. Exp. Med.* **217**, (2020).
167. Baruch, K. *et al.* CNS-specific immunity at the choroid plexus shifts toward destructive Th2 inflammation in brain aging. *Proc. Natl. Acad. Sci. U. S. A.* **110**, 2264–2269 (2013).
168. Fung, I. T. H. *et al.* Group 2 innate lymphoid cells are numerically and functionally deficient in the triple transgenic mouse model of Alzheimer's disease. *J. Neuroinflammation* **18**, (2021).
169. Kiyota, T. *et al.* CNS expression of anti-inflammatory cytokine interleukin-4 attenuates Alzheimer's disease-like pathogenesis in APP+PS1 bigenic mice. *FASEB J. Off. Publ. Fed. Am. Soc. Exp. Biol.* **24**, 3093–3102 (2010).
170. Kawahara, K. *et al.* Intracerebral microinjection of interleukin-4/interleukin-13 reduces  $\beta$ -amyloid accumulation in the ipsilateral side and improves cognitive deficits in young amyloid precursor protein 23 mice. *Neuroscience* **207**, 243–260 (2012).
171. Fu, A. K. Y. *et al.* IL-33 ameliorates Alzheimer's disease-like pathology and cognitive decline. *Proc. Natl. Acad. Sci. U. S. A.* **113**, E2705-2713 (2016).

172. Lau, S.-F. *et al.* IL-33-PU.1 Transcriptome Reprogramming Drives Functional State Transition and Clearance Activity of Microglia in Alzheimer's Disease. *Cell Rep.* **31**, 107530 (2020).
173. Jiang, Y. *et al.* An IL1RL1 genetic variant lowers soluble ST2 levels and the risk effects of APOE-ε4 in female patients with Alzheimer's disease. *Nat. Aging* **2**, 616–634 (2022).
174. Rabenhorst, A. & Hartmann, K. Interleukin-31: A Novel Diagnostic Marker of Allergic Diseases. *Curr. Allergy Asthma Rep.* **14**, 423 (2014).
175. Dillon, S. R. *et al.* Interleukin 31, a cytokine produced by activated T cells, induces dermatitis in mice. *Nat. Immunol.* **5**, 752–760 (2004).
176. Cevikbas, F. *et al.* A sensory neuron-expressed IL-31 receptor mediates T helper cell-dependent itch: Involvement of TRPV1 and TRPA1. *J. Allergy Clin. Immunol.* **133**, 448–460 (2014).
177. Fassett, M. S. *et al.* IL-31-dependent neurogenic inflammation restrains cutaneous type 2 immune response in allergic dermatitis. *Sci. Immunol.* **8**, (2023).
178. Trier, A. M. *et al.* IL-33 signaling in sensory neurons promotes dry skin itch. *J. Allergy Clin. Immunol.* **149**, 1473-1480.e6 (2022).
179. Liu, B. *et al.* IL-33/ST2 signaling excites sensory neurons and mediates itch response in a mouse model of poison ivy contact allergy. *Proc. Natl. Acad. Sci.* **113**, E7572–E7579 (2016).
180. Wilson, S. R. *et al.* The epithelial cell-derived atopic dermatitis cytokine TSLP activates neurons to induce itch. *Cell* **155**, 285–295 (2013).
181. Okano, M. *et al.* Interleukin-33-activated neuropeptide CGRP-producing memory Th2 cells cooperate with somatosensory neurons to induce conjunctival itch. *Immunity* **55**, 2352-2368.e7 (2022).
182. Huang, J. *et al.* Hyperactivity of Innate Immunity Triggers Pain via TLR2-IL-33-Mediated Neuroimmune Crosstalk. *Cell Rep.* **33**, 108233 (2020).

183. Oetjen, L. K. *et al.* Sensory Neurons Co-opt Classical Immune Signaling Pathways to Mediate Chronic Itch. *Cell* **171**, 217-228.e13 (2017).
184. Del Bel, K. L. *et al.* JAK1 gain-of-function causes an autosomal dominant immune dysregulatory and hypereosinophilic syndrome. *J. Allergy Clin. Immunol.* **139**, 2016-2020.e5 (2017).
185. Ahrends, T. *et al.* Enteric pathogens induce tissue tolerance and prevent neuronal loss from subsequent infections. *Cell* **184**, 5715-5727.e12 (2021).
186. Tamari, M. *et al.* Sensory neurons promote immune homeostasis in the lung. *Cell* **187**, 44-61.e17 (2024).
187. Rodig, S. J. *et al.* Disruption of the Jak1 gene demonstrates obligatory and nonredundant roles of the Jaks in cytokine-induced biologic responses. *Cell* **93**, 373–383 (1998).
188. Salvador, A. F., de Lima, K. A. & Kipnis, J. Neuromodulation by the immune system: a focus on cytokines. *Nat. Rev. Immunol.* **21**, 526–541 (2021).
189. Koren, T. & Rolls, A. Immunoception: Defining brain-regulated immunity. *Neuron* **110**, 3425–3428 (2022).
190. Rolls, A. Immunoception: the insular cortex perspective. *Cell. Mol. Immunol.* **20**, 1270–1276 (2023).
191. Poller, W. C. *et al.* Brain motor and fear circuits regulate leukocytes during acute stress. *Nature* **607**, 578–584 (2022).
192. Koren, T. *et al.* Insular cortex neurons encode and retrieve specific immune responses. *Cell* **184**, 6211 (2021).
193. Steinberg, B. E. *et al.* Cytokine-specific Neurograms in the Sensory Vagus Nerve. *Bioelectron. Med.* **3**, 7–17 (2016).
194. Konsman, J. P., Parnet, P. & Dantzer, R. Cytokine-induced sickness behaviour: mechanisms and implications. *Trends Neurosci.* **25**, 154–159 (2002).

195. Pinho-Ribeiro, F. A. *et al.* Bacteria hijack a meningeal neuroimmune axis to facilitate brain invasion. *Nature* **615**, 472–481 (2023).
196. Granton, E. *et al.* Biofilm exopolysaccharides alter sensory-neuron-mediated sickness during lung infection. *Cell* **187**, 1874-1888.e14 (2024).
197. Chiu, I. M. *et al.* Bacteria activate sensory neurons that modulate pain and inflammation. *Nature* **501**, 52–57 (2013).
198. Bin, N.-R. *et al.* An airway-to-brain sensory pathway mediates influenza-induced sickness. *Nature* **615**, 660–667 (2023).
199. Jin, H., Li, M., Jeong, E., Castro-Martinez, F. & Zuker, C. S. A body-brain circuit that regulates body inflammatory responses. *Nature* **630**, 695–703 (2024).
200. Florsheim, E. B. *et al.* Immune sensing of food allergens promotes avoidance behaviour. *Nature* **620**, 643–650 (2023).
201. Plum, T. *et al.* Mast cells link immune sensing to antigen-avoidance behaviour. *Nature* **620**, 634–642 (2023).
202. Su, Y. *et al.* Brainstem Dbh<sup>+</sup> neurons control allergen-induced airway hyperreactivity. *Nature* 1–9 (2024) doi:10.1038/s41586-024-07608-5.
203. Talbot, S. *et al.* Silencing Nociceptor Neurons Reduces Allergic Airway Inflammation. *Neuron* **87**, 341–354 (2015).
204. Tränkner, D., Hahne, N., Sugino, K., Hoon, M. A. & Zuker, C. Population of sensory neurons essential for asthmatic hyperreactivity of inflamed airways. *Proc. Natl. Acad. Sci.* **111**, 11515–11520 (2014).
205. Bao, C. *et al.* A mast cell-thermoregulatory neuron circuit axis regulates hypothermia in anaphylaxis. *Sci. Immunol.* **8**, eadc9417 (2023).
206. Cao, Y. *et al.* Dopamine inhibits group 2 innate lymphoid cell-driven allergic lung inflammation by dampening mitochondrial activity. *Immunity* **56**, 320-335.e9 (2023).

207. Liu, T. *et al.* Local sympathetic innervations modulate the lung innate immune responses. *Sci. Adv.* **6**, eaay1497 (2020).
208. Cardoso, F. *et al.* Neuro-mesenchymal units control ILC2 and obesity via a brain–adipose circuit. *Nature* **597**, 410–414 (2021).
209. Moriyama, S. *et al.*  $\beta$ 2-adrenergic receptor–mediated negative regulation of group 2 innate lymphoid cell responses. *Science* **359**, 1056–1061 (2018).
210. Matheis, F. *et al.* Adrenergic Signaling in Muscularis Macrophages Limits Infection-Induced Neuronal Loss. *Cell* **180**, 64-78.e16 (2020).
211. Roberts, L. B. *et al.* Acetylcholine production by group 2 innate lymphoid cells promotes mucosal immunity to helminths. *Sci. Immunol.* **6**, eabd0359 (2021).
212. Chu, C. *et al.* The ChAT-acetylcholine pathway promotes group 2 innate lymphoid cell responses and anti-helminth immunity. *Sci. Immunol.* **6**, eabe3218 (2021).
213. Cox, M. A. *et al.* Choline acetyltransferase-expressing T cells are required to control chronic viral infection. *Science* **363**, 639–644 (2019).
214. Zhu, X. *et al.* Somatosensory cortex and central amygdala regulate neuropathic pain-mediated peripheral immune response via vagal projections to the spleen. *Nat. Neurosci.* **27**, 471–483 (2024).
215. Wallrapp, A. *et al.* Calcitonin Gene-Related Peptide Negatively Regulates Alarmin-Driven Type 2 Innate Lymphoid Cell Responses. *Immunity* **51**, 709-723.e6 (2019).
216. Sui, P. *et al.* Pulmonary neuroendocrine cells amplify allergic asthma responses. *Science* **360**, eaan8546 (2018).
217. Nagashima, H. *et al.* Neuropeptide CGRP Limits Group 2 Innate Lymphoid Cell Responses and Constrains Type 2 Inflammation. *Immunity* **51**, 682-695.e6 (2019).
218. Tamari, M. *et al.* Sensory neurons promote immune homeostasis in the lung. *Cell* **187**, 44-61.e17 (2024).


219. Lu, Y. Z. *et al.* CGRP sensory neurons promote tissue healing via neutrophils and macrophages. *Nature* **628**, 604–611 (2024).
220. Xu, H. *et al.* Transcriptional Atlas of Intestinal Immune Cells Reveals that Neuropeptide  $\alpha$ -CGRP Modulates Group 2 Innate Lymphoid Cell Responses. *Immunity* **51**, 696-708.e9 (2019).
221. Yang, D. *et al.* Nociceptor neurons direct goblet cells via a CGRP-RAMP1 axis to drive mucus production and gut barrier protection. *Cell* **185**, 4190-4205.e25 (2022).
222. Cardoso, V. *et al.* Neuronal regulation of type 2 innate lymphoid cells via neuromedin U. *Nature* **549**, 277–281 (2017).
223. Li, Y. *et al.* Neuromedin U programs eosinophils to promote mucosal immunity of the small intestine. *Science* **381**, 1189–1196 (2023).
224. Tsou, A. M. *et al.* Neuropeptide regulation of non-redundant ILC2 responses at barrier surfaces. *Nature* **611**, 787–793 (2022).
225. Klose, C. S. N. *et al.* The neuropeptide neuromedin U stimulates innate lymphoid cells and type 2 inflammation. *Nature* **549**, 282–286 (2017).
226. Wallrapp, A. *et al.* The neuropeptide NMU amplifies ILC2-driven allergic lung inflammation. *Nature* **549**, 351–356 (2017).
227. Ju, X. *et al.* Neuromedin-U Mediates Rapid Activation of Airway Group 2 Innate Lymphoid Cells in Mild Asthma. *Am. J. Respir. Crit. Care Med.* (2024) doi:10.1164/RCCM.202311-2164OC.
228. Inclan-Rico, J. M. *et al.* Basophils prime group 2 innate lymphoid cells for neuropeptide-mediated inhibition. *Nat. Immunol.* **21**, 1181–1193 (2020).
229. Green, D. P., Limjunyawong, N., Gour, N., Pundir, P. & Dong, X. A Mast-Cell-Specific Receptor Mediates Neurogenic Inflammation and Pain. *Neuron* **101**, 412-420.e3 (2019).

230. Perner, C. *et al.* Substance P Release by Sensory Neurons Triggers Dendritic Cell Migration and Initiates the Type-2 Immune Response to Allergens. *Immunity* **53**, 1063-1077.e7 (2020).
231. Serhan, N. *et al.* House dust mites activate nociceptor-mast cell clusters to drive type 2 skin inflammation. *Nat. Immunol.* **20**, 1435–1443 (2019).
232. Crosson, T. *et al.* FcεR1-expressing nociceptors trigger allergic airway inflammation. *J. Allergy Clin. Immunol.* **147**, 2330–2342 (2021).
233. Mathur, S. *et al.* Nociceptor neurons promote IgE class switch in B cells. *JCI Insight* **6**, e148510 (2021).
234. Jain, A. *et al.* Nociceptor-immune interactomes reveal insult-specific immune signatures of pain. *Nat. Immunol.* (2024) doi:10.1038/s41590-024-01857-2.
235. Hoeffel, G. *et al.* Sensory neuron-derived TFAFA4 promotes macrophage tissue repair functions. *Nature* **594**, 94–99 (2021).
236. Pascal, M. *et al.* The neuropeptide VIP potentiates intestinal innate type 2 and type 3 immunity in response to feeding. *Mucosal Immunol.* **15**, 629–641 (2022).
237. Han, Y., Woo, Y. R., Cho, S. H., Lee, J. D. & Kim, H. S. Itch and Janus Kinase Inhibitors. *Acta Derm. Venereol.* 5346 (2023) doi:10.2340/actadv.v103.5346.
238. Harb, H. & Chatila, T. A. Mechanisms of Dupilumab. *Clin. Exp. Allergy* **50**, 5–14 (2020).

## Publishing Agreement

It is the policy of the University to encourage open access and broad distribution of all theses, dissertations, and manuscripts. The Graduate Division will facilitate the distribution of UCSF theses, dissertations, and manuscripts to the UCSF Library for open access and distribution. UCSF will make such theses, dissertations, and manuscripts accessible to the public and will take reasonable steps to preserve these works in perpetuity.

I hereby grant the non-exclusive, perpetual right to The Regents of the University of California to reproduce, publicly display, distribute, preserve, and publish copies of my thesis, dissertation, or manuscript in any form or media, now existing or later derived, including access online for teaching, research, and public service purposes.

DocuSigned by:  
  
E1390D519D674F4... Author Signature

11/20/2024  
Date